

## Durham E-Theses

---

*Simulation of non-conservative transport using particle tracking methods with an application to soils contaminated with heavy metals.*

BARNARD, JACK,MICHAEL

### How to cite:

---

BARNARD, JACK,MICHAEL (2014) *Simulation of non-conservative transport using particle tracking methods with an application to soils contaminated with heavy metals.*, Durham theses, Durham University. Available at Durham E-Theses Online: <http://etheses.dur.ac.uk/10625/>

### Use policy

---

The full-text may be used and/or reproduced, and given to third parties in any format or medium, without prior permission or charge, for personal research or study, educational, or not-for-profit purposes provided that:

- a full bibliographic reference is made to the original source
- a [link](#) is made to the metadata record in Durham E-Theses
- the full-text is not changed in any way

The full-text must not be sold in any format or medium without the formal permission of the copyright holders.

Please consult the [full Durham E-Theses policy](#) for further details.

# Simulation of non-conservative transport using particle tracking methods with an application to soils contaminated with heavy metals.

Jack Michael Barnard

Thesis submitted towards the  
degree of Doctor of Philosophy



School of Engineering and Computing Sciences  
Durham University  
United Kingdom

December 2013

Jack M. Barnard

## Abstract

This thesis focuses on the development and application of a discrete time random walk particle tracking model to the simulation of non-conservative transport in porous media. The model includes the simulation of solute transport, reversible bimolecular reactions, and sorption. The functionality of the discrete time random walk method is expanded to allow for the simulation of more complicated chemical systems than previously achieved. The bimolecular reaction simulation is based on a collocation probability function method. This reaction simulation method is analysed to investigate the effects of the controlling parameters on its behaviour. This knowledge is then used to inform a discussion of its application to the simulation of mixing limited reactive transport and comparison with other approaches. The reaction simulation method developed in the thesis possesses a greater flexibility than previously developed methods for the simulation of reactions using particle tracking.

The developed model is also applied, in combination with a chemical speciation model, to enable the production of a reduced complexity model to simulate effects of an amendment scheme on soils contaminated with heavy metals. The effect of the soil amendment scheme on the partitioning of Pb between solution, soil surfaces, and dissolved organic matter is approximated by rules fitted as functions of concentrations of single components within the soil amendment. This allows for the simulation of complicated chemical systems using particle tracking methods.

As well as expanding the functionality of particle tracking methods the issue of the computational expense is also addressed. A scheme for the optimization of the reaction simulation is presented and its effectiveness investigated. Together with the use of graphics processing units for code acceleration, the computational and temporal expense of the solution is reduced. The combination of the expansion in functionality and reduction in run time makes particle tracking a more attractive simulation method.

# Declaration

The work in this thesis is based on research carried out in the Computational Mechanics Group, School of Engineering and Computing Sciences, Durham University. No part of this report has been submitted elsewhere for any other degree or qualification and it is all my own work unless referenced to the contrary in the text. Parts of this work have been published in the following:

## Conferences

### **UK National Conference on Computational Mechanics in Engineering 2011.**

Oral Presentation, ‘Computational modelling of contaminated land: development of a combined stochastic-deterministic model for mass transfer in variably saturated porous media.’ Paper submitted to proceedings.

### **AGU Fall Meeting 2012.**

Oral Presentation, ‘A GPU accelerated, discrete time random walk model for simulating reactive transport in porous media using collocation probability function based reaction methods.’

### **CM13: International Conference on Computational Mechanics 2013.**

Oral Presentation, ‘Simulation of mixing limited bimolecular reactive transport in porous media using particle tracking methods.’ Peer reviewed paper submitted to proceedings.

Copyright © 2013 by Jack M. Barnard.

“The copyright of this thesis rests with the author. No quotations from it should be published without the authors prior written consent and information derived from it should be acknowledged.”

# Acknowledgements

This thesis would not have been possible without the guidance and patience of my supervisors, Charles Augarde and Karen Johnson. This research would not have been possible without generous funding from the U.K. Engineering and Physical Sciences Research Council (EPSRC) via Challenging Engineering Grant EP/G028958/1. The GPU utilised to perform simulations presented in this thesis was been supplied by Nvidia under the Academic Partnership Programme.

Jack Barnard  
Durham, December 2013

# Contents

<b>Abstract</b>	
<b>Declaration</b>	<b>i</b>
<b>Acknowledgements</b>	<b>ii</b>
<b>Contents</b>	<b>iii</b>
<b>List of Figures</b>	<b>v</b>
<b>List of Tables</b>	<b>ix</b>
<b>List of Algorithms</b>	<b>x</b>
<b>Acronyms</b>	<b>xi</b>
<b>1 Introduction</b>	<b>1</b>
1.1 Rationale . . . . .	1
1.2 The Regeneration of Brownfield Using Sustainable Technology (ROBUST) Project . . . . .	2
1.3 Thesis Aims . . . . .	2
1.4 Thesis Overview . . . . .	3
<b>2 Porous Media Flow</b>	<b>4</b>
2.1 Introduction . . . . .	4
2.2 Saturated Porous Media Flow . . . . .	5
2.3 Finite Element Method . . . . .	5
2.4 Conclusion . . . . .	7
<b>3 Conservative Solute Transport</b>	<b>8</b>
3.1 Introduction . . . . .	8
3.2 Particle Tracking Methods . . . . .	10
3.2.1 Path Line Solution . . . . .	11
3.2.2 Discrete Time Random Walk (DTRW) Solution . . . . .	12
3.2.3 DTRW Implementation . . . . .	13
3.2.4 Benchmarking . . . . .	14
3.3 Conclusion . . . . .	23
<b>4 Non Conservative Transport</b>	<b>24</b>
4.1 Introduction . . . . .	24
4.2 Homogeneous Reactions . . . . .	24
4.2.1 Simulating Reactions using Particle Tracking Methods . . . . .	26
Colocation Probability Functions . . . . .	27
Implementation of Reaction Solution . . . . .	29
Reaction Rate Controls . . . . .	30
4.2.2 Benchmarking . . . . .	33
Limiting reaction rates using $\mathbf{P}_{\max}$ . . . . .	36
Limiting reaction rates using $\sigma_s$ . . . . .	40

	Differences between using CTRW or DTRW for reactions . . . . .	40
	Sensitivity Analysis . . . . .	43
4.2.3	Comparison with other numerical simulation studies . . . . .	44
	Sanchez-Vila <i>et al.</i> , 2010 . . . . .	48
	Edery <i>et al.</i> , 2010 . . . . .	49
	Ding <i>et al.</i> , 2012 . . . . .	50
	Zhang <i>et al.</i> , 2013 . . . . .	54
4.3	Sorption . . . . .	54
4.3.1	Simulating Sorption using Particle Tracking Methods . . . . .	55
	Simulating sorption using the DTRW method . . . . .	55
4.3.2	Benchmarking . . . . .	56
4.4	Conclusion . . . . .	61
<b>5</b>	<b>Application to ROBUST</b>	<b>62</b>
5.1	Introduction . . . . .	62
5.2	Sorption Chemistry . . . . .	62
5.2.1	Lead Sorption . . . . .	64
5.3	Sorption Models . . . . .	65
5.4	Windermere Humic Aqueous Model (WHAM) and assessment of key controls . . . . .	66
5.5	Reduced complexity simulations of soil-WTR systems using DTRW . . . . .	73
5.5.1	DTRW methodology for soil-WTR systems . . . . .	76
5.6	Simulations . . . . .	77
5.7	Discussion . . . . .	83
5.8	Conclusion . . . . .	85
<b>6</b>	<b>Optimization and Acceleration of Computer Code</b>	<b>86</b>
6.1	Introduction . . . . .	86
6.2	Optimization of Nearest Neighbour Searches . . . . .	87
6.2.1	Optimization Scheme Implementation . . . . .	87
6.2.2	Optimization Scheme Effectiveness . . . . .	89
6.3	Code Acceleration Using Graphics Processing Units . . . . .	94
6.4	Conclusion . . . . .	98
<b>7</b>	<b>Conclusions</b>	<b>100</b>
	<b>References</b>	<b>103</b>

# List of Figures

2.1	A two dimensional, four noded element in local and global coordinate systems. . . . .	6
3.1	Experimental setup used by Gramling <i>et al.</i> , (2002) and simulated using the DTRW method.	14
3.2	Comparison of DTRW solution and experimental data from Gramling <i>et al.</i> , (2002) at a) 532 s, b) 1032 s, c) 1523 s and d) 2023 s. The DTRW solution is the average of 10 simulations with a maximum particle density of 900 per cm <sup>2</sup> and $\Delta t = 1$ s. . . . .	16
3.3	The effect of particle density on the standard deviation of the DTRW solution. . . . .	16
3.4	Comparison of DTRW solution and experimental data from Gramling <i>et al.</i> , (2002) at 532 s. The DTRW solution is the average of nine simulations with a maximum particle density of 100 per cm <sup>2</sup> and $\Delta t = 1$ s. . . . .	18
3.5	Comparison of DTRW solution and experimental data from Gramling <i>et al.</i> , (2002) at 532 s. The DTRW solution is a single simulation maximum particle density of 900 per cm <sup>2</sup> and $\Delta t = 1$ s. . . . .	18
3.6	Comparison of DTRW solution and experimental data from Gramling <i>et al.</i> , (2002) at 532 s. The DTRW solution is the average of 10 simulations with a maximum particle density of 100 per cm <sup>2</sup> and $\Delta t = 1$ s. . . . .	19
3.7	Comparison of DTRW solution and experimental data from Gramling <i>et al.</i> , (2002) at 532 s. The DTRW solution is the average of 10 simulations with a maximum particle density of 900 per cm <sup>2</sup> and $\Delta t = 1$ s. . . . .	19
3.8	Comparison of DTRW solution and experimental data from Gramling <i>et al.</i> , (2002) at 532 s. The DTRW solution is the average of 10 simulations with a maximum particle density of 2500 per cm <sup>2</sup> and $\Delta t = 1$ s. . . . .	20
3.9	Comparison of DTRW solution and experimental data from Gramling <i>et al.</i> , (2002) at 532 s. The DTRW solution is the average of 10 simulations with a maximum particle density of 900 per cm <sup>2</sup> and $\Delta t = 0.1$ s. . . . .	20
3.10	Comparison of DTRW solution and experimental data from Gramling <i>et al.</i> , (2002) at 532 s. The DTRW solution is the average of 10 simulations with a maximum particle density of 900 per cm <sup>2</sup> and $\Delta t = 1$ s. . . . .	21
3.11	Comparison of DTRW solution and experimental data from Gramling <i>et al.</i> , (2002) at 532 s. The DTRW solution is the average of 10 simulations with a maximum particle density of 900 per cm <sup>2</sup> and $\Delta t = 4$ s. . . . .	21
3.12	Comparison of DTRW solution and experimental data from Gramling <i>et al.</i> , (2002) at 532 s. The DTRW solution is the average of 10 simulations with a maximum particle density of 900 per cm <sup>2</sup> and $\Delta t = 28$ s. . . . .	22
3.13	Comparison of DTRW solution and experimental data from Gramling <i>et al.</i> , (2002) at 532 s. The DTRW solution is the average of 10 simulations with a maximum particle density of 900 per cm <sup>2</sup> , $\Delta t = 1$ s and an underlying finite element grid of 0.25 cm by 0.25 cm elements. . . . .	22
3.14	Comparison of DTRW solution and experimental data from Gramling <i>et al.</i> , (2002) at 532 s. The DTRW solution is the average of 10 simulations with a maximum particle density of 900 per cm <sup>2</sup> , $\Delta t = 1$ s and an underlying finite element grid of 2 cm by 2 cm elements.	23
4.1	A $\log(x)$ graph of $D_h$ against single step reaction rate for initial particle densities ranging from 25 per cm <sup>2</sup> to 2500 per cm <sup>2</sup> and $P_{max} = 1$ . . . . .	31

4.2	A log-log graph showing the relationship between particle density and the average distance of a particle from its nearest neighbour in a second species. . . . .	32
4.3	A graph of $P_{max}$ against single step reaction rate for initial particle densities ranging from 25 per cm <sup>2</sup> to 2500 per cm <sup>2</sup> and $D_h = 1$ . . . . .	32
4.4	A graph of $P_{max}$ against single step reaction rate for number of reaction attempts ranging from 1 to 32 and $D_h = 1$ . . . . .	34
4.5	A graph of $D_h$ against single step reaction rate for number of reaction attempts ranging from 1 to 32 and $P_{max} = 1$ . . . . .	34
4.6	Experimental setup used by Gramling <i>et al.</i> , (2002) and simulated using the DTRW method.	35
4.7	Reproduction and compilation of Figure 5a) from Gramling <i>et al.</i> , (2002) showing experimental data and analytical solutions for 619s, 916s and 1510s. The overprediction of reaction rate caused by the assumption of perfect mixing between reactants is clear. . . . .	35
4.8	Reactant and product concentration profiles for simulation of Gramling <i>et al.</i> , (2002) experiment with $P_{max} = 1$ with non-reactive solute profiles for comparison. . . . .	36
4.9	Comparison of the simulation results for $P_{max} = 1$ with experimental data from Gramling <i>et al.</i> , (2002). . . . .	37
4.10	Comparison of the simulation results for $P_{max} = 10^{-1}$ with experimental data from Gramling <i>et al.</i> , (2002). . . . .	37
4.11	Comparison of the simulation results for $P_{max} = 10^{-2}$ with experimental data from Gramling <i>et al.</i> , (2002). . . . .	38
4.12	Comparison of the simulation results for $P_{max} = 10^{-3}$ with experimental data from Gramling <i>et al.</i> , (2002). . . . .	38
4.13	Comparison of the simulation results for $P_{max} = 0.0025$ with experimental data from Gramling <i>et al.</i> , (2002). . . . .	39
4.14	Reactant and product concentration profiles for simulation of Gramling <i>et al.</i> , (2002) experiment with $P_{max} = 0.0025$ with non-reactive solute profiles for comparison. . . . .	39
4.15	Comparison of the simulation results for $\sigma_s = 1$ with experimental data from Gramling <i>et al.</i> , (2002). . . . .	41
4.16	Comparison of the simulation results for $\sigma_s = 10^{-2}$ with experimental data from Gramling <i>et al.</i> , (2002). . . . .	41
4.17	Comparison of the simulation results for $\sigma_s = 10^{-3}$ with experimental data from Gramling <i>et al.</i> , (2002). . . . .	42
4.18	Comparison of the simulation results for $\sigma_s = 10^{-4}$ with experimental data from Gramling <i>et al.</i> , (2002). . . . .	42
4.23	Comparison of the simulation results for $P_{max} = 0.0025$ with experimental data from Gramling <i>et al.</i> , (2002). . . . .	44
4.19	A log( $x$ ) graph of $D_h$ against single step reaction rate for initial particle densities ranging from 25 per cm <sup>2</sup> to 2500 per cm <sup>2</sup> and $P_{max} = 1$ for DTRW (solid lines) and Continuous Time Random Walk (CTRW) (dashed lines). . . . .	45
4.20	Comparison of the simulation results for $P_{max} = 0.0006$ with experimental data from Gramling <i>et al.</i> , (2002). . . . .	45
4.21	Comparison of the simulation results for $P_{max} = 0.0025$ with experimental data from Gramling <i>et al.</i> , (2002). . . . .	46
4.22	Comparison of the simulation results for $P_{max} = 0.02$ with experimental data from Gramling <i>et al.</i> , (2002). . . . .	46
4.24	Comparison of the simulation results for $P_{max} = 0.0025$ with experimental data from Gramling <i>et al.</i> , (2002). . . . .	47
4.25	Comparison of the simulation results for $P_{max} = 0.0025$ with experimental data from Gramling <i>et al.</i> , (2002). . . . .	47
4.26	Comparison of the simulation results for $P_{max} = 0.0025$ with experimental data from Gramling <i>et al.</i> , (2002) at 619 s, 916 s and 1510 s. . . . .	48
4.27	Comparison of the simulation results presented by Sanchez-Vila <i>et al.</i> , (2010) with experimental data from Gramling <i>et al.</i> , (2002). . . . .	49
4.28	Comparison of the simulation results presented by Edery <i>et al.</i> , (2010) with experimental data from Gramling <i>et al.</i> , (2002). . . . .	50
4.29	Comparison of the DTRW simulation results for initial particle density = 256 per cm <sup>2</sup> with experimental data from Gramling <i>et al.</i> , (2002). . . . .	51

4.30	Comparison of the simulation results presented by Ding <i>et al.</i> , (2012) with experimental data from Gramling <i>et al.</i> , (2002). . . . .	52
4.31	Comparison of DTRW simulation results using arbitrary fitted adsorption and desorption probabilities for particle density of 900 per cm <sup>2</sup> and $\Delta t = 5$ s, 10 s, and 20 s with experimental data from Rubin <i>et al.</i> , (2012). . . . .	59
4.32	Comparison of DTRW simulation results using adsorption and desorption probabilities based on an adsorption isotherm for particle density of 900 per cm <sup>2</sup> and $\Delta t = 5$ s, 10 s, and 20 s with experimental data from Rubin <i>et al.</i> , (2012). . . . .	59
4.33	Comparison of DTRW simulation results using adsorption and desorption probabilities based on an adsorption isotherm for particle densities of 100, 400 and 900 per cm <sup>2</sup> and $\Delta t = 10$ s with experimental data from Rubin <i>et al.</i> , (2012). . . . .	60
5.1	The adsorption isotherm for Lead onto soil A with water treatment residuals additions of 5%, 10% and 20%. . . . .	70
5.2	The adsorption isotherm for Lead onto soil B with water treatment residuals additions of 5%, 10% and 20%. . . . .	70
5.3	The adsorption isotherm for Lead onto soil C with water treatment residuals additions of 5%, 10% and 20%. . . . .	71
5.4	The relationship between total Lead and Lead bound to dissolved organic Carbon for soil A with water treatment residuals additions of 5%, 10% and 20%. . . . .	71
5.5	The relationship between total Lead and Lead bound to dissolved organic Carbon for soil B with water treatment residuals additions of 5%, 10% and 20%. . . . .	72
5.6	The relationship between total Lead and Lead bound to dissolved organic Carbon for soil C with water treatment residuals additions of 5%, 10% and 20%. . . . .	72
5.7	Dissolved Organic Matter (DOM) concentration against $K_d$ for soils A, B and C in their original states and with 5%, 10% and 20% Water Treatment Residual (WTR) addition. . . . .	74
5.8	Soil Organic Matter (SOM) concentration against $K_d$ for soils A, B and C in their original states and with 5%, 10% and 20% WTR addition. . . . .	75
5.9	Fe concentration against $K_d$ for soils A, B and C in their original states and with 5%, 10% and 20% WTR addition. . . . .	75
5.10	Evolution of $K_d$ over time in a system simulating sorption of Pb to soil surface and DOM for soil A with different WTR additions with equilibrium positions taken from WHAM outputs. . . . .	79
5.11	Evolution of $K_d$ over time in a system simulating sorption of Pb to soil surface and DOM for soil A with different WTR additions with equilibrium positions taken from fitted curves. . . . .	79
5.12	Evolution of $K_d$ over time in a system simulating sorption of Pb to soil surface and DOM for soil B with different WTR additions with equilibrium positions taken from fitted curves. . . . .	80
5.13	Evolution of $K_d$ over time in a system simulating sorption of Pb to soil surface and DOM for soil C with different WTR additions with equilibrium positions taken from fitted curves. . . . .	80
5.14	Evolution of $K_c$ over time in a system simulating sorption of Pb to soil surface and DOM for soil A with different WTR additions with equilibrium positions taken from WHAM outputs. . . . .	81
5.15	Evolution of $K_c$ over time in a system simulating sorption of Pb to soil surface and DOM for soil A with different WTR additions with equilibrium positions taken from fitted curves. . . . .	81
5.16	Evolution of $K_c$ over time in a system simulating sorption of Pb to soil surface and DOM for soil B with different WTR additions with equilibrium positions taken from fitted curves. . . . .	82
5.17	Evolution of $K_c$ over time in a system simulating sorption of Pb to soil surface and DOM for soil C with different WTR additions with equilibrium positions taken from fitted curves. . . . .	82
5.18	The change in total Pb levels over a period of 4 years in no flow conditions for a 50cm column of soil A in its original state and with 5%, 10% and 20% WTR additions. . . . .	84
6.1	Change in run time with subdomain area for a single, no flow reaction step in a 9cm by 9cm domain at a range of initial particle densities. . . . .	92
6.2	Change in the fraction of run time required by the solution of Algorithm 6.1 with subdomain area for a single, no flow reaction step in a 9cm by 9cm domain at a range of initial particle densities. . . . .	92

6.3	Change in run time with particle density for a single, no flow reaction step in a 9cm by 9cm domain for the unoptimized solution and optimized solution at a range of different number of subdomains. . . . .	93
6.4	Comparison between optimized and unoptimized reaction solutions run times for a single, no flow reaction step in a 9cm by 9cm domain with a range of initial particle densities. . .	93
6.5	A schematic diagram showing the architecture of the chip used in an Nvidia Tesla C2075 Graphics Processing Unit (GPU). . . . .	95
6.6	A comparison of the run times required for the transport and reaction solutions in the simulations of the reactive transport problem presented by Gramling <i>et al.</i> , (2002) for the GPU accelerated and Central Processing Unit (CPU) based version of the solution. . . . .	97

# List of Tables

4.1	Values of $P_{max}$ used to achieve best fit outputs for varying time step length $\Delta t$ . . . . .	44
5.1	Concentrations of soil components for three soil samples, A, B and C, and WTR. . . . .	64
5.2	WHAM trace element concentration inputs for soil A with 5%, 10% and 20% WTR additions. . . . .	68
5.3	WHAM trace element concentration inputs for soil B with 5%, 10% and 20% WTR additions. . . . .	69
5.4	WHAM trace element concentration inputs for soil C with 5%, 10% and 20% WTR additions. . . . .	69
5.5	$K_d$ and $K_c$ values for soils A, B and C in their initial states and with 5%, 10% and 20% WTR additions. . . . .	73
5.6	Best fit power laws for relationships between $K_d$ and the three components which the addition of WTR has the greatest effect on. . . . .	74
5.7	Best fit exponential rules for the effect of DOM concentration on $K_c$ . . . . .	74

# List of Algorithms

3.1	Discrete Time Random Walk Solution . . . . .	13
3.2	Box-Muller Transform . . . . .	14
3.3	Particle Influx . . . . .	17
4.1	Solution of reaction between two solutes in a particle tracking framework. . . . .	30
4.2	Algorithm for estimating concentration at nodal coordinates. . . . .	56
5.1	Reverse reaction. . . . .	76
6.1	Subdomain array build. . . . .	89
6.2	Optimized solution of reaction between two solutes in a particle tracking framework. . . . .	90

## A note on algorithm style

All of the simulations presented in this thesis have been performed using computer codes written in the Fortran90 programming language. Algorithms presented are presented in a similar style to, and using the syntax of Fortran90. Additionally the calls to intrinsic Fortran90 functions are be written verbatim, *e.g* `MINVAL(M)` is the function that finds the minimum value held in the matrix  $M$  and would be used in an algorithm instead of the statement ‘Find the maximum value stored in the matrix  $M$ ’.

# Acronyms

<b>CLPF</b>	Colocation Probability Function
<b>CPU</b>	Central Processing Unit
<b>CTRW</b>	Continuous Time Random Walk
<b>CUDA</b>	Compute Unified Device Architecture
<b>DOM</b>	Dissolved Organic Matter
<b>DTRW</b>	Discrete Time Random Walk
<b>FDM</b>	Finite Difference Method
<b>FEM</b>	Finite Element Method
<b>GPU</b>	Graphics Processing Unit
<b>LPF</b>	Location Probability Function
<b>MIMD</b>	Multiple Instruction Multiple Data
<b>MISD</b>	Multiple Instruction Single Data
<b>PDE</b>	Partial Differential Equation
<b>PDF</b>	Probability Density Function
<b>PRNG</b>	Pseudorandom Number Generator
<b>RAM</b>	Random Access Memory
<b>ROBUST</b>	Regeneration of Brownfield Using Sustainable Technology
<b>RWPT</b>	Random Walk Particle Tracking
<b>SIMD</b>	Single Instruction Multiple Data
<b>SISD</b>	Single Instruction Single Data
<b>SOM</b>	Soil Organic Matter
<b>SM</b>	Streaming Multiprocessor
<b>TBNPA</b>	Tribromoneopentyl Alcohol
<b>WHAM</b>	Windermere Humic Aqueous Model
<b>WTR</b>	Water Treatment Residual

# Chapter 1

## Introduction

### Summary

This thesis forms part of the Regeneration of Brownfield Using Sustainable Technology (ROBUST) project lead by Dr. Karen Johnson and Prof. Clare Bamba, which aims to develop a novel, low cost, environmentally low impact method for the remediation of contaminated land. It focuses on the development and investigation of a computational model for the simulation of the effects of said remediation scheme on the movement of heavy metals within soils.

### 1.1 Rationale

Previously developed, or brownfield, land is defined in the U.K. as land which has had some previous development on it, with the exception of land used for recreation, agriculture, or defence, or land which has been used for mining or landfill and has subsequently been regenerated after use. In 2007 there were an estimated 62,130 hectares of brownfield land in England, of which an estimated 16,810 hectares required some kind of treatment prior to development [1]. The amount of new housing built in England on previously developed land has been steadily increasing over the past 20 years, from ~50% in 1989 to ~75% in 2010.

To allow for the reuse of a contaminated site, the risk posed by the contamination must be reduced to acceptable levels as determined by the U.K. Environment Agency, by limiting the exposure of receptors (*i.e.* people) to contaminants. The remediation of a site can be achieved by a range of methods such as reducing or removing the contaminant material, blocking the contaminant pathway to the receptor, reducing exposure to the contamination, or removing the receptor from the site [2].

The method of remediation used on a site is dependent on three main factors: cost-effectiveness, speed, and flexibility [3]. The most common techniques used for the remediation of contaminated land in England are containment; either capping of the site to prevent human access to the contaminated soil, the emplacement of a barrier within the soil, or a combination of the two, and excavation and removal. These two methods account for over 90% of the proposed remediation schemes in England [2]. A wide range of other techniques are used in small numbers of cases across England. These methods take a myriad of forms and are divided into three groups: bioremediation, where microorganisms are used to metabolize organic contaminants into less toxic products, chemical remediation, where chemical amendments are used to immobilize contaminants or reduce their bioaccessibility, and physical remediation, where contaminants are either removed from the soil by a method such as washing, heating or electrolysis, or reduced in toxicity by a method such as by thermal vitrification [4, 5]

The cost of remediation is generally absorbed by the profits made from redevelopment of the land. If the land is not attractive to potential developers then the likelihood of remediation happening is low [3]. Reduction of the costs of remediation can potentially allow low value contaminated sites to be remediated, both for housing and for other purposes.

A positive association between brownfield land and poorer health has been shown in England even after adjusting for other factors, such as socio-economic status [6]. In addition to the potential benefits with regards to housing development, the regeneration of brownfield land for no specific purpose is also, therefore, a worthwhile exercise. The improvement, or reduction in cost of remediation technologies is important. The development of a low cost, environmentally low impact method for the remediation of contaminated land is the aim of the ROBUST project.

## 1.2 The ROBUST Project

The remediation technique developed and investigated within the ROBUST project is a chemical remediation scheme using Water Treatment Residual (WTR) as a soil amendment with the aim of reducing the bioaccessibility or mobility of contaminants. WTR is a waste product produced during the treatment of drinking water by the addition of minerals which act as flocculants to remove suspended material including organic matter. These flocculants include, for example,  $\text{FeO}_2^-$  [7] and  $\text{Al}_2(\text{SO}_4)_3$  [8]. The WTR produced contains high concentrations of organic matter, which is one of the main components removed by the flocculation process, as well as of the compounds used as flocculants.

The technology has been tested on a field site, at the former Pygall coachworks in Easington Colliery, County Durham, and experimentally on soils taken from the site of the former St. Anthony's leadworks in Newcastle-upon-Tyne. As the experimental work in ROBUST has focused on soils taken from the former St. Anthony's leadworks, the computational work focuses on soils contaminated with Pb. As over 80% of the designated contaminated land sites in England and Wales are contaminated with metals or metalloids [2] this is of use to a large amount of the contaminated land in the United Kingdom. The WTR used as the soil amendment is an Fe based WTR taken from the Northumbrian Water treatment works at Mosswood, County Durham.

## 1.3 Thesis Aims

The general aim of this thesis is to develop a model which can be used to simulate the effect of WTR addition to a soil contaminated with Pb. The model developed must be capable of simulating the transport of solutes in porous media, the interactions of different solutes with one another, and their interactions with the soil solids. This model is developed using the Discrete Time Random Walk (DTRW) method, which is a member of the particle tracking family of methods.

There are large number of computer models available for the simulation of complex systems involving solute transport in porous media such as MODFLOW [9–12] and its extensions, MT3D [13–15] and RT3D [16, 17], HYDRUS [18, 19], FEMWATER [20], and STOMP [21, 22]. All of these models use continuum methods, *e.g.* the Finite Element Method (FEM) or the Finite Difference Method (FDM), to simulate porous media flow and reactions between solutes, though they vary in the methods used to simulate solute transport. HYDRUS and STOMP use a continuum based solution for the advection-dispersion transport solutions, whereas FEMWATER and MT3D, and its extension RT3D, use Eulerian-Lagrangian particle based schemes.

The particle tracking family of computational methods, to which the DTRW method belongs, offer advantages over continuum methods for the simulation of reactive transport in porous media, but have mostly been used in the simulation of simple chemical systems, such as bimolecular reactive transport

or the sorption of a single solute, although simulations of more complicated systems, such as dissolution and precipitation, have been simulated by a small number of studies. A large potential field of work is therefore available to be performed on the expansion of particle tracking methods, both in characterizing their behaviour and in expanding their functionality. The development of a model using particle tracking, including expansions of the method to simulate more complicated systems, is a useful contribution to the field as well as to the ROBUST project.

Due to the nature of the DTRW method the complexity of the chemical systems that can be described by the model produced in this thesis cannot reach that possible with other available models. A reduced complexity method based on the outputs of a chemical speciation model, Windermere Humic Aqueous Model (WHAM), is developed here and used to simulate a complex chemical system using a smaller number of species, thereby reducing the developmental difficulty and computational cost.

## 1.4 Thesis Overview

The outline of this thesis is as follows:-

- The DTRW particle tracking method presented in this thesis is developed under the assumption that any solution used to drive the advective transport will be produced using the FEM. To help contextualize the work presented in Chapters 3 and 4, the FEM solution of saturated porous media flow is briefly discussed in Chapter 2.
- The simulation of conservative solute transport in porous media using the DTRW method is the focus of Chapter 3. The initial rationale behind the development of particle tracking methods, and their pros and cons are discussed. The derivation and implementation of the DTRW conservative transport solution is presented followed by an assessment of the robustness of the solution by a sensitivity analysis of various factors controlling the solution.
- The expansion of the DTRW transport solution presented in Chapter 3 to include the simulation of bimolecular reactions and sorption is the focus of Chapter 4. The method for the simulation of bimolecular reactions is described and its behaviour analysed in detail. It is then benchmarked against experimental data and other simulation studies and its robustness assessed by a sensitivity analysis of various factors controlling its solution. The sorption solution is outlined and compared with other numerical studies and experimental data.
- The DTRW model described in Chapters 3 and 4 is then adjusted and applied to the simulation of the effect of WTR addition on the partitioning of Pb between its different potential states. Due to the lack of experimental data available, this is performed by utilizing the DTRW with the WHAM chemical speciation model [23, 24].
- One of the main downsides of particle tracking methods is their high computational cost. Chapter 6 of this thesis focuses on the optimization and acceleration of the implemented DTRW model.

# Chapter 2

## Porous Media Flow

### Summary

In this chapter the Partial Differential Equation (PDE) used to describe the flow of fluids through porous media in saturated conditions is presented alongside the method of its solution using the Finite Element Method (FEM). Though no finite element solutions are utilized in the rest of this thesis, the non-conservative Discrete Time Random Walk (DTRW) solute transport model presented is developed on the assumption that any fluid flow solution used in conjunction with it will be produced using the FEM. The outline of the FEM solution of porous media flow is presented to help contextualize the work presented in later chapters.

### 2.1 Introduction

Contaminants are more mobile if in solution than in the solid phase, either by movement through the groundwater or by being transported with it. The movement of ground water is therefore an important aspect in the movement of contaminants within a soil, and any model developed for the simulation of contaminant transport in soils must include some description of the groundwater flow regime to be able to properly address the fate of contaminants within a soil.

All of the simulations presented within this thesis are either recreations of experiments conducted under constant flow conditions or purely investigative studies of the model behaviour in the absence of fluid flow, and either occur in, or make the assumption of, purely saturated conditions. The numerical solution of the groundwater flow behaviour is therefore not required at any point in this thesis. A model which did not possess the capacity to include variable flow regimes would be severely hampered in its usefulness. To account for this the solute transport and reaction model presented in the following work is developed under the assumption that any flow simulations used in tandem with it would be produced using the FEM, even though no such solutions are presented.

The flow field used to drive solute transport is calculated from a set of nodal pressure values produced as outputs of a FEM solution. This flow field and the set of nodal coordinates are used in the transport solution. The transport solution assumes four noded quadrilateral finite elements, and will operate as long as all of the internal angles in an element are  $<180$  degrees. This restriction applies to isoparametric finite elements to ensure a one to one mapping between the global and local coordinate systems [25]. By developing the transport model to work for arbitrary two dimensional quadrilateral finite elements, it is capable of also operating if a groundwater flow solution produced using the Finite Difference Method (FDM) is passed to it, as this would present the same input data as a special case of the FEM.

Some aspects of the FEM, such as the transformation of coordinate systems used with isoparametric elements, are used elsewhere in this thesis. It is therefore useful to present a brief description of the FEM, and its application to the solution of groundwater flow problems, in order to help contextualise the following chapters. The description of the FEM is preceded by the PDE used to describe the flow of water through porous media.

## 2.2 Saturated Porous Media Flow

The macroscopic flow of a fluid through a saturated porous medium can be described by Darcy's Law [26] which takes the form

$$q = -K_h \nabla h \quad (2.1)$$

where  $q$  is fluid flux,  $h$  is hydraulic pressure, or head, and  $K_h$  is the hydraulic conductivity of the soil. Under the assumptions of incompressibility and conservation of mass Equation 2.1 can be altered to take the form

$$S_s \frac{\partial h}{\partial t} = \nabla \cdot K_h \nabla h \quad (2.2)$$

where  $S_s$  is the specific storage. Solutions are normally required for a situation where water is either entering the domain, exiting the domain, or both. As such Equation 2.2 is altered to take the form

$$S_s \frac{\partial h}{\partial t} = \nabla \cdot K_h \nabla h + Q \quad (2.3)$$

where  $Q$  represents all sources and/or sinks.

## 2.3 Finite Element Method

The Finite Element Method (FEM) is a numerical method for the solution of partial differential equations based on the idea of dividing up a domain of interest into smaller areas, referred to as finite elements. Solutions are then estimated based on approximations about the variation of variables within each element. The set of finite elements makes up a grid or mesh which encompasses the entire simulation domain. Information, *e.g.*  $h$  or  $K_h$ , is stored at a set of nodes which, in the case of linear finite elements, are located at element vertices. Values of any of the nodal variables required elsewhere are estimated using interpolation functions, referred to as shape functions. The model developed in Chapters 3 and 4 of this thesis operate under the assumption that four-noded quadrilateral elements are used. As such the description of the FEM presented below is for four-noded quadrilateral elements.

For the regular, two dimensional, bilinear quadrilaterals used in this research the shape functions are

$$N_1(\xi, \eta) = \frac{1}{4}(1 - \xi)(1 - \eta) \quad (2.4)$$

$$N_2(\xi, \eta) = \frac{1}{4}(1 + \xi)(1 - \eta) \quad (2.5)$$

$$N_3(\xi, \eta) = \frac{1}{4}(1 + \xi)(1 + \eta) \quad (2.6)$$

$$N_4(\xi, \eta) = \frac{1}{4}(1 - \xi)(1 + \eta) \quad (2.7)$$

The nodes are numbered, by convention, starting in the bottom left corner and proceeding anticlockwise around the element.

One advantage of the FEM over the FDM is that it can use irregular or deformable grids of nodes. The integrals performed during the solution of a finite element problem are much easier if the element is regular (*e.g.*, a square). In the FEM the integrals are performed over a 'parent element' which is

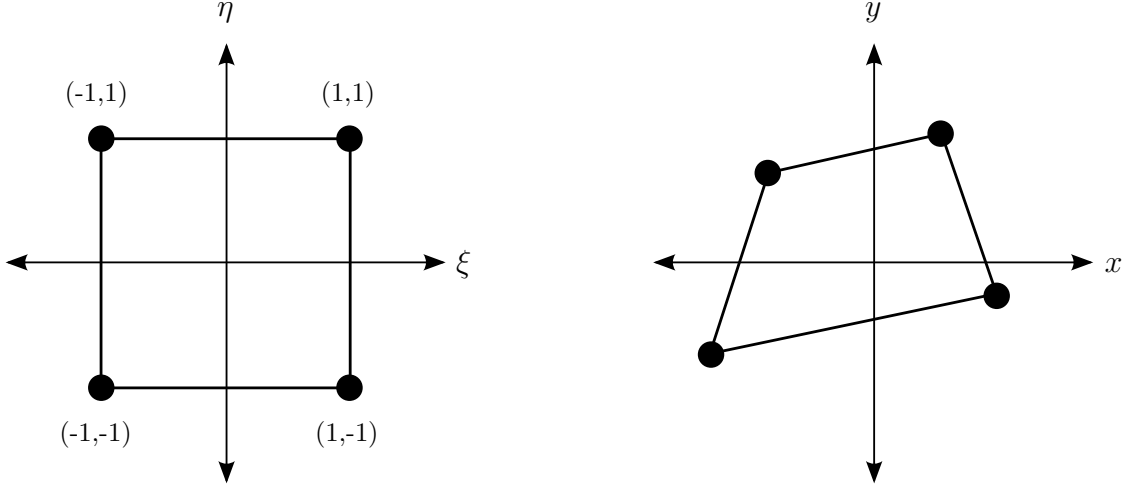


Figure 2.1: A two dimensional, four noded element in the local (left) and global (right) coordinate systems.

regular in shape and exists within the coordinate system  $-1 \leq \eta \leq 1$ ,  $-1 \leq \xi \leq 1$  (see Figure 2.1). The integrals are then transferred to the global coordinate system via the Jacobian matrix  $[\mathbf{J}]$ , a matrix of the differentials of the global coordinates with respect to the parent coordinate system using relation

$$\nabla N_{xy}[\mathbf{J}] = \nabla N_{\xi\eta} \quad (2.8)$$

where

$$[\mathbf{J}] = \begin{bmatrix} \frac{\partial x}{\partial \xi} & \frac{\partial y}{\partial \xi} \\ \frac{\partial x}{\partial \eta} & \frac{\partial y}{\partial \eta} \end{bmatrix}. \quad (2.9)$$

$\xi(x, y)$  and  $\eta(x, y)$  can be determined from

$$\begin{bmatrix} b_1 & c_1 \\ b_2 & c_2 \end{bmatrix} \begin{Bmatrix} \xi \\ \eta \end{Bmatrix} = \begin{Bmatrix} 4x - (x_1 + x_2 + x_3 + x_4) - a_1\xi\eta \\ 4y - (y_1 + y_2 + y_3 + y_4) - a_2\xi\eta \end{Bmatrix}. \quad (2.10)$$

The coefficients can be determined using

$$\begin{bmatrix} a_1 & a_2 \\ b_1 & b_2 \\ c_1 & c_2 \end{bmatrix} = \begin{bmatrix} 1 & -1 & 1 & -1 \\ -1 & 1 & 1 & -1 \\ -1 & -1 & 1 & 1 \end{bmatrix} \begin{bmatrix} x_1 & y_1 \\ x_2 & y_2 \\ x_3 & y_3 \\ x_4 & y_4 \end{bmatrix} \quad (2.11)$$

for the standard node numbering system of anticlockwise from the bottom left node where

$$a_1 = x_1 - x_2 + x_3 - x_4 \quad (2.12)$$

$$a_2 = y_1 - y_2 + y_3 - y_4 \quad (2.13)$$

$$b_1 = -x_1 + x_2 + x_3 - x_4 \quad (2.14)$$

$$b_2 = -y_1 + y_2 + y_3 - y_4 \quad (2.15)$$

$$c_1 = -x_1 - x_2 + x_3 + x_4 \quad (2.16)$$

$$c_2 = -y_1 - y_2 + y_3 + y_4. \quad (2.17)$$

The reverse coordinate transformation is given by

$$x(\xi, \eta) = \sum_{i=1}^4 N_i(\xi, \eta) x_i \quad (2.18)$$

$$y(\xi, \eta) = \sum_{i=1}^4 N_i(\xi, \eta) y_i. \quad (2.19)$$

This coordinate transformation is used on several other occasions in this thesis.

The solution to the Darcy equation can then be determined using an standard FEM formulation.

## 2.4 Conclusion

In this chapter the solution of porous media flow problems using the FEM has been outlined. Although no solutions produced using the FEM are utilized in this thesis, it is important to have outlined the method as the solute transport, reaction, and sorption simulations methods presented in the following chapters are all designed under the assumption that they will need to be used in conjunction with a finite element solution for porous media flow. In the next chapter the method used for the simulation of conservative solute transport is discussed.

# Chapter 3

## Conservative Solute Transport

### Summary

This chapter focuses on the simulation of conservative transport of solutes through porous media using the Discrete Time Random Walk (DTRW) method. The equations used to describe mass transport are outlined followed by the concept behind particle tracking methods and the reasons for using them. The DTRW method is described and the differences between the DTRW and Continuous Time Random Walk (CTRW) outlined. The DTRW solution is then compared to a set of experimental data and a sensitivity analysis performed in order to demonstrate the robustness of the method.

### 3.1 Introduction

The transport of a chemical species within a fluid is the combination of two processes, advection and diffusion. Advection is the transport of the chemical species by the movement of the fluid in which it is contained. Diffusive transport is the transport of a chemical by the combination of the random movements and collisions of the individual atoms or molecules [27]. The macroscopic effect of diffusion is described by Fick's law, which takes the form

$$\frac{\partial C}{\partial t} = \nabla \cdot (D_m \cdot \nabla C) \quad (3.1)$$

where  $t$  is time,  $C$  is solute concentration and  $D_m$  is molecular diffusivity. Advective transport can be described by

$$\frac{\partial C}{\partial t} = -\nabla \cdot VC \quad (3.2)$$

where  $V$  is flow velocity. In addition to advection and diffusion, mass transport in porous media occurs by dispersion. Dispersion is the product of several mechanisms that combine to produce transport which leads to the reduction of concentration gradients in the same manner as Fickian diffusion. These mechanisms all cause variation in flow rates on small scales. The variations in flow direction and hydraulic conductivity, and therefore flow rate, in different pores within the medium and the variation in flow rate across pores due to Poiseuille flow both contribute to dispersion. The macroscopic effects of dispersion are similar in appearance to those of diffusion and at the macro scale the two processes are inseparable [28]. Due to this the two are often combined into a single term referred to as hydrodynamic dispersion. The macroscopic effect of hydrodynamic dispersion takes the same form as Equation 3.1 and is given as

$$\frac{\partial C}{\partial t} = \nabla \cdot (D_h \cdot \nabla C) \quad (3.3)$$

where  $D_h$  is hydrodynamic dispersion. The combined effects of transport via advection and dispersion (including diffusion) can be described by the advection-dispersion equation

$$\frac{\partial C}{\partial t} = \nabla \cdot (D_h \cdot \nabla C - VC) + Q \quad (3.4)$$

where  $Q$  represents all possible sources and sinks such as reactions, in or outflow of solute bearing pore fluids, and diffusion of molecules into or out of the domain.

Equation 3.4 can be solved analytically in simple situations or by a numerical scheme such as the Finite Difference Method (FDM) or Finite Element Method (FEM), though the use of continuum based numerical schemes such as these can lead to the solution being degraded by numerical artefacts. Depending on the order of the approximation used in the numerical scheme, the solution can be degraded by oscillation or numerical dispersion. These issues are discussed in depth in Bear [28] and are outlined below.

Assume a purely advective, one dimensional case, *i.e.*  $D_h = 0$ , where a step front is being advected at velocity  $V$  as in Equation 3.2. If the central difference method, a form of the FDM, is used, the solution produced is

$$C_i^{n+1} = C_i^n - \frac{V\Delta t}{2\Delta x}(C_{i+1}^n - C_{i-1}^n) \quad (3.5)$$

where  $i$  is the spatial index and  $n$  is the temporal index. In this formulation the step front is represented by  $C_{i-1}^t = C_i^t = C^0$  and  $C_{i+1}^t = 0$ . It is clear that at time step  $n + 1$  the concentration  $C_i^{n+1} > C^0$  when it should equal  $C^0$ . Conversely, if  $V = \Delta x/\Delta t$  where  $\Delta x$  is the distance between nodes and  $\Delta t$  is the time step length, the concentration at  $i + 1$  at time  $n + 1$  will be  $C_{i+1}^{n+1} = C^0/2$  when it should equal  $C^0$ . The use of the central difference scheme therefore causes oscillations in the concentration front. This can be countered using a backwards difference scheme which only uses information from behind the concentration step, rather than in front of it and behind as with the central difference scheme. The new concentration at  $i$  is now given as

$$C_i^{n+1} = C_i^n - \frac{V\Delta t}{\Delta x}(C_i^n - C_{i-1}^n). \quad (3.6)$$

This eliminates the problem of oscillation but introduces a new problem in the form of numerical dispersion. If the Taylor series expansion, of which the backwards difference scheme is the first term, is examined it is seen that

$$V \frac{\partial C}{\partial x} = V \frac{C(x) - C(x - \Delta x)}{\Delta x} + V \frac{\Delta x}{2} \frac{\partial^2 C}{\partial x^2} + \dots \quad (3.7)$$

The error introduced by using the backwards difference scheme to approximate the advection term is of the same form as the dispersion term in Equation 3.4 with  $D_h = V\Delta x/2$ . This has the effect of reducing concentration gradients leading to smearing of the concentration front parallel to the direction of flow.

This can be dealt with in various ways [29]. Numerical dispersion can be artificially damped by introducing an apparent numerical dispersion coefficient [30, 31] though this requires an estimation of the rate of numerical dispersion. Alternatively the effects of solution oscillation can be reduced by reducing the grid spacing or element size used in the solution. The effect of oscillations can be eliminated if the Peclet number,  $Pe = V \cdot \Delta x/D_h$ , is less than 2 [29], though this has the effect of increasing the computational cost required for the solution. Leonard [32] proposed two methods based on quadratic upstream interpolation to limit the effects of numerical dispersion and oscillations which have since been used by other researchers *e.g.* [29, 33, 34].

Alternatively particle tracking methods, in which the concentration field is described by the distribu-

tion of a set of particles rather than a set of nodal concentration values, can be used. Particle tracking methods are completely free from numerical dispersion or oscillation and have also been shown to have some useful properties when used to simulate reactive transport between solutes, such as simulating the limiting of reaction rates by diffusive mixing *e.g.* [35–37]. Due to these advantages over continuum methods, particle tracking methods are used for the simulation of solute transport in this work.

## 3.2 Particle Tracking Methods

The way in which particle tracking methods describe mass transport is different to the way in which continuum methods such as the FEM do. Rather than describing the concentration field using a set of nodal concentration values and a set of interpolation functions, the concentration field is instead described using the distribution of a set of particles. Each of these particles represents a discrete ‘packet’ of a solute which is transported through the domain. The amount of solute which each particle represents is fixed. This differs from the Lagrangian forward particle tracking method [28, 38–41] where a particle stores the concentration at a point and that concentration is then advected to a new position. By contrast, in the random walk particle tracking scheme the concentration at a location is determined by the particle density in that area. This means that unless a very large number of particles are used, the solution of the concentration field is not smooth.

Itō [42] demonstrated that a random walk is equivalent to the Fokker-Planck equation in the limit of a large number of particles. The Fokker-Planck equation [43, 44], sometimes referred to as the Kolmogorov forward equation when used to describe diffusion [45], describes the evolution with time of the probability distribution of the location of a particle. The combination of multiple realizations of the movement of a particle takes the form of this probability distribution and so its form describes the concentration profile of the diffusing solute. As dispersion is assumed to take a Fickian form it can be inferred that the effect of dispersion leads to concentration profiles of the same form. This idea was then developed into the concept of a random walk particle tracking method by Montroll & Weiss [46] for simulating the movements of electrons through semiconductors [47–49] but has also been used to simulate mass transport in porous media [50–59]. The particle tracking method used by [46–59] is the CTRW method. Here the particle can only exist at set locations on a lattice and the time at which they move from one lattice site is randomly determined. This differs from DTRW, or Random Walk Particle Tracking (RWPT), methods *e.g.* [60–65] where particles can occupy any location within the domain and the timesteps over which they are moved are of set sizes. The stochastic aspect of the DTRW method is the distance which the particles are dispersed. In the DTRW method transport is separated into advective and dispersive transport. Particles are advected according to the fluid velocity field, determined from a FD or FE solution, and then dispersed by adding a random walk to their position. The DTRW is the particle tracking method which is used in this work.

To explain how a random walk is used to simulate dispersive transport consider a one dimensional case where at  $t = 0$  the concentration profile forms a pulse source or Dirac delta. The analytical solution of the Fokker-Planck equation for  $t > 0$  is

$$C(x, t) = (4\pi D_h t)^{-1/2} \exp \left[ -\frac{(x - Vt)^2}{4D_h t} \right]. \quad (3.8)$$

The right hand side takes a Gaussian form and so could be seen as a Gaussian probability density function with mean  $Vt$  and variance  $2D_h t$ . By advecting the particles a distance  $Vt$  and then subjecting them to a normally distributed random walk with mean 0 and variance  $2D_h t$ , the distribution of particles fits the analytical solution. For two or three dimensional cases particles are advected along path lines. Dispersion

is then performed longitudinally and transversely to the path line.

### 3.2.1 Path Line Solution

The method used to calculate the path lines along which particles are advected is that presented by Pollock [66]. This has been used in particle tracking simulations *e.g.* [67–71]. In the method presented in [66] path lines are determined semianalytically. Though this method was developed for use within finite difference cells it is applicable to finite element flow simulations [72]. Velocities are assumed to vary linearly within elements for the FEM or cells for the FDM.

For a given particle location and flow field the method presented by Pollock [66] determines where the particle exits the element and how long it takes to do so. The derivation of this method is in two spatial dimensions, as are all of the particle tracking simulations presented in this work. From here on all equations pertaining to the DTRW solution are in two spatial dimensions unless stated otherwise. Pollock [66] assumes that the cells/elements are rectilinear but this is not always the case for finite elements. To account for this, the particle coordinates, nodal coordinates and boundary fluxes are transformed to a local coordinate system (as described in Chapter 2) such that the element is square extending from -1 to 1 in both the coordinate direction directions. Using linear interpolation the  $x$  and  $y$  components of the flow velocity can be given as

$$v_x = \frac{1}{\Delta x}(x - x_1)(v_{x_2} - v_{x_1}), \quad (3.9)$$

$$v_y = \frac{1}{\Delta y}(y - y_1)(v_{y_2} - v_{y_1}), \quad (3.10)$$

$$\left(\frac{dv_x}{dt}\right)_p = \left(\frac{dv_x}{dx}\right) \left(\frac{dx}{dt}\right)_p, \quad (3.11)$$

$$v_{x_p} = \left(\frac{dx}{dt}\right)_p \quad (3.12)$$

Where  $x_1$ ,  $x_2$ ,  $y_1$  and  $y_2$  are the minimum and maximum  $x$  and  $y$  coordinates of the element respectively, and  $v_{x_1}$ ,  $v_{x_2}$ ,  $v_{y_1}$  and  $v_{y_2}$  are the flow velocities at  $x_1$ ,  $x_2$ ,  $y_1$  and  $y_2$  respectively. Differentiation of Equation 3.9 with respect to  $x$  gives

$$\frac{dv_x}{dx} = \frac{1}{\Delta x}(v_{x_2} - v_{x_1}). \quad (3.13)$$

Substitution of Equations 3.12 and 3.13 into Equation 3.11 gives

$$\left(\frac{dv_x}{dt}\right)_p = \frac{v_{x_p}}{\Delta x}(v_{x_2} - v_{x_1}). \quad (3.14)$$

Equation 3.14 can the be rearranged into the form

$$\left(\frac{1}{v_{x_p}}\right) dv_{x_p} = \frac{1}{\Delta x}(v_{x_2} - v_{x_1})dt \quad (3.15)$$

and then integrated between times  $t_1$  and  $t_2$  to give

$$\ln\left(\frac{v_{x_p}(t_2)}{v_{x_p}(t_1)}\right) = \frac{1}{\Delta x}(v_{x_2} - v_{x_1})\Delta t \quad (3.16)$$

where  $\Delta t = t_2 - t_1$ . By taking the exponential of Equation 3.16, substituting Equation 3.9 and rearranging,

the  $x$  and  $y$  positions of the particle at  $t_2$  can be given as

$$x_p(t_2) = x_1 + \frac{\Delta x}{(v_{x_2} - v_{x_1})} [v_{x_p}(t_1) e^{(v_{x_2} - v_{x_1})\Delta t / \Delta x} - v_{x_1}] \quad (3.17)$$

$$y_p(t_2) = y_1 + \frac{\Delta y}{(v_{y_2} - v_{y_1})} [v_{y_p}(t_1) e^{(v_{y_2} - v_{y_1})\Delta t / \Delta y} - v_{y_1}] \quad (3.18)$$

respectively. Equations 3.17 and 3.18 can be used to determine where a particle leaves an element. By definition  $v_x = v_{x_2}$  when  $x = x_2$ . If at  $t_2$  the particle is at  $x_2$  then

$$\Delta t_x = \frac{\Delta x}{(v_{x_2} - v_{x_1})} \ln \left( \frac{v_{x_2}}{v_{x_p}} \right). \quad (3.19)$$

Corresponding statements for the time to reach the other three element edges,  $x = x_1$ ,  $y = y_1$  and  $y = y_2$ , are given by

$$\Delta t_x = \frac{\Delta x}{(v_{x_1} - v_{x_2})} \ln \left( \frac{v_{x_1}}{v_{x_p}} \right) \quad (3.20)$$

$$\Delta t_y = \frac{\Delta y}{(v_{y_2} - v_{y_1})} \ln \left( \frac{v_{y_2}}{v_{y_p}} \right) \quad (3.21)$$

$$\Delta t_y = \frac{\Delta y}{(v_{y_1} - v_{y_2})} \ln \left( \frac{v_{y_1}}{v_{y_p}} \right). \quad (3.22)$$

The particle leaves through the edge to which it has the lowest positive, non-zero travel time. Having determined which element edge the particle leaves through, the particle is moved along the path line until it either reaches the element edge or  $t_2$  is reached. If the element edge is reached before  $t_2$  then the particle is moved through the new element until  $t_2$  is reached.

### 3.2.2 DTRW Solution

The DTRW solution for the movement of particle  $p$ , located at  $(x_p^i, y_p^i)$  at timestep  $i$ , is given as

$$x_p^{i+1} = x_p^i + v_x \Delta t + R_N \sqrt{2D_{h_x} \Delta t} \quad (3.23)$$

$$y_p^{i+1} = y_p^i + v_y \Delta t + R_N \sqrt{2D_{h_y} \Delta t} \quad (3.24)$$

where  $v_x$  and  $v_y$  are the two spatial components of the flow velocity,  $D_{h_y}$  and  $D_{h_x}$  are the two spatial components of hydraulic dispersivity, which are constant in space, and  $R_N$  is a  $N[0,1]$  pseudorandom number.  $D_{h_y}$  and  $D_{h_x}$  depend on the direction of flow and the longitudinal and transverse hydraulic dispersivities  $D_{h_L}$  and  $D_{h_T}$  respectively. For flow at an angle  $\theta_f$  from vertical the relationship between  $D_{h_y}$  and  $D_{h_x}$ , and  $D_{h_L}$  and  $D_{h_T}$  is given as

$$D_{h_x} = \sin(\theta_f) D_{h_L} + \cos(\theta_f) D_{h_T} \quad (3.25)$$

$$D_{h_y} = \cos(\theta_f) D_{h_L} + \sin(\theta_f) D_{h_T}. \quad (3.26)$$

If  $D_{h_y}$  and  $D_{h_x}$  are variable in space, which may be due to spatial variation of  $v_x$  and  $v_y$ , this scheme can lead to the gathering of particles in low dispersion areas [73]. Itō [42] shows that this can be corrected by altering 3.23 and 3.24 to take the form

$$x_p^{i+1} = x_p^i + \left( v_x + \frac{\partial D_{h_x}}{\partial x} \right) \Delta t + R_N \sqrt{2D_{h_x} \Delta t} \quad (3.27)$$

$$y_p^{i+1} = y_p^i + \left( v_y + \frac{\partial D_{h_y}}{\partial y} \right) \Delta t + R_N \sqrt{2D_{h_y} \Delta t}. \quad (3.28)$$

An alternative formulation, presented by [74], is possible though this requires an iterative approach to its solution. The Itô [42] approach is preferred due to this [64]. All of the applications of particle tracking schemes in Chapters 3 and 4 have constant dispersivities and so are unaffected by this issue.

### 3.2.3 DTRW Implementation

The DTRW solution using the method presented in [66] is implemented in Fortran 90. The general framework of the solution is given in Algorithm 3.1.

---

**Algorithm 3.1** Discrete Time Random Walk Solution

---

1. Determine the nearest node,  $(n_n)$ , to the particle location.
  2. Retrieve the set of nodes which are adjacent to  $n_n$ .
  3. For each element edge for which  $n_n$  forms one of the end nodes, determine which side of the edge the particle is on.
    - (a) For each element edge calculate the area of a triangle with  $n_n$  at one corner, an adjacent node at the second and the particle at the third, and preserve the sign of the solution.
    - (b) The signs of the area of the triangle formed between the particle, node  $n_n$  and each adjacent node can then be used to determine which of the four elements a particle is within. This is stable for elements where all of the internal angles are less than 180 degrees. If the particle lies on an element edge the direction of the fluid flow is used to determine which element a particle lies within, with particles being placed at the edge of the element they will be advected into.
  4. Transform particle location, local coordinates and element boundary fluxes into local coordinate system, as described in Chapter 2.
  5. Move particle along path line determined from method presented in [66].
  6. If particle reaches element boundary return to 1. Otherwise,
  7. Move particle randomly in  $x$  and  $y$  using an  $N[0, \sqrt{2D_h \Delta t}]$  Pseudorandom Number Generator (PRNG) where  $D_h$  is the hydraulic dispersivity.
- 

The  $N[0,1]$  pseudorandom numbers are generated by applying a Box-Muller transform (Algorithm 3.2) to the outputs of the built-in Fortran  $U[0,1]$  PRNG. This is then scaled by multiplying the output by  $\sqrt{2D_h \Delta t}$  to give a  $N[0, \sqrt{2D_h \Delta t}]$  PRNG.

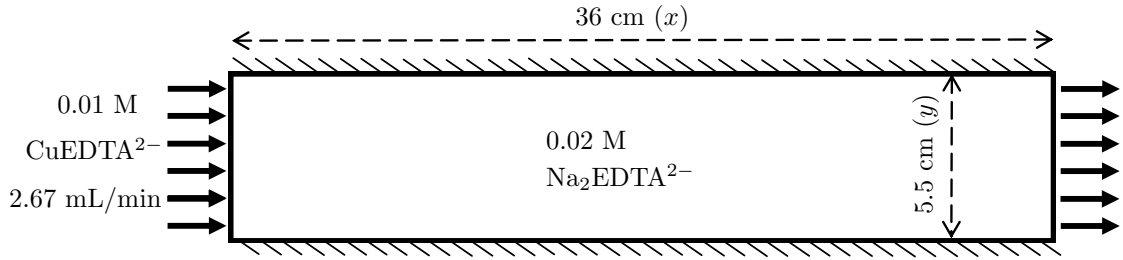


Figure 3.1: Experimental setup used by [75] and simulated using the DTRW method.

---

**Algorithm 3.2** Box-Muller Transform

---

```

w = 2.0
do while (w ≥ 1) & (w ≠ 0)
    RU1 = U[0,1]
    RU2 = U[0,1]
    RU1 = 2RU1 - 1
    RU1 = 2RU1 - 1
    w = RU12 + RU12
end do
RN1 = RU1√(-2ln(w)/w)
RN2 = RU2√(-2ln(w)/w)

```

---

### 3.2.4 Benchmarking

The DTRW solution is compared to experimental data for transport under steady flow conditions from Gramling *et al.* [75]. The data presented in Gramling *et al.* [75] provides concentration profiles at four times during a steady flow experiment. The experimental setup used in Gramling *et al.* [75] is shown in Figure 3.1. A flow chamber 36 cm by 5.5 cm by 1.8 cm is filled with cryolite sand with an average grain size of 0.13 cm. The chamber is initially saturated with a 0.02 M Na<sub>2</sub>EDTA<sup>2-</sup> solution ( $C^0$ ) which is then displaced by a 0.01 M Cu<sub>2</sub>EDTA<sup>2-</sup> solution at a flow rate of 2.67 mL/min. The dispersivity value measured for this flow rate is  $1.75 \times 10^{-3} \text{ cm}^2 \text{ s}^{-1}$ . Most column flow experiments only produce one set of results in the form of a breakthrough curve *e.g.* [76] by measuring solute concentrations at the outflow boundary and plotting these against time. The experimental data presented in Gramling *et al.* [75] has the advantage that the evolution of concentration curve over time can be recorded. The concentration curve for four different times over the course of the experiment are presented.

The non-physical variables which affect the DTRW solution are the density of particles which represents  $C^0$ , the size of the time step  $\Delta t$ , and the element size. The DTRW simulation performed takes place in a two dimensional domain 36 cm by 5.5 cm. The concentration is then averaged in the direction perpendicular to flow to give a one dimensional concentration profile. Unless otherwise stated  $\Delta t = 1$  s, the finite element mesh underlying the DTRW solution is a regular grid of 0.5 cm by 0.5 cm square elements and the particle density representing 0.5  $C^0$  is 900 per cm<sup>2</sup>.

The one dimensional concentration profiles shown below and in later chapters are the sum of a set of one dimension Gaussian functions centred at each particle's  $x$  location. As the flow field is invariant in

$y$  the concentration field is averaged in  $y$ . The one dimensional concentration profile is calculated as

$$C(x) = 0.025D_p(y_{max} - y_{min}) \sum_{p=1}^{N_p} e^{(x-x_p)^2/2 \times 10^{-4}}, \quad (3.29)$$

where  $x_p$  is particle  $p$ 's  $x$  coordinate,  $N_p$  is the number of particles and  $D_p$  is particle density per  $\text{cm}^2$ . The scaling value 0.025 is chosen in tandem with the spatial interval at which this function sampled (0.01cm) so that the spaces between particles do not appear as areas of low concentration. All particles contribute to the concentration profile and the small scale spatial variation in particle density in visible in the concentration profiles.

A benchmark against the experimental data presented in Gramling *et al.* [75] is presented, followed by an exploration of the effects of the non physical controls (*e.g.* particle density, time step length) on the solution quality.

Figure 3.2 compares the averaged DTRW solution of 10 simulations and the experimental data from Gramling *et al.* [75] at four times during the experiment. The characteristic ‘lumpy’ solution can be clearly seen. Despite this the solution’s fit to the experimental data is good. The nature of the DTRW method means that there are small scale variations in the concentration field from the larger scale average. The ease with which a concentration profile can be compared with experimental data is dependent on variance of the concentration profile from the large scale average. The amount of variability in the concentration profile decreases as more particles are used to represent a set concentration, as shown by Figure 3.3. This variability is expressed as the standard deviation of the concentration profile as calculated using Equation 3.29 at a set particle density for the average concentration. The relationship between the particle density and the standard deviation of the solution follows a power law relationship, and so the amount of particles required to improve the quality of the solution increases exponentially. The number of particles used to represent  $C^0$  can be increased in one of two ways. As the concentration profile is produced by adding contributions from each particle as described by Equation 3.29 and, for conservative solute transport, the transport of individual particles is independent from the others, there are two ways in which the addition of extra particles can be implemented. Either more particles can be included in a simulation or the results from several simulations can be added together. Increasing the quality of the solution beyond a certain level by increasing the amount of particles in a single simulation is obviously limited by the amount of memory available. If the desired solution quality cannot be achieved due to memory constraints then the solution can be improved by averaging the outputs of multiple simulations.

Figures 3.4 and 3.5 show the DTRW solution for the average of 9 DTRW solutions with a maximum particle density of 100 per  $\text{cm}^2$  and a single solution with a maximum particle density of 900 per  $\text{cm}^2$  respectively. The quality of the solution is similar though the runtimes vary. The runtime for the single 900 particle per  $\text{cm}^2$  run is  $\sim 17$  s. The runtime for nine 100 particle per  $\text{cm}^2$  run is  $\sim 70$  s. The only limiting factor on increasing the number of particles for a simulation without reactions is memory. This is the preferred method for simulations that do not include reactions as it leads to shorter run times. Though a single run requires shorter run times it is not possible to produce solutions of the quality of Figure 3.7 in this manner due to memory restrictions. The addition of reactions to the simulation further complicates which of these methods is the most efficient. This is discussed in depth in Chapter 6. Figures 3.6, 3.7 and 3.8 show the averages of 10 DTRW simulations for maximum particle densities of 100 per  $\text{cm}^2$ , 900 per  $\text{cm}^2$  and 2500 per  $\text{cm}^2$  respectively. The solution clearly improves as more particles are added as the variability in the solution is reduced.

Figures 3.9 - 3.12 show the effect of timestep on the DTRW solution. The effect is minimal except close to the inflow boundary where larger time steps produce a large anomaly in the solution. This is

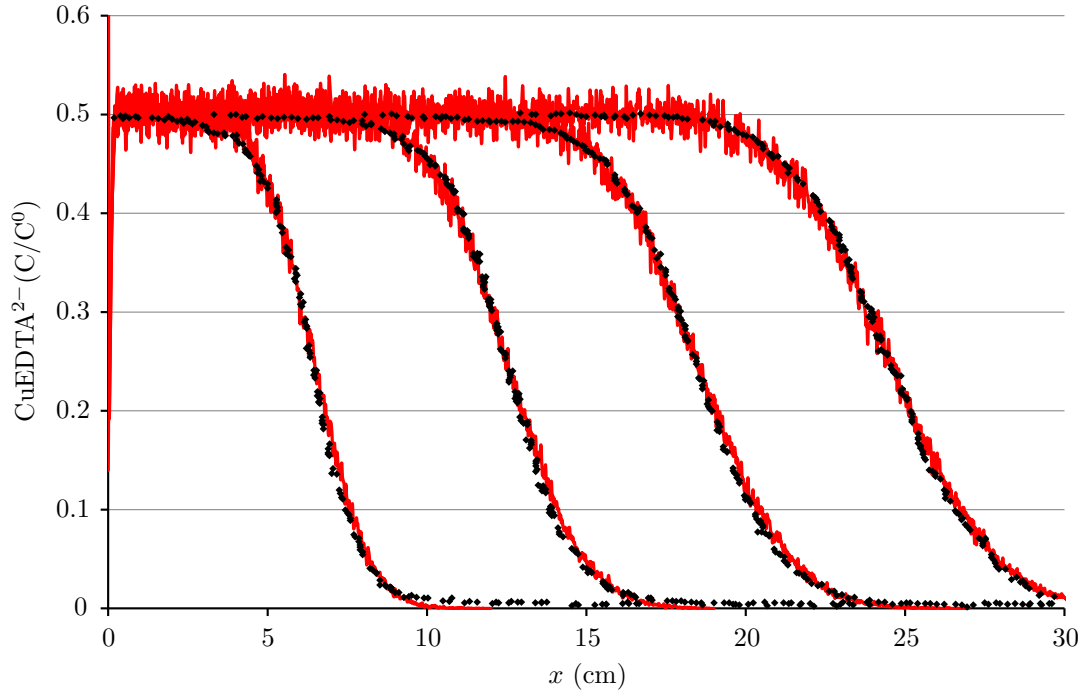


Figure 3.2: Comparison of DTRW solution (red lines) and experimental data from [75] at a) 532 s, b) 1032 s, c) 1523 s and d) 2023 s (black diamonds). The DTRW solution is the average of 10 simulations with a maximum particle density of 900 per  $\text{cm}^2$  and  $\Delta t = 1$  s.

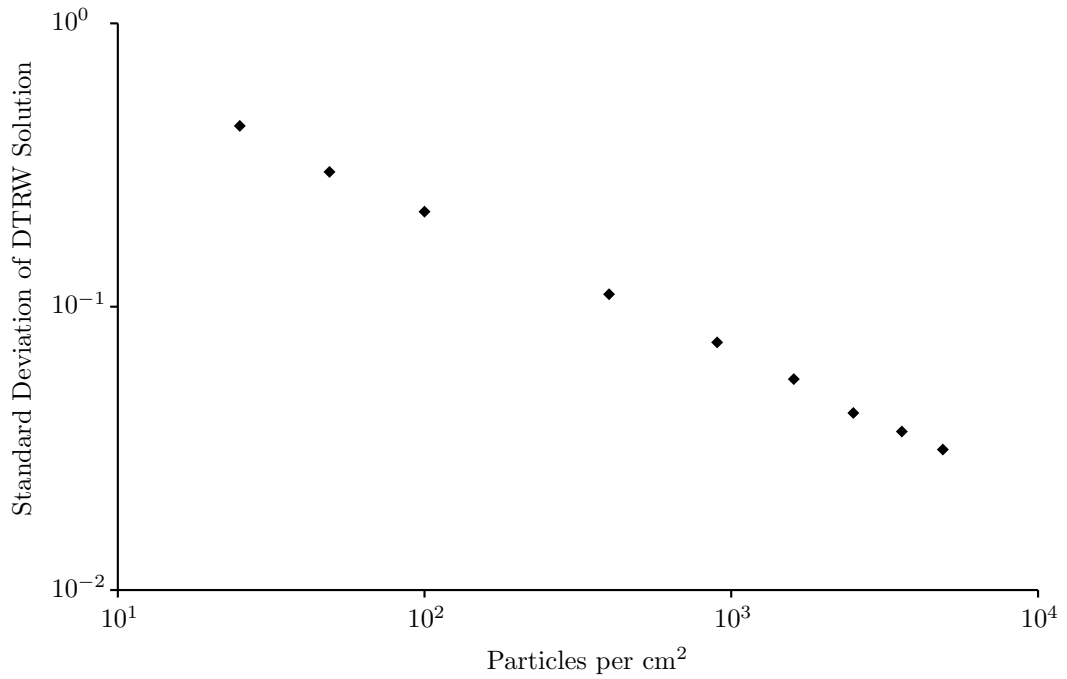


Figure 3.3: The effect of particle density on the standard deviation of the DTRW solution. The DTRW solutions are scaled so that  $C^0 = 1$ . The best fit relationship takes the form  $\sigma = 2.129P_d^{-0.497}$

due to the manner in which particles are added to the domain at inflow boundaries. The addition of particles to the domain at inflow boundary conditions is performed under the assumption that the flow is entering the domain perpendicular to the boundary. Assume in this situation that the inflow boundary is at  $x = 0$  for a domain where  $0 \leq x \leq l$ . Say that  $x_{s0}$  is the separation between two particles, in the  $x$  direction, for a uniformly distributed set of particles at particle density  $PD$ , so that  $x_{s0} = 1/\sqrt{PD}$ . For a flow velocity  $V$  and time step  $\Delta t$  the time and  $x$  location at which new particles are placed in the domain is determined by Algorithm 3.3. The  $x$  and  $y$  coordinates of particles being added to the domain are randomly distributed within the imposed limits.

This addition of particles is performed after the particle transport step has been completed. Some particles disperse against the flow direction into the space left by their advection. These particles should essentially swap places with some of the particles from the solute which has just entered the domain, but these particles do not yet exist. When new particles are then added to the domain at  $C^0$  this influx combined with the particles which have dispersed into the area lead to the anomalous concentration spike. The amount of the domain affected by this is determined by the length of  $V\Delta t$ . This peak is flattened out during the subsequent dispersive transport step but would still be in existence during the reaction simulation. Attempting to flatten this peak by adding a drift to the location of the newly added particles causes the quality of the solution to be reduced at the advancing front. This area is the most important part of the solution to correctly simulate as its form controls the form of product concentration curves and breakthrough curves. The quality of the solution by the inflow boundary is sacrificed to ensure the quality of the solution where it is most important.

---

**Algorithm 3.3** Particle Influx

---

```

 $x_{s0} = 1/\sqrt{PD}$ 
 $x_s = 0$ 
do  $i = 1$  , No. of timesteps
     $x_s = x_s + V\Delta t$ 
    do while  $(x_s - x_{s0}) \geq 0$ 
        Add particles.
        do  $j = 1$  ,  $\text{int}[PD(y_{max} - y_{min})]$ 
             $x_j = x_s - x_{s0} + \text{U}[0, 1]x_{s0}$ 
             $y_j = \text{U}[y_{min}, y_{max}]$ 
        end do
         $x_s = x_s - x_{s0}$ 
    end do while
end do

```

---

Figures 3.13 and 3.14 show that the change in the resolution of the underlying finite element grid from 0.25 cm by 0.25 cm to 2 cm by 2 cm has no visible effect on the quality of the solution. In simulations with variable flow fields the element size affects the particle transport as it affects the quality of the flow field solution used to drive the advective transport.

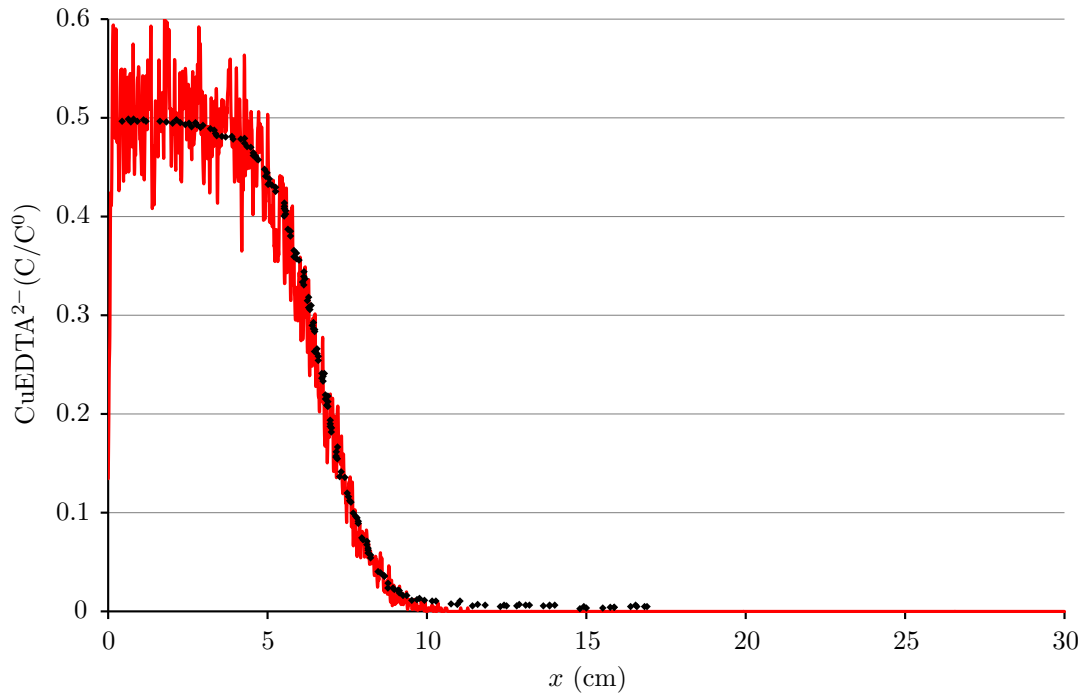


Figure 3.4: Comparison of DTRW solution (red lines) and experimental data from [75] at 532 s (black diamonds). The DTRW solution is the average of nine simulations with a maximum particle density of 100 per  $\text{cm}^2$  and  $\Delta t = 1$  s.

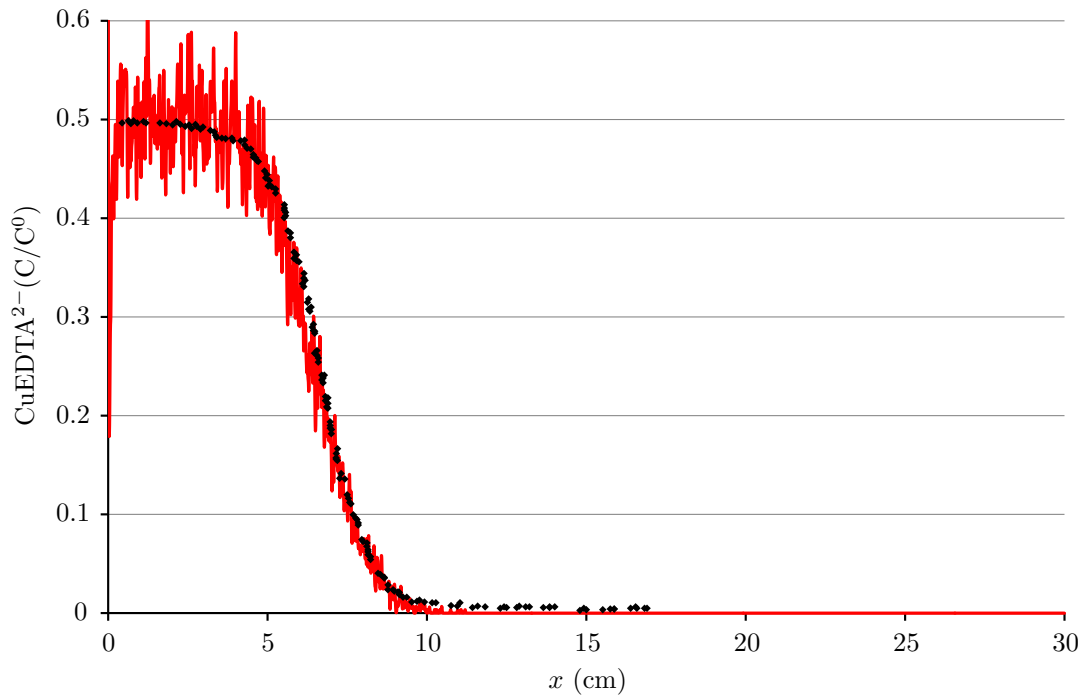


Figure 3.5: Comparison of DTRW solution (red lines) and experimental data from [75] at 532 s (black diamonds). The DTRW solution is a single simulation maximum particle density of 900 per  $\text{cm}^2$  and  $\Delta t = 1$  s.

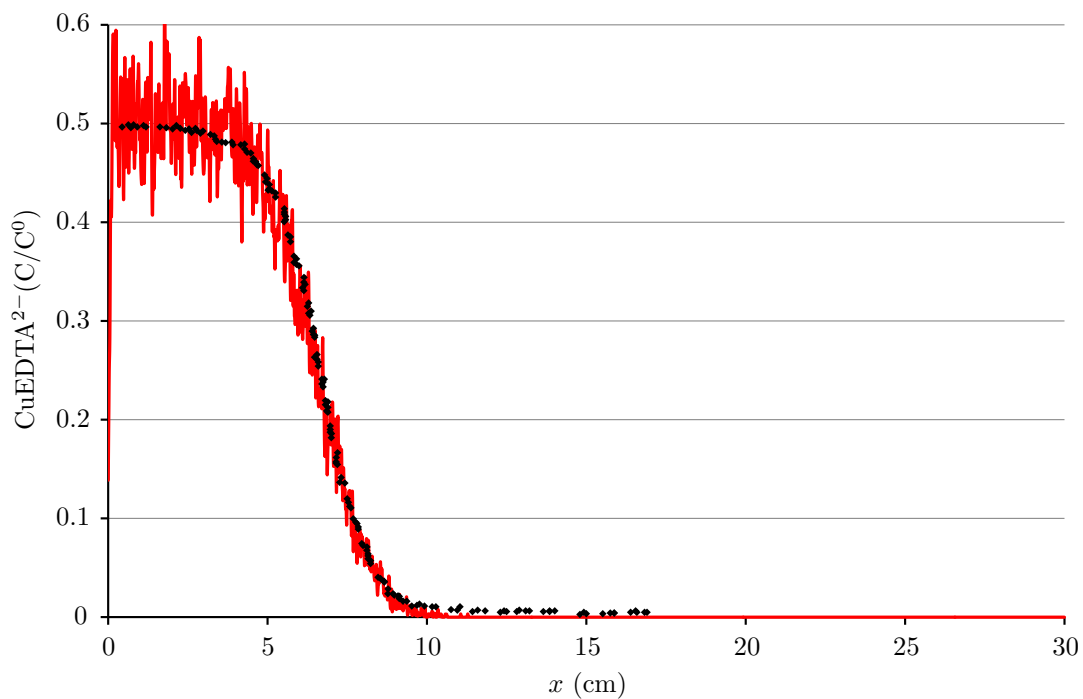


Figure 3.6: Comparison of DTRW solution (red lines) and experimental data from [75] at 532 s (black diamonds). The DTRW solution is the average of 10 simulations with a maximum particle density of 100 per  $\text{cm}^2$  and  $\Delta t = 1$  s.

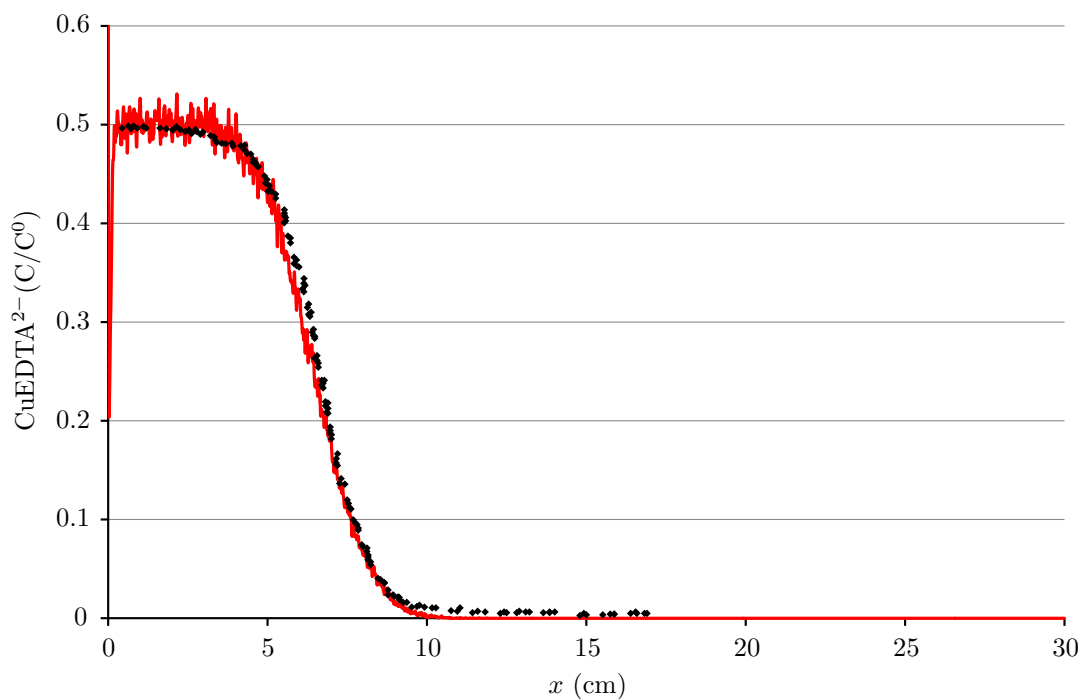


Figure 3.7: Comparison of DTRW solution (red lines) and experimental data from [75] at 532 s (black diamonds). The DTRW solution is the average of 10 simulations with a maximum particle density of 900 per  $\text{cm}^2$  and  $\Delta t = 1$  s.

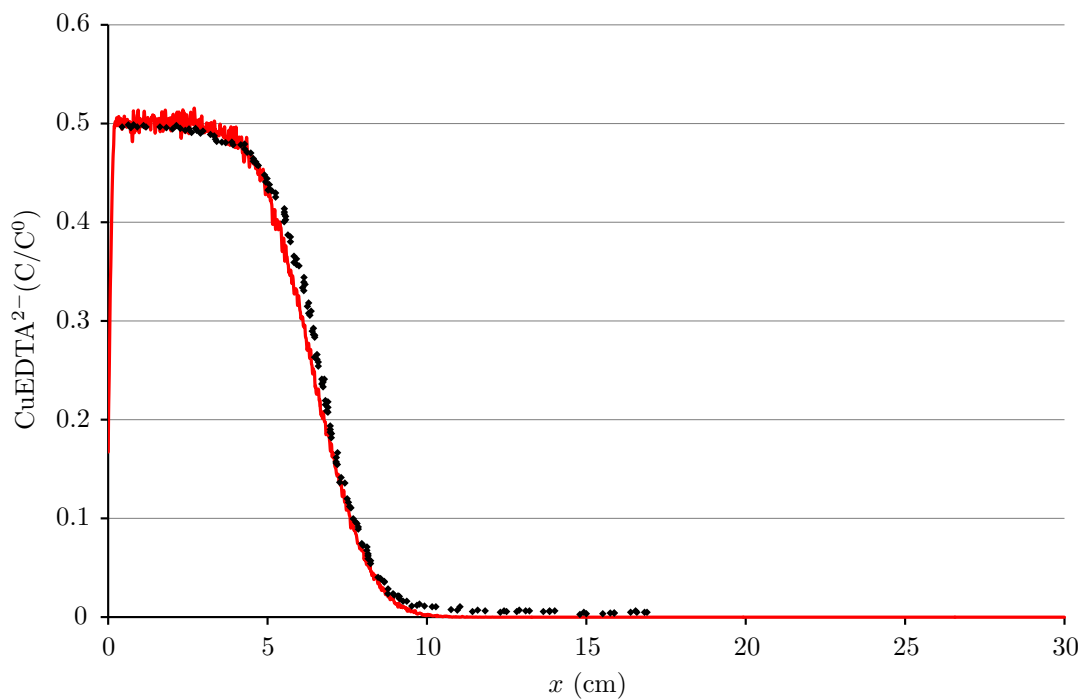


Figure 3.8: Comparison of DTRW solution (red lines) and experimental data from [75] at 532 s (black diamonds). The DTRW solution is the average of 10 simulations with a maximum particle density of 2500 per  $\text{cm}^2$  and  $\Delta t = 1$  s.

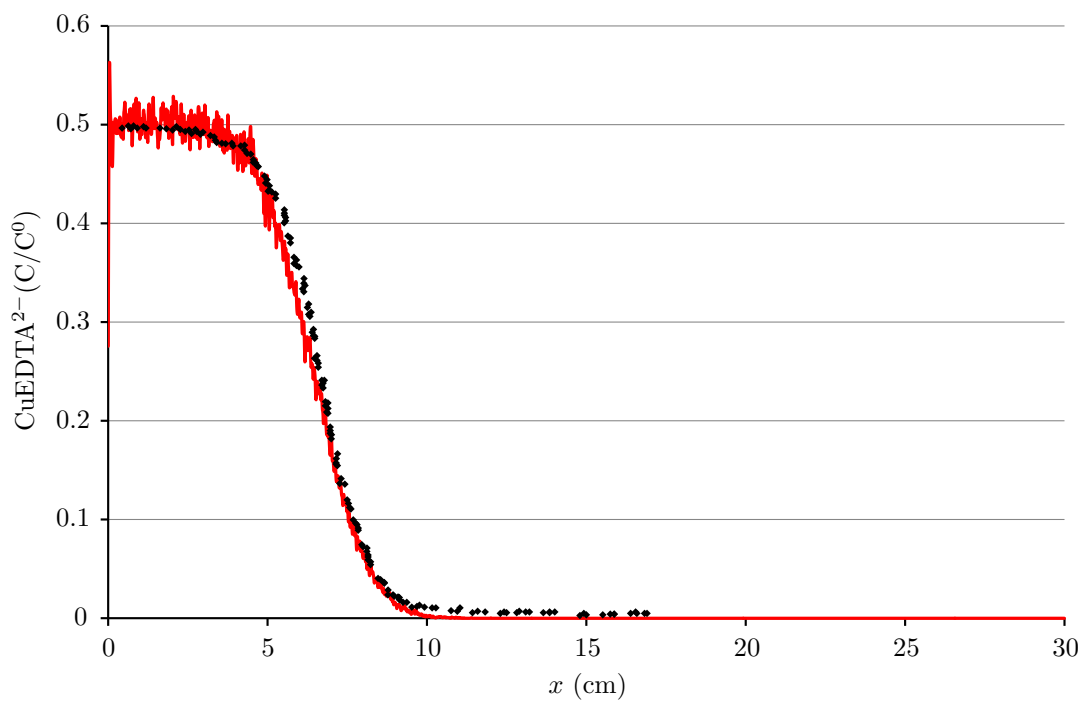


Figure 3.9: Comparison of DTRW solution (red lines) and experimental data from [75] at 532 s (black diamonds). The DTRW solution is the average of 10 simulations with a maximum particle density of 900 per  $\text{cm}^2$  and  $\Delta t = 0.1$  s.

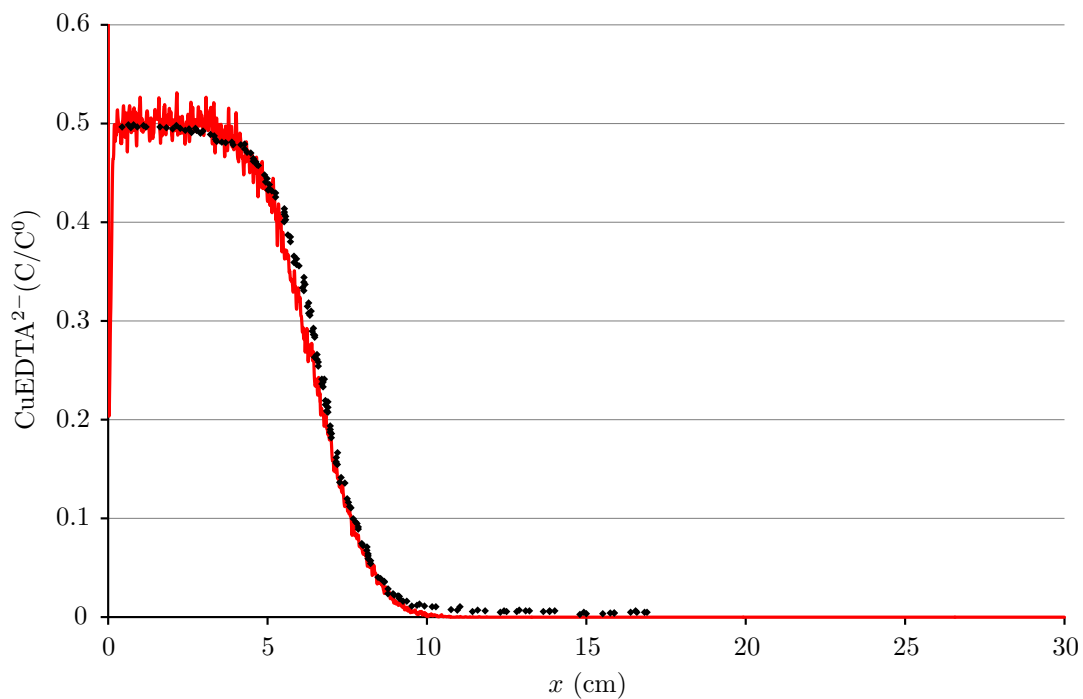


Figure 3.10: Comparison of DTRW solution (red lines) and experimental data from [75] at 532 s (black diamonds). The DTRW solution is the average of 10 simulations with a maximum particle density of 900 per  $\text{cm}^2$  and  $\Delta t = 1$  s.

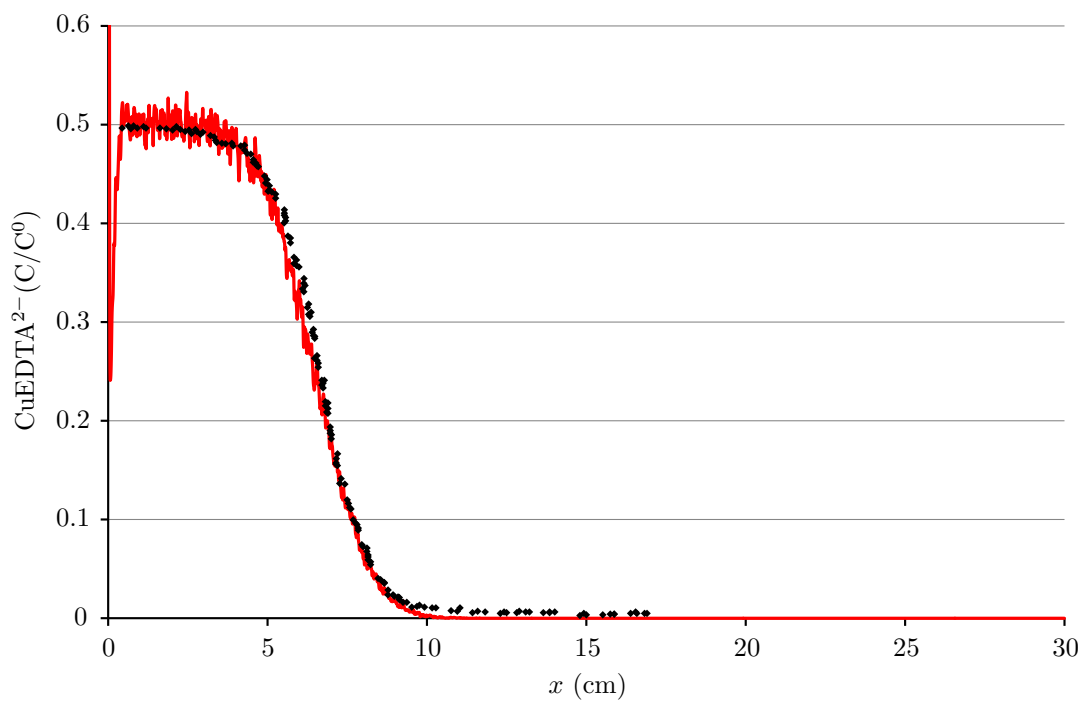


Figure 3.11: Comparison of DTRW solution (red lines) and experimental data from [75] at 532 s (black diamonds). The DTRW solution is the average of 10 simulations with a maximum particle density of 900 per  $\text{cm}^2$  and  $\Delta t = 4$  s.

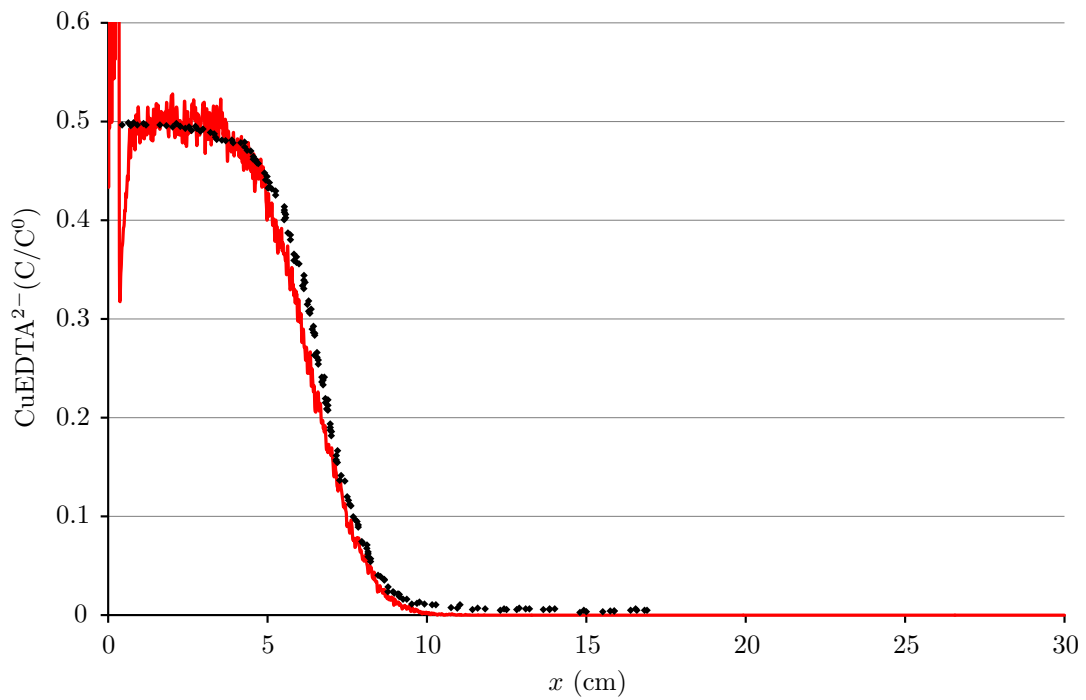


Figure 3.12: Comparison of DTRW solution (red lines) and experimental data from [75] at 532 s (black diamonds). The DTRW solution is the average of 10 simulations with a maximum particle density of 900 per  $\text{cm}^2$  and  $\Delta t = 28$  s.

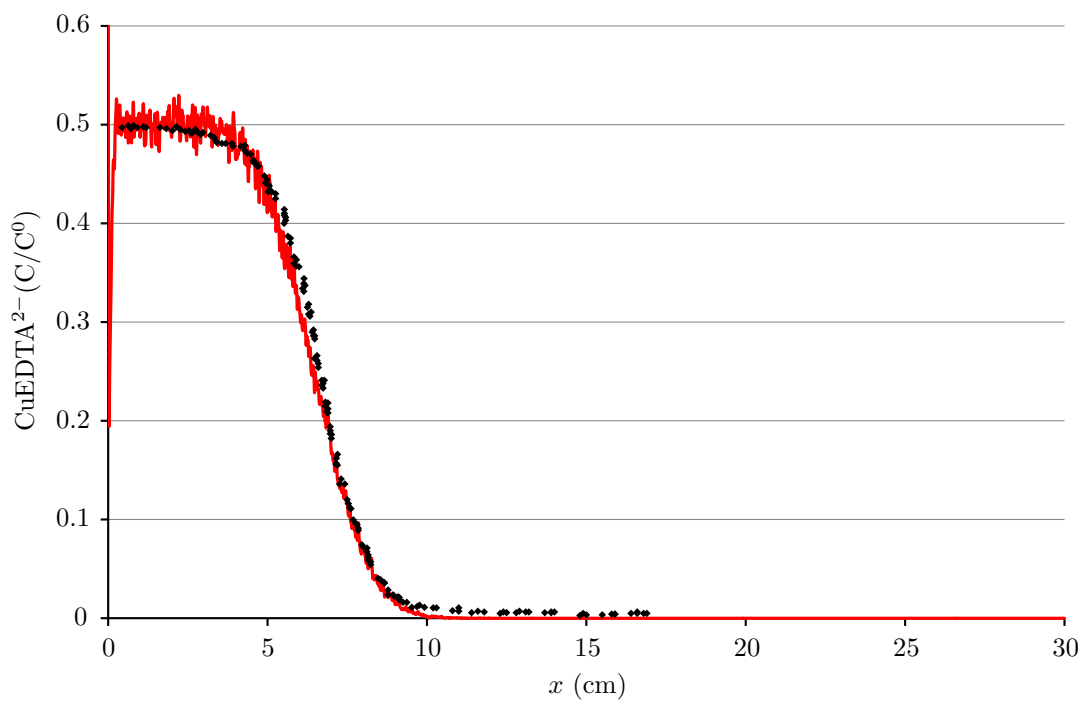


Figure 3.13: Comparison of DTRW solution (red lines) and experimental data from [75] at 532 s (black diamonds). The DTRW solution is the average of 10 simulations with a maximum particle density of 900 per  $\text{cm}^2$ ,  $\Delta t = 1$  s and an underlying finite element grid of 0.25 cm by 0.25 cm elements.

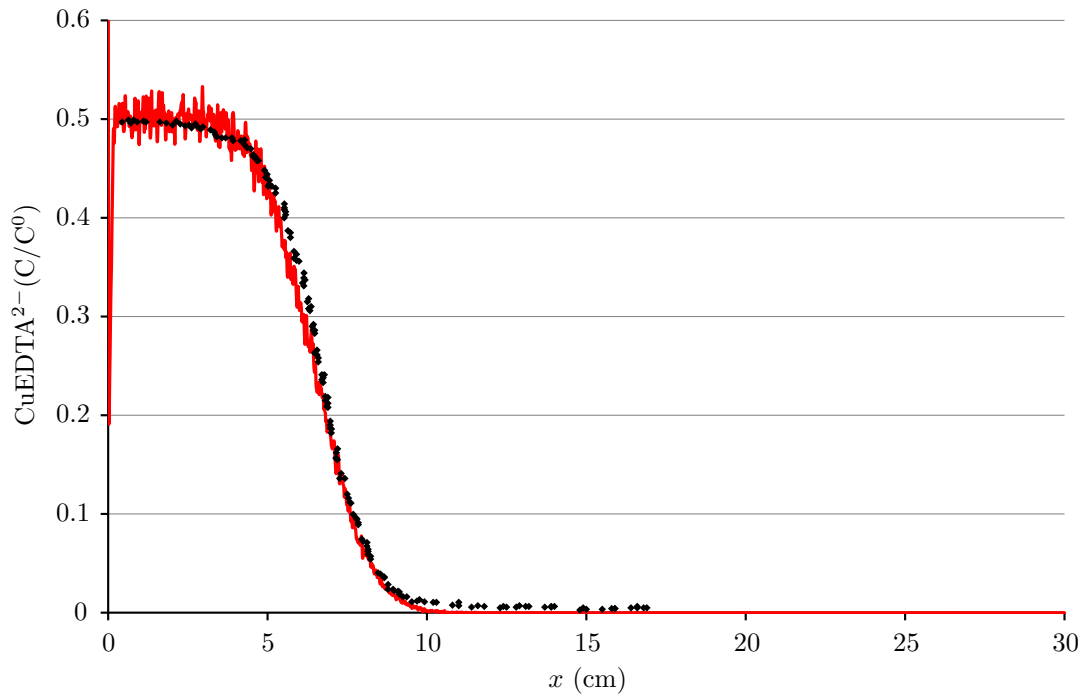


Figure 3.14: Comparison of DTRW solution (red lines) and experimental data from [75] at 532 s (black diamonds). The DTRW solution is the average of 10 simulations with a maximum particle density of 900 per  $\text{cm}^2$ ,  $\Delta t = 1$  s and an underlying finite element grid of 2 cm by 2 cm elements.

### 3.3 Conclusion

In this chapter the rationale behind the use of the DTRW method for the solution of solute transport in porous media and the framework of the method have been outlined. The DTRW method is free of the oscillation or numerical dispersion caused by using 2<sup>nd</sup> or 1<sup>st</sup> order approximation of advection using continuum based approaches such as FEM. This is the primary reason for its use in this study.

The DTRW method and how it utilizes a FEM solution for porous media flow used to drive the advective transport, as outlined in Chapter 2, has been described along with the specifics of its implementation in Fortran90. The differences between the DTRW and the CTRW particle tracking methods have been outlined. The DTRW solution has been shown to produce results that fit very well to the experimental data presented in [75] and its robustness under differing  $\Delta t$ , maximum particle density and underlying finite element grid resolution conditions has been demonstrated. The standard deviation of the DTRW solution from the mean concentration with maximum particle density has been shown to follow an inverse power law. The number of particles included in a solution can be increased either by using a higher number of particles in a single solution or by summing several solutions. The averaging of solutions is generally preferred as it allows for solutions to be produced which would not be possible in a single run on due to memory restrictions.

In the next chapter the DTRW method is expanded to include the simulation of reactions between different solutes and the sorption of solutes to soil solids.

## Chapter 4

# Non Conservative Transport

### Summary

In this chapter the simulation of reactions and adsorption of chemical species is the primary focus. The basic chemistry of homogeneous reactions between solutes and of sorption of solutes to the soil solids is discussed. This is followed by the equations used to describe these processes on the macroscopic scale and how these are simulated within a particle tracking framework. These methods are then compared with experimental data and other simulations. Finally a sensitivity analysis is presented to demonstrate the robustness of the approach for variations in nonphysical parameters. The chapter begins by focussing on bimolecular reactions, followed by sorption.

### 4.1 Introduction

The behaviour of many of the chemical species which are of interest in contaminated land cannot be accurately described under the assumption that their transport is conservative. Solutes often react homogeneously, with other solutes, or adsorb onto soil solids. Reactions can transform species into forms which are more or less mobile, or more or less harmful. Adsorption can reduce or effectively stop the transport of a chemical species. The inclusion of these chemical processes is therefore important for the accurate simulation of contaminant transport in soils. Simulation of reactions and sorption of solutes in soils using continuum based approaches is a well developed field of study. Simulating these chemical processes using particle tracking methods is not so well advanced. Simulation of reactions has tended to focus on homogeneous bimolecular reactions of the form  $A + B \rightarrow C$  with a number of studies presenting comparisons with the experimental results from Gramling *et al.* [75] due to the high quality of the data presented therein [35, 36, 77–79]. Likewise simulation of sorption of solutes using particle tracking methods has generally been limited to comparisons with data from laboratory column experiments [80–83]. The simulation of homogeneous reactions is the topic of the first section of this chapter.

### 4.2 Homogeneous Reactions

Homogeneous reactions are those that occur between two chemical species within the same phase though here this term is always used to refer to reactions between two solutes. To begin with consider an irreversible, homogeneous reaction between two solutes A and B, to form a product C



The reaction rate  $R_r$ , *i.e.* the amount of moles of a solute added to or removed from the system by the reaction over time, is

$$R_r = -\frac{d[A]}{dt} = -\frac{d[B]}{dt} = \frac{d[C]}{dt} \quad (4.2)$$

where  $[A]$ ,  $[B]$  and  $[C]$  are concentrations of the chemical species A, B and C respectively. The reaction rate is determined by

$$R_r = k[A][B] \quad (4.3)$$

where  $k$  is the rate constant. The rate constant can be experimentally determined using the modified Arrhenius equation [84]. Whether a chemical reaction takes place depends upon whether a collision contains enough energy to equal the activation energy of the reaction [85, 86]. The modified Arrhenius equation gives a statistical description of how often this happens for a given chemical reaction at a certain temperature. The inclusion of temperature dependence within the model is beyond the scope of this work.

Reactions between chemical species which are both solutes can be limited by their rates of diffusion [85, 87]. Consider a bimolecular, irreversible reaction with a rate constant  $k$



This reaction can be thought of as the net result of three different reactions



In Equation 4.5 the two molecules of reactants  $A$  and  $B$  diffuse at a rate  $k_d$  until they collide at which point they form the complex  $AB$ . This complex can either separate back into  $A$  and  $B$ , at a rate  $k_r$ , or continue to form the product  $C$ , at a rate  $k_p$ . This is consistent with the standard statement of reaction rate for a bimolecular reaction with a rate coefficient  $k_p$

$$R_r = k_p [AB]. \quad (4.8)$$

By making a steady state approximation the concentration of this intermediate product can be expressed in terms of the reactants as

$$\frac{d[AB]}{dt} = 0 = k_d [A][B] - k_r [AB] - k_p [AB] \quad (4.9)$$

$$\therefore [AB] = \frac{k_d [A][B]}{k_r + k_p}. \quad (4.10)$$

By substituting Equation 4.10 into Equation 4.8 the reaction rate becomes

$$R_r = \frac{k_p k_d [A][B]}{k_r + k_p}. \quad (4.11)$$

If  $k_p \gg k_r$ , *i.e.* where a molecule collision is far more likely to lead to a reaction than not, Equation 4.11 becomes

$$R_r = k_d [A][B] \quad (4.12)$$

where

$$k_d = 4\pi N_A(r_A + r_B)(D_A + D_B) \quad (4.13)$$

and  $N_A$  is the number of molecules,  $r_A$  and  $r_B$  are the molecular radii for  $A$  and  $B$  respectively and  $D_A$  and  $D_B$  are the molecular diffusivities for  $A$  and  $B$  respectively [86].

In a porous medium diffusion is not the only factor affecting the spreading, and therefore the mixing of reactive solutes. They are also transported in a Fickian type manner by hydrodynamic dispersion and so the rate of diffusion is not the only limiting factor on reaction rates. Reaction rates between solutes in porous media can be less than those measured experimentally in fluids, and neglecting this can lead to the overprediction of reaction rates [75, 76]. This overprediction is attributed to the imperfect mixing of reactants. In porous media this is not just due to the limiting of mixing by diffusion but the segregation of reactants into different pore spaces.

Consider the type experimental setup used in [75, 76] where a porous medium is saturated with a solute  $A$  and then flushed with a second solute  $B$  which reacts with the first. In these examples the rate of dispersion is two orders of magnitude greater than the rate of diffusion so we can safely focus the following discussion on the effect of differential flow rates within the porous medium. The two solutes spread via dispersion and, from a macroscopic view point, a mixing zone exists where both occupy the same space. This dispersive spreading is partly due to the different flow rates in different parts of the porous medium. The solute molecules of  $A$  which have travelled furthest into the domain have travelled along paths where the fluid flow rate is highest. These molecules have flowed into different pores from those which hold the  $B$  molecules which have travelled the least distance as they are in the parts of the domain with the lowest flow rates. On the macro scale this gives the impression of mixing of concentration plumes but at the pore scale the two solutes can in fact simply be occupying different parts of the porous medium, at the pore scale, and so are unable to react.

### 4.2.1 Simulating Reactions using Particle Tracking Methods

In a continuum method such as the Finite Element Method (FEM), assuming that  $R_r = k[A][B]$  adequately describes the reaction rate, it is straightforward to simulate Equation 4.1. In particle tracking methods it is more complicated. Conversions can be made from a particle concentration field to a nodal concentration field *e.g.* [88] though this produces errors which are propagated through the reaction calculations and conversion back to particles.

To simulate reaction in the particle tracking method, reactions are modelled as occurring between discrete numbers of particles. For example, Equation 4.1 would be simulated by one  $A$  particle and one  $B$  particle combining to produce one  $C$  particle. To perform reactions in the Discrete Time Random Walk (DTRW) or Continuous Time Random Walk (CTRW) framework some way of determining whether two particles react needs to be formulated. This is referred to as the reaction criterion.

Gillespie [89, 90] developed a method for simulating reactions between particles referred to as the stochastic simulation algorithm. In this method the number of reactions between two sets of particles is determined stochastically based on the probability of a collision occurring between one particle of each species possessing enough energy for a reaction to occur. Attempting to work out the solution of this stochastic problem in a standard analytical or numerical sense is challenging [89]. Instead the reaction probabilities are with the output of a Pseudorandom Number Generator (PRNG) which decides whether to allow or disallow each potential reaction [89]. Multiple realizations of the system are then run to determine the average reaction rate. This reaction simulation is developed independently of any particle tracking transport simulation.

The determination of reactions within either the DTRW or CTRW framework is based on the same

concept despite the fact that particles in either of these methods do not represent individual molecules or atoms. Due to this the effect of molecular radii is removed from the equation as the particles do not collide in the same manner. As the particles in the DTRW method represent packets of solute particles there is no physical problem with two of them occupying the same space. The main difference in method between different researchers simulating reactions using either the DTRW or CTRW framework is in how the reaction criterion is determined. Edery *et al.* [77, 78] use a deterministic rule for the reaction criterion. If the nearest particle of the other reactant species is less than some set distance, or reaction radius, away from the particle being checked then a reaction takes place. This reaction radius is set at the beginning of the simulation. In [77, 78] this value is set to be of the same order as the grain size in the porous medium. Reaction rates are not solely determined by the probability of reactants coming into contact, as discussed earlier. This method, in the form used in [77, 78], assumes that reactants always react if they come into contact and would need to be expanded to simulate slower reactions.

Alternatively a probabilistic reaction criterion can be used [35]. The probability of two particles being colocated over a time step is a function of their initial separation and the distance that either one may move by diffusion or hydrodynamic dispersion [35]. The Location Probability Functions (LPFs) used to determine the dispersive transport of the two particles can be convoluted to produce a Colocation Probability Function (CLPF) which gives the probability of the two particles being colocated as a function of space. This CLPF is then scaled by a rate constant  $k$  to give a probability of reaction. This probability of reaction is then compared to a U[0,1] PRNG to determine whether a reaction has taken place. This method has been shown to be mathematically consistent with the diffusion reaction equation for spatially constant advection [79]. The CLPF method is used here due to its superior flexibility.

### Colocation Probability Functions

As described in Chapter 3, in this thesis the dispersive transport of solutes is simulated by a random walk. This random walk has a Gaussian distribution with a standard deviation,  $\sigma$ , equal to  $\sqrt{2D_h\Delta t}$ . In two dimensions, assuming equal longitudinal and transverse dispersivities, the LPF takes the form

$$P(x, y) = \frac{1}{2\pi\sigma^2} \exp \left[ -\frac{(x - x_p)^2 + (y - y_p)^2}{2\sigma^2} \right] \quad (4.14)$$

where  $P(x, y)$  is the probability of a particle being at a location as a function of  $x$  and  $y$  for a particle initially situated at  $(x_p, y_p)$  undergoing dispersive transport with a dispersivity of  $D_h$  a time step  $\Delta t$  into the future. The probability of two particles being colocated  $P_c$ , or the CLPF, is the convolution of their respective LPFs. For two particles,  $i$  and  $j$ , located at  $(x_i, y_i)$  and  $(x_j, y_j)$  respectively, this is given by

$$P_c(x, y) = P_i(x, y)P_j(x, y) = \frac{1}{4\pi^2\sigma^4} \exp \left[ \frac{(x - x_i)^2 + (y - y_i)^2 + (x - x_j)^2 + (y - y_j)^2}{2\sigma^2} \right]. \quad (4.15)$$

The total probability of colocation can be given by the integral over  $x$  and  $y$ ,

$$P_c = \int_{-\infty}^{\infty} \int_{-\infty}^{\infty} \frac{1}{4\pi^2\sigma^4} \exp \left[ \frac{(x - x_i)^2 + (y - y_i)^2 + (x - x_j)^2 + (y - y_j)^2}{2\sigma^2} \right] dx dy. \quad (4.16)$$

The indefinite integral takes the form

$$\frac{\pi\sigma^2}{16\pi^2\sigma^4} \operatorname{erf} \left[ -\frac{-2x + x_i + x_j}{2\sigma} \right] \operatorname{erf} \left[ -\frac{-2y + y_i + y_j}{2\sigma} \right] \exp \left[ -\frac{(x_i - x_j)^2 + (y_i - y_j)^2}{4\sigma^2} \right] \quad (4.17)$$

and so the definite integral from  $-\infty$  to  $+\infty$  in  $x$  and  $y$  evaluates to give the probability of colocations as,

$$P_c = \frac{1}{4\pi\sigma^2} \exp \left[ -\frac{(x_i - x_j)^2 + (y_i - y_j)^2}{4\sigma^2} \right]. \quad (4.18)$$

As we know from Chapter 3 that  $\sigma = \sqrt{2D_h\Delta t}$  this can be substituted into Equation 4.18 to give

$$\frac{1}{8\pi D_h \Delta t} \exp \left[ -\frac{(x_i - x_j)^2 + (y_i - y_j)^2}{8D_h \Delta t} \right]. \quad (4.19)$$

For  $D_h\Delta t > (8\pi)^{-1}$  the value of Equation 4.19 can be  $>1$ . This is obviously an issue as a probability can never be  $>1$  or  $<0$ . To alleviate this problem the function is multiplied by  $8\pi D_h\Delta t$  to give

$$P_c(x_i, y_i, x_j, y_j) = \exp \left[ -\frac{(x_i - x_j)^2 + (y_i - y_j)^2}{8D_h \Delta t} \right]. \quad (4.20)$$

If the particles are colocated initially (*i.e.*  $x_i = x_j$  and  $y_i = y_j$ ) then  $P_c = 1$ .

In a simulation we may want to limit the reaction rate in some way. To achieve this two extra terms,  $P_{max}$  and  $\sigma_s$  are added.  $P_{max}$  scales the maximum probability of reaction, *i.e.*, the probability of reaction at colocation and  $\sigma_s$  scales the variance of the CLPF. The addition of these two terms gives the CLPF as

$$P_c(x_i, y_i, x_j, y_j) = P_{max} \exp \left[ -\frac{(x_i - x_j)^2 + (y_i - y_j)^2}{8D_h \Delta t \sigma_s} \right] \quad (4.21)$$

for the situation where  $D_h$  is equal for both reactants and is equal in the longitudinal and transverse directions. The alteration to Equation 4.21 to account for the reactants having different diffusivities is simple and the form of the CLPF becomes

$$P_c(x_i, y_i, x_j, y_j) = P_{max} \exp \left[ -\frac{(x_i - x_j)^2 + (y_i - y_j)^2}{8\sqrt{D_{h_i}}\sqrt{D_{h_j}}\Delta t\sigma_s} \right] \quad (4.22)$$

where  $D_{h_i}$  and  $D_{h_j}$  are the dispersivities of particles  $i$  and  $j$  respectively.

It is important to note at this point that the standard deviation is scaled by the hydraulic diffusivity  $D_h$  not the molecular diffusivity  $D_m$ . The theoretical construction of this reaction criterion is based on the probabilities of molecules colliding with one another but the particles represent groups of molecules rather than individual molecules. The CLPF is therefore scaled by the movement of the group of particles on the macroscale, which is controlled by  $D_h$ , rather than the movement of individual particles on the microscopic scale, which is controlled by  $D_m$ . This will be discussed in depth, later in the chapter.

In particle tracking methods, as in reality, reactions rates are limited by two factors; how likely two particles are to come into contact and how likely they are to react when they do so. So far the probability of colocation occurring has been discussed but the probability of a reaction occurring when this happens has not. In chemistry the probability of a reaction occurring between two molecules is determined by the energy the colliding molecules possess and the activation energy of the reaction [86]. To think in the same terms for the probability of reaction occurring in a particle tracking simulation is a mistake. The particles in a particle tracking simulation *do not represent individual molecules*. This assumption is made when it is useful, such as for simulating transport, but otherwise should be avoided. If simulation particles are to represent molecules then the domain they are transported through should possess the heterogeneity of the porous medium which the simulation domain does not.

The probability of two colocated particles reacting, denoted by  $P_{max}$ , represents a range of physical and chemical controls on the reaction rate. This includes the rate constant, the pore scale mixing rate

and the microscopic mixing rate. The concept of a rate constant has been discussed earlier in this chapter so we shall proceed to pore scale and microscopic mixing. Homogenous reactions between solutes can be limited by the rate at which they diffuse through the solvent [86]. As the solute molecules move through the solvent they are prevented from colliding with other solute molecules by the solvent molecules which surround them, and as such the mixing of the molecules on the microscopic scale affects the reaction rate. If particles are unlikely to come into contact with one another but the probability of them reacting when they do so is high the reaction rate is diffusion limited. The reaction rate can also be limited by pore scale mixing. Due to the nature of a porous medium solutes can be mixed at the macro scale, but at the pore scale a situation can arise where some of the pores predominantly contain one solute reactant and others another. From the macro scale viewpoint the two reactants are in the same space and should be reacting but at the pore scale there is very little contact between them and so little reaction occurs. This is an important aspect in the accurate simulation of reactive transport in porous media and is discussed in depth later in this chapter.

As particle tracking methods are a method for reproducing the macroscopic behaviour of solutes in porous media the variables  $P_{max}$  and  $\sigma_s$  must encapsulate all of these factors, not just the rate constant of the reaction being simulated or the diffusion limiting of this rate. The following section presents the implementation of the CLPF reaction method used in this thesis.

### Implementation of Reaction Solution

For two fields of solute particles,  $A$  and  $B$ , containing  $N_A$  and  $N_B$  particles respectively, which can react to form a product  $C$  the solution of the reaction simulation between the two solutes is performed using Algorithm 4.1. The indexing notation used is  $ii$  and  $jj$  for loops over  $N_A$  and  $N_B$  and  $i$  and  $j$  for loops over other variables. For coordinates the notation used is  $x_{P_{ii}}$  is the  $x$  coordinate of particle  $ii$  and  $y_{N_j}$  is the  $y$  coordinate of node  $j$ .

In Algorithm 4.1 species  $A$  and  $B$  do not necessarily correlate with species  $A$  and  $B$  in the other aspect of the simulation method. The species which forms the outer  $ii$  loop of Algorithm 4.1 is alternated between the two input species each time step to cancel out any effect that one species being the outer loop rather than the inner loop may have on the solution. The coordinates of the reacted particles are set to  $(10^9, 10^9)$ . This is a nonsense value used to signify that a location with the array of particle coordinates does not contain a particle. It is large enough that the dimensions of the domain should never equal it and if a non-existent particle is accidentally passed into the reaction solution then no reaction will occur between the non-existent particle and a particle of the other species.

Algorithm 4.1 requires an  $N_B$  search for every pass through the  $i = 1, N_A$  loop. Though this decreases as reactions remove particles from the  $A$  and  $B$  fields this is still very inefficient. The reaction algorithm included in the code used to produce the plots presented in this chapter has been optimised in various ways. The optimisation and acceleration of the code is discussed in Chapter 6.

---

**Algorithm 4.1** Solution of reaction between two solutes in a particle tracking framework.

---

```

do  $ii = 1, N_A$ 
  if  $(x_{A_{ii}} \neq 10^9)$  then
     $d = \sqrt{[(x_{A_{ii}} - x_{B_1})^2 + (y_{A_{ii}} - y_{B_1})^2]}$ 
     $e = 1$ 
    do  $jj = 2, N_B$ 
      if  $\sqrt{[(x_{A_{ii}} - x_{B_{jj}})^2 + (y_{A_{ii}} - y_{B_{jj}})^2]} < d$  then
         $d = \sqrt{[(x_{A_{ii}} - x_{B_{jj}})^2 + (y_{A_{ii}} - y_{B_{jj}})^2]}$ 
         $e = jj$ 
      end if
    end do
     $P_r = P_{max} \exp[-((x_{A_{ii}} - x_{B_e})^2 + (y_{A_{ii}} - y_{B_e})^2)/(8D_h\Delta t\sigma_s)]$ 
    if  $P_r < U[0, 1]$  then
       $i = 1$ 
      do while  $i \leq N_C$ 
        if  $(x_{C_i}, y_{C_i}) \notin \Omega$  then
          exit
        end if
         $i = i + 1$ 
      end do
       $x_{C_i} = (x_{A_{ii}} + x_{B_e})/2$ 
       $y_{C_i} = (y_{A_{ii}} + y_{B_e})/2$ 
       $x_{A_{ii}} = 10^9$ 
       $y_{A_{ii}} = 10^9$ 
       $x_{B_e} = 10^9$ 
       $y_{B_e} = 10^9$ 
    end if
  end if
end do

```

---

### Reaction Rate Controls

As well as the factors within the CLPF,  $P_{max}$ ,  $\sigma_s$ ,  $\Delta t$  and  $D_h$ , reaction rates are also affected by the particle density and the number of reaction attempts that are allowed for each step of the outermost loop in Algorithm 4.1. To investigate these controls separately from other factors the reaction simulations are performed in a test setup. This test setup is a two dimensional domain 3 cm by 3 cm in size. A set number of particles of each of the two reactants are then randomly distributed throughout the domain using the inbuilt Fortran U[0,1] PRNG. A single 1 s timestep is then performed for reaction only and the amount of reactant produced measured. The term ‘reaction rate’ is used to refer to the fractional amount of product formed by the reaction between well mixed reactants in a single reaction step. A reaction rate of 1 indicates that all of the reactants are converted to the product, and conversely a reaction rate of 0 indicates than no product is formed.

Figure 4.1 shows the effect of changing  $\sigma$ , the standard deviation of the CLPF, on reaction rate for simulations performed in the test setup. There is a sharp decrease in reaction rate below a certain value of  $\sigma$  and this value decreases as particle density is increased. As the particle density increases, the average distance between a particle and its nearest neighbour from the other reactant species decreases. Figure 4.2 shows the change in average minimum particle separation with particle density. Average minimum separation, in two dimensions, reduces as a function particle density by the relationship

$$\text{Average Minimum Particle Separation} = \frac{1}{2} [\text{Particle Density per cm}^2]^{-\frac{1}{2}}. \quad (4.23)$$

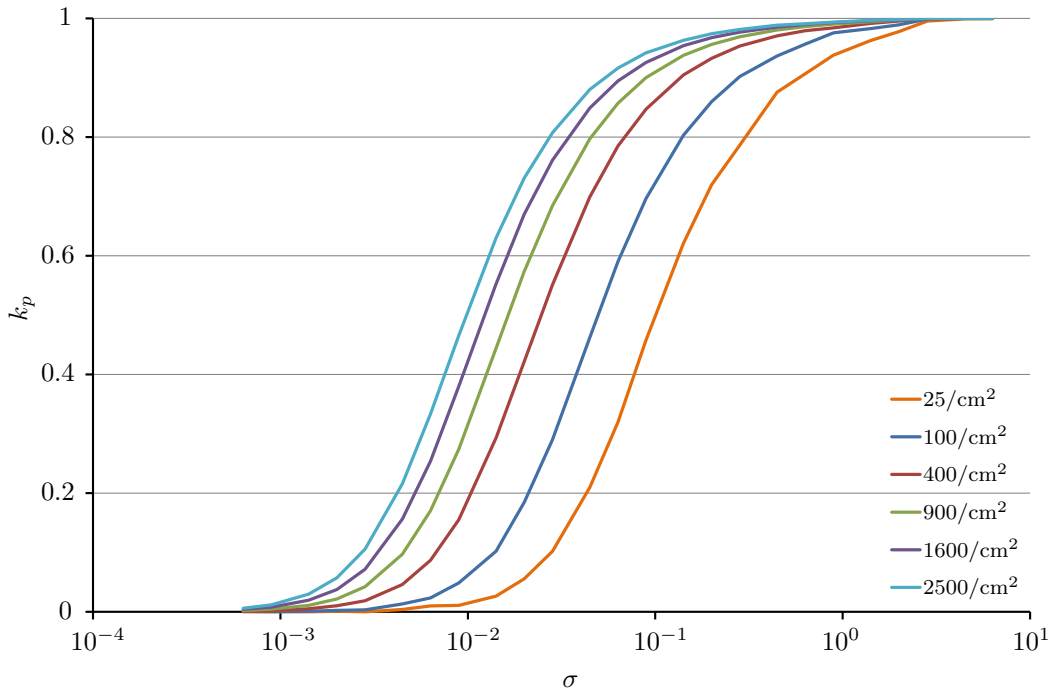


Figure 4.1: A  $\log(x)$  graph of  $D_h$  against single step reaction rate for initial particle densities ranging from 25 per  $\text{cm}^2$  to 2500 per  $\text{cm}^2$  and  $P_{max} = 1$ .

Low  $\sigma$  in combination with low particle densities leads to low reaction rates. The reaction between  $\text{CuSO}_4(\text{aq})$  and  $\text{Na}_2\text{EDTA}^{2-}$  used for the experiments presented in Gramling *et al.* [75] has a formation rate constant of  $2.3 \times 10^9 \text{ M}^{-1} \text{ s}^{-1}$  for the concentration used, making it essentially instantaneous. The diffusivities of the reactants are  $7.02 \times 10^{-7} \text{ cm s}^{-2}$  and  $6.3 \times 10^{-6} \text{ cm s}^{-2}$ . To achieve the expected reaction rates with the CLPF standard deviation based on these values would require a very high particle density.

At this point it is important to note that the assumption that forms the basis of particle tracking methods, that the behaviour is invariant of particle number so that the behaviour of a smaller number of particles can be used to simulate the behaviour of a much larger number of particles, begins to break down in this situation. The use of particle tracking methods for the simulation of reactive transport in situations where the dispersivity is low and the reaction rates are high should be approached with care.

Figure 4.3 shows the effect of changing  $P_{max}$  on reaction rate for simulations performed in the 3 cm by 3 cm, no flow test setup. There is a 1 to 1 relationship between  $P_{max}$  and reaction rate for a single reaction step. This varies slightly at low particle densities due to the heightened effect of the probabilistic nature of the simulation. At lower particle densities the deviations due to random fluctuations in the solution are more pronounced.

Though the effects of  $P_{max}$  on reaction rate are unaffected by particle density they are affected by how many attempts a particle in the outer loop of Algorithm 4.1 has at reacting with a particle from the other reactant species. It is possible to alter Algorithm 4.1 so that if particle  $i$  fails to react with the closest particle from the other reactant species then a reaction is attempted with the next closest particle. This can be repeated until either a reaction takes place or a predetermined limit on the number of attempts allowed is reached. The effect of changing the maximum number of reaction attempts per particle per timestep for different values of  $P_{max}$  and  $\sigma$  are shown in Figures 4.4 and 4.5 respectively. The control that the number of attempts an outer loop particle has at reacting,  $N_{ra}$ , on the reaction rate

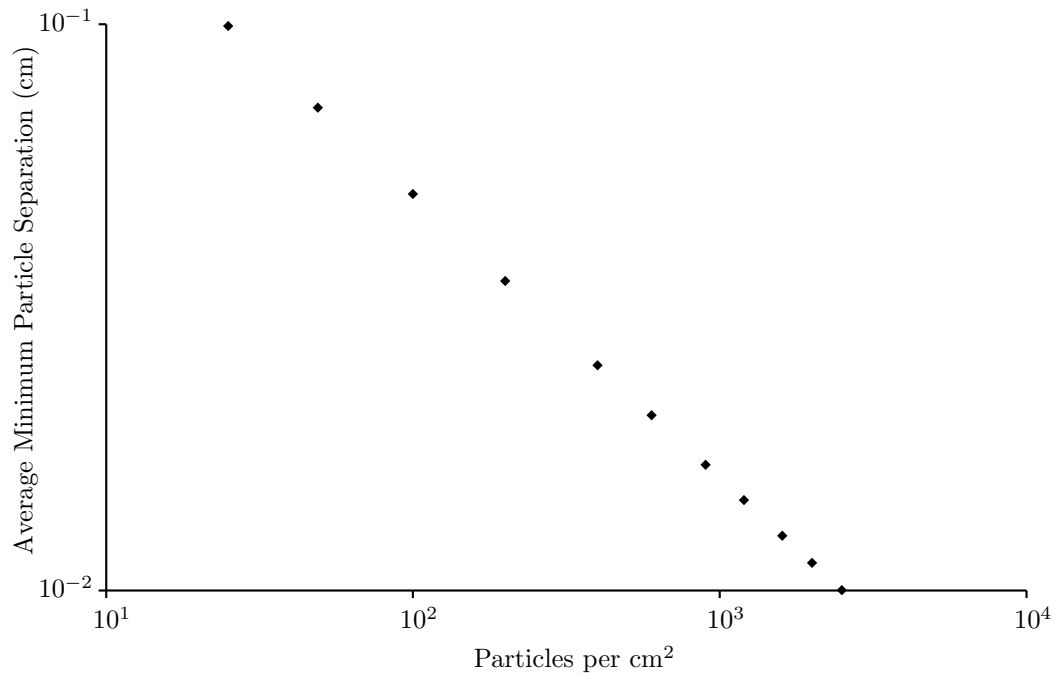


Figure 4.2: A log-log graph showing the relationship between particle density and the average distance of a particle from its nearest neighbour in a second species.

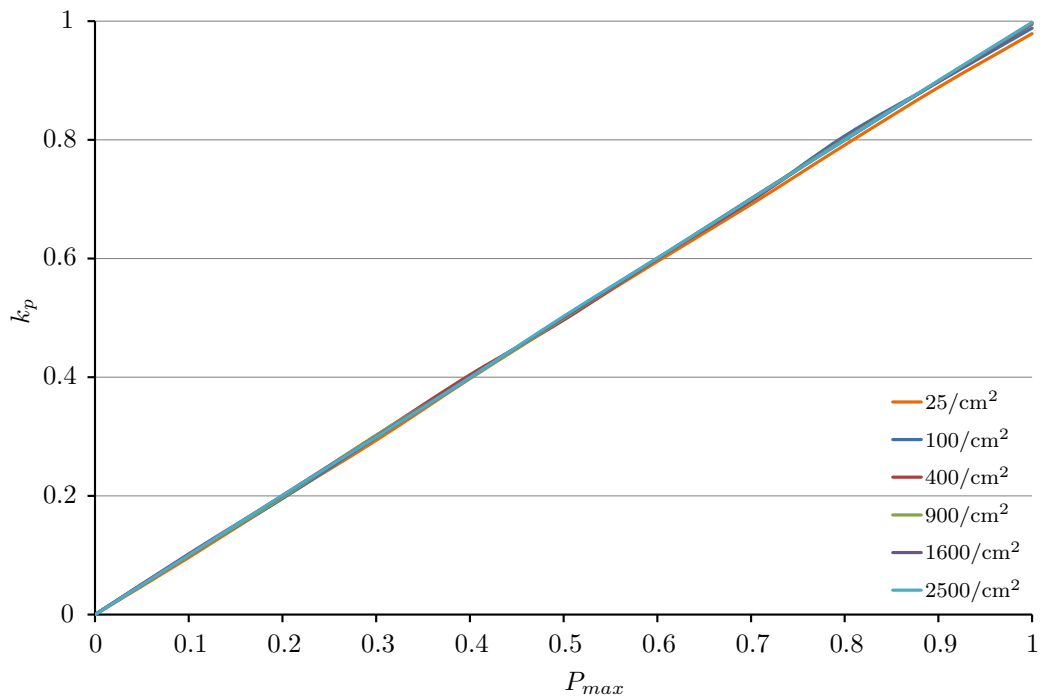


Figure 4.3: A graph of  $P_{max}$  against single step reaction rate for initial particle densities ranging from 25 per cm<sup>2</sup> to 2500 per cm<sup>2</sup> and  $D_h = 1$ .

can be approximated by

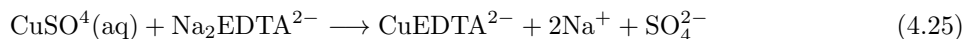
$$R_r \approx (1 - P_{max}) \exp \left[ -P_{max} \left( N_{ra} - \frac{1}{N_{ra}} \right) \right]. \quad (4.24)$$

The advantages of only allowing one reaction attempt, per outer loop particle, per timestep are that run times are reduced and that relationship between reaction rate and  $P_{max}$  is linear, which should make it simpler to control reaction rate.

### 4.2.2 Benchmarking

Benchmarking of the DTRW solution for reactive transport is, as with conservative transport solutions presented in Chapter 3, performed against results from Gramling *et al.* [75] due to the high quality of the experimental data therein and the number of other simulation studies available for comparison [36, 77, 78, 91–93]. Comparisons of the outputs of the DTRW solutions are made with outputs from other particle based solutions and continuum based solutions. The effects of the reaction rate controls,  $P_{max}$  and  $\sigma$ , on the solution are discussed with regards to accuracy of the solution produced and ease of solution control. A sensitivity analysis on the effects of non-physical parameters on the solution quality is also included. The form of the product concentration profile produced varies but is always approximately symmetrical and has the same general form. When discussing the form of the product concentration profiles the following terms are used to refer to the different parts of the profile. The area of highest product concentration is referred to as the ‘peak’, the areas of approximately linear change in concentration adjacent to the peak are referred to as the ‘sides’, and the areas at the edges of the profile where the change in concentration is no longer approximately linear are referred to as the ‘tails’. The area where the two mixing solutes have approximately the same concentration, where the ‘peak’ forms is referred to as the ‘mixing zone’.

The experimental setup used in Gramling *et al.* [75] and simulated using the DTRW method here is shown in Figure 4.6. This is same experimental setup used for the conservative transport simulations presented in Chapter 3 with the exception that the inflowing solute is changed from  $\text{CuEDTA}^{2-}$  to  $\text{CuSO}_4$ . As with the conservative transport simulations the concentration  $C^0 = 0.02$  M. The reaction between the resident and inflowing solutes takes the form



and is simulated by a reaction in the form  $A + B \longrightarrow C$ . Only the product  $\text{CuEDTA}^{2-}$  is of interest. The analytical solution of this system presented in Gramling *et al.* [75] shows that the effect of assuming perfect mixing between reactants leads to an overprediction of the amount of product formed by  $\sim 20\%$  (reproduced in Figure 4.7). The overprediction is greater at the peak of the concentration profile, in the mixing zone, than at the profile tails. The DTRW solution for  $\sigma = 2\sqrt{D_h}$  and  $P_{max} = 1$  is also shown in Figure 4.7. It is clear that under the same assumption the DTRW solution suffers from the same problem as the analytical solution presented in [75]. The DTRW solution accurately reproduces this analytical solution.

Figure 4.8 shows the concentration profiles of both reactants and the product for the DTRW simulation shown in Figure 4.7 along with the concentration profiles the two reactants would take if no reaction occurred between them. Figure 4.8 confirms that all of the proximal reactants are consumed by the reaction as there is no spatial overlap of the two reactants. The form of the product concentration profile follows the lower of the two reactant concentration profiles in the same manner as the analytical solution presented in [75]. Though the form of the product concentration profile appears to be determined by the dispersive transport properties of the reactants this is not the case. The two reactants have little

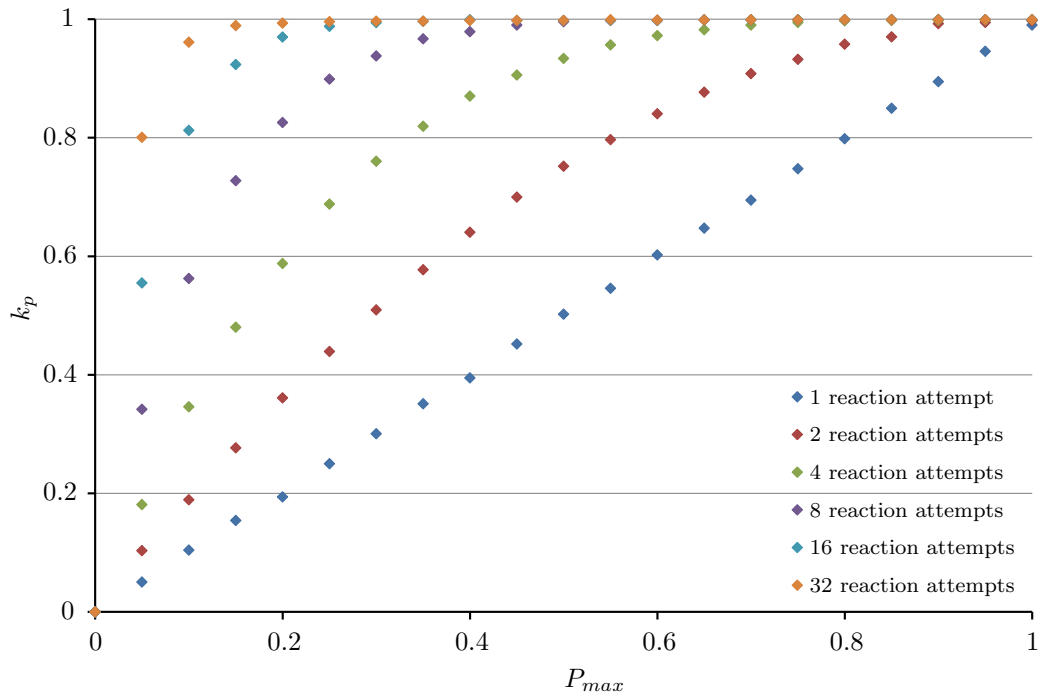


Figure 4.4: A graph of  $P_{max}$  against single step reaction rate for number of reaction attempts ranging from 1 to 32 and  $D_h = 1$ .

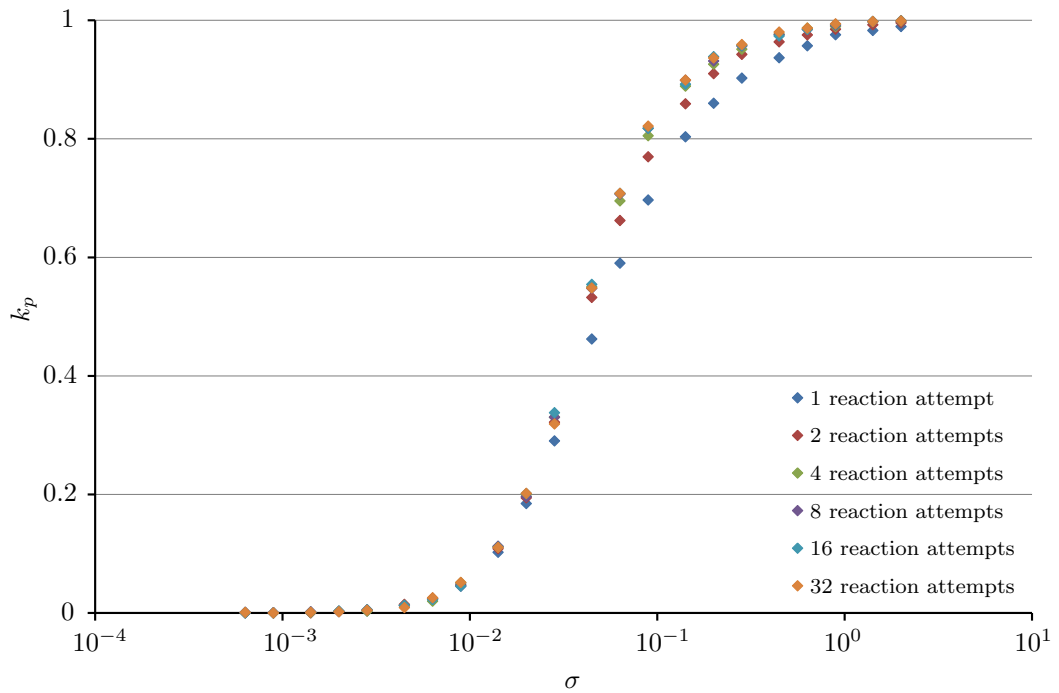


Figure 4.5: A graph of  $D_h$  against single step reaction rate for number of reaction attempts ranging from 1 to 32 and  $P_{max} = 1$ .

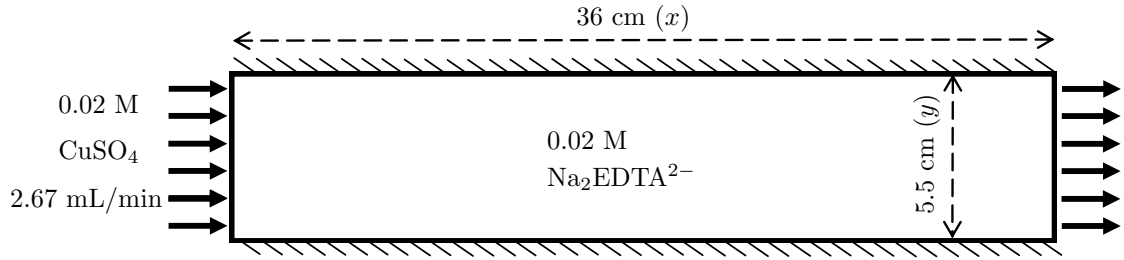


Figure 4.6: Experimental setup used by [75] and simulated using the DTRW method.

or no spatial overlap as the reaction is fast enough to consume any reactants in the same locality. It can be inferred that the product is formed at the interface between the two reactants, which, due to the speed of the reaction, is a thin strip. The product then disperses outwards to form the concentration profile seen in Figure 4.8. The shape of the product concentration profile is determined by the the rate of dispersion of the two reactants and the product, and the reaction rate. The dispersivities of the two reactants control how quickly they mix, affecting the rate of product formation. The reaction rate, as well as the obvious consequence of controlling the rate of product formation, affects the spatial distribution of where the product is formed. A lower reaction rate allows the reactants to remain in close proximity for longer before being consumed by the reaction. This allows reactants to travel further into the areas of the domain containing the other reactant before reacting, which in turn leads to the product forming in a wider strip. The form the profile takes is then determined by the dispersivity of the product.

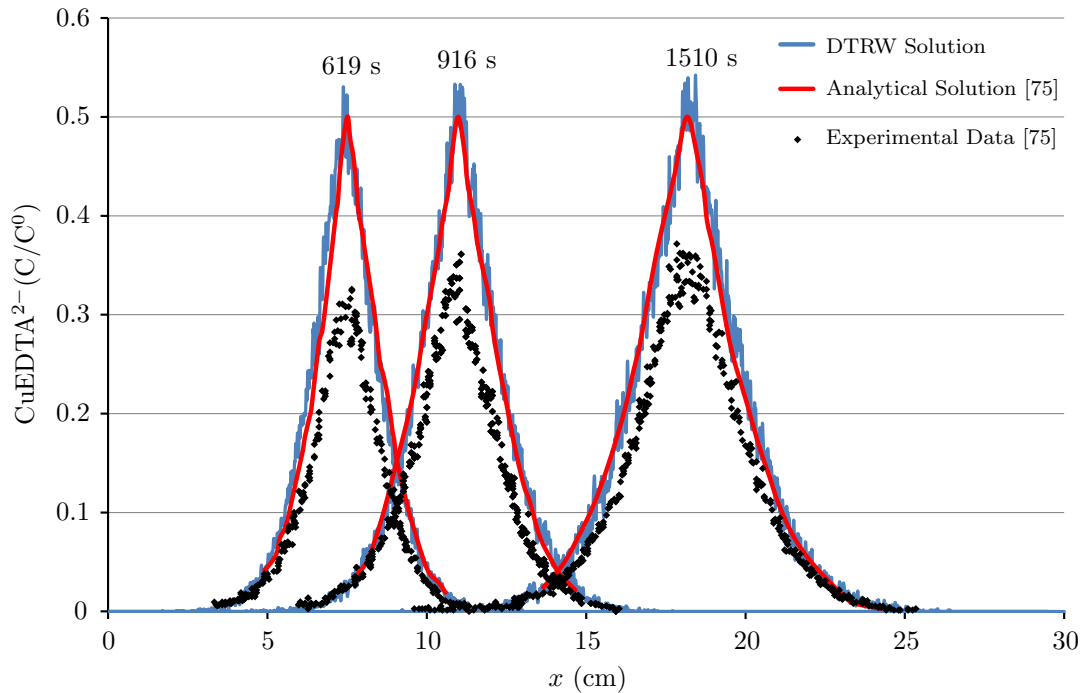


Figure 4.7: Reproduction and compilation of Figure 5a) from [75] showing experimental data and analytical solutions for (from left to right) 619s, 916s and 1510s. The overprediction of reaction rate caused by the assumption of perfect mixing between reactants is clear.

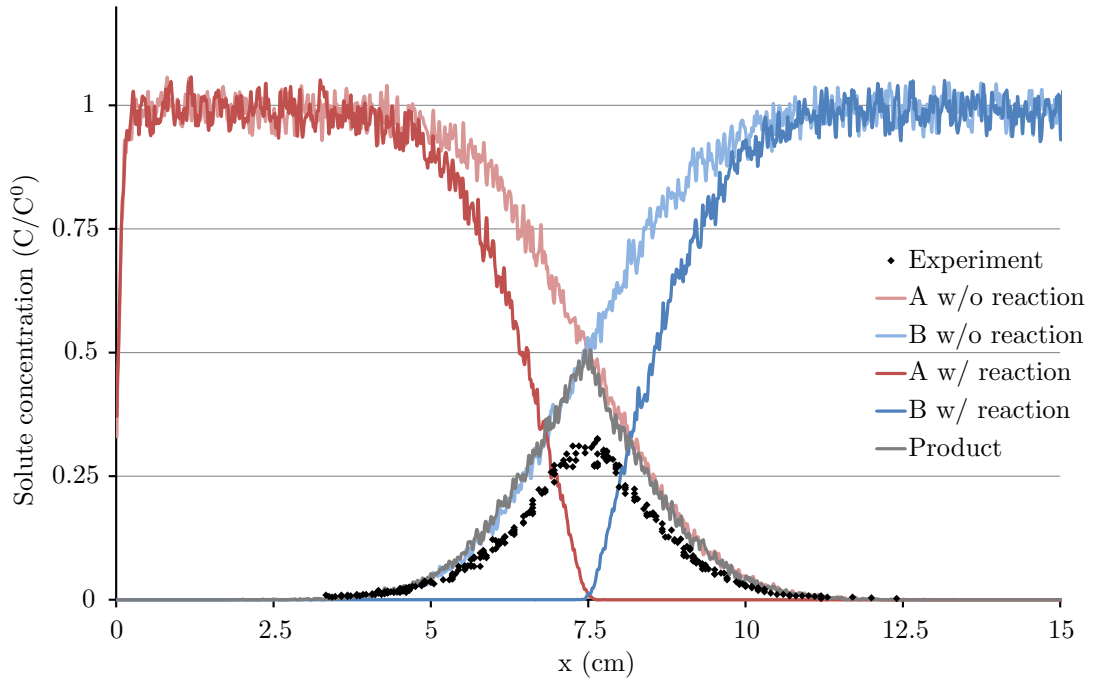


Figure 4.8: Reactant and product concentration profiles for simulation of [75] experiment with  $P_{max} = 1$  at 619 s with non-reactive solute profiles for comparison.

### Limiting reaction rates using $P_{max}$

Figures 4.9 - 4.12 show the effect of changing  $P_{max}$  by three orders of magnitude on the reaction rate for simulations run with an initial particle density of 900 per  $\text{cm}^2$  and a time step length of 1 s. There are two main factors in the way that the reduction of  $P_{max}$  changes the form of the product concentration profile. Firstly the reduction in reaction rate only significantly affects the form of the peak of the product concentration profile. The tails of the concentration profile change very little, if at all, with the change in  $P_{max}$ . This is similar to the effect of mixing limiting reaction shown in experiments presented in [75], where the analytical solution overpredicts the reactant concentration profile at the peak but not in the tails. The second thing of note is that, though  $P_{max}$  has been shown to have a linear relationship with reaction rate for a single reaction step, over multiple reaction steps larger reductions of  $P_{max}$  are required to produce significant reductions in the amount of product formed. This is simply a product of multiple reaction steps being simulated. In a system where a single reaction step with  $P_{max}$  set to 1.0 results in approximately complete reaction then a reduction of  $P_{max}$  to 0.5 yields close to complete reaction in 10 reaction steps.

The best fit, for a particle density of 900 per  $\text{cm}^2$  and  $\Delta t = 1$ , is achieved by setting  $P_{max} = 2.5 \times 10^{-3}$  as shown in Figure 4.13. Though the solution produced is a good fit it deviates from the experimental data slightly on the sides of the profile. The profile peak is also not a perfect fit, though this is less of an issue as the experimental data has a higher variability in this area. Figure 4.14 shows the reactant profiles in the same manner as Figure 4.8 but for  $P_{max} = 2.5 \times 10^{-3}$ .

The area controlling the form of the reactant concentration profile is the zone in which the two reactants are mixing and reacting. In the case of total reaction the reactants do not ever occupy the same space for more than one time step, as shown in Figure 4.8. The transport step moves the reactants into proximity of each other and then they are all consumed during the following reaction step. The product

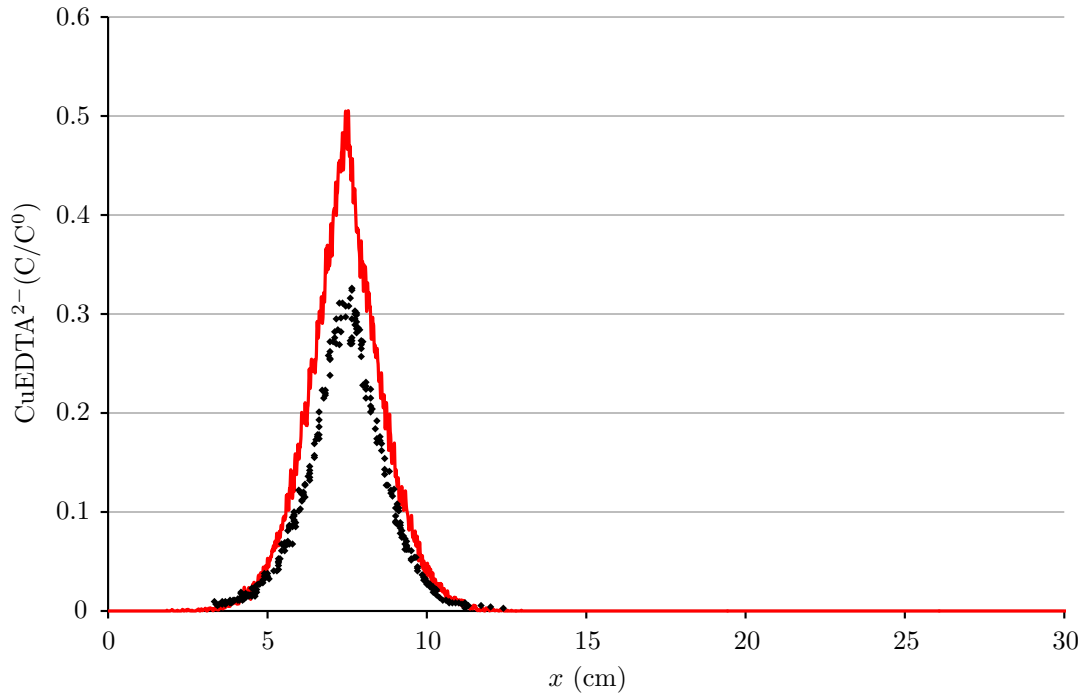


Figure 4.9: Comparison of the DTRW simulation results for  $P_{max} = 1.0$  (red lines) with experimental data from [75] (black diamonds). The DTRW solution is the average of 10 simulations with a maximum particle density of 900 per  $\text{cm}^2$  and  $\Delta t = 1$  s at 619 s.

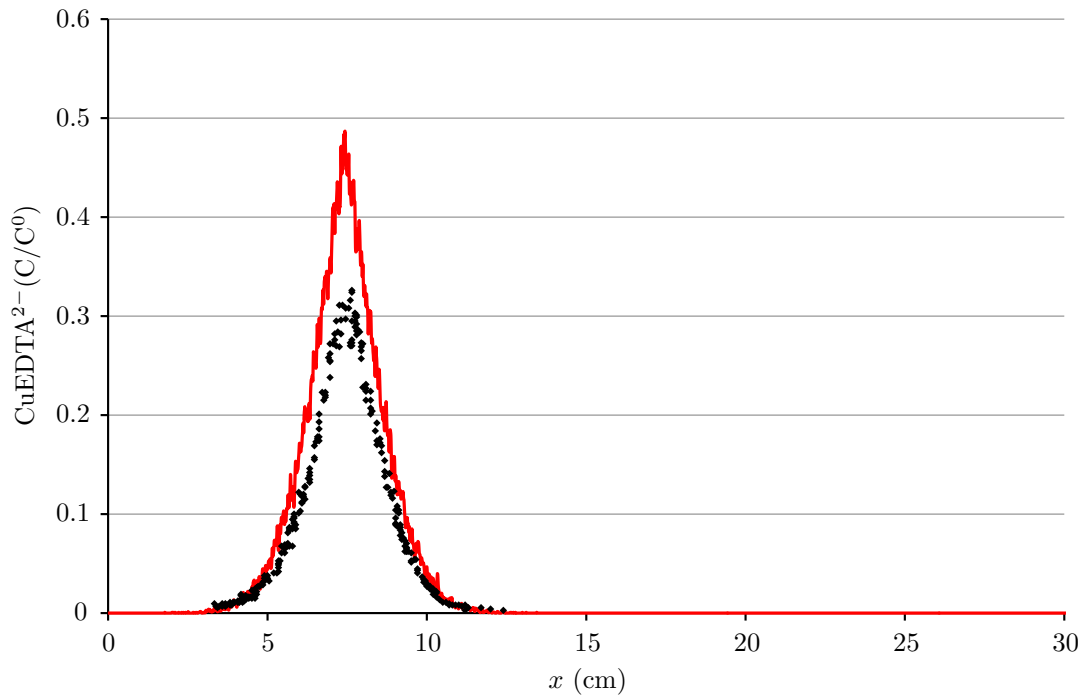


Figure 4.10: Comparison of the DTRW simulation results for  $P_{max} = 10^{-1}$  (red lines) with experimental data from [75] (black diamonds). The DTRW solution is the average of 10 simulations with a maximum particle density of 900 per  $\text{cm}^2$  and  $\Delta t = 1$  s at 619 s.

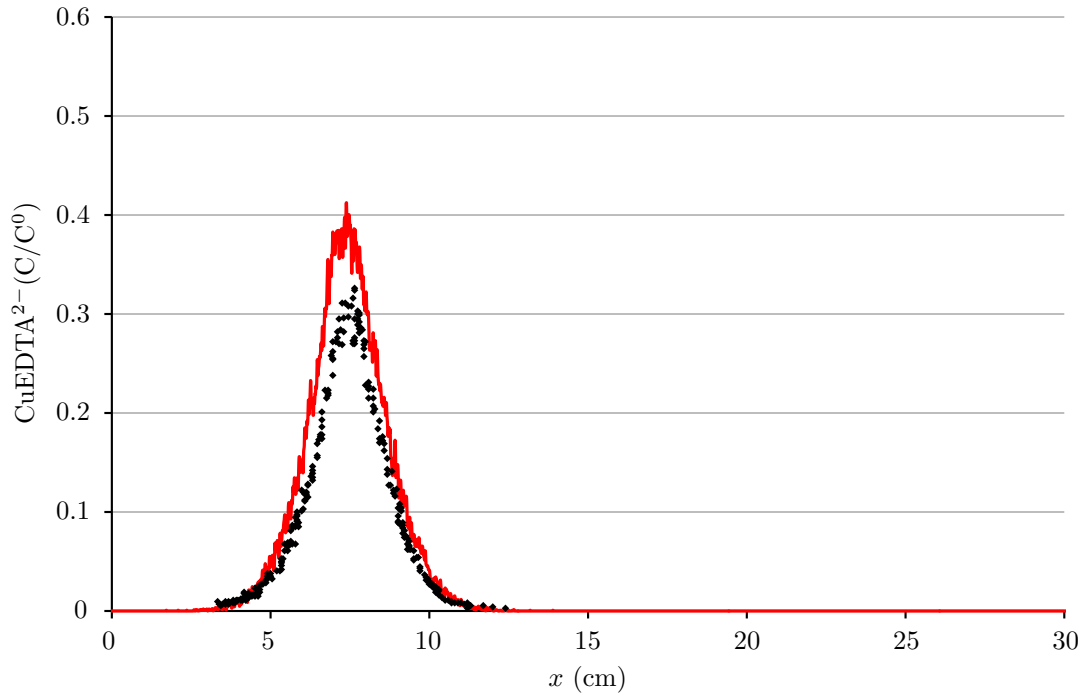


Figure 4.11: Comparison of the DTRW simulation results for  $P_{max} = 10^{-2}$  (red lines) with experimental data from [75] (black diamonds). The DTRW solution is the average of 10 simulations with a maximum particle density of 900 per  $\text{cm}^2$  and  $\Delta t = 1$  s at 619 s.

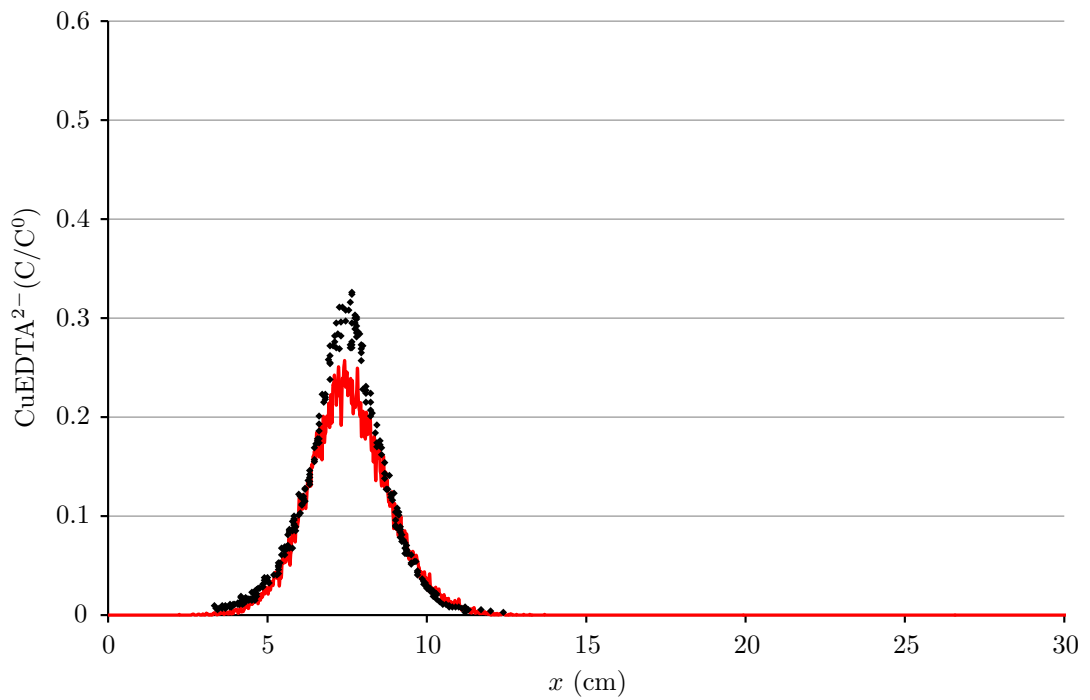


Figure 4.12: Comparison of the DTRW simulation results for  $P_{max} = 10^{-3}$  (red lines) with experimental data from [75] (black diamonds). The DTRW solution is the average of 10 simulations with a maximum particle density of 900 per  $\text{cm}^2$  and  $\Delta t = 1$  s at 619 s.

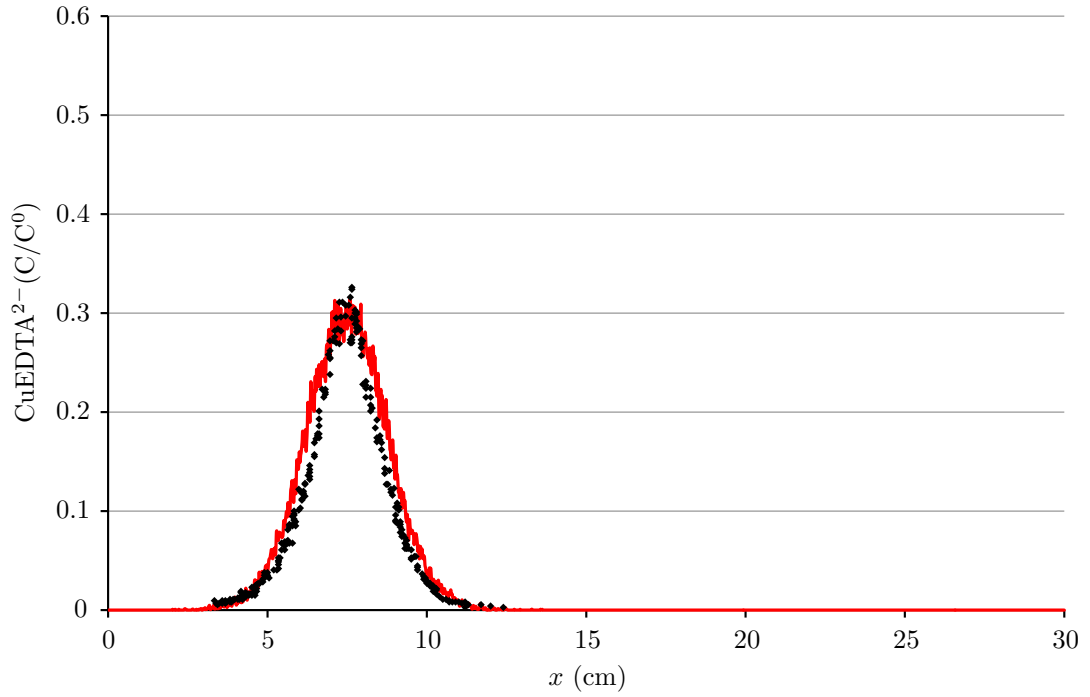


Figure 4.13: Comparison of the DTRW simulation results for  $P_{max} = 0.0025$  (red lines) with experimental data from [75] (black diamonds). The DTRW solution is the average of 10 simulations with a maximum particle density of 900 per  $\text{cm}^2$  and  $\Delta t = 1$  s at 619 s.

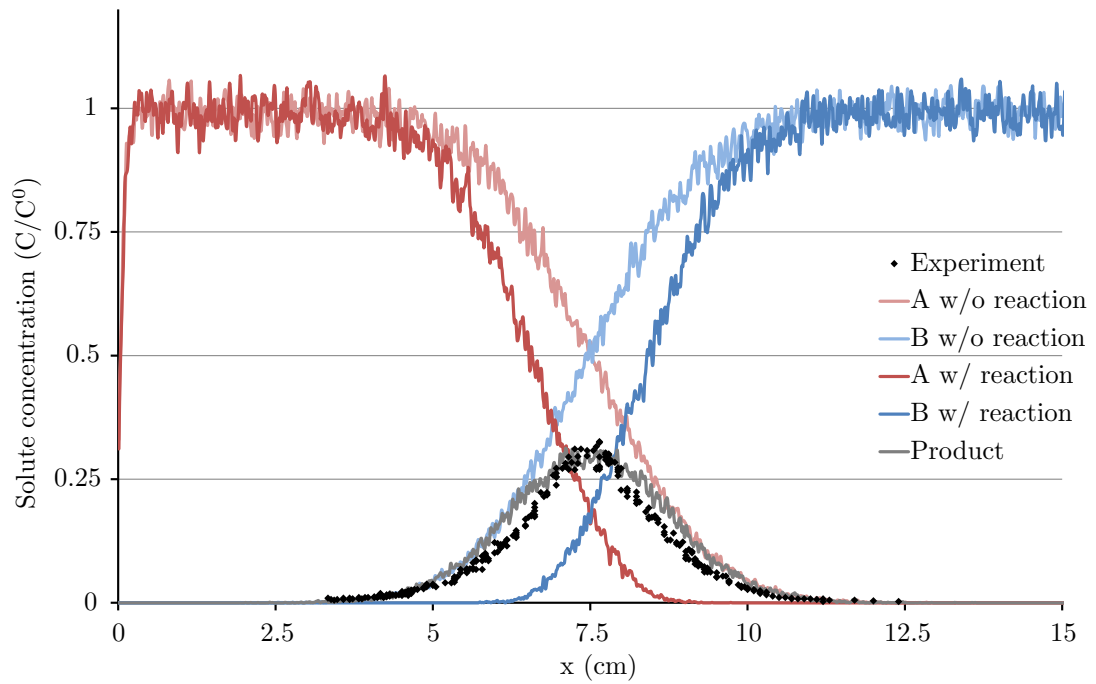


Figure 4.14: Reactant and product concentration profiles for simulation of [75] experiment with  $P_{max} = 0.003$  at 619 s with non-reactive solute profiles for comparison.

particles are being formed in a thin strip where the two reactant species meet. The product particles are then spread out by dispersion to form the concentration profile observed. The only effect the dispersive movement of the reactants has on the product concentration profile is to control how fast the reactants move into contact with each other, and by doing so control how much product is formed each timestep. The other features of the profile, such as the shape of the profile tails, are controlled by the dispersive behaviour of the product. When the reaction rate decreases, whether by reducing  $P_{max}$  or by some other factor, the distance a particle can travel into the space occupied by the other reactant species before reacting increases and so the zone in which reactions take place widens, as shown by Figure 4.14. As this reaction zone is thinner than the product concentration profile it only reduces the height of the reactant profile near the peak.

Ding *et al.* (2012) [36] propose the idea that if reaction is diffusion or mixing limited then solutes can travel further into macro scale areas containing the other solute before reacting. This is stated to cause an increase in the concentration in the tails relative to the well mixed solution. Figure 4.14 shows that this is not the case. Rather than the tails being increased in size the main difference is a decrease in the peak concentration. The two reactant solutes do indeed move further into the space occupied by the other before reacting but this has no impact on the concentrations in the tails. The discrepancy in the tails of the profiles is visible in the early time conservative transport simulations presented in [75] and so could be the product of a slightly non-Fickian dispersive transport behaviour rather than of the mixing limited reaction. The form of the reactant concentration in a location is limited to the lower of the two reactant concentrations at that location in the conservative case, as shown in Figure 4.8, though this is only the case because the dispersivity of the product is the same as the dispersivities of the reactants. Therefore increasing the size of the tails of the product concentration profile can only be achieved by altering the specifics of the dispersive transport of the product. This is the approach taken in [78], though in attempting to improve the fit to the product profile tails they sacrifice the quality of the rest of their solution.

### Limiting reaction rates using $\sigma_s$

The reaction rate can also be controlled by altering the value of  $\sigma_s$  instead, or in conjunction with,  $P_{max}$ . Figures 4.15 - 4.18 show the effect of changing  $\sigma_s$  on the reaction rate in the same bimolecular reaction system. The solution produced as a best fit is of the same quality as that produced using  $P_{max}$ , and therefore the issue of which to use can be decided purely on the basis of ease of use. Fitting the solution using a parameter which alters the reaction rate in a linear fashion which is unchanged by particle density, is less complicated than fitting using a parameter which alters the solution in a non-linear fashion which is affected by particle density.

The way in which  $\sigma_s$  effects the solution as it is changed takes a more complicated form than the effect of  $P_{max}$ . As was shown in Figure 4.1 the large changes in reaction rate can be caused by small variations in  $\sigma_s$  for some parts of the  $\sigma_s$ -reaction rate curve and large changes in  $\sigma_s$  can cause very little variation in the reaction rate. In addition to this the scaling of reaction rate with  $P_{max}$  is independent of particle density and this is not the case with  $\sigma_s$ . These effects contribute to  $\sigma_s$  being more complicated to use to control the reaction rate, making  $P_{max}$  the preferred option.

### Differences between using CTRW or DTRW for reactions

Though the method outlined above was developed for use with the CTRW method it has been implemented here using the DTRW method. Both of these methods have the same basic concept, that the solute field is described using a field of particles. The differences between the methods have been outlined in Chapter 3. When investigating reactions the only difference of importance is the spatial distribution of

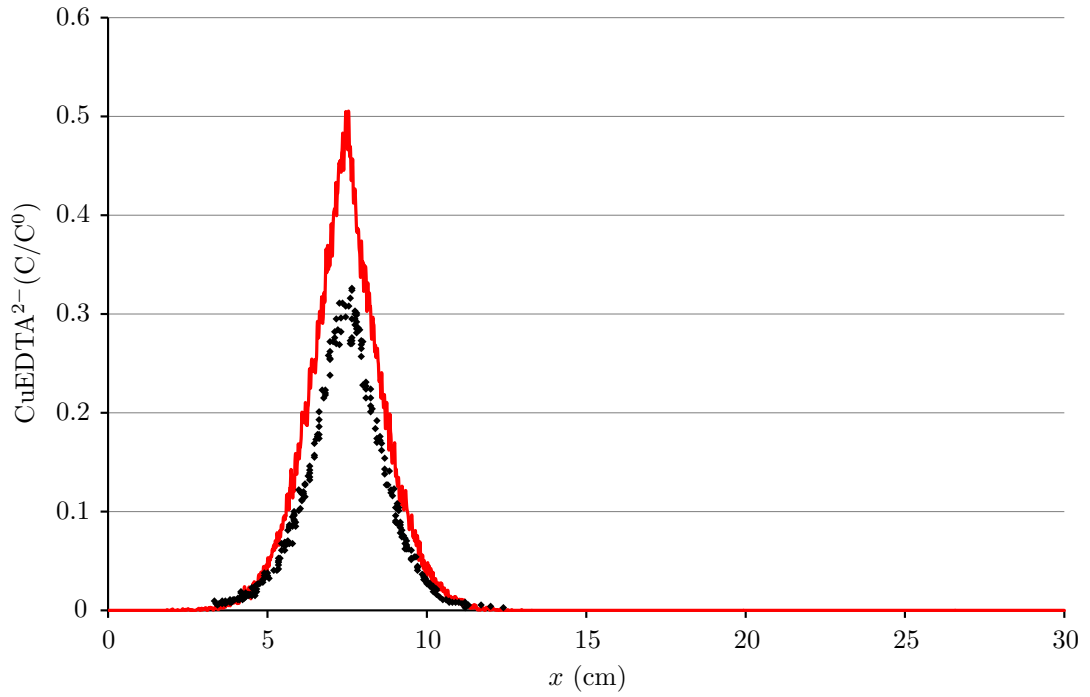


Figure 4.15: Comparison of the DTRW simulation results for  $\sigma_s = 1.0$  (red lines) with experimental data from [75] (black diamonds). The DTRW solution is the average of 10 simulations with a maximum particle density of 900 per  $\text{cm}^2$  and  $\Delta t = 1$  s at 619 s.

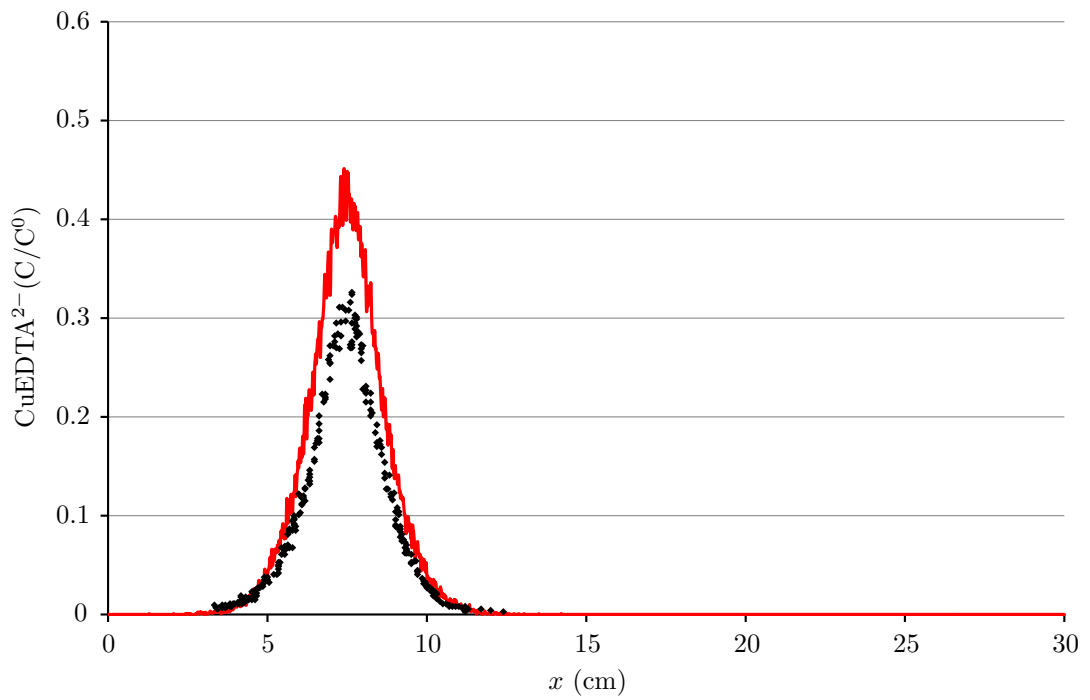


Figure 4.16: Comparison of the DTRW simulation results for  $\sigma_s = 10^{-2}$  (red lines) with experimental data from [75] (black diamonds). The DTRW solution is the average of 10 simulations with a maximum particle density of 900 per  $\text{cm}^2$  and  $\Delta t = 1$  s at 619 s.

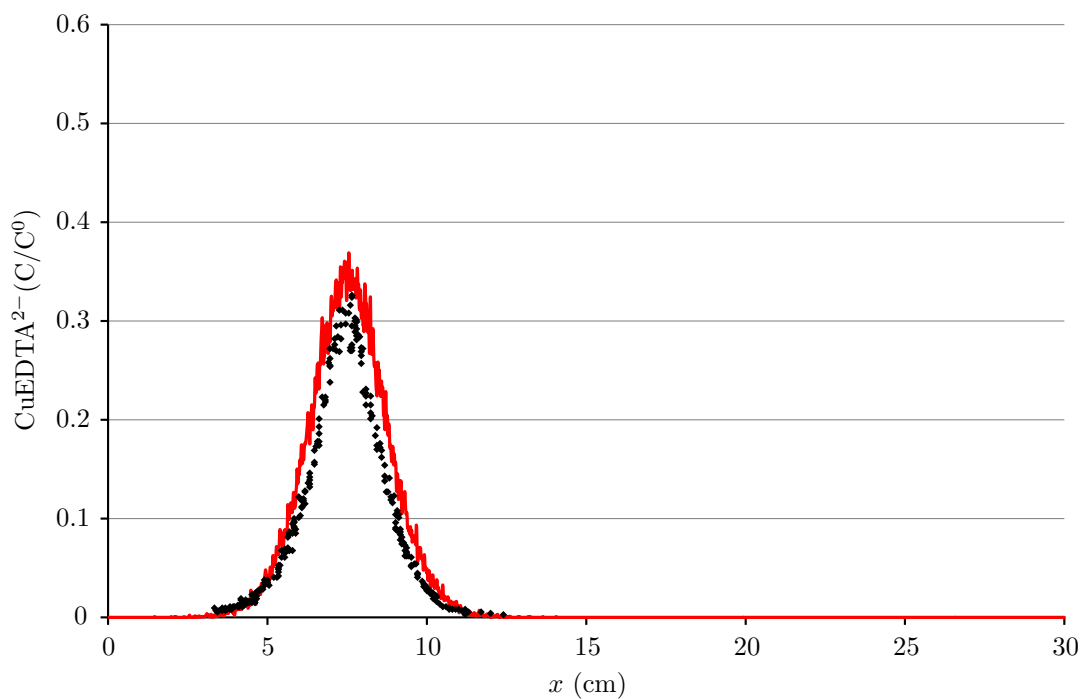


Figure 4.17: Comparison of the DTRW simulation results for  $\sigma_s = 10^{-3}$  (red lines) with experimental data from [75] (black diamonds). The DTRW solution is the average of 10 simulations with a maximum particle density of 900 per  $\text{cm}^2$  and  $\Delta t = 1$  s at 619 s.

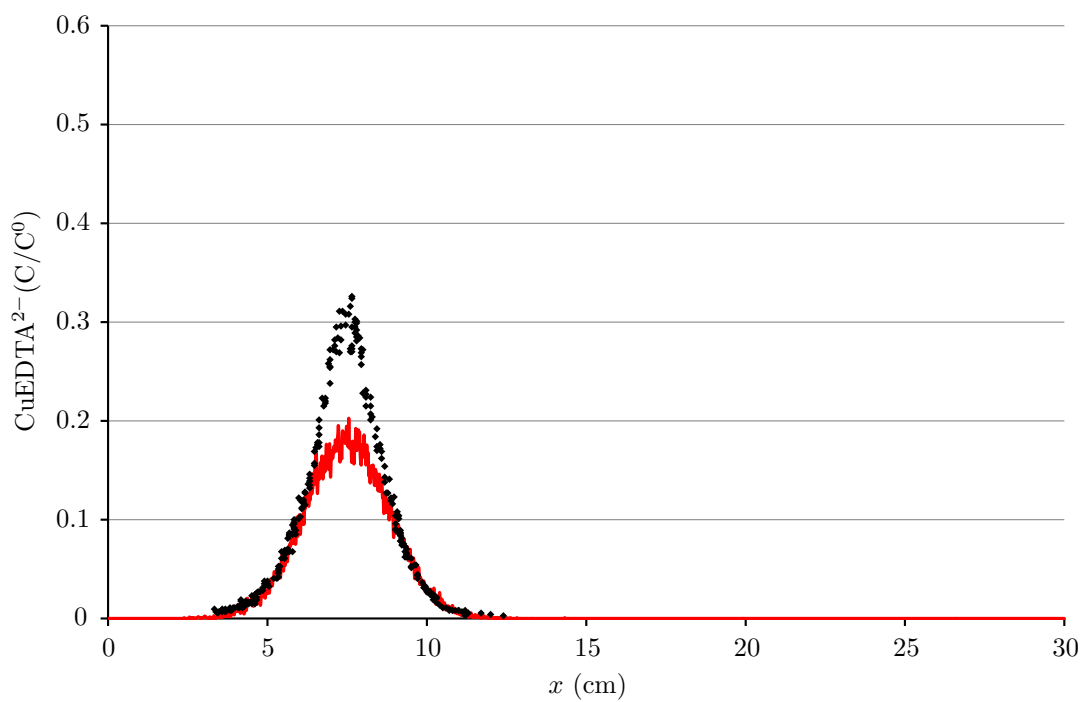


Figure 4.18: Comparison of the DTRW simulation results for  $\sigma_s = 10^{-4}$  (red lines) with experimental data from [75] (black diamonds). The DTRW solution is the average of 10 simulations with a maximum particle density of 900 per  $\text{cm}^2$  and  $\Delta t = 1$  s at 619 s.

the particles. In the CTRW method particles are stopped at fixed timesteps to allow reactions to occur and so the timestepping method involved in transport via CTRW becomes irrelevant. In the CLPF method particles can only exist at lattice sites whereas for the DTRW method they can take any location that the precision of the coordinate variables allow. When this difference is considered with relation to Figure 4.2 it is apparent that this has some effect on the behaviour of reactions simulated using the CLPF method.

Figure 4.19 shows the effect of  $D_h$  on reaction rate for the application of two simulation methods to the same 3 cm by 3 cm single step reaction problem used to investigate the behaviour of the CLPF reaction method earlier in this chapter, one in which particles can take any location within the domain and another where they are restricted to locations on a regular lattice. The lattice sites have a spacing of 0.1cm. The effect of constraining particle locations is clear. At  $D_h \approx 1.0 \times 10^{-3}$  the lattice bound reaction rate begins to deviate from the free location rate and below  $D_h \approx 2.0 \times 10^{-4}$  the reaction rate does not decrease further. The higher the particle density is the higher this minimum reaction rate.

The standard deviation of the CLPF is  $2\sqrt{D_h}$ . For the  $D_h$  value at which the lattice bound reaction rate begins to deviate the lattice spacing is  $\sim 1.6$  standard deviations and the reaction rate decreases no further once the lattice spacing is greater than  $\sim 3.5$  standard deviations. For a particle separation of  $\sim 3.5$  standard deviations the probability of colocation given by the CLPF is  $\sim 4.8 \times 10^{-6}$ . At this point the probability of reaction with a particle at another lattice site is negligible.

When particles can be placed anywhere in the domain the probability of two being very close is low. The probability of colocation decreases rapidly as particle separation increases. For very low values of  $D_h$  particles are unlikely to be close enough to react if they can take any location within the domain. Conversely if particles are restricted to lattice sites then if the number of particles is greater than the number of lattice sites the probability of two particles being colocated, along with their probability of reaction, is much greater. When the probability of reaction with a particle at a neighbouring lattice site is essentially zero then all of the reactions occurring are between colocated particles. In this case reaction rates do not decrease for any further decrease in  $D_h$  as is shown in Figure 4.19. The minimum reaction rate is increased with particle density as the fraction of the particles which can react before particles become isolated from particles of the other species is greater. As the particles are randomly distributed some lattice sites end up with more particles of one reactant species than the other leaving particles isolated as particles are removed due to reaction.

Ederly *et al.* [78] describes simulations with a lattice spacing of 0.1 cm and  $5 \times 10^4$  particles ( $\sim 16$  particles per  $\text{cm}^2$ ), and 0.05 cm spacing and  $2 \times 10^5$  particles ( $\sim 32$  particles per  $\text{cm}^2$ ). Though they use a reaction radius method this gives some idea as to what the lattice spacings would be used in other articles where this information is not provided, *e.g* [36].

### Sensitivity Analysis

As with the conservative transport simulations presented in Chapter 3, the effect of timestep length and particle density on the quality of the solution is assessed. It has been shown earlier that both the particle density and the timestep length affect the reaction rate and so  $P_{max}$  needs to be altered with these parameters to maintain a good fit to the experimental data.

Reducing the timestep length decreases the standard deviation of the CLPF which, as shown by Figure 4.1, decreases the reaction rate per timestep. Reducing this also increases the number of reaction steps occurring. This produces a similar effect to increasing the number of attempts a particle gets at reaction per timestep, which affects the reaction rate in the manner shown by Figure ??, increasing the reaction rate over the total simulation time.

Figures 4.20 - 4.22 show the best fit solutions for timestep lengths of 0.1 s, 1 s and 10 s respectively. The

$\Delta t$ (s)	0.1	1	2	5	10	20
$P_{max}$	0.0006	0.0025	0.045	0.01	0.02	0.04

Table 4.1: Values of  $P_{max}$  used to achieve best fit outputs for varying time step length  $\Delta t$ .

values of  $P_{max}$  used to produce Figures 4.20 - 4.22, along with the values used to produce good fits with other timestep lengths are shown in Table 4.1. At larger timesteps there is a linear relationship between the increase in timestep length and the reduction in  $P_{max}$  required to maintain a good experimental fit. The changes to the quality of the solution caused by changing the timestep length are minimal. The fit on the sides of the product concentration profile for the  $\Delta t$  is slightly worse as it overpredicts the product concentration in these areas, though this may be due to the slight increase in simulation time over the other two simulations, because of the increased distance which particles can react at due to the effect of  $\Delta t$  on the CLPF, or a combination of the two.

Figures 4.23 - 4.25 show the effect of changing particle density on the solution. As would be expected the quality of the solution deteriorates with decreasing particle density and, as with the non reactive transport simulations shown in Chapter 3, this can be alleviated by averaging the results of several simulations. The changes in reaction rate with particle density can be adjusted for by scaling  $\sigma_s$  with particle density.

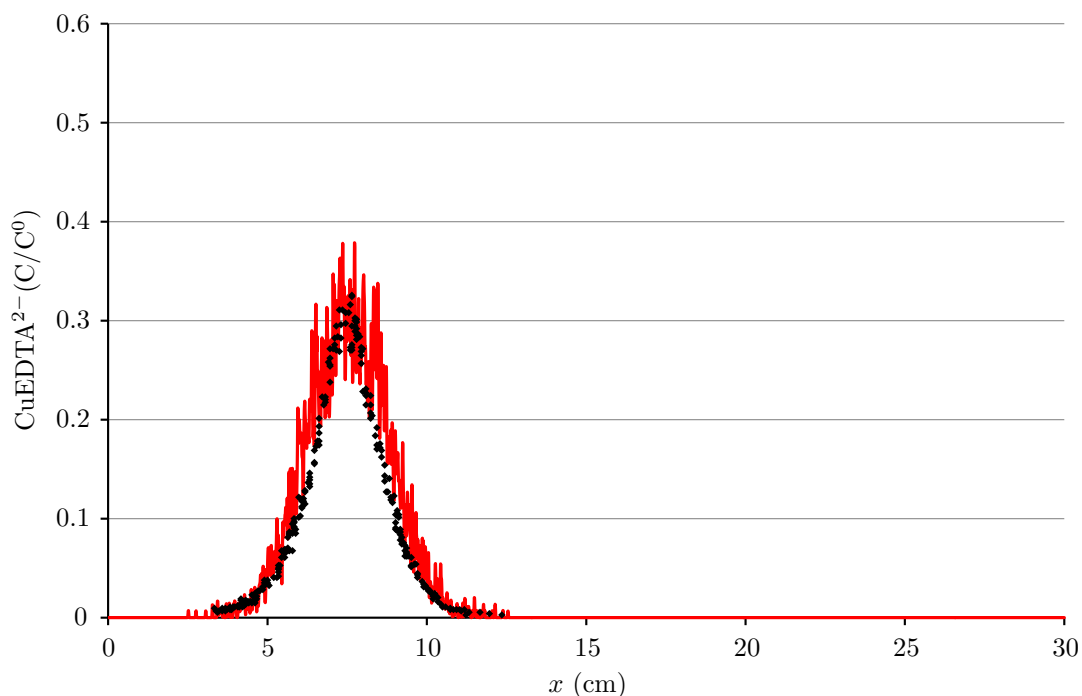


Figure 4.23: Comparison of the DTRW simulation results for  $P_{max} = 0.0025$  (red lines) with experimental data from [75] (black diamonds). The DTRW solution is the average of 10 simulations with a maximum particle density of 100 per  $\text{cm}^2$  and  $\Delta t = 1$  s at 619 s.

### 4.2.3 Comparison with other numerical simulation studies

Several studies have used the experimental data from Gramling *et al.* [75] to benchmark computational methods for simulating bimolecular reactions in porous media. These have included models based on

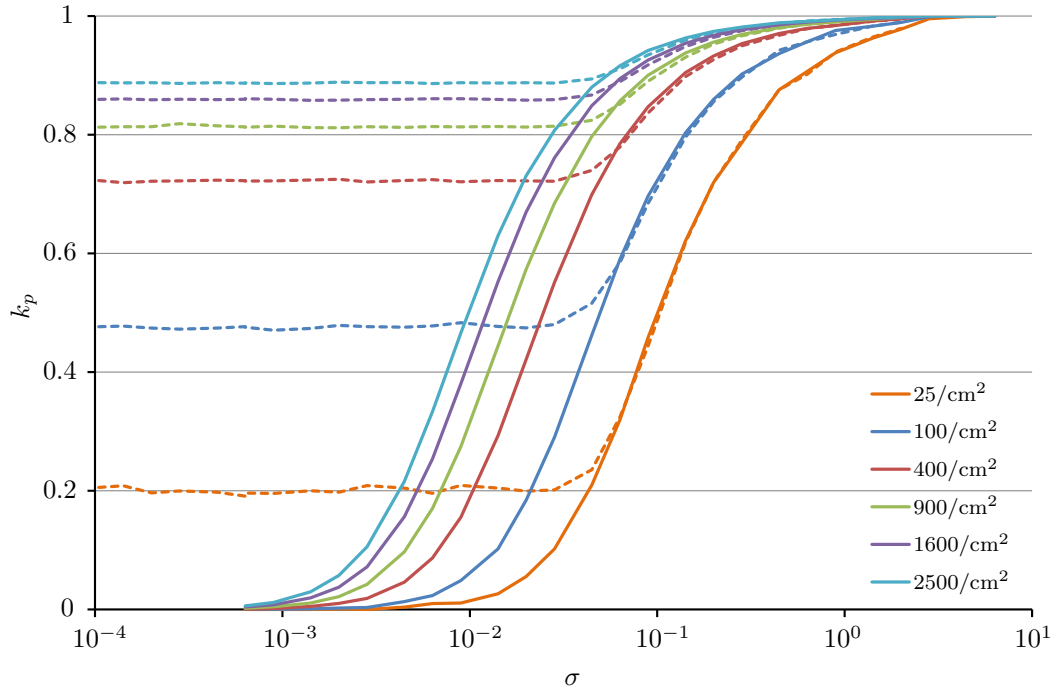


Figure 4.19: A  $\log(x)$  graph of  $D_h$  against single step reaction rate for initial particle densities ranging from 25 per  $\text{cm}^2$  to 2500 per  $\text{cm}^2$  and  $P_{max} = 1$  for DTRW (solid lines) and CTRW (dashed lines).

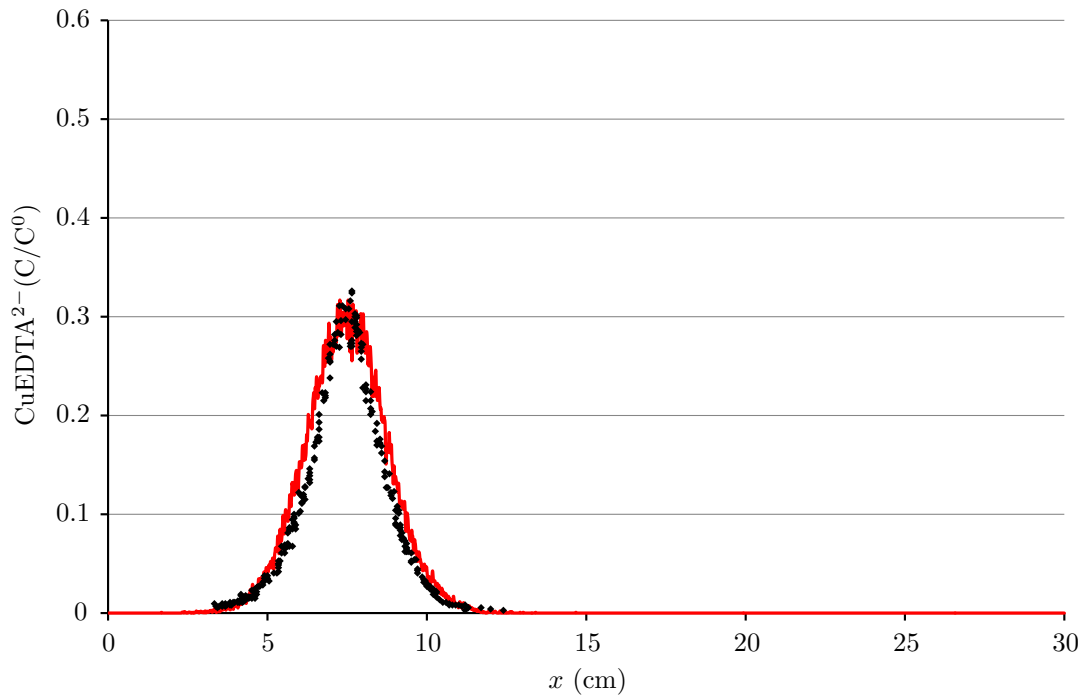


Figure 4.20: Comparison of the DTRW simulation results for  $P_{max} = 0.0006$  (red lines) with experimental data from [75] (black diamonds). The DTRW solution is the average of 10 simulations with a maximum particle density of 900 per  $\text{cm}^2$  and  $\Delta t = 0.1$  s at 619 s.

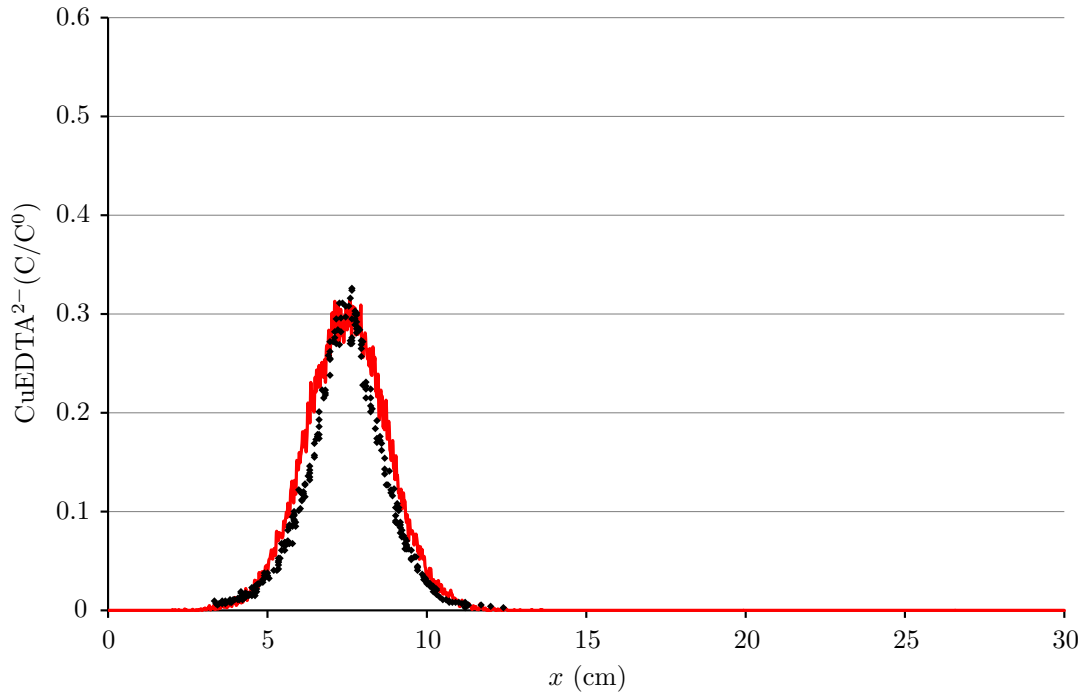


Figure 4.21: Comparison of the DTRW simulation results for  $P_{max} = 0.0025$  (red lines) with experimental data from [75] (black diamonds). The DTRW solution is the average of 10 simulations with a maximum particle density of 900 per  $\text{cm}^2$  and  $\Delta t = 1$  s at 619 s.

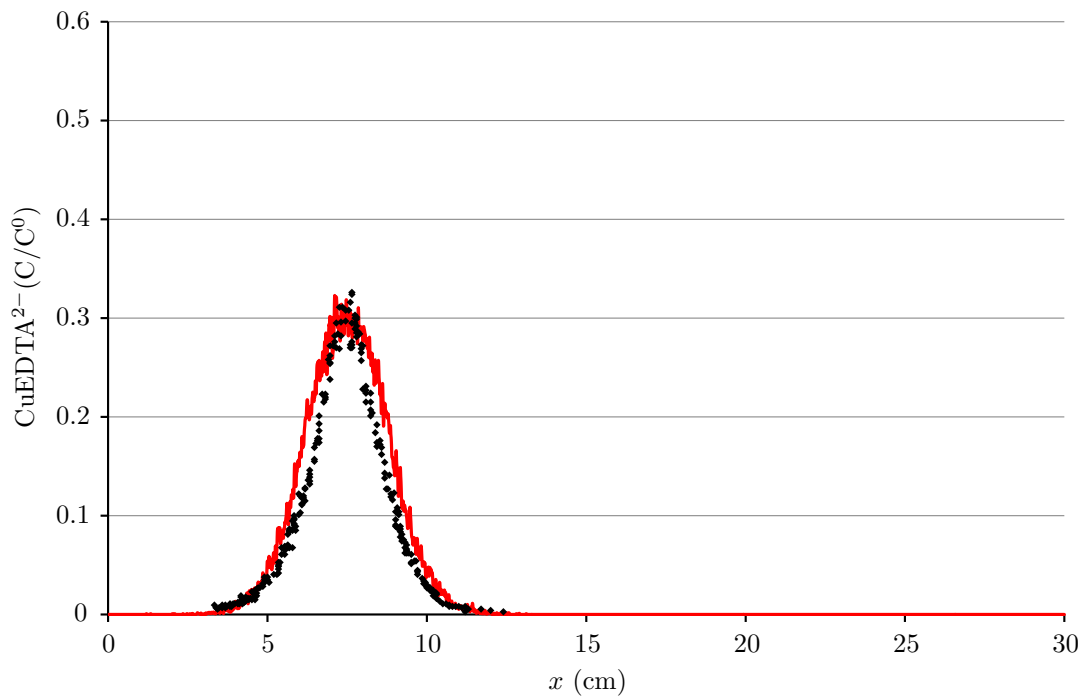


Figure 4.22: Comparison of the DTRW simulation results for  $P_{max} = 0.02$  (red lines) with experimental data from [75] (black diamonds). The DTRW solution is the average of 10 simulations with a maximum particle density of 900 per  $\text{cm}^2$  and  $\Delta t = 10$  s at 619 s.

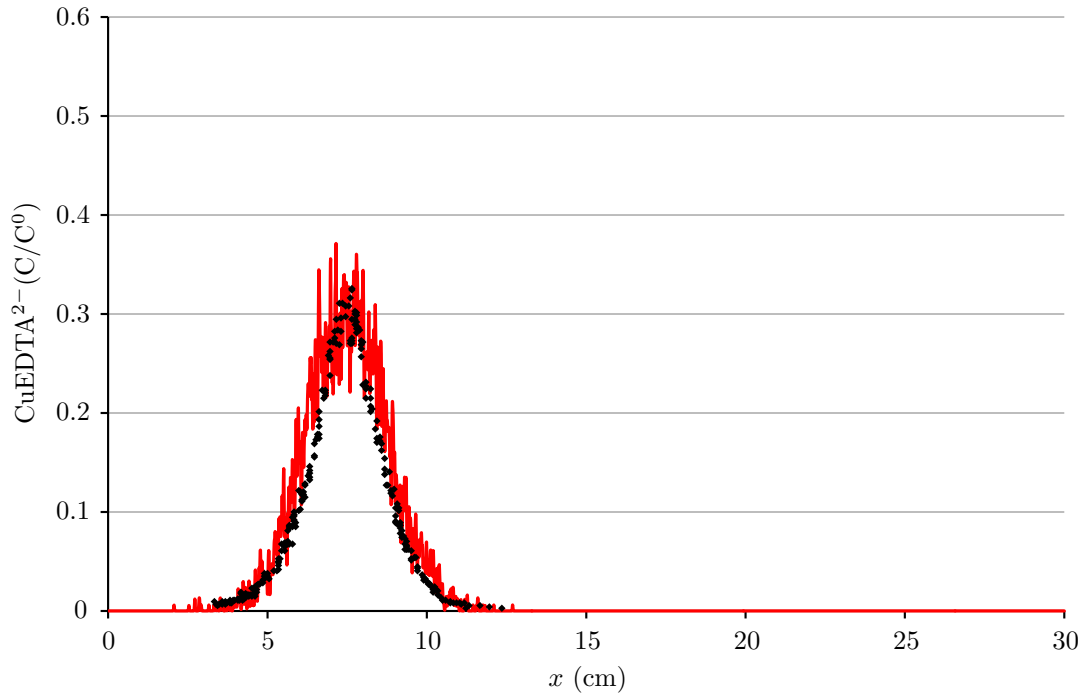


Figure 4.24: Comparison of the DTRW simulation results for  $P_{max} = 0.0025$  (red lines) with experimental data from [75] (black diamonds). The DTRW solution is the average of 10 simulations with a maximum particle density of 400 per  $\text{cm}^2$  and  $\Delta t = 1$  s at 619 s.

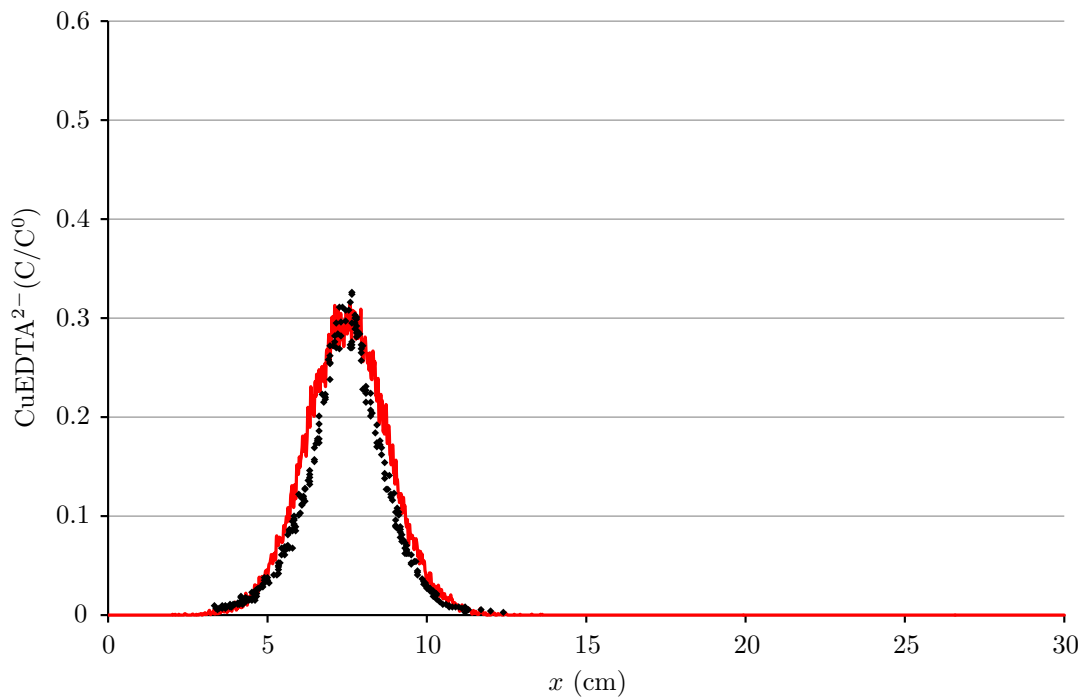


Figure 4.25: Comparison of the DTRW simulation results for  $P_{max} = 0.0025$  (red lines) with experimental data from [75] (black diamonds). The DTRW solution is the average of 10 simulations with a maximum particle density of 900 per  $\text{cm}^2$  and  $\Delta t = 1$  s at 619 s.

particle tracking methods, specifically the CTRW method [36, 78], and models using continuum methods [92]. The results from these three studies are compared with the results presented above and critically assessed. The three studies used for comparison all present simulation results compared to data recorded at three different times during the course of the same experiment presented by [75]. For comparison, Figure 4.26 shows the comparable best fit DTRW simulation.

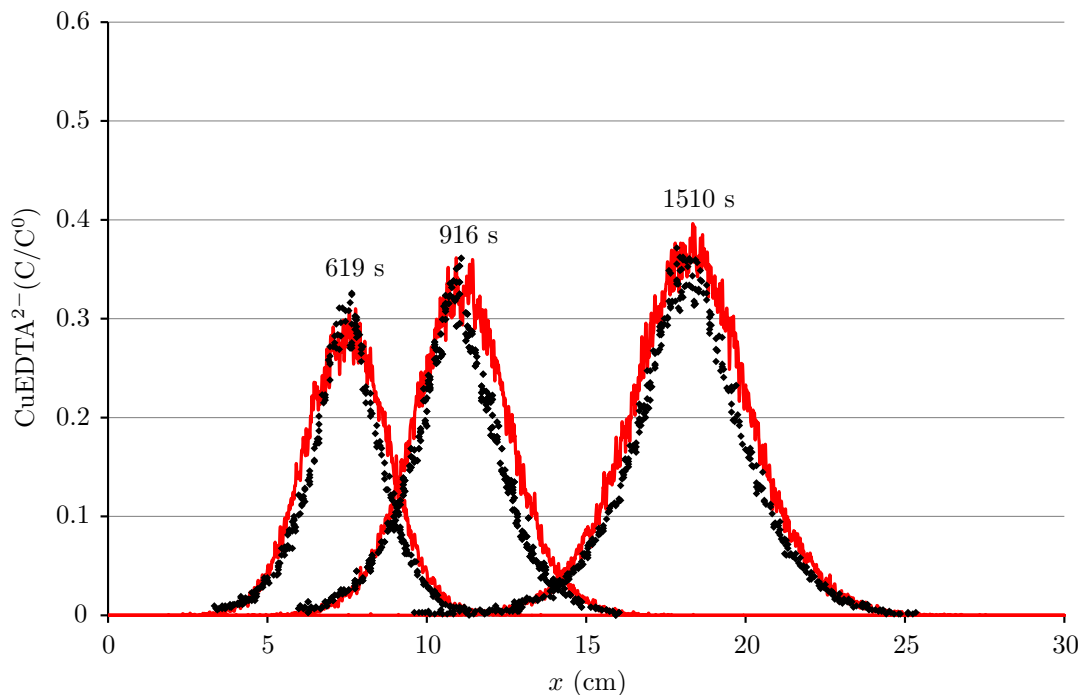


Figure 4.26: Comparison of the DTRW simulation results for  $P_{max} = 0.0025$  (red lines) with experimental data from [75] (black diamonds). The DTRW solution is the average of 10 simulations with a maximum particle density of 900 per  $\text{cm}^2$  and  $\Delta t = 10$  s at 619 s, 916 s and 1510 s.

### Sanchez-Vila *et al.*, 2010

Sanchez-Vila *et al.*, [92] use a continuum based approach with a time dependent kinetic reaction term to limit the reaction rate. The rate constant used incorporates the chemical rate limiting as well as the mixing rate limiting factors. The rate constant is a time dependent term of the form

$$k = k_0 t^{-m} \quad (4.26)$$

where  $k_0$  and  $m$  are fitted parameters. The value of  $m$  used to produce the results reproduced in Figure 4.27 is close to the value presented in [94] for the exponent controlling the relationship between advection time and the first-order mass transport coefficient. The rate of diffusion between low porosity zones and the main pore water body is suggested as the controlling parameter on the limiting of reaction rate. A reproduction of the simulation data presented in Sanchez-Vila *et al.* [92] with the experimental data from [75] is given in Figure 4.27.

The solution produced fits the experimental data well except for in the centre of the product concentration profile. The sides of the profiles at each of the three time fit well and the tails have a reasonable fit. The experimental data from [75] has a sizeable degree of uncertainty in the peak product concentration. Despite this there is a clear trend of increasing peak concentration between the three measurements. The simulation results of Sanchez-Vila *et al.* [92] fail to reproduce this instead producing outputs with

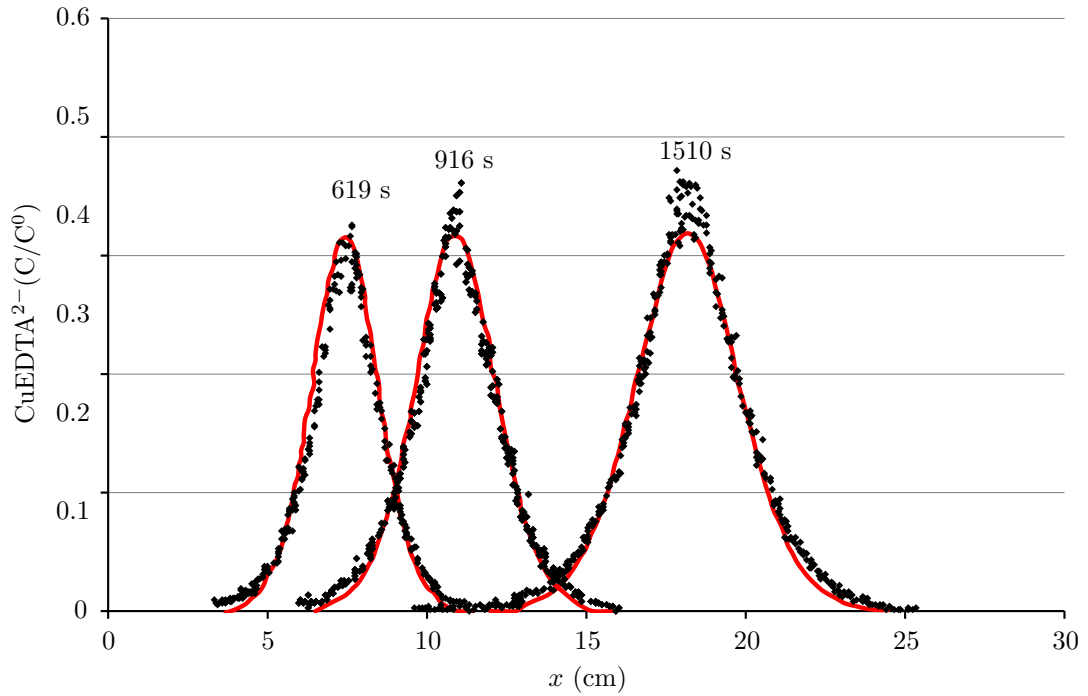


Figure 4.27: Comparison of the simulation results presented by [92] with experimental data from [75].

a minimal increase in peak concentration. Sanchez-Vila *et al.* [92] state that the value of  $D_h$  used to produce the best fit output is  $1.30 \times 10^{-3} \text{ cm}^2 \text{ s}^{-1}$  whereas the experimentally measured value is  $1.75 \times 10^{-3} \text{ cm}^2 \text{ s}^{-1}$ . The method used to limit the reaction rate reduces the reaction rate by the same factor across the domain. Figure 4.14 shows that, for the DTRW simulations which provides the best fit to the [75] experiment, the reaction rate needs to be limited in such a way that the product concentration profile is lowered in the centre but maintains its full height in the tails. This change in the value of  $D_h$  used is presumably to account for this homogenous reduction in reaction rate. Nonetheless the simulations presented by [92] are a significant improvement over the analytical solution [75].

#### **Ederly *et al.*, 2010**

Ederly *et al.*, [78] uses a CTRW approach for their simulations. The experimental setup is simulated by a two dimensional domain. The reaction criterion used is the reaction radius method with a value of 0.3 cm. This is of the same order as the size of the grains in experimental porous medium used in [75]. In addition a truncated power law, rather than a Fickian description, is used for the time dependence of dispersive transport. This alters the form of the dispersive transport and is used to achieve an optimal fit to the experimental data and is specifically aimed at achieving the best fit in the tails of the product concentration profiles. The reaction criterion used in Ederly *et al.* [78] is simple, if the nearest particle of the other reactant species is within 0.3 cm then a reaction occurs. A reproduction of the simulation data presented in Ederly *et al.* [78] with the experimental data from [75] is given in Figure 4.28

At a separation of 0.3 cm the probability of two particles reacting for  $\sigma = 2\sqrt{D_h}$  and  $P_{max} = 1$  using the CLPF is  $1.6 \times 10^{-3}$ . Figure 4.29 shows that using this reaction criterion with a similar total number of particles, corresponding to an initial maximum particle density of 256 per  $\text{cm}^2$ , all of the proximal reactants are consumed and any mixing limiting effects have little effect on the amount of product created.

The data presented above, in Chapter 3, and by [36, 75, 92, 93] suggest that altering the form of the transport solution is not necessary to achieve a good fit to the experimental form of the dispersive

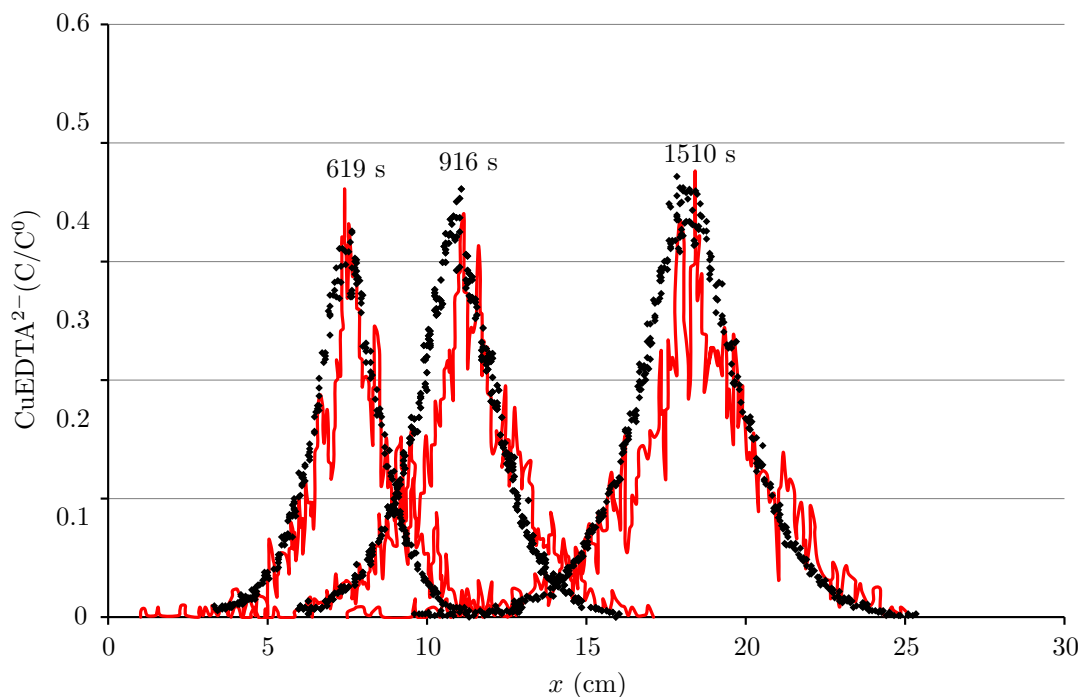


Figure 4.28: Comparison of the simulation results presented by [78] with experimental data from [75].

transport. Though the use of a Fickian description does fail to accurately describe the tailing of the concentration profiles the size of the errors shown in [36, 75, 92, 93] are far smaller than those shown in CTRW simulations using a Fickian time dependence for dispersive transport shown in Edery *et al.* [78].

The primary issue with the analytical solution of [75] is that it overpredicts the reaction rate. The simulation presented by [78] which is meant to reproduce the results of this analytical solution visibly underpredicts the amount of product formed, yet the CTRW solution using a Fickian time dependence for dispersive transport shown in Edery *et al.* [78] shows a large underprediction of the total amount of product formed.

Due to the number of particles used in Edery *et al.* [78] the concentration profiles produced have large variability so precise comparisons with experimental data are difficult. Nevertheless it appears that in using a truncated power law to accurately describe the product concentration profiles tails they have sacrificed the ability to accurately replicate the centre of the concentration profile. In addition the level of improvement which this makes over a solution using a Fickian dispersive transport description is questionable.

### Ding *et al.*, 2012

Ding *et al.*, [36], like Edery *et al.* [78], use a CTRW approach but manage to achieve a better fit to the experimental data presented in [75]. The simulations presented in Ding *et al.* [36] are one dimensional and use the dispersive transport parameters presented in [75] and the CLPF reaction method presented in [35], though the standard deviation of the CLPF is scaled according to the molecular diffusivity of the reactants,  $D_m$ , rather than their hydraulic dispersivities,  $D_h$ . The reaction rate is controlled by altering the particle density used to represent  $C^0$ , which ranges from 200 particles per cm to 2 particles to cm, equivalent in two dimension to  $4 \times 10^4$  particles per  $\text{cm}^2$  to 4 particles per  $\text{cm}^2$ . A reproduction of the simulation data presented by Ding *et al.*, [36] with the experimental data from [75] is given in Figure 4.30

As discussed earlier, one of the controls on the simulated reaction rate is the standard deviation of the

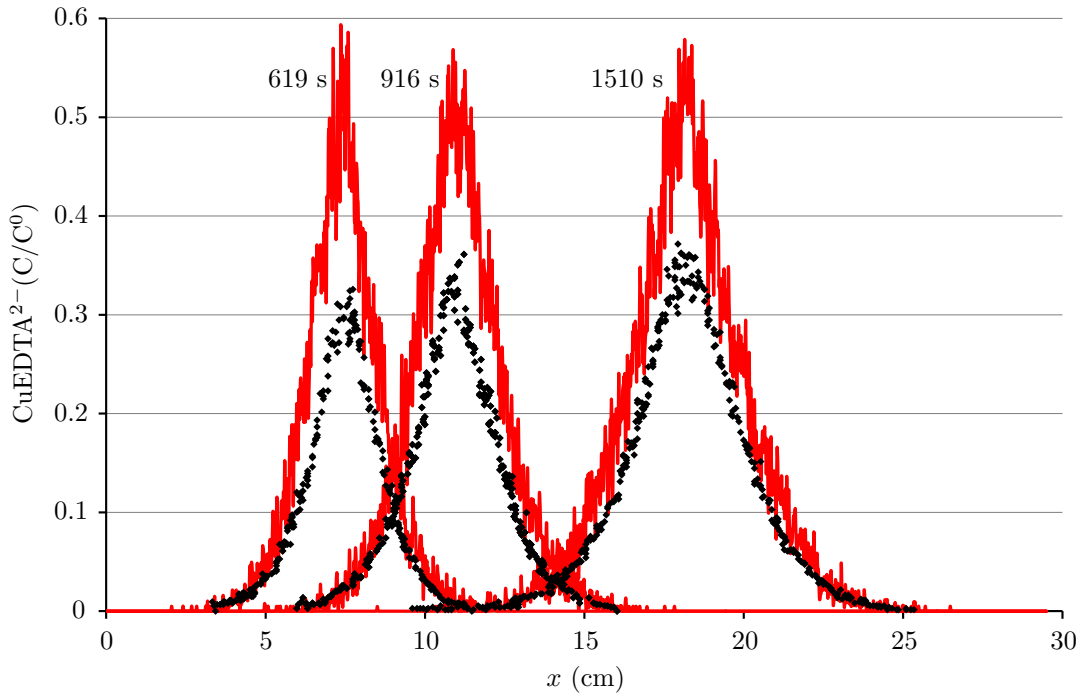


Figure 4.29: Comparison of the DTRW simulation results for initial particle density = 256 per  $\text{cm}^2$  with experimental data from [75]. The particle density corresponds to approximately the same total number of particles used by [78] in their simulations.

CLPF. In this research this is scaled by a scaling factor  $\sigma_s$  and the hydraulic dispersivity  $D_h$ , which for the Gramling *et al.* [75] experiments has a value of  $1.75 \times 10^{-3}$ , whereas Ding *et al.*, [36] use  $D_m$ , which has a value of  $7.02 \times 10^{-7} \text{ cm}^2 \text{ s}^{-1}$ . By using  $D_m$  rather than  $D_h$  it is implied that the reaction rate is limited solely by the rate of diffusion, in the manner described by Equations 4.5 - 4.11. The first issue with this with regards to Ding *et al.*, [36] is that the diffusivity used for the reactants is the diffusivity of the reaction product,  $\text{CuEDTA}^{2-}$ . Values for the diffusivity of the reactants are not given by Gramling *et al.* [75] though they can be found elsewhere. The diffusivity of  $\text{CuSO}_4$  is  $\sim 8 \times 10^{-6} \text{ cm}^2 \text{ s}^{-1}$  under the similar conditions [95]. The diffusivity of  $\text{Na}_2\text{EDTA}^{2-}$  should be similar to that of  $\text{CuEDTA}^{2-}$ . For spherical, or near spherical, solutes the Stokes-Einstein equation states that the diffusivity of a solute particle is given as

$$D_m = \frac{k_b T}{6\pi\eta_f r} \quad (4.27)$$

where  $k_b$  is the Boltzmann constant,  $T$  is the temperature,  $\eta_f$  is the fluid viscosity and  $r$  is the particle radius. The diffusivity is therefore inversely proportional to the size of the particle. The replacement of Cu with Na has little effect on the size of the molecule and so little effect on the diffusivity.

The second issue is that the diffusivity of the reactants is not the only control on the reaction rate. Raju & Kapoor [76] present data showing the bimolecular reaction between two species in a porous media column flow experiment. One reactant is displaced by the other under constant flow conditions. The reaction rate is determined experimentally under well mixed conditions for a range of initial concentrations. The reaction rates determined from these experiments include the effect of diffusion limiting described by Equations 4.5 - 4.6. The simulations performed using this reaction rate overestimated the amount of product formed over the course of the experiments, showing that some factor other than the rate of diffusive mixing is limiting the reaction rate. Raju & Kapoor [76] state that this is due to spatial

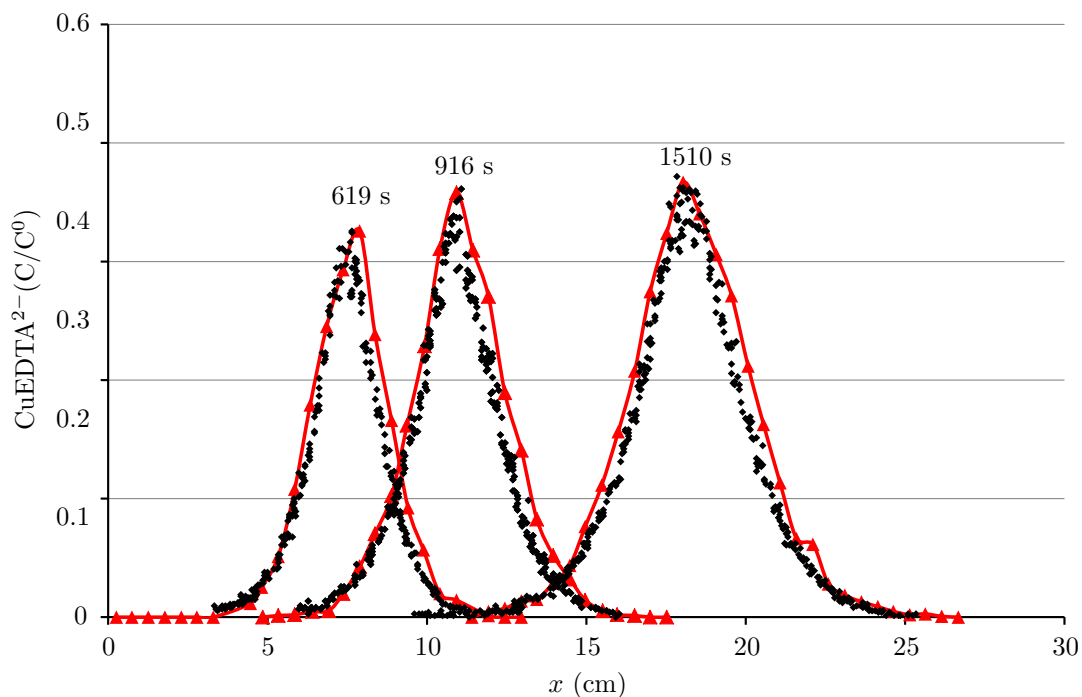


Figure 4.30: Comparison of the simulation results presented by [36] with experimental data from [75].

segregation of the two reactants into flow paths with different hydraulic conductivities. The variation of flow rates between pores which leads to the spatial segregation of the reactants is one of the processes which contributes to the effect of hydrodynamic dispersion.

The reaction rate is controlled by a combination of all the factors involved in dispersion. Higher dispersivities lead to a greater amount of macroscale mixing. This means that a larger mass of each solute is proximal to the other, increasing the reaction rate over a purely diffusive case. The effect of differential flow rates is to reduce the observed reaction rate for the macroscale view of how mixed the reactants are. A larger difference in flow rates leads to a larger macroscale area in which the two reactants appear to be proximal when in fact they are partially segregated. The degree of segregation is reduced by the differential flow rates within pores and the rate of diffusion. The effect of Poiseuille flow leads to the reactant molecules close to pore walls being advected slower than the molecules in the centre of the pore. The molecules of the injected reactant in the faster moving solute then catch up with the molecules left behind facilitating reactions. Higher dispersivities therefore include mechanism which both increases and decreases reaction rates. Higher rates of diffusion increase the reaction rate between proximal solutes if the reaction is diffusion limited and increase the rate at which solutes segregated by the effects of differential flow rates are brought together.

Thinking about simulation particles as real molecules is acceptable when describing their transport behaviour, but continuing the assumption into the position that the probability of reaction is controlled solely by the rate of diffusion leads to problems. As discussed earlier, if particles are separated by a distance greater than  $\sim 3.5$  CLPF standard deviations there is essentially zero chance of reaction occurring. If  $D_m$  is used as the controlling variable for then  $\sim 3.5$  CLPF standard deviations equates to  $\sim 1.185 \times 10^{-3}$  cm. As stated in Equation 4.23 the average minimum separation between particles scales as a power law with the particle density. The average minimum separation between particles at a particle density of 900 per  $\text{cm}^2$  is 0.016 cm. In a 0.02 M solution the two dimensional particle density would be  $\sim 5.25 \times 10^{12}$  particles per  $\text{cm}^2$  and the average minimum separation between particles would be  $\sim 2.2 \times 10^{-7}$  cm.

The issue with treating the simulation particles as real particles and using the diffusivity as the control on reaction rate is that at a particle concentration where the problem can be solved with in an acceptable time and using an acceptable amount of memory the separation between the particles is much larger than the separation between real particles, and yet the proximity to one another they are expected to achieve is as would be the case for real particles.

Despite these issues, the simulations presented in Ding *et al.*, [36] are able to achieve a good fit to the experimental data presented in [75]. As Figure 4.19 shows, the reaction rate in a particle tracking framework can be strongly affected by whether the particles are constrained to a set of lattice sites or not, and that this has the effect of artificially increasing low reaction rates. This minimum reaction rate is controlled by the spacing of the lattice sites, where a finer spaced lattice allows for lower reaction rates to be achieved, and the particle density, where lower particle densities also allow for lower reaction rates to be achieved. The lattice spacing used in Ding *et al.*, [36] is not stated but more insight can still be provided by further discussion. Figure 4.19 shows that if the spacing between lattice sites in a CTRW solution is greater than  $\sim 3.5$  standard deviations of the CLPF the only reactions possible are between those on the same lattice site, and any further reduction in the standard deviations of the CLPF result in no further reductions in the reaction rate. If the diffusivity is the controlling factor on the CLPF then the lattice spacing used in the simulations in Ding *et al.* [36] should be small enough that the diffusivity has an effect. The solute used by [75] has a diffusivity of  $7.02 \times 10^{-7} \text{ cm}^2 \text{ s}^{-1}$  which would require a lattice spacing no larger than  $\sim 4 \times 10^{-3} \text{ cm}$ , which would result in there being  $\sim 7500$  lattice sites in the 30 cm long, one dimensional domain used [36]. For the setup used to produce the best fit, where the initial condition is a uniform concentration of one of the reactants across the entire domain represented by 600 particles, this would mean there would be, on average, one particle for every 12.5 lattice sites. This could potentially cause the reaction rate in the simulations presented in [36] to be artificially high, allowing them to justify the use of  $D_m$  as the scaling parameter for the CLPF, whereas it has been argued above that this is incorrect and the CLPF should be scaled according to  $D_h$ .

The final point to discuss with regards to Ding *et al.* [36] is the flexibility of the method and its ability to simulate more complicated systems, specifically with using particle density as the controlling parameter to achieve this. In the case of bimolecular reaction in a uniform flow regime, using the particle density as the controlling factor is acceptable. If a more complicated reaction system is being simulated then using the particle density as the controlling factor is not viable. This method cannot cope with any system where the reactions rate varies with any factor other than the concentration of the reactants as it is not possible to vary the controlling parameter across the domain and maintain the validity of the simulation. As the observed reaction rate is controlled by the mixing of the two reactants, itself controlled by the rates of dispersive and diffusive mixing, and the thermodynamic reaction rate. This limits the complexity of the systems which can be simulated using this method. If there are multiple different reactions within the system which either have different thermodynamic rate constants or different diffusivities, thereby affecting the diffusion limiting of the reaction rates then controlling the reaction rate by the particle density is not a flexible enough method to accommodate the full complexity of such a system. As discussed earlier the flow regime affects the reaction rate via its effect on the dispersivity of the solutes. The macroscopic reaction rate is therefore also affected by the flow regime, both in terms of pressure driven variations in the flow field and by heterogeneities in the porous medium. This means that using particle density to control the reaction rate is also unviable for a system where the fluid flow regime changes either spatially, due to differences in the soil structure or composition, or temporally due to changes in the pressure conditions driving the flow.

### Zhang *et al.*, 2013

Zhang *et al.* [96] also present particle tracking simulations of the Gramling *et al.* [75] experiments in which the reaction radius method of Ederly *et al.* [77, 78] but extended to allow for the reaction radius to be varied over the course of the simulation. The reaction radius  $R_s$  is given according to the function

$$R_s(t) = \gamma \beta_{particle} \frac{[A_0]L\Delta t}{N_A^0} t^{-\eta} \quad (4.28)$$

where  $\gamma$  is a unit parameter to controls the units of the expression,  $\beta_{particle}$  is a fitting parameter for scaling the reaction rate,  $A_0$  is the initial chemical concentration of species  $A$ ,  $L$  is the domain size,  $\Delta t$  is the time step length,  $N_A^0$  is the initial number of particles in species  $A$ ,  $t$  is the time since the simulation start and  $\eta$  is a fitting parameter to control the change in reaction rate over time.

For the simulations of the Gramling *et al.* [75] experiments,  $\beta_{particle}$  and  $N_A^0$  are used to fit the simulated reaction rate to the observed rate. As with [36] the method used in Zhang *et al.* [96] is able to produce a good experimental fit for the experiments it is tested against but is not flexible enough to cope with situations where variable dispersion rates would cause varying degrees of mixing between reactants and so, in turn, cause variable reaction rates in different areas of the simulation domain. Interestingly, Zhang *et al.* [96] also state that they only identify one combination of  $\beta_{particle}$  and  $N_A^0$  which is capable of producing their presented best fit output. Figures 4.23 - 4.25 show that this is not the case with the CLPF method as presented here.

Overall the quality of the solution shown in Figure 4.26 is of similar quality or better than those presented by [36, 77, 78, 92, 96] without resorting to using different transport parameters to those measured by [75]. The method presented here for controlling the reaction rates is also much more flexible, and has much greater potential for expansion, than those presented by [36, 77, 78, 96].

## 4.3 Sorption

Another process which affects the non-conservative transport behaviour of a solute is sorption, which is can be semantically separated into two processes, adsorption and desorption. Adsorption is the accumulation of solute particles on the surface of the soil solids. Desorption is the process of these particles returning to the pore fluid. Adsorption should not be confused with absorption, the process by which solutes are incorporated into the soil solids rather than just attaching to their surface. It also is important to acknowledge that adsorption and desorption are distinct from precipitation and dissolution. Precipitation is the process of solutes coming out of solution and forming a solid phase, though this can form on the soil solids. Precipitation is the formation of a three dimensional molecular structure, whereas adsorption is the formation of a two dimensional structure on the interface between the soil solid and the pore fluid [97]. Only adsorption is to be simulated in this work. As the adsorbed layer is only ever a few molecules thick the effect on the hydraulic conductivity of the soil can be safely ignored. By comparison precipitation can fill pore spaces and alter the hydraulic conductivity of the soil. This leads to a non linear transport behaviour. This is an active research topic in its own right *e.g.* [98, 99] and adds an additional layer of complexity to the simulation which is beyond the scope of this work.

To begin, the method by which CTRW solutions for the transport of sorbing solutes has been achieved is outlined. The general method by which sorption is simulated using the DTRW method in this work is then outlined and comparisons with experimental data and CTRW solutions presented.

### 4.3.1 Simulating Sorption using Particle Tracking Methods

The CTRW method has been used to simulate the transport of a sorbing chemical, *e.g.* [80, 81, 83]. The method that has been used to achieve this is to alter the time dependence of the dispersive transport in the same manner as for the simulation of non-Fickian transport [58, 100]. This non-Fickian transport is simulated by using a truncated power law to describe the time dependence of the transport equation. The Probability Density Function (PDF) for the transition time between lattice sites,  $\psi(t)$ , takes the form

$$\psi(t) = (C) \frac{\exp(-t/t_2)}{(1 + t/t_1)^{1+\beta}} \quad (4.29)$$

where  $\beta$  is the power law exponent,  $t_1$  the characteristic transition time, and  $t_2$  the cutoff time to Fickian transport. Values of  $\beta$  between 1 and 2 produce asymmetrical breakthrough curves associated with the transport of sorbing solutes [101]. Equation 4.29 describes the combined result of all of the aspects which produce a non-Fickian transport behaviour. This can include the effects of dispersion, low permeability zones and sorption. As description of all of these physio-chemical mechanisms is contained in Equation 4.29 it is not possible to separate the effects of one particular mechanism from the others.

The solution used to achieve the best fit to experimental data is produced by varying the parameters  $\beta$ ,  $t_1$  and  $t_2$  [80]. This has the issue that the description of the sorption behaviour can only be developed *a posteriori* by altering the parameters  $\beta$ ,  $t_1$  and  $t_2$  to achieve a fit to data.

Li & Ren [81] attempt to address this issue by determining a relationship between the parameters controlling the time dependence of the CTRW solution and two of the controlling variables on sorbing transport behaviour in the HYDRUS 1-D model [18, 19], the pore water velocity,  $v$ , and the retardation factor,  $R$ . The retardation factor is given as

$$R_f = 1 + \rho_b K_d / \theta \quad (4.30)$$

where  $\rho_b$  is the bulk density of the soil,  $K_d$  is the distribution coefficient, the ratio between the adsorbed concentration and concentration in solution, and  $\theta$  is volumetric water content. This then extrapolated to the simulation of three experimental data sets, which CTRW simulations achieve mixed success in reproducing.

Though this method for describing the transport of a sorbing solute has been shown to produce good fits to experimental data *e.g.* [80, 81] the differential equations used contain no explicit description of the sorption behaviour or of the adsorbed and aqueous concentrations of a sorbing solute.

This is an issue as even the simplest of the models used for describing sorption take the sorbed and aqueous concentration as inputs [97]. There is also very little room to expand the method to include more complicated chemical systems, such as the competition between solute species for sorption sites, as these would require some description of the adsorbed and aqueous concentrations.

#### Simulating sorption using the DTRW method

The method by which sorption is simulated in this work is simple and yet allows for additional complexity to be added without requiring large alterations to the code used. Each particle has a logical variable associated with it which defines the sorption state as either true or false. If the sorption state is true it is skipped by the transport simulation and so does not move during the time step. The state of each particle is switched by calculating a probability of adsorption or desorption and then comparing this probability to a U[0,1] PRNG. The computational issue then becomes how to determine the probability of a particle switching state between being adsorbed and being desorbed.

This requires some approximation of the concentration at a particle's location. This is achieved by

transforming the nodal and particle coordinates from the global coordinate system into the local system using the coordinate transformation presented in Chapter 2, then calculating the contributions of each particle to a set of nodal concentration values as

$$C_i = \frac{C^0 A_e}{P_d} \sum_{p=1}^{N_p} N_i(\xi_p, \eta_p) \quad (4.31)$$

where  $C^0$  is the concentration represented by the particle density  $P_d$ ,  $A_e$  is the element area,  $N_p$  is the number of particles in the element,  $N_i$  is the element shape function for node  $i$  and  $(\xi_p, \eta_p)$  is the particle's location in the local coordinate system.

$$N_1(\xi, \eta) = \frac{1}{4}(1 - \xi)(1 - \eta) \quad (4.32)$$

$$N_2(\xi, \eta) = \frac{1}{4}(1 + \xi)(1 - \eta) \quad (4.33)$$

$$N_3(\xi, \eta) = \frac{1}{4}(1 + \xi)(1 + \eta) \quad (4.34)$$

$$N_4(\xi, \eta) = \frac{1}{4}(1 - \xi)(1 + \eta) \quad (4.35)$$

where  $\xi$  and  $\eta$  are the local coordinate variables and  $i$  is the node number. The nodal concentrations are then scaled by the initial particle density. The approximate concentration at a particle's location is

---

**Algorithm 4.2** Algorithm for estimating concentration at nodal coordinates.

---

- Determine which element a particle is located in and designate it as element  $e$ .
  - Retrieve indices of the nodes which make up element  $e$  and their spatial coordinates.
  - Convert the nodal and particle coordinates from the global to the local coordinate system.
  - Sum contributions from all particles and scale according to particle density representing  $C^0$ , element size and nodal connectivity.
  - Concentrations at particle locations are then calculated as the sum of the contributions from each node of the element in which the particle resides. The contributions are determined using the element shape functions.
- 

calculated as

$$C_p = \sum_{i=1}^4 N_i C_i(\xi_p, \eta_p) \quad (4.36)$$

where  $C_i$  is the concentration at node  $i$ . Algorithm 4.2 describes the method by which  $C_p$  is calculated. The concentration at a particle's location can then be determined from the contributions from the nodal concentrations using the same shape functions. This method is used to calculate the adsorbed and aqueous concentrations of a chemical species and so there are to calculated values of  $C_p$  for the adsorbed and aqueous solutions respectively. The adsorption and desorption probabilities for a particle are then some function of these two concentrations at the particle's location.

### 4.3.2 Benchmarking

Benchmarking for the DTRW simulation is performed against experimental data and CTRW simulation outputs from [83] for a sorbing solute. The experimental setup used in [83] is a column 20 cm long with an internal radius of 1.55 cm filled with soil taken from Bet Dagan in Israel to a porosity of 0.4. The

column was flushed with double-distilled water then a solute pulse was transported through the column followed by double-distilled water. This solute pulse is retarded by adsorption onto the soil.

The experiments were performed using the flame retardant Tribromoneopentyl Alcohol (TBNPA). A solute pulse with a concentration of 100 mg/L was injected into the column for 34.44 minutes with a flow rate of  $3.0 \times 10^{-3} \text{ mL s}^{-1}$ . The relationship between the adsorbed concentration and the solution concentration at equilibrium is given by the empirically fitted power law

$$q_{eq} = 1.604c_{eq}^{0.906} \quad (4.37)$$

where  $q_{eq}$  is the adsorbed concentration at equilibrium, in mg/kg of soil solid, and  $c_{eq}$  is the solute concentration at equilibrium, in mg/L. This power law is referred to as the adsorption isotherm. A factor to take into account is that the adsorption of all of the solute within a solution at 1 mg/L concentration does not lead to an adsorbed concentration of 1 mg/kg on the soil solids. This depends on the porosity and density of the soil. The soil porosity in the experimental columns was 0.4 and the bulk density was  $1.46 \text{ g/cm}^3$  (personal correspondence, Ishai Dror). This means that, assuming the pore fluid has a density of  $1 \text{ g/cm}^3$ , 1 g/L solute concentration represents the same amount of solute as 0.584 g/kg adsorbed concentration. Two DTRW models are shown, one in which the adsorption and desorption probabilities have been fitted to produce the best possible fit with no regard for the adsorption isotherm (Equation 4.37), and a second where the probability of adsorption and desorption are dependent on the adsorbed and aqueous concentration so that the local partitioning tends towards equilibrium as defined by Equation 4.37. The simulation begins with an initial concentration of zero across the entire domain.

Figure 4.31 shows DTRW results alongside experimental data and CTRW simulation results from [83]. The DTRW results generated using the the following probabilities for adsorption and desorption,

$$P_a = 1.2 \times 10^{-3} \Delta t \frac{C_p - Q_p}{C_p^{1.3}} \quad (4.38)$$

$$P_d = 5 \times 10^{-4} \Delta t \frac{Q_p - C_p}{Q_p^{0.4}} \quad (4.39)$$

where  $P_a$  and  $P_d$  are the probabilities of a particle adsorbing and desorbing respectively and  $C_p$  and  $Q_p$  are the solute concentration and adsorbed concentration at particle  $p$ 's location. The coefficients are altered with no regard for the adsorption isotherm (Equation 4.37) to achieve the fit shown in Figure 4.31. The fit achieved by the DTRW simulation to the experimental data presented in [83] is good in all areas of the breakthrough curve except in the tail. Beyond around five pore volumes the DTRW solution under predicts the solute concentration flowing out of the domain. The DTRW solution also compares well with the CTRW solution from [83]. Though the simulation results presented in [83] fit well to the tail of the profile they overpredict the peak outflow concentration and produce a concentration pulse which arrives slightly early. The CTRW results presented in [83], as with the DTRW results shown in Figure 4.31, are fitted with no regard for the adsorption isotherm (Equation 4.37) and contain no description of the sorption chemistry, though they are achieved using a different method for controlling the retardation of the solute pulse.

A second set of simulations were then performed where the partitioning of the solute between the solid and fluid phases predicted by the adsorption isotherm determined in [83] for TBNPA onto the Bet Dagan soil was incorporated into the equations for the adsorption and desorption probabilities. If the adsorbed and aqueous concentrations are at equilibrium, as predicted by the adsorption isotherm, no particles can adsorb or desorb. If the adsorbed concentration is below the predicted equilibrium value then only

adsorption occurs, and likewise if the aqueous concentration is below the predicted equilibrium value then only desorption occurs. Using this as a basis, the following adsorption and desorption probability functions were produced by parameter fitting

$$P_a = 3.0 \times 10^{-3} \Delta t \frac{1.604 C_p^{0.906} - Q_p}{C_p} \quad (4.40)$$

$$P_d = 3.0 \times 10^{-4} \Delta t \frac{Q_p - 1.604 C_p^{0.906}}{Q_p^{-0.125}}. \quad (4.41)$$

The DTRW output produced using these adsorption and desorption probabilities is shown in Figure 4.32, in comparison with experimental data and a CTRW solution. The results achieved with these adsorption and desorption probabilities are not as good as those produced using the entirely arbitrary fit, though they are still reasonable. The solute pulse arrives slightly early and the peak concentration arrives slightly late. The fit of the tail is superior to that achieved using the purely arbitrarily fitted adsorption and desorption probabilities.

A possible explanation for this is that the sorption isotherm from [83] is produced by fitting a power law to a set of seven data points. By forcing the equilibrium position in the DTRW simulation to fit to a sorption isotherm, which is in itself a best fit to a small dataset, the quality of the DTRW solution is then partially determined by the quality of the sorption isotherm. The method used to estimate the concentration at particle locations also has the effect of smearing the concentration front when determining the adsorbed and aqueous concentrations. This leads to some errors occurring at advancing or retreating fronts where the smearing of the concentration front means that, for example, the probability of adsorption at the head of an advancing front is over-estimated.

For both the purely arbitrary fit and the fit produced using the adsorption isotherm, simulations were run at three different time step lengths, 5 s, 10 s and 20 s. With the exception of the increase in variability of the solution with decreasing time step length the solution is unaffected by changes in time step length as the adsorption and desorption probabilities are scaled with the timestep length.

Figure 4.33 shows the effect of changing particle density on the solution. Simulations were performed with particle densities of 100, 400 and 900 per  $\text{cm}^2$ ,  $\Delta t = 10$  s and the adsorption and desorption probabilities given by Equations 4.40 and 4.41. The number of simulations averaged to produce each of the series plotted in Figure 4.33 was adjusted to allow of easier comparison between the different simulations. The variation with particle density is shown to be minimal, with the exception that lower particle densities produce more variable simulation outputs. Larger particle densities, or the averaging of multiple simulations, are also required to clearly visualise the tail of the breakthrough curve on a log  $y$  graph.

The method presented here for the simulation of sorption within the DTRW method has been shown to produce outputs which fit well to experimental data when the controlling parameters are allowed to be entirely arbitrary fitted, and acceptably well when constrained by the description of sorption proscribed by and experimentally determined sorption isotherm. Any variability in the solution with time step length can be accounted for by scaling the adsorption and desorption probabilities with  $\Delta t$ . Likewise variability in the solution with particle density can be removed by the averaging of multiple simulation outputs.

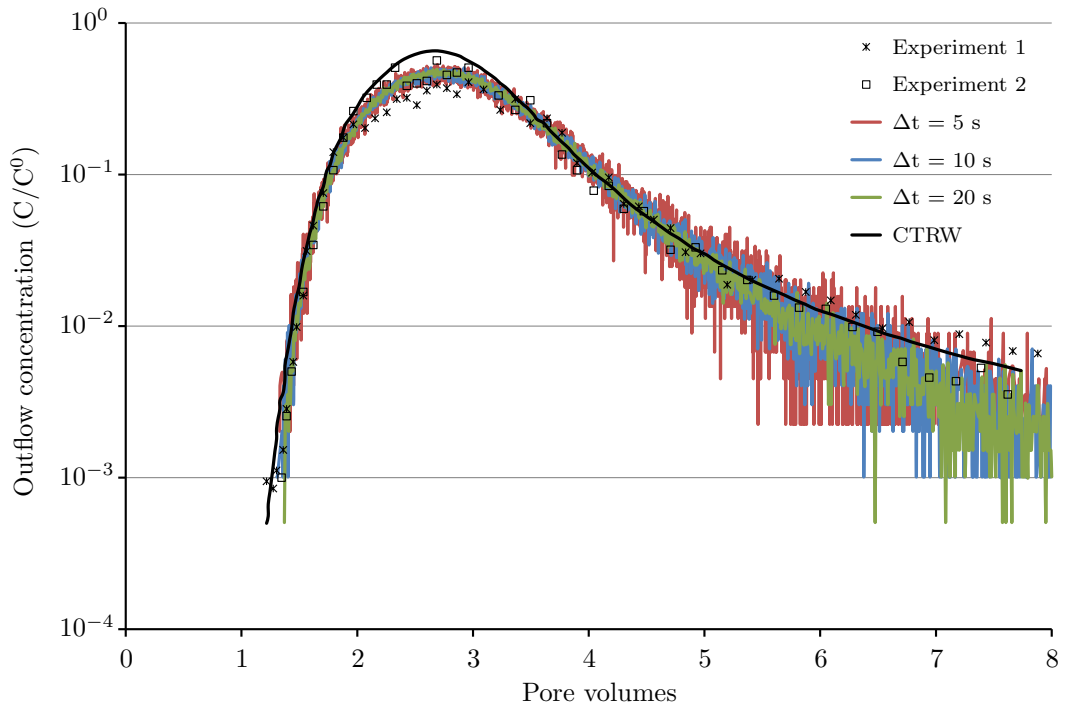


Figure 4.31: Comparison of DTRW simulation results using arbitrary fitted adsorption and desorption probabilities for particle density of 900 per  $\text{cm}^2$  and  $\Delta t = 5$  s, 10 s, and 20 s with experimental data and simulation results from [83].

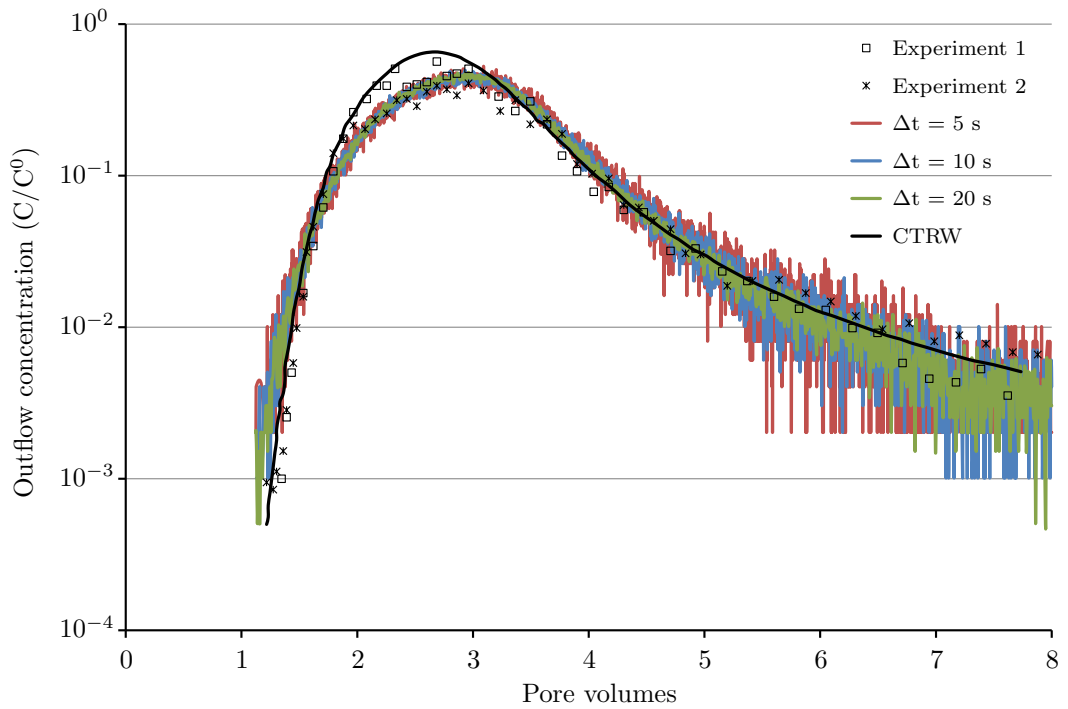


Figure 4.32: Comparison of DTRW simulation results using adsorption and desorption probabilities based on an adsorption isotherm for particle density of 900 per  $\text{cm}^2$  and  $\Delta t = 5$  s, 10 s, and 20 s with experimental data and simulation results from [83].

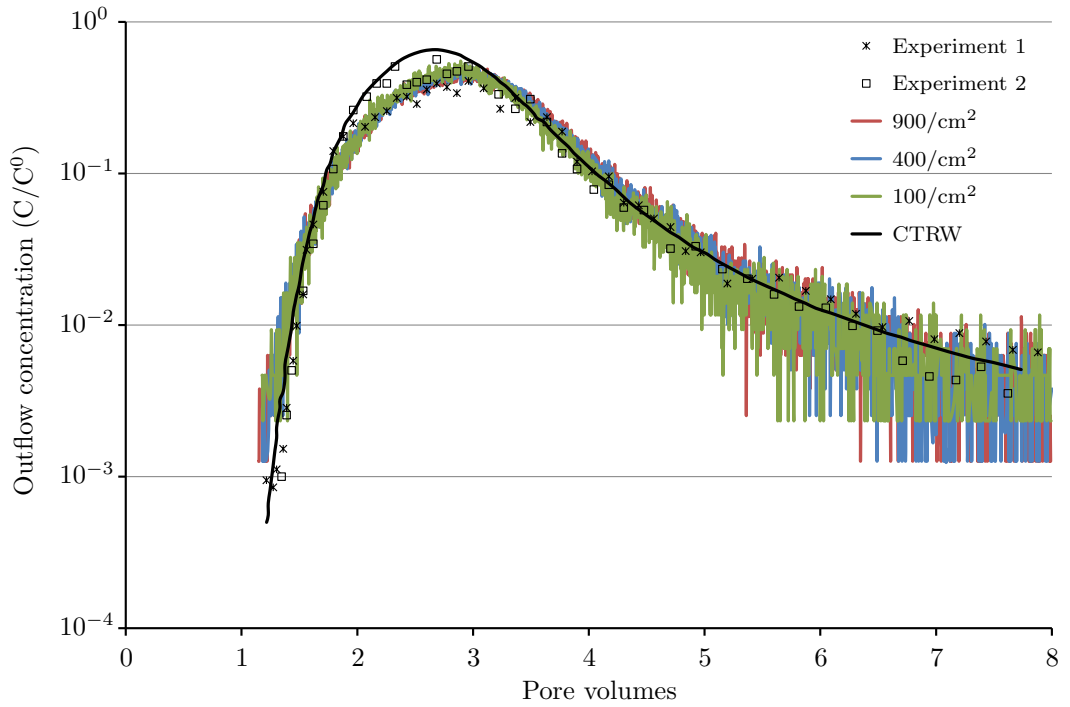


Figure 4.33: Comparison of DTRW simulation results using adsorption and desorption probabilities based on an adsorption isotherm for particle densities of 100, 400 and 900 per  $\text{cm}^2$  and  $\Delta t = 10$  s with experimental data and simulation results from [83].

## 4.4 Conclusion

In this chapter the DTRW transport solution presented in Chapter 3 has been expanded to include the simulation of reactions between solutes and sorption of solutes. The reaction simulations have been simulated using a modified version of the CLPF method presented in [35]. The controls of reaction rate,  $P_{max}$ ,  $\sigma_s$ ,  $\Delta t$  and particle density, have been investigated both in no flow and constant flow regimes. They have also been investigated in relationship to one another to attempt to understand in as much depth as possible the manner in which this reaction simulation method behaves. The method for simulating reactions has been developed with the aim of producing a method which has potential to be expanded to include more complicated physical and chemical processes and this has been achieved. The simulation of reactions using this method has been shown to produce good fits to experimental data in [75]. The quality of the results produced, as well as the flexibility of the method used and the assumptions made to achieve it, have been compared and contrasted with three other numerical simulations which all used the same experimental data to benchmark their simulations. The method presented here compares favourably to these other studies with regards to the quality of the solution produced and the flexibility of the method used to produce them.

The simulation of sorption with the DTRW method has also been implemented. This method has included a description of the sorption chemistry within the system which, though simple, is completely absent from previous CTRW sorption simulations. This method, as well as a purely fitted method, have been used to simulate experiments and has been compared with CTRW simulation outputs in [83]. The variability of the both the reaction and sorption solutions with changes to particle density and time step length have also been investigated and the measures required to ensure that these are as minimal as possible have been outlined.

The next chapter aims to take the framework for non-conservative transport developed here and apply them to the simulation of soils contaminated with heavy metals.

## Chapter 5

# Application to ROBUST

### Summary

The aim of this chapter is to take the Discrete Time Random Walk (DTRW) framework developed in Chapters 3 & 4 and use it to simulate a situation where soil contaminated with Pb has been remediated with Water Treatment Residual (WTR). This involves the assessment of the key factors in controlling Pb partitioning between the different soil phases, and the development of a reduced complexity model which can reasonably reproduce this scenario. As a precursor to this the chemistry of adsorption and the various models used to simulate it are discussed in greater depth than in Chapter 4.

### 5.1 Introduction

In Chapter 4 the DTRW method is demonstrated for bimolecular reactions and the transport of a single sorbing solute. As discussed in Chapter 1, this research forms part of a larger project which is focussed on the remediation of contaminated soils. The experimental aspects of the project have investigated the effectiveness of WTR in remediating land contaminated with heavy metals, specifically Pb. Simulating the entire soil chemistry system is beyond the scope of this project. Models which address the entire chemical system tend to entirely ignore transport or even spatial variation [24]. The aim is therefore to produce a reduced complexity model of the soil chemistry system that occurs in Pb contaminated soils that are remediated using mineral based amendments such as WTR that can be used to predict the partitioning of Pb between the different soil phases. The primary issue in producing a reduced complexity model is to determine what can be safely neglected. In a chemical system of the complexity found in contaminated soils there are multiple feedback relationships between different elements, molecules and soil particles. Determining the effect of changing the concentration of one species on the parameter to be investigated is therefore a complicated question. To this end a chemical speciation model is used to assess the effect of the concentrations of various chemical species on the partition coefficient,  $K_d$ , of Pb. The chemical speciation model is used to determine which factor can be safely neglected and a reduced complexity model produced. This reduced complexity model is then be tested against results produced by the chemical speciation model. First a deeper discussion of the chemistry of adsorption and the various methods used to simulate it are presented.

### 5.2 Sorption Chemistry

In Chapter 4 sorption was defined as the accumulation of solute particles onto the soil surface in a layer only a few molecules thick, as distinct from precipitation. This can be further subdivided into three different types of adsorption; inner sphere (or specific adsorption), outer sphere and diffuse ion swarm.

Inner sphere adsorption involves ionic or covalent bonding between the adsorbate and the soil surface. Outer sphere bonding involves the adsorbate being electrostatically bonded to the soil surface with at least one water molecule in between the adsorbate ion and the soil surface. Diffuse ion swarm adsorption is where the adsorbate ions are held in a cloud of by attractive electrostatic forces. This is counteracted by the Brownian motion of the particles resulting in diffusion of the particles away from the soil surface. As the surface charges of clays and Soil Organic Matter (SOM) tend to be negative, except in some cases such as for clays at low pHs, the adsorbate ions tend to be cations [97, 102].

The amount of a solute which can adsorb on the soil surface is controlled by a wide range of factors. The simplest control is the amount of an adsorbate, both in solution and adsorbed onto the soil surface. Adsorbate molecules are attached to the soil surface by negating some of the charge possessed by the soil surface. If all of that charge has been negated then no more of the adsorbate can attach to the soils. In addition to this, higher concentrations of an adsorbate in solution increase the amount of material that is adsorbed at equilibrium. In outer sphere and diffuse ion swarm adsorption, adsorbate molecules are not strongly attached to the soil skeleton and so molecules are constantly attaching and detaching from the soil surface. When the net movement of adsorbate between solute and soil surface is zero then the system is at equilibrium. The higher the concentration in solution the more often solute particles are colliding with the soil surface. This increases the rate at which particles adsorb and so increases the adsorbed concentration at equilibrium.

The concentration of other solutes can also have an effect on the sorbed concentration of an adsorbate if the two are in competition for sorption sites. Different metals adsorb with different preferences depending on their ionic radius and electron configurations [97]. This leads to competition between metal ions for sorption sites [97, 103]. If a solute is in competition for sorption sites with another solute which preferentially adsorb instead of it then the adsorbed concentration is lower.

The degree of adsorption of metal cations is also affected by the pH of the soil solution. pH is the measure of the activity of hydrogen ions,  $a_{\text{H}^+}$  within a solution defined as

$$\text{pH} = -\log_{10} (a_{\text{H}^+}) \quad (5.1)$$

so lower pH's represent higher activities of hydrogen ions. The hydrogen ions tend not to exist as  $\text{H}^+$  ions but as hydronium ions,  $\text{H}_3\text{O}^+$ , formed by the bonding of an  $\text{H}^+$  ion to a water molecule. The  $\text{H}^+$  ions are formed by the reaction



This reaction is ongoing and so tends to an equilibrium position. This gives a constant concentration of  $\text{H}_3\text{O}^+$ , from which  $\text{H}^+$  activity and pH are determined [102]. Metal ions tend to be positively charged and so adsorb more readily onto negatively charged surfaces. Increasing pH increases the amount of negative charge on clay surfaces *e.g.* [104]. This allows larger concentrations of metal ions to adsorb onto clays at higher pH levels. Similar relationships have been shown between metal sorption and pH for gibbsite and quartz *e.g.* [105]. This is generally the case unless the pore fluids contain large concentrations of ligands, such as those found in Dissolved Organic Matter (DOM), which can compete for the metal ions [97].

The amount of organic carbon in a soil also affects the partitioning of metals. Metals can bind strongly to organic matter, whether it is in the solid phase, SOM, or is itself dissolved in the pore fluids, DOM. The soil organic matter is itself partitioned between the solid and the fluid phases. Higher pH values have been shown to lead to larger fractions of organic matter in solution relative to the amount in the solid phase. This in turn has been shown to lead to increased fractions of Cu and Pb in solution [106].

The adsorption of metals also depends on the relative abundances of other metals that can compete for sorption sites. Metals ions which are more likely to form inner sphere complexes tend to be more likely to adsorb. For metal ions with the same charge, *e.g.* 2+, the tendency to form inner sphere complexes increases with ionic radius [97] in what is known as the Irving-Williams order [107].

### 5.2.1 Lead Sorption

In this chapter the focus is on the effect of the addition of WTR to soils contaminated with Pb. The experimental aspects of the Regeneration of Brownfield Using Sustainable Technology (ROBUST) project have used soil taken from the former St. Anthony’s lead works in Newcastle-upon-Tyne. The remediation scheme involves the addition of WTR taken from the Northumbrian Water treatment works at Mosswood, in County Durham, to the St. Anthony’s lead works soils.

Trace element concentrations for three soil samples and four WTR samples were determined by Northumberland Water with the exception of the DOM measurements which were determined by Nina Finlay from the Durham University School of Engineering and Computing Sciences and Ed Tipping from the Centre for Ecology and Hydrology. The component concentrations are shown in Table 5.1. The soil pH values are in the range 6.6 - 7.0 and the WTR pH value are in the range 6.0 - 6.5. The component concentration data for the three soil samples does not include Mg, Al, K or Ca whereas the WTR data does. The effect of these components, or their absence, is investigated later in this chapter. Triplicate soil samples were analysed to reduce the heterogeneity of Pb distribution at the St. Anthony’s site [108].

Component	Units	Soil A	Soil B	Soil C	WTR
SOM	g/kg	49	18	34	485
DOM	mg/kg	5.58	5.58	5.58	3756
Mg	mg/kg	n/a	n/a	n/a	335
Al	mg/kg	n/a	n/a	n/a	4475
K	mg/kg	n/a	n/a	n/a	832.5
Ca	mg/kg	n/a	n/a	n/a	3000
Cr	mg/kg	18	34	37	31.5
Mn	mg/kg	460	340	420	1825
Fe	g/kg	27	38	34	287.5
Ni	mg/kg	33	23	31	91.5
Cu	mg/kg	120	76	64	26.75
Zn	mg/kg	520	1300	210	665
Cd	mg/kg	1.5	33	0.73	2.36
Hg	mg/kg	2	5.4	0.69	0.36
Pb	mg/kg	320	7600	340	85
SO <sup>4</sup>	mg/kg	2900	4100	680	1022

Table 5.1: Concentrations of soil components for three soil samples, A, B and C, and WTR. Note that no data for the concentrations of Mg, Al, K and Ca are available for the three soil samples.

There are a large number of component elements and species within the soil and WTR samples, each of which has some effect on the partitioning of Pb, either through competition for sorption sites or changing the pH of the solution. The effects of some of the components may counteract the effects of the others. Trying to build a system that can include all of these effects within a particle tracking framework

is beyond the scope of this thesis. Nevertheless it is still work briefly discussing the effects of the main WTR components on Pb sorption.

The largest changes in component concentrations caused by the addition of WTR are for SOM, DOM and Fe and should have the largest effect on the partitioning of Pb between its three potential states, in solution, bound to the soil surface, or bound to DOM. At the pH levels measured for the soils and WTR, Pb has been shown to bind strongly to Iron-oxide coated sands [109]. At lower pH levels this effect is weakened [109]. As the WTR has a lower pH than the soil, due in part to its higher organic matter levels, its addition lowers the overall pH. Pb also is known to bind strongly to DOM and SOM [24]. Increased organic carbon levels reduce the concentration of Pb adsorbed to soil surface and so increase Pb mobilisation [106, 110].

Rather than attempting to build a system involving all of these components within the DTRW framework, which would be complicated to build and validate, and yet would still not capture the full complexity of the real system, a different approach is taken. The chemical speciation model Windermere Humic Aqueous Model (WHAM) [23, 24] is used to assess the overall effect of the addition of WTR on the partitioning of Pb. This is performed for several different amounts of WTR addition. Fitted rules are then determined to estimate the relationship between WTR addition and Pb partitioning. These fitted rules are used to produce a reduced complexity simulation of the effect of WTR on Pb partitioning within the DTRW framework. Before this, an overview of the methods used for the simulation of sorption is presented.

### 5.3 Sorption Models

Sorption models can be separated into two main groups, empirical models and mechanistic models. Empirical models are simple mathematical rules describing the approximate relationship between concentrations of a chemical species in the liquid phase and the solid phase for a constant temperature. Mechanistic (or semi-empirical) involve a description of the reactions occurring between ions in solution and the charged soil surface including the effects of pH and competition between solutes. Reviews of the sorption of heavy metal ions onto soil surface and the models used to describe the sorption behaviour can be found in [111] and [112].

Empirical models take the form of adsorption isotherms. These are produced by parameter fitting to experimental data giving the amount of a species in the solid phase for a set solute concentration. Though the material in the solid phase is referred to as being adsorbed an empirical model contains no information on the mechanism by which a solute has adsorbed or whether it has adsorbed or precipitated [97]. The two commonly used empirical isotherms are the Freundlich [113] and Langmuir [114] isotherms. Freundlich isotherms take the form

$$q_i = ac_i^\beta \quad (5.3)$$

where  $a$  and  $\beta$  are fitting parameters with  $\beta$  limited to the range 0 to 1. The parameters  $a$  and  $\beta$  are then estimated by plotting  $\log(q_i)$  against  $\log(c_i)$ . Langmuir isotherms take the form

$$q_i = b \left( \frac{Kc_i}{1 + Kc_i} \right) \quad (5.4)$$

where  $q_i$ , the amount of species  $i$  adsorbed ( $\text{mg kg}^{-1}$ ), is related to  $c_i$ , the equilibrium concentration of  $i$  in solution ( $\text{mg l}^{-1}$ ), by the fitting parameters  $K$  and  $b$ . The upper limit of  $q_i$  is given by  $b$  which represents the adsorptive capacity of the soil surface. By altering 5.4 into the form

$$\frac{q_i}{c_i} = bK - Kq_i \quad (5.5)$$

the ratio  $q_i/c_i$ , the distribution coefficient  $K_d$ , can then be plotted against  $q_i$ . If the Langmuir description is viable this produces a linear relationship from which  $K$  and  $b$  can be determined.

These adsorption isotherm models do not include any description of how the charges of the solute ions and the soil surfaces affect the adsorptive behaviour of the solutes [112]. As such they need to be fitted to a set of experimental data and are not well suited to extrapolation. By conducting a range of sorption experiments over a variable space, the value of  $K_d$  can be estimated as a function of some controlling parameter such as pH or SOM concentration though these relationships tend to only be capable of predicting general trends in behaviour, *e.g.* [115]. The advantage of this type of model is that in depth knowledge of the physio-chemical mechanisms controlling the sorptive behaviour is not required by the model.

Models that do include descriptions of these reactions between solute ions and the soil surface, and the effects this has on the soil surface charge are referred to as mechanistic, semiempirical or molecular adsorption models [97, 112]. An example of this type of model is the diffuse double layer model [116, 117]. In these models the simulated solute ions can bind to the soil surface at different types of sorption sites, representing inner sphere and outer sphere adsorption. In doing so they affect the charge of the soil surface and so the affinity of the solute ions for the soil surface and the capacity of the soil surface to hold more adsorbed ions. Producing model outputs from mechanistic models that fit experimental data requires the fitting of some parameters though there tend to be too many parameters, making the model too flexible. This allows there to be multiple setups which can fit to the experimental data for any of them to be meaningful [118, 119]. This leads to a situation where the model definition becomes part of the fitting process [112], hence the semi-empirical name attached to these types of models.

Two such mechanistic models are WHAM [23, 24] and PHREEQC [120], both of which have been used widely for soil sorption simulations *e.g.* [121–128]. Both models have similar capabilities, in that they both simulate competition between a range of different elements for sorption sites, the availability of which is determined by the soil composition and the pH of the pore water. Whereas WHAM includes the simulation of trace elements binding to DOM and SOM in competition with the other particulates, PHREEQC does not. Both WHAM and PHREEQC include databases that are used to define the behaviours of each component of the system and their possible interactions. In effect the fitting required has been performed by the code developers. In this manner models of the complexity of WHAM and PHREEQC can be used predictively provided a data-set of soil component concentrations is available. As organic matter forms a large component of WTR, any model used to simulate its effects on the behaviour of other trace element species must include the effects of organic matter. WHAM is therefore used in this thesis rather than PHREEQC.

As comprehensive experimental data are not available for the soils used in the experimental parts of the ROBUST project to characterise the sorptive behaviour of Pb in the soil-WTR mixtures, WHAM is used to provide information on the effect of WTR addition on the sorption of Pb. The aim of the next section of this chapter is therefore to utilize WHAM to assess the overall effect of the addition of WTR to the soil on the partitioning of Pb so that a relationship between WTR addition and the partitioning of Pb can be derived. This relationship can then be used to inform controls on the behaviour of the DTRW simulations.

## 5.4 WHAM and assessment of key controls

Simulations were performed using WHAM to determine the partitioning of Pb in each of the three soils in their original state and with 5%, 10% and 20% additions of WTR. The soils used in the experimental aspects of ROBUST were initially at 22% water content. This means that for 1 kg of soil solids 61 g

of WTR is added for 5% addition, 122 g for 10% addition and 244 g for 20% addition. The component concentrations used as the inputs for WHAM are for 1 l of soil-WTR mixture and so the inputs units are mg/l or g/l rather than mg/kg or g/kg as in Table 5.1. Tables 5.2 - 5.4 show the WHAM inputs for each of the soil-WTR mixtures.

Simulations were then run using WHAM with these inputs and Pb concentrations at 1/2, 1/4, 1/8, 1/6 and 1/32 of the measured Pb concentrations to determine values for  $K_d$ . This is a direct replication of the method used to determine values for  $K_d$  experimentally, where different concentrations of the adsorbent are used so that best fit isotherms can be produced. The outputs are shown in Figures 5.1 - 5.3. In all of the cases presented a linear isotherm is capable of producing a very good fit to the WHAM outputs. This is useful as it makes determining relationships between the WTR components and  $K_d$  more straightforward. In soil A (Figure 5.1) the effect of WTR addition on  $K_d$  is clear. Adding WTR reduces the amount of Pb bound to the soil surface with respect to the amount of Pb in solution. Increasing the amount of WTR added further reduces this ratio. In soils B (Figure 5.2) and C (Figure 5.3) the effect is less clear cut. The overall effect of WTR addition is to reduce the Pb bound to the soil surface with respect to the amount of Pb in solution, as with soil A, but the addition of greater amounts of WTR do not alter  $K_d$  in a monotonic fashion as with soil A. Both soil B and soil C have the lowest  $K_d$  with a 10% addition of WTR, and a slightly lower  $K_d$  for a 20% addition than a 5% addition.

As mentioned earlier, the trace element concentration data for the three soil samples does not include values for Mg, Al, K or Ca. To assess the relative impact of not including Mg, Al, K and Ca in the behaviour predicted by WHAM simulations were performed with and without Mg, Al, K and C, and also with and without the DOM, SOM and Fe contributions of WTR. Not including Mg, Al, K or Ca in the WTR addition reduces the value of  $K_d$  by between ~3 and 7% in soil A, ~1 and 2% in soil B and ~2 and 4% in soil C. By comparison not including the addition of the organic matter increases the value of  $K_d$  by between ~45 and 84% in soil A, ~14 and 18% in soil B and ~3 and 11% in soil C. Not including the addition of the organic matter reduces the value of  $K_d$  by between ~60 and 95% in soil A, ~27 and 69% in soil B and ~35 and 71% in soil C. The effect of setting the concentrations of Mg, Al, K and Ca to zero on the partitioning of Pb should be small in comparison to the effects of the other, more major, components.

Figures 5.4 - 5.6 show the relationship between the total Pb concentration and the Pb concentration bound to DOM, referred to here as  $K_c$ . As with determining  $K_d$ , simulations were performed with Pb concentrations at 1/2, 1/4, 1/8, 1/6 and 1/32 of the measured Pb concentrations. In all cases  $K_c$  can be described very well as a linear relationship between total Pb concentration and the Pb concentration bound to DOM. For all three soils, the addition of WTR produces a large increase in the fraction of Pb bound to DOM. For soils A and B, larger WTR additions result in a larger fraction of the total Pb being bound to DOM. Note that for soil B with no WTR addition the value for the concentration of Pb bound to DOM was zero at the two highest total Pb concentrations, and so is not able to be included on a log-log plot. The concentrations of Pb bound to DOM are calculated as the difference between the total aqueous Pb and the Pb in true solution. At these values the difference between the total aqueous Pb and the Pb in true solution was less than the precision of the results outputted by WHAM, hence the calculated value of zero. This only occurred with soil B as the Pb concentrations are much higher than those in soil A or soil C. The value of  $K_c$  for soil B is calculated from the four non-zero data points. The calculated values of  $K_d$  and  $K_c$  are shown in Table 5.5. For all three soils, the addition of WTR increases the concentration of Pb in solution, lowering the value of  $K_d$ , and increases the fraction of Pb bound to DOM.

Though pH has an effect on the partitioning of Pb it is not suitable as a controlling factor as it is not

explicitly controllable as an input for WHAM. The pH is calculated and given as an output by WHAM and ranges between  $\sim 7.5$  and  $\sim 8.5$ . This is also not a large enough change in pH for a clear cut effect on  $K_d$  to be noticeable [115].

Experimental data from small scale lysimeter studies on the effects of WTR on Pb partitioning show a general trend of increasing Pb concentration in solution with WTR addition [129] correlating with the simulation outputs produced by WHAM. For a 10% addition of WTR the concentration of Pb in solution increases by a factor of approximately 5. This data is from a small sample set but is still statistically significant ( $P < 0.05$ ). The WHAM simulations predict increases by factors of approximately 3.5, 1.15 and 1.4 for 10% WTR addition to soils A, B and C respectively. The effects of different levels of WTR addition vary between the three samples. Soil A shows a monotonic decrease in  $K_d$  with increasing WTR addition, whereas soils B and C exhibit a minimum  $K_d$  for 10% WTR addition. Soils A, B and C show a monotonic increase in  $K_c$  with increasing WTR addition.

Component	Units	Soil A + 5% WTR	Soil A + 10% WTR	Soil A + 20% WTR
SOM	g/l	153.1	180.0	225.8
DOM	g/l	5.33	10.54	20.61
Mg	mg/l	20.8	39.3	71.0
Al	mg/l	277.9	525.5	948.0
K	mg/l	51.7	97.8	176.4
Ca	mg/l	186.3	352.3	635.5
Cr	mg/l	45.7	86.4	94.0
Mn	mg/l	1268	1356	1503
Fe	mg/l	85640	100780	126430
Ni	mg/l	88.5	92.7	99.5
Cu	mg/l	303.0	301.0	269.9
Zn	mg/l	1347	1369	1403
Cd	mg/l	3.91	4.00	4.14
Hg	mg/l	5.04	5.01	4.93
Pb	mg/l	808.7	804.3	794.6
SO <sup>4</sup>	mg/l	7340	7310	7239

Table 5.2: WHAM trace element concentration inputs for soil A with 5%, 10% and 20% WTR additions.

Component	Units	Soil B + 5% WTR	Soil B + 10% WTR	Soil B + 20% WTR
SOM	g/l	75.3	101.6	146.4
DOM	g/l	5.33	10.54	20.61
Mg	mg/l	20.8	39.3	71.0
Al	mg/l	277.9	525.5	948.0
K	mg/l	51.7	97.8	176.4
Ca	mg/l	186.3	352.3	635.5
Cr	mg/l	87.3	88.1	89.2
Mn	mg/l	967	1058	1212
Fe	mg/l	113260	128090	153130
Ni	mg/l	63.4	68.0	75.2
Cu	mg/l	192.5	192.0	190.1
Zn	mg/l	3305	3305	3296
Cd	mg/l	83.0	82.2	80.6
Hg	mg/l	13.58	13.45	13.18
Pb	mg/l	19090	18880	18460
SO <sup>4</sup>	mg/l	10350	11200	10150

Table 5.3: WHAM trace element concentration inputs for soil B with 5%, 10% and 20% WTR additions.

Component	Units	Soil C + 5% WTR	Soil C + 10% WTR	Soil C + 20% WTR
SOM	g/l	115.5	141.4	185.3
DOM	g/l	5.33	10.54	20.61
Mg	mg/l	20.8	39.3	71.0
Al	mg/l	277.9	525.5	948.0
K	mg/l	51.7	97.8	176.4
Ca	mg/l	186.3	352.3	635.5
Cr	mg/l	94.9	95.5	96.5
Mn	mg/l	1168	1257	1406
Fe	mg/l	103220	118160	143420
Ni	mg/l	83.5	88.0	94.6
Cu	mg/l	162.4	162.0	161.0
Zn	mg/l	569	599	651
Cd	mg/l	1.98	2.09	2.27
Hg	mg/l	1.75	1.75	1.75
Pb	mg/l	858.9	854.0	843.2
SO <sup>4</sup>	mg/l	1766	1799	1851

Table 5.4: WHAM trace element concentration inputs for soil C with 5%, 10% and 20% WTR additions.

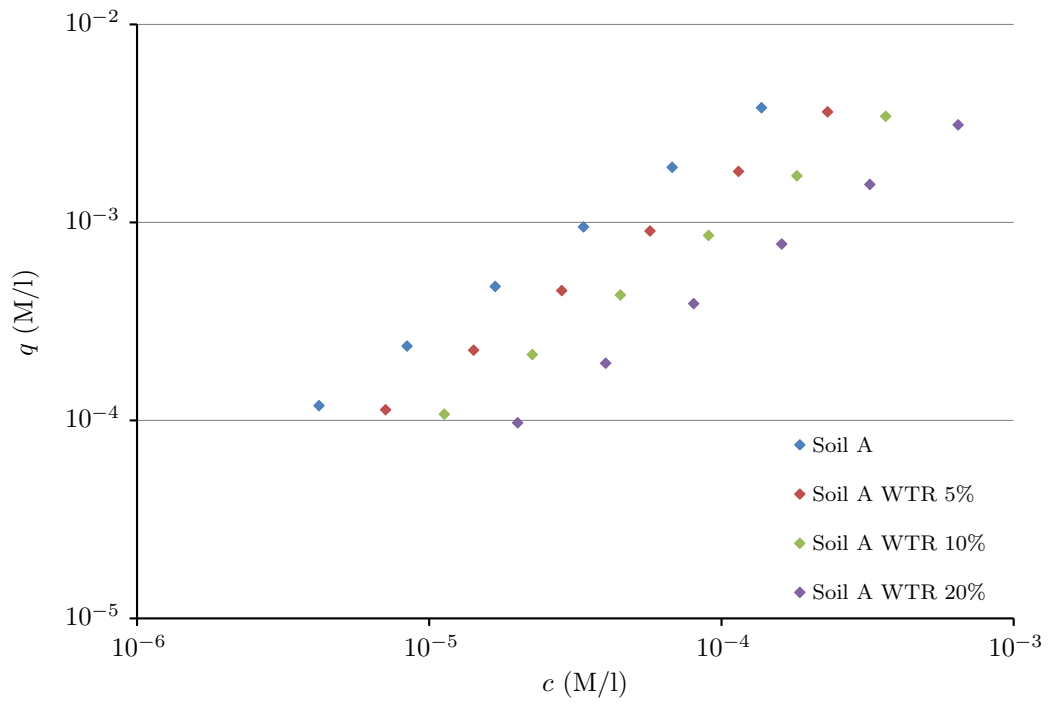


Figure 5.1: The adsorption isotherm for Pb onto soil A with water treatment residuals additions of 5%, 10% and 20%. The partition coefficients  $K_d$  are 27.77, 15.72, 9.44 and 4.82 respectively.

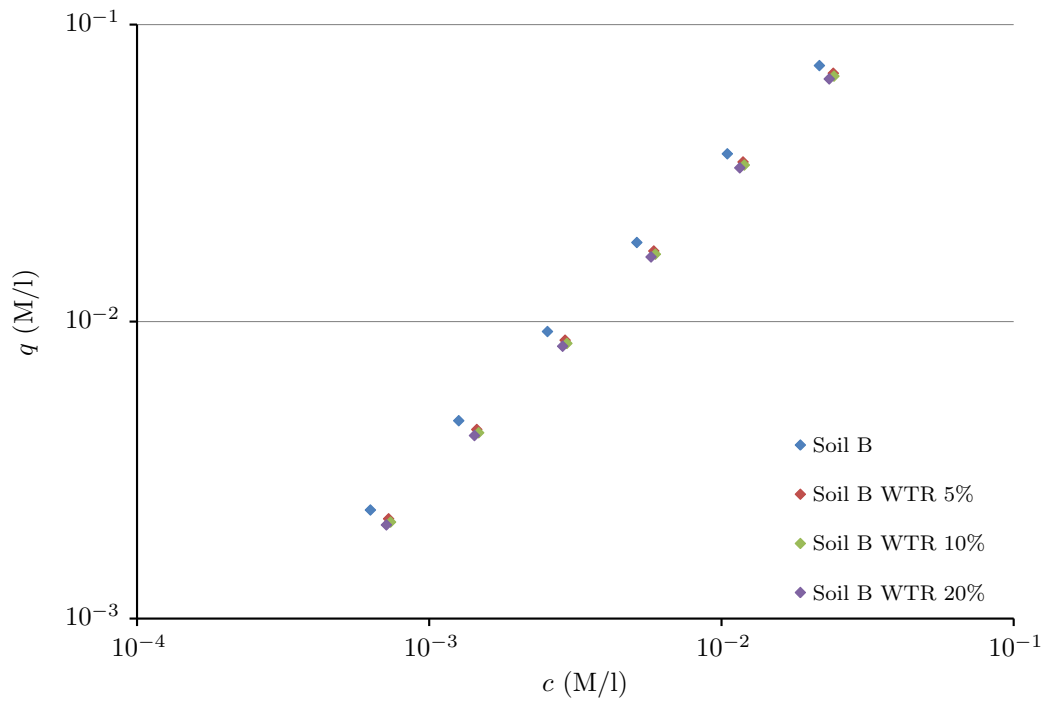


Figure 5.2: The adsorption isotherm for Pb onto soil A with water treatment residuals additions of 5%, 10% and 20%. The partition coefficients  $K_d$  are 3.40, 2.86, 2.78 and 2.82 respectively.

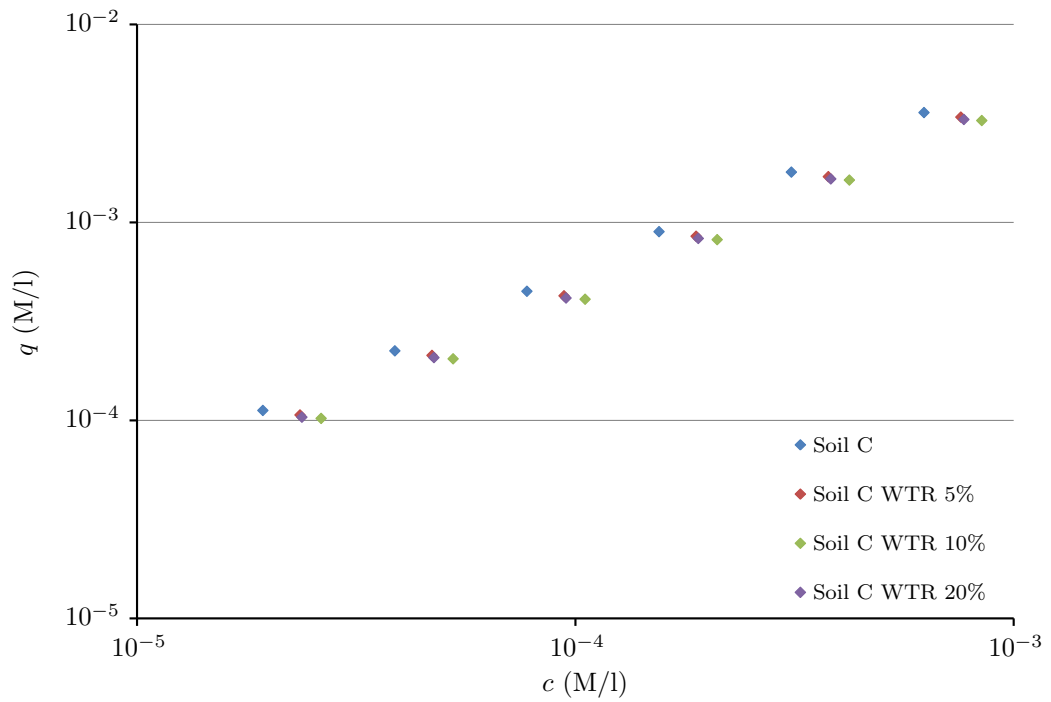


Figure 5.3: The adsorption isotherm for Pb onto soil A with water treatment residuals additions of 5%, 10% and 20%. The partition coefficients  $K_d$  are 5.76, 4.50, 3.87 and 4.31 respectively.

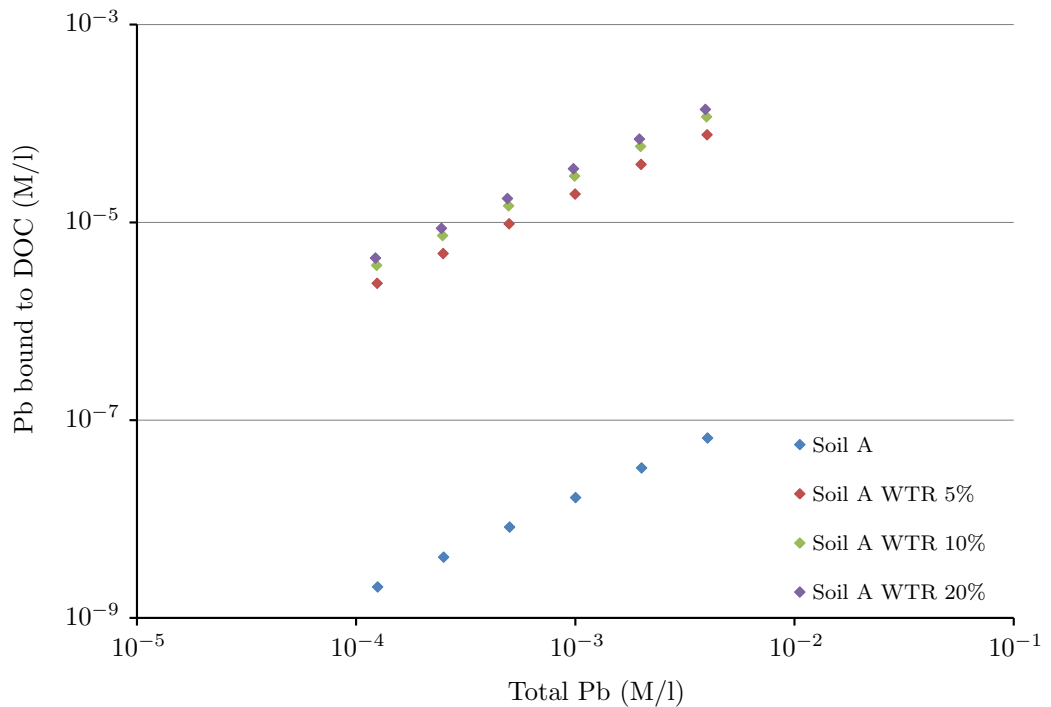


Figure 5.4: The relationship between total Pb and Pb bound to DOM for soil A with water treatment residuals additions of 5%, 10% and 20%. The linear coefficients relating the two have values of  $2.0 \times 10^{-5}$ , 0.0193, 0.0295 and 0.0354 respectively.

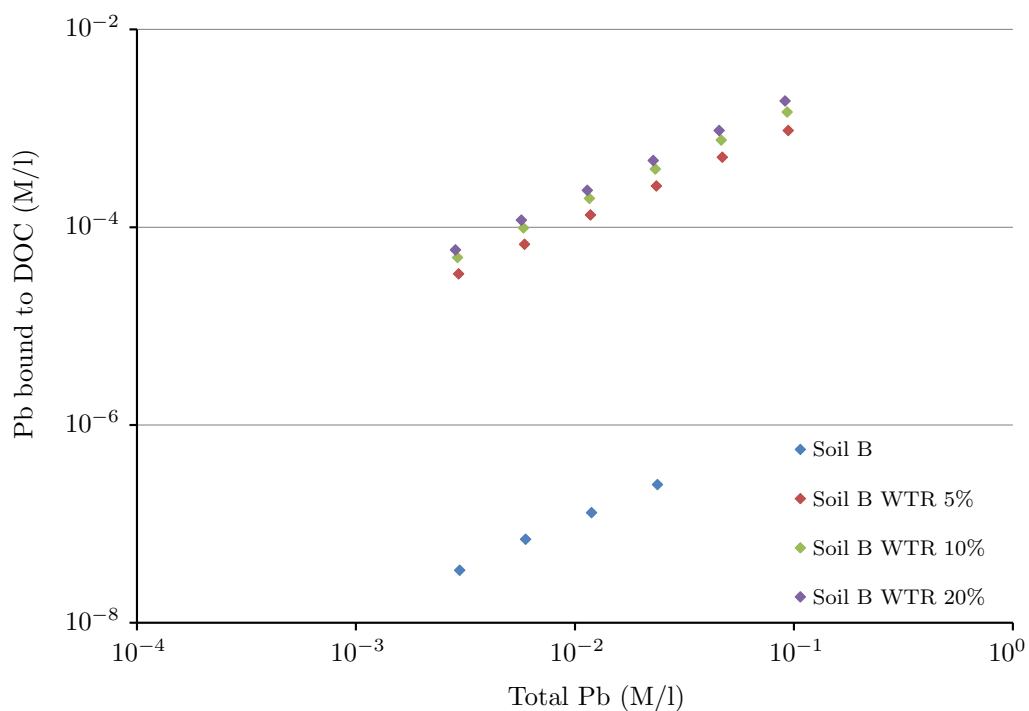


Figure 5.5: The relationship between total Pb and Pb bound to DOM for soil B with water treatment residuals additions of 5%, 10% and 20%. The linear coefficients relating the two have values of  $1.0 \times 10^{-5}$ , 0.0103, 0.0159 and 0.0208 respectively.

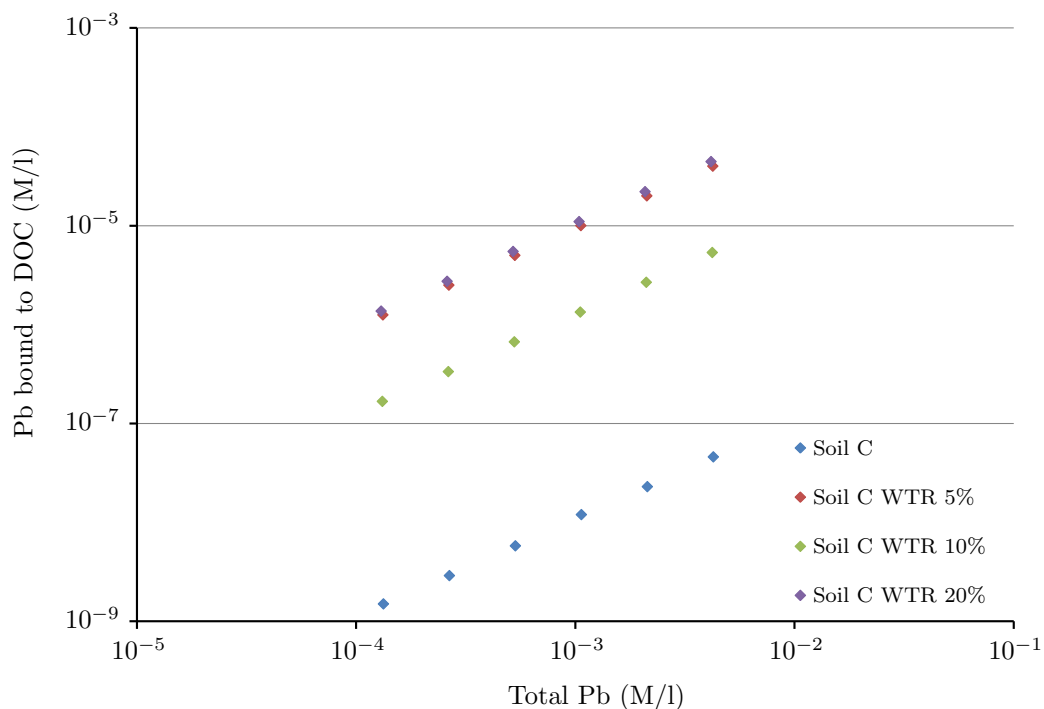


Figure 5.6: The relationship between total Pb and Pb bound to DOM for soil C with water treatment residuals additions of 5%, 10% and 20%. The linear coefficients relating the two have values of  $1.0 \times 10^{-5}$ , 0.0013, 0.0094 and 0.0107 respectively.

Sample	$K_d$	$K_c$
Soil A	27.77	$2 \times 10^{-5}$
Soil A + 5% WTR	15.72	0.0193
Soil A + 10% WTR	9.44	0.0295
Soil A + 20% WTR	4.82	0.0354
Soil B	3.40	$1 \times 10^{-5}$
Soil B + 5% WTR	2.86	0.0103
Soil B + 10% WTR	2.78	0.0159
Soil B + 20% WTR	2.82	0.0208
Soil C	5.76	$1 \times 10^{-5}$
Soil C + 5% WTR	4.50	0.0013
Soil C + 10% WTR	3.87	0.0094
Soil C + 20% WTR	4.31	0.0107

Table 5.5:  $K_d$  and  $K_c$  values for soils A, B and C in their initial states and with 5%, 10% and 20% WTR additions.

## 5.5 Reduced complexity simulations of soil-WTR systems using DTRW

The results generated by WHAM are used to produce a reduced complexity model of the soil-WTR system using the DTRW framework developed in Chapters 3 and 4. For the two relationships of importance, between adsorbed Pb and Pb in true solution, and between total Pb and Pb bound to DOM, empirical relationships are determined by the linear coefficients  $K_d$  and  $K_c$ , and one of the main components of the WTR. The main components in the WTR which affect the partitioning of Pb are DOM, SOM and  $\text{Fe}^{2+}$ .

Figures 5.7 - 5.9 show the relationships between  $K_d$  and DOM, SOM and  $\text{Fe}^{2+}$  respectively. The best fit power laws take the form  $y = \alpha x^\beta$  and are shown as black lines. The values of  $\alpha$  and  $\beta$  for these power laws, as well as the  $R^2$  values showing the quality of the fit are shown in Table 5.6. The power laws used to control the partitioning within the DTRW simulations are those that are functions of SOM. As can be seen from Figures 5.7, DOM is a reasonable measure of the amount of adsorbed Pb for soils B and C, but is very poor for soil A. DOM will bind with Pb reducing the amount of Pb available to adsorb onto the soil surface. As can be seen from Figures 5.4 - 5.6, the fraction of Pb bound to DOM is small, and so the magnitude of this effect will also be small. Figures 5.8 and 5.9 show that SOM and  $\text{Fe}^{2+}$  provide similarly good measures of Pb adsorption for all three soil samples.

The fitted relationship for predicting  $K_c$  is given as a function of DOM concentration in the form

$$K_c = C_{\text{DOM}} * \alpha \exp[\beta C_{\text{DOM}}] \quad (5.6)$$

where  $C_{\text{DOM}}$  is the concentration of DOM in mg/l and  $\alpha$  and  $\beta$  are fitting parameters. This form was chosen via experimentation with a range of function types. The fit to the data for soil A and soil B is very good, though this is at the expense of the fit to soil C, which is very poor. This was done as the fit between the WHAM and power law values of  $K_d$  was worst for soil C. The  $K_c$  values for the soil without the WTR addition have also been excluded from this fitting process. The inclusion of these data points reduced the quality of the fit at the other three data points for soils A and B. As the DOM concentration

Soil	Component	$\alpha$	$\beta$	$R^2$
A	DOM	12.515	-0.154	0.7079
B	DOM	2.9778	-0.023	0.9823
C	DOM	4.6205	-0.039	0.8692
A	SOM	$3.3146 \times 10^7$	-2.902	0.9985
B	SOM	6.1298	-0.164	0.7352
C	SOM	33.053	-0.409	0.6152
A	Fe <sup>2+</sup>	51.606	-2.88	0.9983
B	Fe <sup>2+</sup>	3.9829	-0.286	0.6369
C	Fe <sup>2+</sup>	6.8644	-0.596	0.5789

Table 5.6: Best fit power laws for relationships between  $K_d$  and the three components which the addition of WTR has the greatest effect on.

Soil	Component	$\alpha$	$\beta$	$R^2$
A	DOM	0.0047	-0.049	1.0
B	DOM	0.0024	-0.042	0.9983
C	DOM	0.0003	-0.0353	0.176

Table 5.7: Best fit exponential rules in the form of Equation 5.6 for the effect of DOM concentration on  $K_c$ .

is so low in the soil without WTR addition the absolute error between the value of  $K_c$  produced by WHAM and that produced by the exponential function is of the same order of magnitude as those for the other data points using the curve fitted just to the points with WTR addition. With its inclusion the error for the soil with WTR addition is approximately halved by the for soils A and B, whereas the errors for the soils with WTR all increase by at least two orders of magnitude.

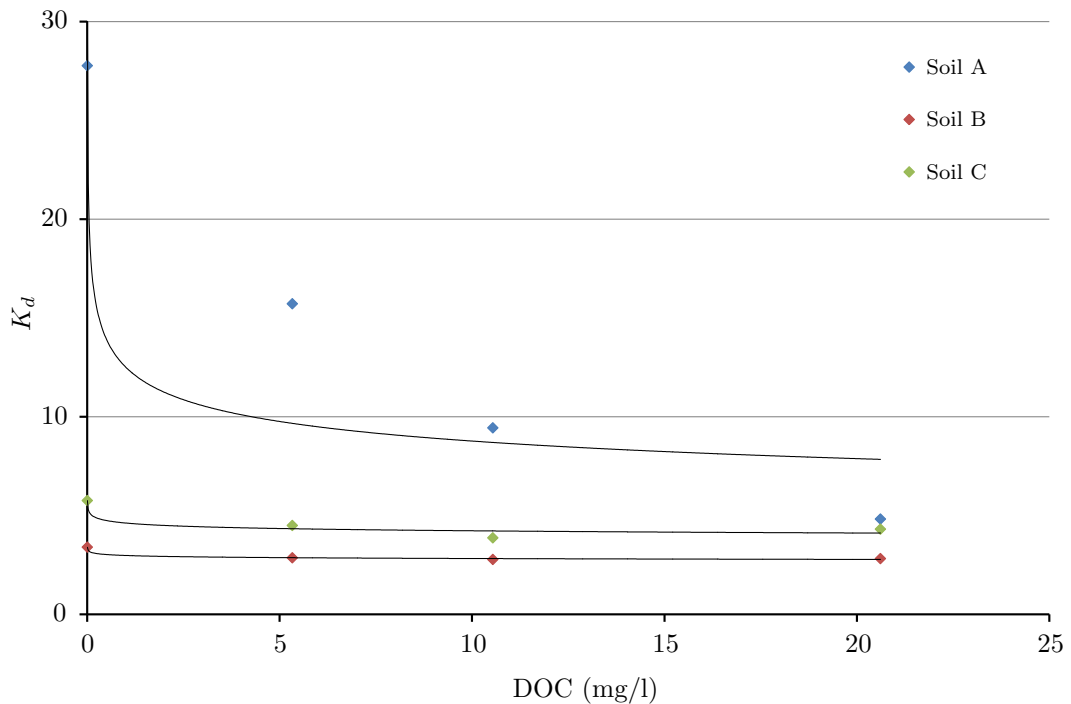


Figure 5.7: DOM concentration against  $K_d$  for soils A, B and C in their original states and with 5%, 10% and 20% WTR addition.

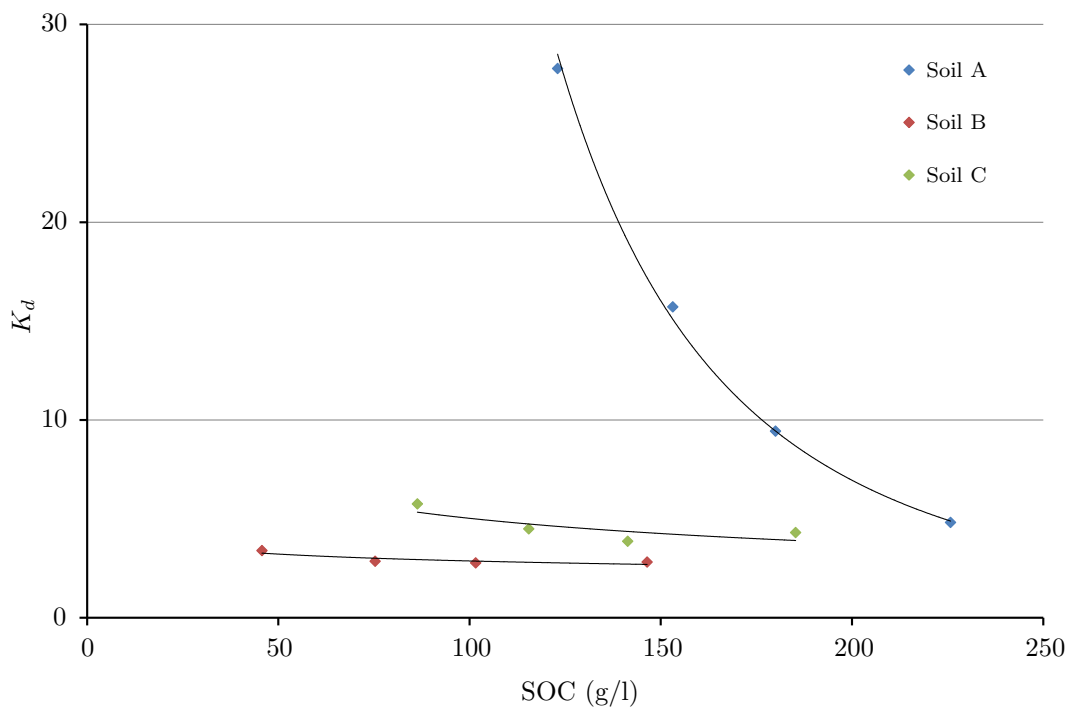


Figure 5.8: SOM concentration against  $K_d$  for soils A, B and C in their original states and with 5%, 10% and 20% WTR addition.

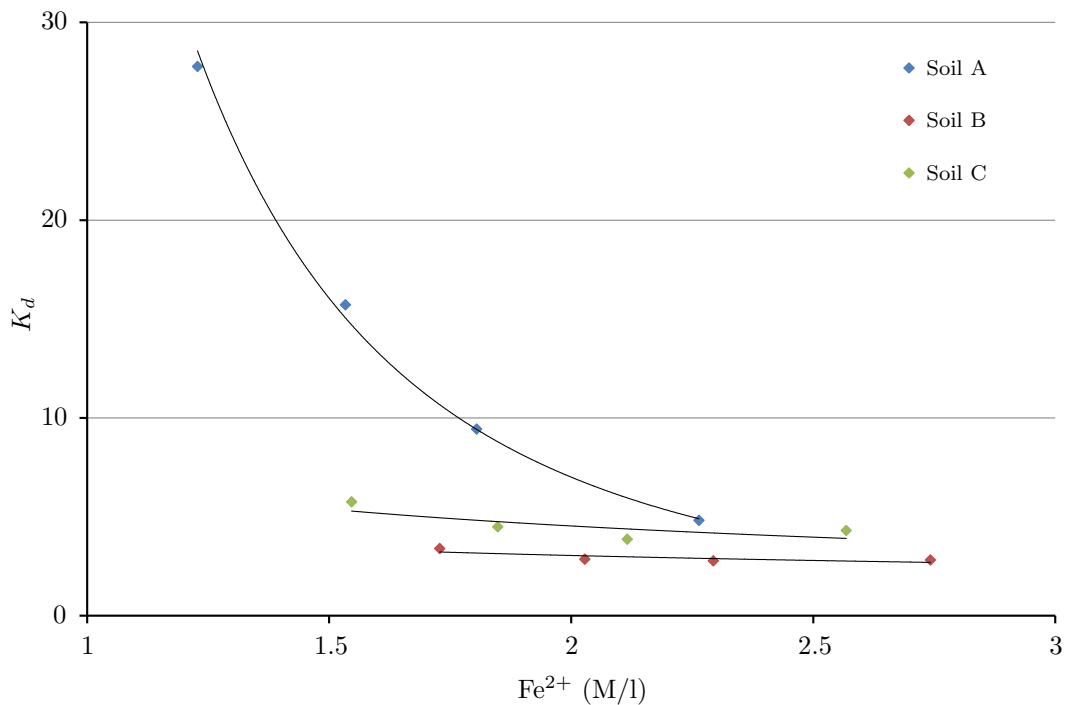


Figure 5.9: Fe concentration against  $K_d$  for soils A, B and C in their original states and with 5%, 10% and 20% WTR addition.

### 5.5.1 DTRW methodology for soil-WTR systems

The adsorption of Pb onto the soil surface and SOM is simulated within the DTRW framework using the method described in Chapter 4. Particles have a probability of changing their sorption state based on the local ratio between adsorbed and aqueous particles so that the local sorption state is driven towards some desired ratio between adsorbed and aqueous particles.

---

**Algorithm 5.1** Reverse reaction.

---

```

do  $i = 1, N_C$ 
  if ( $x_{C_i} \neq 10^9$ ) then
    set  $R_b$ 
     $R_U = U[0, 1]$ 
    if ( $R_U < R_b$ ) then
       $j = 1$ 
      counter = 1
      do while ( $j \leq N_A$ )
        if ( $x_{A_j} = 10^9$ ) then
          counter =  $j$ 
           $j = N_A + 1$ 
        else
           $j = j + 1$ 
        end if
      end do
       $x_{A_{\text{counter}}} = x_{C_i}$ 
       $y_{A_{\text{counter}}} = y_{C_i}$ 
       $j = 1$ 
      counter = 1
      do while ( $j \leq N_B$ )
        if ( $x_{B_j} = 10^9$ ) then
          counter =  $j$ 
           $j = N_B + 1$ 
        else
           $j = j + 1$ 
        end if
      end do
       $x_{B_{\text{counter}}} = x_{C_i}$ 
       $y_{B_{\text{counter}}} = y_{C_i}$ 
       $x_{C_i} = 10^9$ 
       $y_{C_i} = 10^9$ 
    end if
  end if
end do

```

---

The binding of Pb to DOM is achieved using the bimolecular reaction method as described in Chapter 4, but with the addition of a reversible reaction. The amount of Pb bound to DOM is a constant fraction of the total amount of Pb. To have the system reach, and remain at an equilibrium position, each time step a set of forward and reverse reactions are performed. The rate of forward and backwards reaction together control the equilibrium position of the reaction. The method by which backwards reaction are performed is shown in Algorithm 5.1. As with the algorithm detailing the forward reaction method presented in Chapter 4,  $A$  and  $B$  are the reactant species and  $C$  is the product species, the size of the particle arrays are given in the form  $N_S$ , where  $S$  would be the species in question, and  $(x_{S_i}, y_{S_i})$  would

be the  $x$  and  $y$  coordinates of the particle at index  $i$  in species  $S$ .  $R_f$  and  $R_b$  are the forward and backward reaction rates respectively.

The target fraction of the total Pb is as given by WHAM. It is important that adsorbed Pb particles should not be allowed to bind to DOM. The calculated equilibrium position must be that between the Pb bound to DOM and the Pb in true solution. This ratio depends on the  $K_d$  as well as  $K_c$ . The derivation of this is presented below.

The total amount of Pb can be divided into three fractions; the Pb bound to the DOM,  $q_{DOM}$ , the Pb adsorped onto the soil surface,  $q_{sorb}$ , and the Pb in true solution,  $c$ . By definition

$$q_{DOM} + q_{sorb} + c = c^0 \quad (5.7)$$

where  $c^0$  is the total concentration. The ratio between the amount of Pb adsorped to the soil and the amount in true solution is

$$q_{sorb} = K_d c. \quad (5.8)$$

The ratio between the amount of Pb bound to DOM and the total amount is

$$q_{DOM} = K_c c^0. \quad (5.9)$$

The ratio between the amount of Pb bound to DOM and the amount in true solution is

$$q_{DOM} = K'_c c. \quad (5.10)$$

The aim is to determine the  $K'_c$  as a function of the WHAM outputs,  $K_d$  and  $q_{DOM}$ . By substitution of 5.8 into 5.7 and rearranging,  $c$  can be given as

$$c = \frac{c^0 - q_{DOM}}{1 + K_d}. \quad (5.11)$$

Substitution of 5.11 into 5.10 and rearranging yields

$$K'_c = \frac{q_{DOM}(1 + K_d)}{1 - q_{DOM}}. \quad (5.12)$$

$K_c$  can also be defined as

$$K_c = \frac{R_f(1 - R_b)}{R_b} \quad (5.13)$$

where  $R_f$  and  $R_b$  are also the forward and backwards reaction rates respectively. This can be rearranged into the form

$$R_b = \left(1 + \frac{K_c}{R_f}\right)^{-1}. \quad (5.14)$$

The value of  $R_f$  controls the rate at which the equilibrium position is approached. At set of simulations were performed to assess the accuracy of the method presented above, using both the values for  $K_d$  and  $K_c$  produced by WHAM and those produced by the fitted curves.

## 5.6 Simulations

A set of DTRW simulations were performed in a 10 cm by 10 cm domain, initially filled with Pb and DOM particles at a density of 900 particles per  $\text{cm}^2$ . For each soil, in its original state and with WTR additions of 5%, 10% and 20%, two simulations were run, one using the  $K_d$  and  $K_c$  values produced by

WHAM and one using the  $K_d$  and  $K_c$  values produced by the best fit functions. Figures 5.10 - 5.13 show the change in  $K_d$  over time and Figures 5.14 - 5.17 show the change in  $K_c$  over time.

Figure 5.10 shows that the simulation converges accurately to the set equilibrium position for the adsorption-desorption system. Likewise, Figure 5.14 shows that the equilibrium state created using a reversible reaction as outlined in Equations 5.7 - 5.14 operates as desired. The convergence of the solution sorption equilibrium position shows only slight deviation once equilibrium is reached. The deviation from the reversible reaction equilibrium position is more pronounced. This is as the equilibrium position for the sorption system has over two thirds of the particles adsorbed in any of the cases. Deviations of a small number of particles are therefore damped by the large number of particles in either state of the system. By contrast, in the reversible reaction system there is more deviation around the equilibrium position. This is because only a small fraction of the particles exist in the combined state at the equilibrium position and so a small deviation in the number of particles leads to a larger relative deviation from the equilibrium position.

Figures 5.11, 5.12 and 5.13 show the convergence to the sorption equilibrium positions as defined by the fitted curves shown in Figure 5.8 and outlined in Table 5.6. The fit achieved by the fitted curves for soil A is the best, with a relative error in the value of  $K_d$  produced by the fitted curve ranging from  $\sim 5\%$  for the 5% WTR addition to  $\sim 0.5\%$  in the 10% WTR addition. The relative errors range from  $\sim 3\%$  in the 10% addition soil, to  $\sim 5.5\%$  in the 5% addition soil for soil B, and from  $\sim 5\%$  in the 5% addition soil to  $\sim 12.5\%$  in the 10% addition soil for soil C.

Figures 5.15, 5.16 and 5.17 show the convergence to the reaction equilibrium positions as defined by the fitted curves outlined in Table 5.7. The quality of the curve fitted solutions shown in Figures 5.15 and 5.16 is good and the fitted  $K_c$  values are close to those predicted by WHAM. The quality of the solution given by the curve fitted equilibrium position for soil C is much worse though this was to be expected as the form of the relationship chosen to fit the relationship between  $K_c$  and DOM concentration sacrificed the quality of the fit to soil C to achieve high quality fits for soils A and B.

The evolution of the Pb-DOM system shows an initial peak in the fraction of Pb bound to DOM and then tends towards the equilibrium position. This initial peak is caused by the forward reaction rate being high with respect to the equilibrium position of the system. The fraction of Pb bound to DOM is low in absolute terms. This peak can be eliminated by reducing the forward and reverse reaction rates, though this has the effect that the number of simulation steps required to reach equilibrium is increased. As the desired output is the convergence of the simulation to the equilibrium position this was deemed to be an acceptable trade-off.

Overall, given the simplicity of the curves used to describe the relationships between  $K_d$  and SOM, and  $K_c$  and DOM, the quality of the fits achieved by the solutions are good, especially for soil A. In light of this, further, more complicated simulations, are only performed for soil A.

For the more complicated simulations the diffusivity of Pb used is  $9.4 \times 10^{-10} \text{ cm s}^{-2}$  [130] and the diffusivity used for DOM is  $3.5 \times 10^{-6} \text{ cm s}^{-2}$  [131]. The diffusivity of DOM is used for the particles representing Pb bound to DOM. The mobility of DOM is not altered by the presence of Pb but the mobility of Pb is altered by the presence of DOM [132]. All of the Pb particles begin the simulation in solution. The simulations were performed using a domain 5 cm wide and 50 cm deep. The domain was filled with Pb and DOM particles at a density of 900 particles per  $\text{cm}^2$  and the time step length was 2 days.

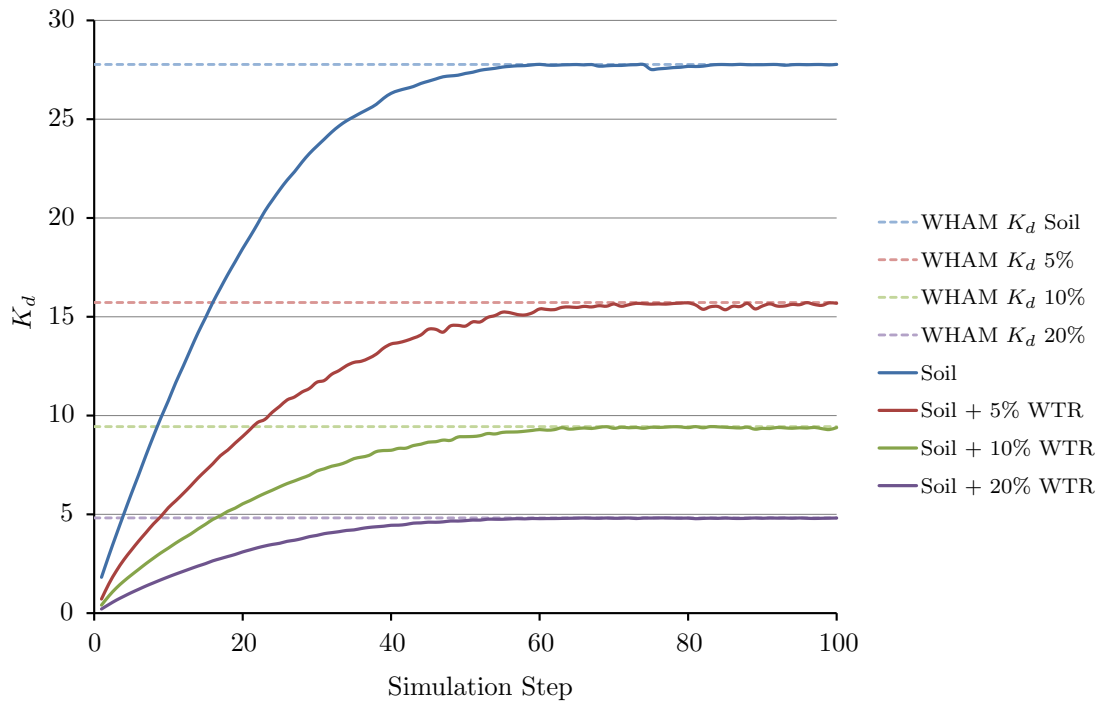


Figure 5.10: Evolution of  $K_d$  over time in a system simulating sorption of Pb to soil surface and DOM for soil A in its original state and with 5%, 10% and 20% WTR addition. The equilibrium positions of  $K_d$  and  $K_c$  are taken directly from WHAM.

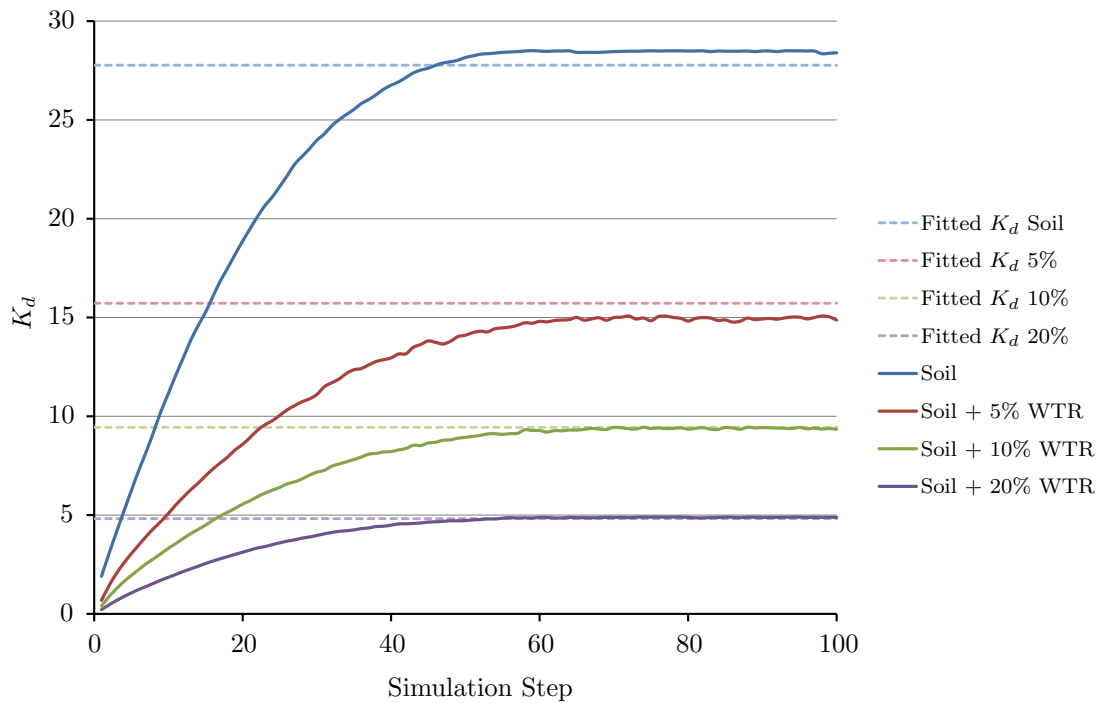


Figure 5.11: Evolution of  $K_d$  over time in a system simulating sorption of Pb to soil surface and DOM for soil A in its original state and with 5%, 10% and 20% WTR addition. The equilibrium positions of  $K_d$  and  $K_c$  are determined using the fitted curves described in Tables 5.6 and 5.7.

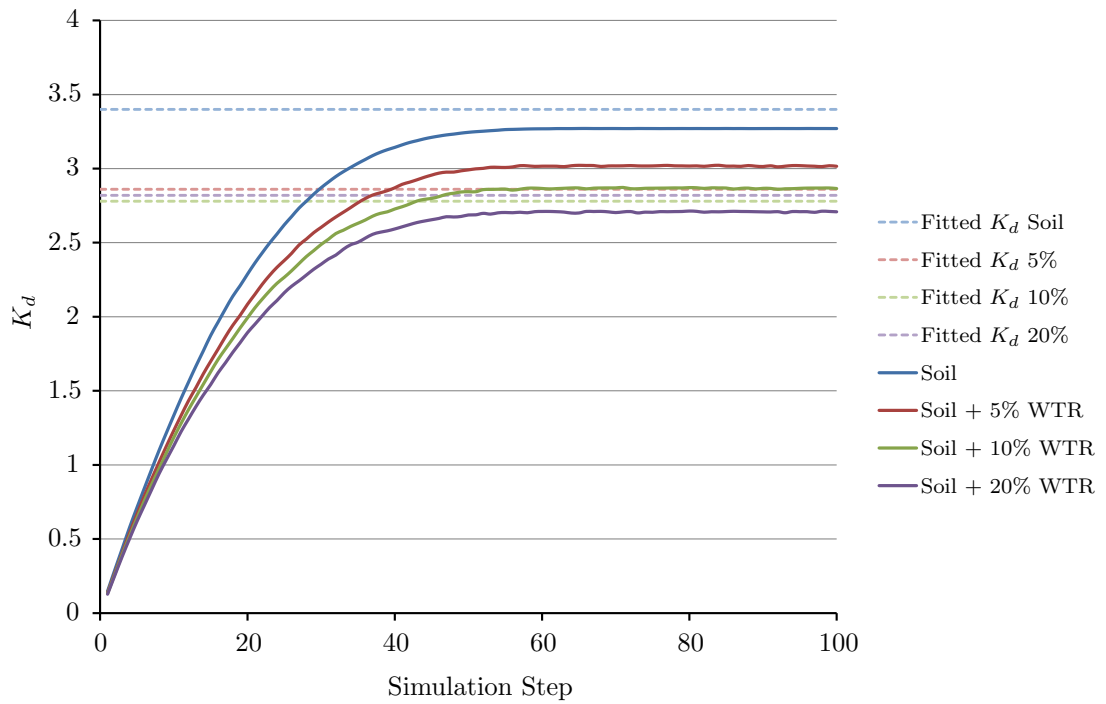


Figure 5.12: Evolution of  $K_d$  over time in a system simulating sorption of Pb to soil surface and DOM for soil B in its original state and with 5%, 10% and 20% WTR addition. The equilibrium positions of  $K_d$  and  $K_c$  are determined using the fitted curves described in Tables 5.6 and 5.7.

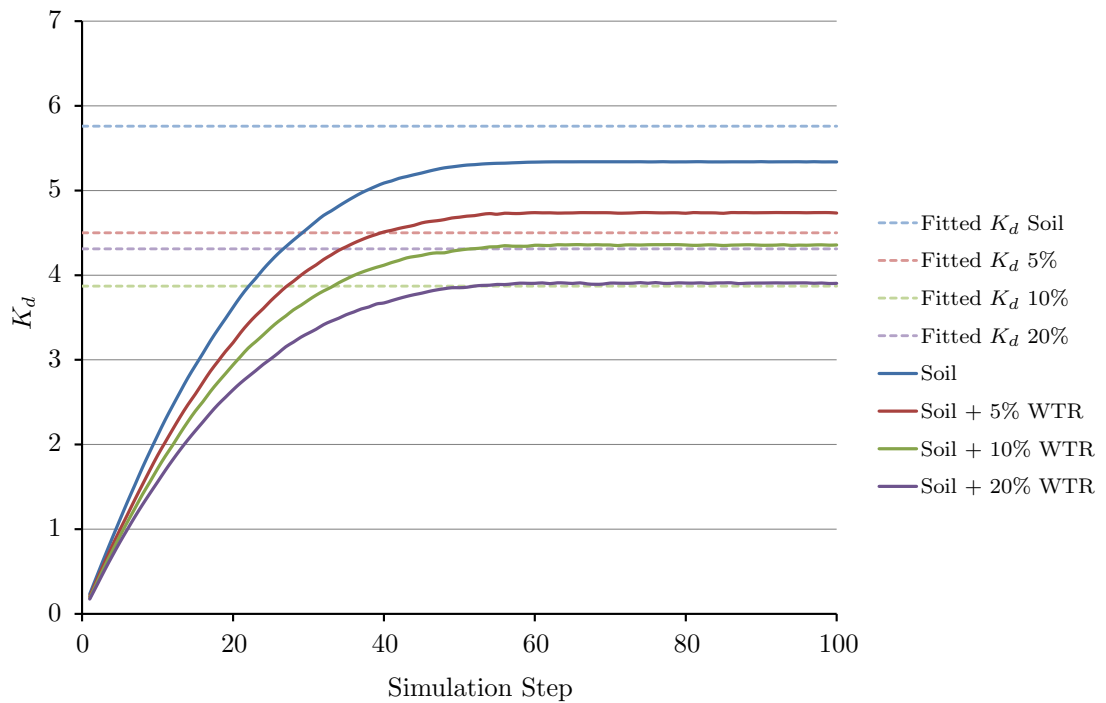


Figure 5.13: Evolution of  $K_d$  over time in a system simulating sorption of Pb to soil surface and DOM for soil C in its original state and with 5%, 10% and 20% WTR addition. The equilibrium positions of  $K_d$  and  $K_c$  are determined using the fitted curves described in Tables 5.6 and 5.7.

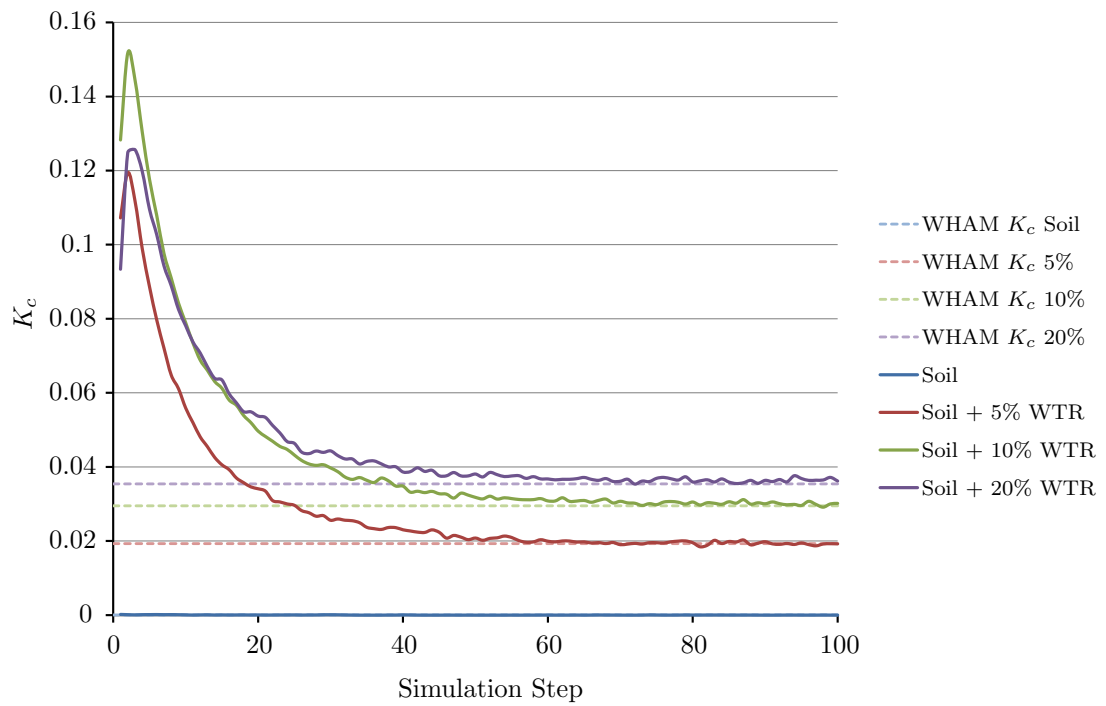


Figure 5.14: Evolution of  $K_c$  over time in a system simulating sorption of Pb to soil surface and DOM for soil A in its original state and with 5%, 10% and 20% WTR addition. The equilibrium positions of  $K_d$  and  $K_c$  are taken directly from WHAM.

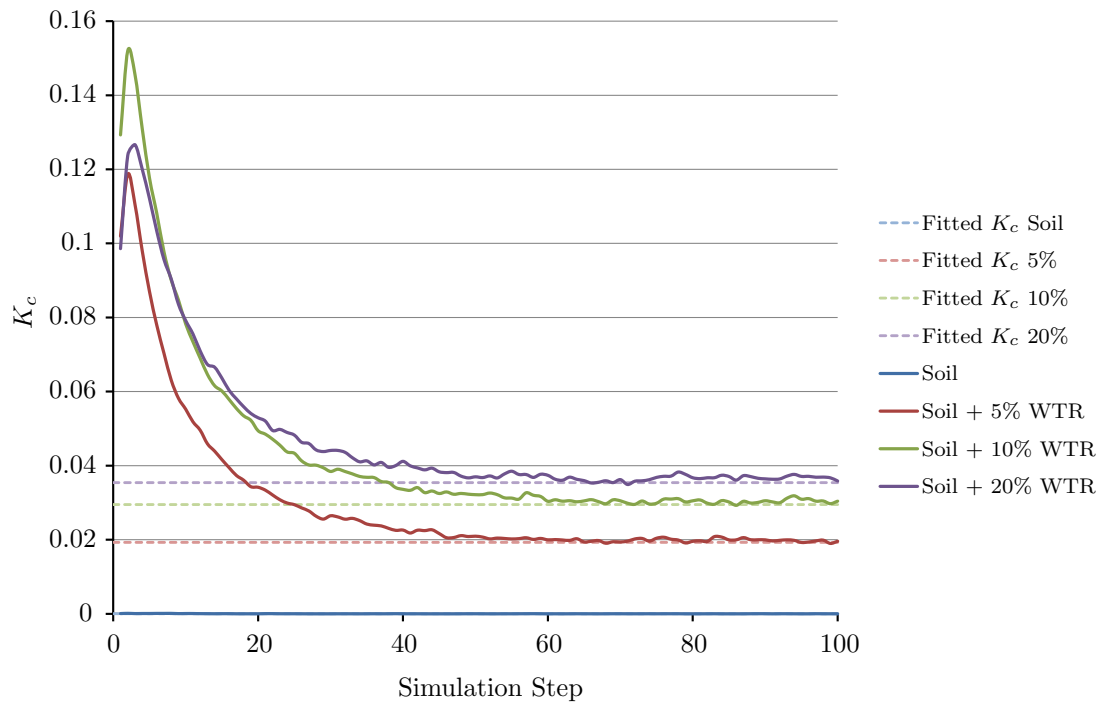


Figure 5.15: Evolution of  $K_c$  over time in a system simulating sorption of Pb to soil surface and DOM for soil A in its original state and with 5%, 10% and 20% WTR addition. The equilibrium positions of  $K_d$  and  $K_c$  are determined using the fitted curves described in Tables 5.6 and 5.7.

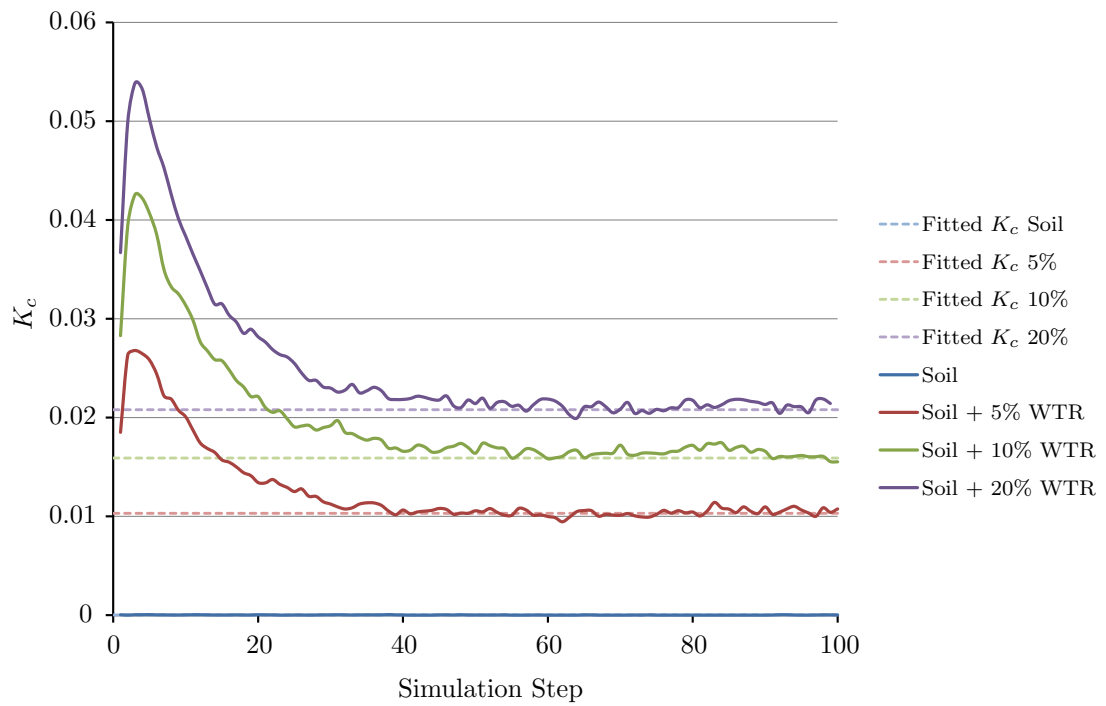


Figure 5.16: Evolution of  $K_c$  over time in a system simulating sorption of Pb to soil surface and DOM for soil B in its original state and with 5%, 10% and 20% WTR addition. The equilibrium positions of  $K_d$  and  $K_c$  are determined using the fitted curves described in Tables 5.6 and 5.7.

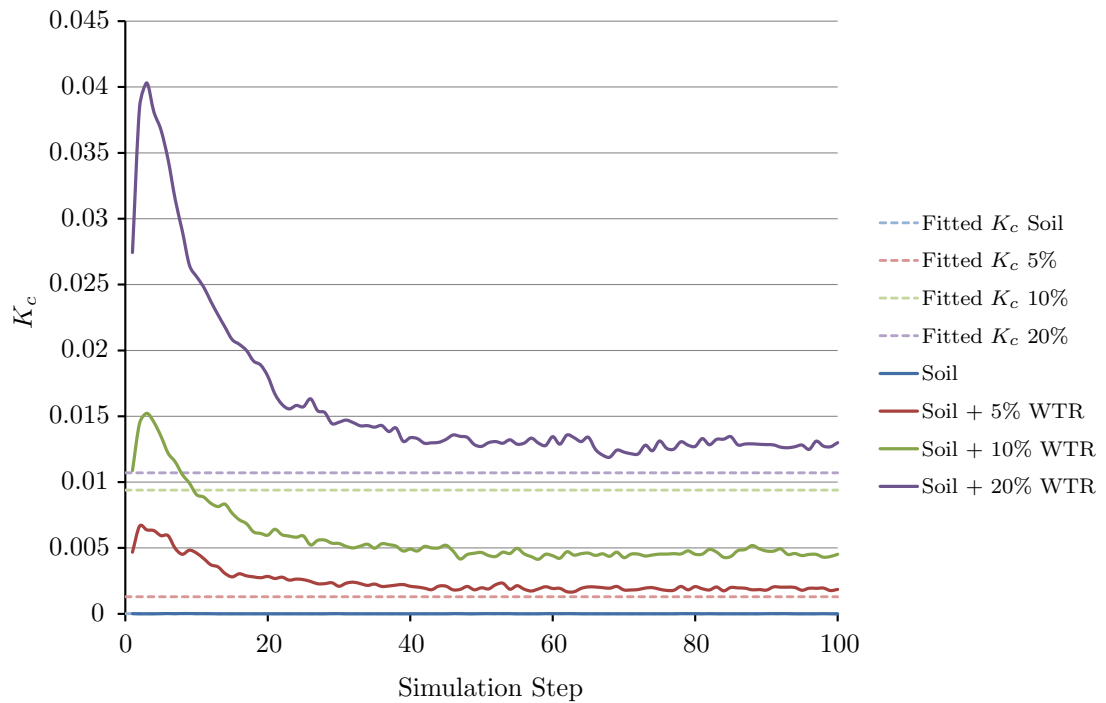


Figure 5.17: Evolution of  $K_c$  over time in a system simulating sorption of Pb to soil surface and DOM for soil C in its original state and with 5%, 10% and 20% WTR addition. The equilibrium positions of  $K_d$  and  $K_c$  are determined using the fitted curves described in Tables 5.6 and 5.7.

As was discussed in Chapter 4, for Colocation Probability Functions (CLPFs) with low standard deviations, such as for reactants with low diffusivities or dispersivities, the reaction rate is significantly reduced. This can be counteracted by either increasing the particle density or increasing the standard deviation of the CLPF, either by increasing the time step length or by artificially increasing the standard deviation using a multiplier. The accuracy of the reversible reaction scheme is dependent on the accuracy of the forward reaction rate. If it is significantly less than one then some measure of the actual rate must be produced and used to scale the backwards reaction rate to preserve the desired equilibrium position. Increasing the time step to account for this has the additional benefit of allowing long simulation times to be reached in reasonable run times.

The simulations was initially run for 100 time steps to allow the solution to converge to the equilibrium position. The bottom boundary was then altered to allow particles to exit the domain. The simulation then proceeded for an additional 730 time steps and the amount of Pb remaining in the domain recorded. The time required for adsorptive equilibrium to be reached is much larger than would be expected [109]. The rate of adsorption is limited as high rates of adsorption can lead to overshoot of the equilibrium position and, in some cases, an oscillating solution. This is only an issue in that the setup time required before the simulation proper is begun is quite large.

Once the simulation begins, Pb begins to exit the domain and desorption of Pb is the dominant process rather than adsorption. Desorption of Pb is a much slower process and so this is not a major issue in these simulations [133]. The initial peak in the fraction of Pb bound to DOM seen in Figures 5.15 - 5.17 is not an issue as it occurs only when the fraction of Pb bound to DOM is significantly below the equilibrium position. This does not occur over the course of the simulation apart from at the very beginning of the equilibrating process performed prior to the start of the simulation proper.

No flow conditions are assumed for a range or reasons. The large time step length and simulation time allow for the assumption of no net water flow to be reasonable. The assumption of no flow conditions also removes the issue of the uncertainty of the rate of dispersivity. The relationship between dispersivity and flow rate is not straightforward and is almost always determined empirically [134]. By introducing fluid flow, some amount of hydrodynamic dispersion of the transported solutes would occur. Knowing what the rate of dispersivity would be without experimental data is not feasible, and estimating it would add more uncertainty to simulations already containing a large amount of it. It is therefore best to leave the issue of fluid flow and dispersivity out of this simulation and present it as a base case, used to demonstrate the potential of this DTRW based, reduced complexity model.

As Figure 5.18 shows, the overall effect of WTR addition is to increase the mobility of Pb, though the mobility is still low. The main cause of this is the increase of Pb in solution with increasing WTR addition. Increased DOM levels lead to an increase in the mobility of Pb [132]. DOM competes with sorption sites on the soil surface and SOM for Pb. This leads to a larger fraction of Pb being in solution. Pb bound to DOM is also more mobile than free Pb. The fraction of the total Pb bound to DOM is small, and so the total effect of these two factors is slight. The total amount of Pb exiting the domain is so small that this could be an important factor on the amount of Pb leaving the domain, even if it does not have a large effect on the partitioning of Pb.

## 5.7 Discussion

Though the reduced complexity DTRW model presented above has shown the potential to describe the partitioning of Pb well in some cases using simple relationships to describe the net effect of WTR addition in batch experiment conditions, and the expanded simulations presented in Figure 5.18 have agreed in broad trends with experimental data from other studies, there are still a large number of factors which

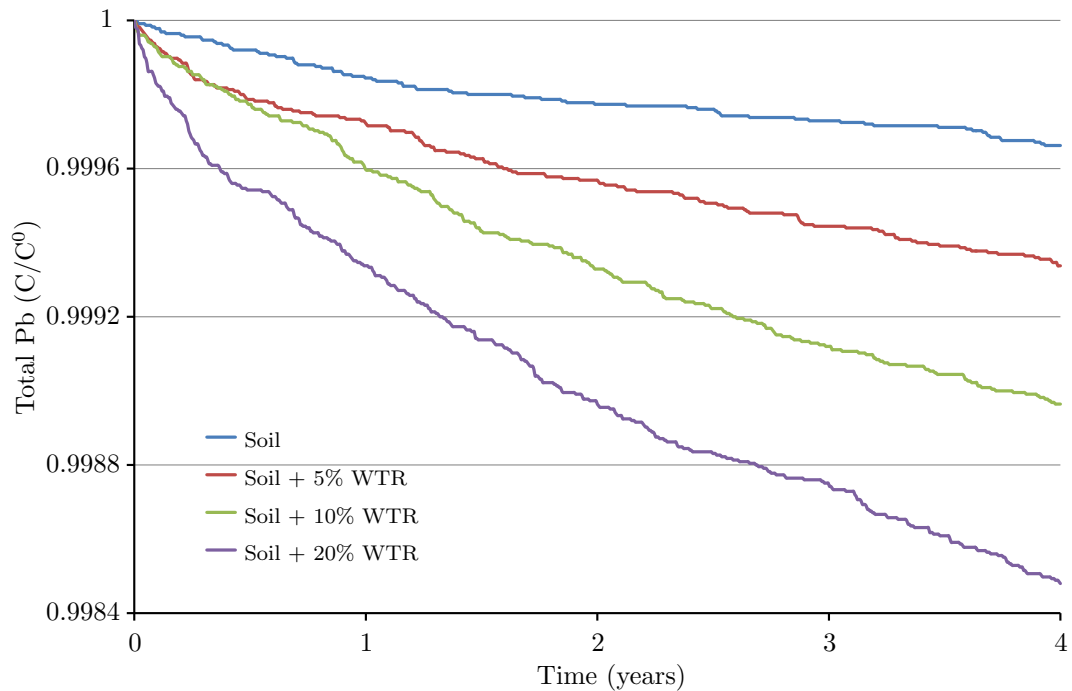


Figure 5.18: The change in total Pb levels over a period of 4 years in no flow conditions for a 50cm column of soil A in its original state and with 5%, 10% and 20% WTR additions. The equilibrium positions of  $K_d$  and  $K_c$  are determined using the fitted curves described in described in Tables 5.6 and 5.7.

could affect the behaviour of the system which have not been included. Any further research on this topic should be to address one or more of these issues.

The outputs generated by WHAM are not necessarily correct as the program does not include an exhaustive set of potential interactions between different trace elements. As the subsequent work is dependent on the quality of the outputs produced by WHAM this is a potential source of error. The general trend predicted by WHAM of the effect of WTR on the partitioning of Pb correlates with the limited amount of experimental data available [129]. In addition WHAM has been used by a large range of other researchers in the years since its original publication. It is therefore reasonable to assume that the results produced by WHAM are largely accurate.

The DOM levels used as inputs for WHAM were not taken at the same time or from the same exact samples as the other data for the trace element concentrations in the soils and WTR. They were instead taken from the soils used in the experimental aspects of the ROBUST project. The DOM levels used were probably different to the levels that would have existed in each of the three soil samples. By taking DOM measurements from the experimental soils, which are of much higher volume, an averaging effect was achieved, hopefully mitigating this effect.

WHAM assumes that saturated conditions are in place when performing its calculations. The interactions with air with the soil will produce a source and a sink of various chemical species which has some effect on the soil chemistry. The assumption of saturated conditions in effect leads to the assumption of anoxic conditions. The breakdown of organic matter is reduced in anoxic conditions due to the absence of biota [135]. This correlates with another imposed assumption that the only change in the levels of organic matter is due to the exiting of DOM at the bottom boundary of the domain. In reality organic would be removed by demcomposition throughout the domain, and added in the form of leaf litter at the surface. Plant life would also affect the chemical, as well as the hydraulic behaviour of the soil close

to the surface. As the study of Pb in soil tends to be with regards to its nature as a contaminant, the behaviour of Pb close to the surface, where the shortest pathway to human contact exists, this becomes an important aspect of the simulation of Pb in soil.

The addition of WTR has some effect on the hydraulic conductivity of the soil to which it is added. This in turn affects the dispersivity of solutes being transported through the soil. This is an important aspect of any more in-depth simulations of the effects of WTR on Pb contaminated soils, but is not realistically possible without a comprehensive experimental data set, which is currently not available. This is the most important next step in any further research.

Despite all these issues the framework for the simulation of Pb transport in soils using DTRW methods is a useful advance. Most importantly the methods presented here and in Chapters 3 and 4 have been designed so that they can easily be expanded to include capabilities that have not been included here.

## 5.8 Conclusion

In this chapter the method for the simulation of reactive and sorbing transport with the DTRW method has been utilised in the simulation of the effects of the addition of a WTR to soils contaminated with Pb. To achieve this a reversible reaction method was also implemented in the DTRW method which could be useful for other studies. The capacity of the DTRW solution to converge to the equilibrium position produced as an output from the WHAM [127] has been demonstrated. Simple rules for simulating the net effect of WTR addition on the partitioning of Pb were developed, compared with simulations based purely on simulation outputs from WHAM and used in a simple assessment on the effect of WTR addition on the diffusive mobility of Pb in a contaminated soil. The work presented in this chapter demonstrates a step up in the complexity of many models presented using particle tracking methods compared to those in the literature *e.g.* [35, 36, 77, 78, 81]. Models including similar levels of complexity are limited to a small number of studies *e.g.* [98].

Particle tracking methods are known to be computationally expensive, and the DTRW method presented here is no exception. In light of this the next chapter focuses on the optimization and acceleration of the DTRW model presented in this chapter and the two preceding it.

## Chapter 6

# Optimization and Acceleration of Computer Code

### Summary

One of the main issues associated with particle tracking methods is that they require more computational effort than continuum based approaches, especially for the simulation of reactions between solutes. This chapter discusses which parts of the Discrete Time Random Walk (DTRW) reactive transport solution require the most computational effort, and how this can be reduced by optimization, and acceleration using parallel computing.

### 6.1 Introduction

One of the main problems with using particle tracking methods for simulating chemical reactions is the computational cost required for the solution, as mentioned as an issue by other researchers *e.g.* [35, 36], and that this is mainly due to the nearest neighbour searches between the two particle species required for the solution of Algorithm 4.1. Particles are checked against the reaction criterion in order of decreasing separation, and therefore decreasing reaction probability. For the most naïve solution the nearest neighbour search between a particle from reactant species  $A$  and all of the particles from reactant species  $B$  this is an  $\mathcal{O}N^2$  problem when species  $B$  contains  $N$  particles. In this situation the computational effort to perform these nearest neighbour searches is the largest component of the program run time.

For example, the run time required to produce a single run of the reactive experimental setup shown in Figure 4.6 with  $\Delta t = 1\text{s}$  and particle density of 900 per  $\text{cm}^2$  and no optimization using a laptop with a dual-core, 2.1 GHz processor is  $\sim 2.67$  days. Of this run time  $\sim 3.4$  hours ( $\sim 5.4\%$ ) is taken up by the transport simulation and  $\sim 60.72$  hours ( $\sim 94.6\%$ ) is taken up by the reaction simulation. Approximately 40 seconds is addition of particles, array resizing and other housekeeping. For an optimization scheme to be efficient the reaction simulation is the first part of the solution which should be addressed. Of the time taken to perform the reaction simulations the nearest neighbour searches between particles of different species account for  $\sim 60.70$  hours. This is  $\sim 99.98\%$  of the run time required by the reaction simulation subroutine, and  $\sim 94.6\%$  of the total simulation run time. Expanding the DTRW method presented in Chapters 3 and 4 into three dimensions would require a large increase in the number of particles required for the simulation and would make the nearest neighbour searches an even larger fraction of the total run time. Increasing the complexity of the reaction system, *e.g.* from an  $A + B \rightarrow C$  system to a multicomponent system would also increase the proportion of the run time taken up by the nearest

neighbour searches. If there were several reactant species and multiple possible reactions between them then multiple nearest neighbour searches would need to be performed per particle, per time step. This would cover any increase in the run time produced by more complicated reaction criteria. Any effective optimization scheme should therefore focus first on the nearest neighbour searches required by these reaction simulation.

## 6.2 Optimization of Nearest Neighbour Searches

Benson & Meerschaert [35] state that “effective ordering of the particle arrays” is used to reduce the computational effort required for the nearest neighbour searches though offer no further explanation of how this is done. Ding *et al.* [36] use a  $k$ -d tree method developed by [136] to optimize their nearest neighbour searches. A  $k$ -d tree organizes a set of  $k$  dimensional data points into a tree structure. The tree begins with taking the coordinates of one of the particles and determining a plane that intersects the particle location and is constant in one dimension. All of the other particles are split into two subarrays depending on which side of the plane they are on. This is then repeated for each branch using one of the particles within its subarray. If the coordinates have more than one dimension then the dimension the splitting plane is parallel to is cycled with progression down the branches. Using a  $k$ -d tree for a nearest neighbour search is an  $\mathcal{O}(\log N)$  operation though implementing it with this performance is not straightforward [137].

Another method that can be used to reduce the computational cost of the nearest neighbour searches is spatial, or location sensitive, hashing. Here every particle in one of the species is allocated one or more subdomains within the simulation domain. When a nearest neighbour search is performed it is only performed for the particles within the same subdomain, limiting the size of the nearest neighbour searches and preventing searches being performed if there are no particles close enough for a reaction to occur. This has the advantage that if the two particle species are segregated and are far enough apart then no nearest neighbour searches need to be performed. This is elaborated on once the method by which the spatial hashing scheme is included in the reaction algorithm has been shown. A spatial hashing scheme is a much simpler method to implement than a  $k$ -d tree and can, in some situations, be more efficient [138] and so is the method used here.

### 6.2.1 Optimization Scheme Implementation

If there is no overlap between the subdomains within the solution domain used in the spatial hashing method there is the possibility for particles to be in very close proximity to a potential reaction partner and yet be unable to react due to it being in a different subdomain. To counter this subdomains overlap and are circular, for a two dimensional simulation domain. This has the added advantage that the check to see whether a particle lies within a subdomain is simpler than would be the case for rectilinear subdomains. It is important to make sure that a particle is not allowed to react more than once to maintain the mass balance, *e.g.* that for an  $A + B \rightarrow C$  system the total number of particles, if none are flowing into or out of the domain, is  $N_A + N_B + 2N_C$ . The method implemented to maintain the mass balance is outlined later.

The method by which the particles are placed into subdomains is shown in Algorithm 6.1. The outer loop of Algorithm 6.1,  $i = 1, N_N$ , proceeds over the set of nodes used in the Finite Element Method (FEM) solution of the water flow problem as, in every case shown so far in this thesis, they have been evenly spaced and generating a new set of variables is not required and would be a waste of memory. If the nodes used in the FEM solution were not evenly spaced then a new array would need to be generated to store the locations of the subdomain centroids. As such, in the following the discussion both ‘nodes’ and ‘subdomain centroids’ refer to the same points within the simulation domain. Each subdomain is

therefore formally defined as the locus of the points less than a distance  $r_{sd}$  from a one of a set of points laid out in a regular grid across the simulation domain, in practice the set of nodes. The distance  $r_{sd}$  is given as

$$r_{sd} = \frac{1}{2}\sqrt{x_s^2 + y_s^2} + 6\sqrt{D_h\Delta t} \quad (6.1)$$

where  $D_h$  is the hydraulic dispersivity,  $\Delta t$  is the timestep length and  $x_s$  and  $y_s$  are the spacings between the subdomain centroids in  $x$  and  $y$  respectively. The number of subdomains,  $N_{sd}$ , is linked to the spacing between the subdomain centroids by the expression

$$N_{sd} = \left(\frac{\Gamma_x}{x_s} + 1\right) \left(\frac{\Gamma_y}{y_s} + 1\right) \quad (6.2)$$

where  $\Gamma_x$  is the size of the domain in the  $x$  dimension and  $\Gamma_y$  is the size of the domain in the  $y$  dimension.

Subdomain  $i$  refers to the subdomain centred at node  $i$ . For each node all of the particles of the species over which the inner loops of Algorithm 4.1 are checked to see if they are less than the distance  $r_{sd}$  from node  $i$  and those which are, are within subdomain  $i$ . This gives all of the particles within three Colocation Probability Function (CLPF) standard deviations, as defined in Chapter 4, of a hypothetical particle whose closest subdomain centroid is the centroid of this subdomain. Particles that are further than  $6\sqrt{D_h\Delta t}$  apart have a very small probability of reaction and so can be left out of each subdomain without reducing the quality of the solution.

Algorithm 6.2 shows how the spatial hashing data produced by Algorithm 6.1 is utilized in the optimization of the reaction simulation solution (Algorithm 4.1). The outer loop of Algorithm 6.2 is over the set of particles of one of the reactant species, labelled species  $A$ . This is the species which was not run through Algorithm 6.1, which is labelled species  $B$ . The first action in the main loop is to determine which subdomain centroid is closest to particle  $ii$ . This subdomain is labelled subdomain  $e$ . The subroutine then proceeds in exactly the same manner as Algorithm 4.1 except that when any loop would be performed over the whole set of particles in species  $B$  it is instead performed over the set of particles in subdomain  $e$ .

Two important factors to take into account in the implementation of this optimization scheme are that the number of particles in each subdomain is almost certainly different, and that they probably change in size with every time step. The data stored in the subdomain arrays is the indices of the particles in the tracer location array rather than the locations of the tracers. This has the advantage of requiring less space, as the data stored are integers rather than floats, and that the subdomain data do not need to be changed during the reaction simulation. The locations in the tracer information array which do not contain particles instead contains nonsense values used to distinguish themselves from particle location data. If a particle does not exist, such as those removed by a reaction, then the  $x$  and  $y$  coordinates stored in the array are set to an artificially high value which, if used by some fault, will return no reaction. This means that the reacted particles do not need to be removed from the subdomain arrays. The first search on the particle locations in Algorithm 6.2 checks to see if the outer loop and inner loop particles are less than some distance,  $R_{max}$ , apart. If an outer loop particle is checked against a removed particle then this initial check always returns a negative result. Not having to rebuild each of the subdomain arrays each time a reaction takes place increases the run speed for no detrimental effects. This also maintains the mass balance of the system by preventing a particle from reacting more than once without having to rebuild the subdomain data arrays.

The subdomain data is stored as a linked list, denoted in Algorithm 6.1 as *ptr*. Each entry in the list contains the number of the node which located at the centroid of the subdomain, denoted as *ptr%n*, a one dimensional array of the indices of the particles located in that subdomain, *ptr%tr*, and a pointer to

the next entry in the list,  $ptr\%p$ . This first entry in the list is labelled head and the final entry tail, and both have the same suffixes. This is flexible and allows for efficient storage of the list of particle indices. Storing this data as an array would result in a large number of zero values being stored, especially if the particles only reside in a small part of the domain. Algorithm 6.1 is performed each timestep.

---

**Algorithm 6.1** Subdomain array build.

---

```

do  $i = 1, N_N$ 
  if (.NOT. ASSOCIATED(headB)) then
    ALLOCATE(headB)
    tailB => headB
    nullify(tailB%p)
    tailB%n = i
    counter = 0
    do  $j = 1, N_B$ 
      if  $\left(\sqrt{(x_{B_j} - x_{N_i})^2 + (y_{B_j} - y_{N_i})^2} \leq \left[0.5\sqrt{2\Delta x^2} + 12\sqrt{D_h\Delta t}\right]\right)$  then
        counter = counter + 1
      end if
    end do
    ALLOCATE(tailB%tr(counter))
    counter = 0
    do  $j = 1, N_B$ 
      if  $\left(\sqrt{(x_{B_j} - x_{N_i})^2 + (y_{B_j} - y_{N_i})^2} \leq \left[0.5\sqrt{2\Delta x^2} + 12\sqrt{D_h\Delta t}\right]\right)$  then
        counter = counter + 1
        tailB%tr(counter) = j
      end if
    end do
  else
    ALLOCATE(tailB%p)
    tailB => tailB%p
    nullify(tailB%p)
    tailB%n = i
    counter = 0
    do  $j = 1, N_b$ 
      if  $\left(\sqrt{(x_{B_j} - x_{N_i})^2 + (y_{B_j} - y_{N_i})^2} \leq \left[0.5\sqrt{2\Delta x^2} + 12\sqrt{D_h\Delta t}\right]\right)$  then
        counter = counter + 1
      end if
    end do
    ALLOCATE(tailB%tr(counter))
    counter = 0
    do  $j = 1, N_B$ 
      if  $\left(\sqrt{(x_{B_j} - x_{N_i})^2 + (y_{B_j} - y_{N_i})^2} \leq \left[0.5\sqrt{2\Delta x^2} + 12\sqrt{D_h\Delta t}\right]\right)$  then
        counter = counter + 1
        tailB%tr(counter) = j
      end if
    end do
  end if
end do

```

---

## 6.2.2 Optimization Scheme Effectiveness

The effectiveness of the spatial hashing scheme depends upon the particle density of the two species and the area of the subdomains used in the scheme, which is linked to the number of subdomains as shown by Equations 6.1 and 6.2. To test how effective the optimization scheme is, reactions of the form

---

**Algorithm 6.2** Optimized solution of reaction between two solutes in a particle tracking framework.

---

```

do ii = 1, NA
  if (xAii ≠ 109) then
    do i = 1, NN
      d(i) = √[(xPii - xNi)2 + (yPii - yNi)2]
    end do
    e = MINLOC(d)
    ptr => headB
    do
      if (.NOT. ASSOCIATED(ptr)) exit
      if (ptr%n = e) exit
      ptr => ptr%p
    end do
    counter = 0
    if (ALLOCATED(ptr%tr) = .TRUE.) then
      do i = 1, size(ptr%tr)
        if (√[(xAii - xptr%tr(Bjj))2 + (yAii - yptr%tr(Bjj))2] < Rmax) then
          counter = counter + 1
        end if
      end do
    end if
    if (counter > 0) then
      ALLOCATE(Rn(counter))
      ALLOCATE(Sr(counter))
      counter = 0
      do jj = 1, size(ptr%tr)
        if (√[(xAii - xptr%tr(Bjj))2 + (yAii - yptr%tr(Bjj))2] < Rmax) then
          counter = counter + 1
          Rn(counter) = ptr%tr(jj)
        end if
      end do
      do j = 1, size(Rn)
        Sr(j) = √[(xBip(j) + xAii)2 + (yBip(j) + yAii)2]
      end do
      e = Rn(MINLOC(Sr))
      Pr = Pmax exp [ -((xBip(e) - xAii)2 + (yBip(e) - yAii)2) / (8DhΔt) ]
      RU = U[0, 1]
      if (RU > Pr) then
        xC = (xAii + xRn(e)) / 2
        yC = (yAii + yRn(e)) / 2
        xA = 109
        yA = 109
        xB = 109
        yB = 109
      end if
    end if
  end if
end do

```

---

$A + B \longrightarrow C$  are run in a 9 cm by 9 cm domain containing particles of both reactant species. Both species are randomly distributed throughout the domain at the same density using a uniform Pseudorandom Number Generator (PRNG). The run times presented are for a single reaction step. Figure 6.1 shows the effect of subdomain area on run time for different initial particle densities. There is an optimal size for the subdomains to take, they do not simply improve run times as they decrease in size. This is due to the

balance between the improvement in the run time produced by using smaller subdomains and the extra time required to run the subdomain setup (Algorithm 6.1) as using smaller subdomains requires a greater number to cover the simulation domain. Figure 6.2 shows the change in the fraction of the run time of the reaction solution taken up by setting up the spatial hashing scheme (Algorithm 6.2). For this example the spatial hashing scheme is most effective when Algorithm 6.1 accounts for  $\sim 10\%$  of the reaction simulation run time. By displaying the data shown in Figure 6.1 in a different format the increase in time required by Algorithm 6.1 can be clearly seen. Figure 6.3 shows the change in run time with particle density for the unoptimized solution, and the optimized solution with different numbers of subdomains. The amount of subdomains correlates directly with the subdomain areas used as the controlling variable for Figures 6.1 and 6.2. For small particle densities and a large number of subdomains the optimized solution is slower than the unoptimized solution, the extra time required by Algorithm 6.1 outweighing the gains from reducing the amount of time required by the nearest neighbour searches.

In the simulation setup used to produce Figures 6.1 and 6.2 the two reactant species occupy the same parts of the domain until enough reactions have occurred to produce some sort of segregation, where the particles exist in pockets where none of the other reactant species exists and so no more reactions can occur. This is the situation in which a spatial hashing optimization scheme is least effective, whereas it is more effective in a situation where the two reactant species are spatially segregated except in a thin mixing zone where all of the reactions take place. If the particles are spatially segregated a nearest neighbour search still needs to be performed for particles which are too far away from any of the particles of the other reactant species for any reactions to occur. For example, in a simulation of the Gramling *et al.*, [75] a particle which has just entered the domain through the inflow boundary will be several cm from the nearest particle of the other reaction species, and so has zero probability of taking part in a reaction. Without the spatial hashing optimization scheme, when this particle is reached in the reaction subroutine a nearest neighbour search over all of the particles of the other reaction species is performed. When the spatial hashing scheme is in use no nearest neighbour search would be performed as there would be no particles of the other reactant species in the same subdomain. When the reactant species are well mixed across the entire domain, as in the setup used to generate the results shown in Figures 6.1 and 6.2, for most of the reaction solution there are some particles from the other reactant species in the same subdomain as a particle, so less unneeded nearest neighbour searches are performed. An additional factor is that in a well mixed scenario more of the reactants are removed by reactions each time step, reducing the number of particles for the nearest neighbour searches to loop over, reducing the run time in subsequent time steps. In the unoptimized solution of a scenario where sections of the two reactants species are segregated such that no reaction is possible between them, not only are a greater number of larger nearest neighbour searches required but, as a small fraction of the total number of particle is removed by reaction each time step, the amount of nearest neighbour searches required does not decrease as quickly as in the well mixed scenario.

In comparison to the unoptimized simulation run time mentioned earlier, in which a single run of the reactive experimental setup shown in Figure 4.6 with  $\Delta t = 1$  s and particle density of 900 per  $\text{cm}^2$  took  $\sim 1.84$  days ( $\sim 44.2$  hours), a simulation of the same setup utilizing the spatial hashing algorithm described in Algorithms 6.1 and 6.2 took  $\sim 6.85$  hours. The run time split between transport and reaction is  $\sim 52.5\%$  for transport and  $\sim 47.4\%$  for reactions. This makes the simulation  $\sim 6.45$  times faster to run and the time needed for the reaction simulation is reduced by a factor of  $\sim 12.5$ . Figure 6.4 shows how run time increases with particle density for a non optimized solution (Algorithm 4.1) and an optimized solution (Algorithm 6.2). The improvement in run time is roughly one order of magnitude, regardless of particle density.

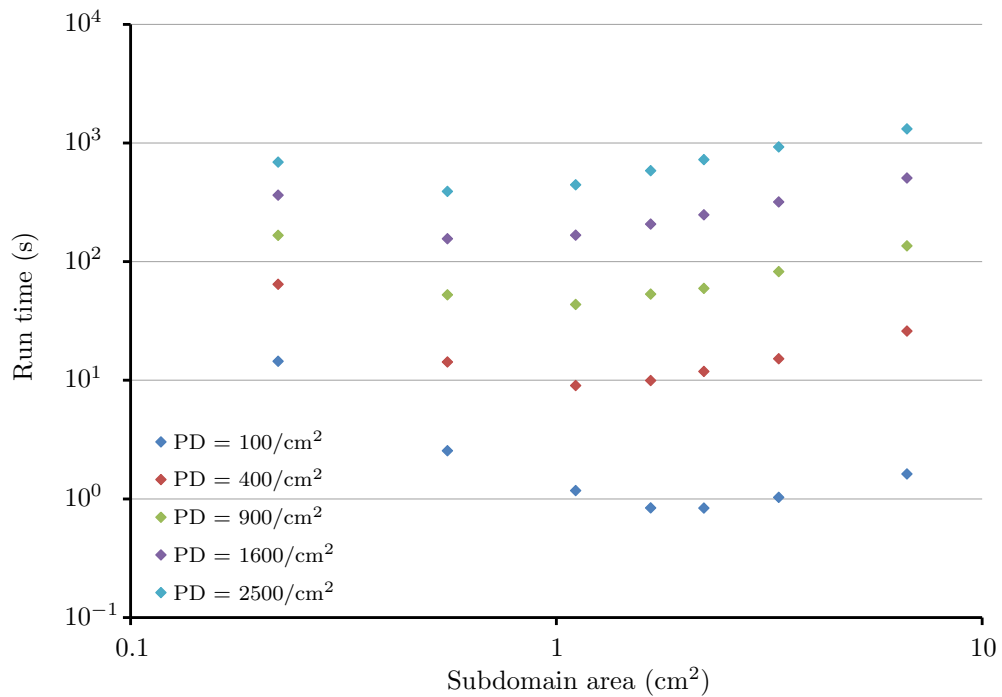


Figure 6.1: Change in run time with subdomain area for a single, no flow reaction step in a 9cm by 9cm domain at a range of initial particle densities.

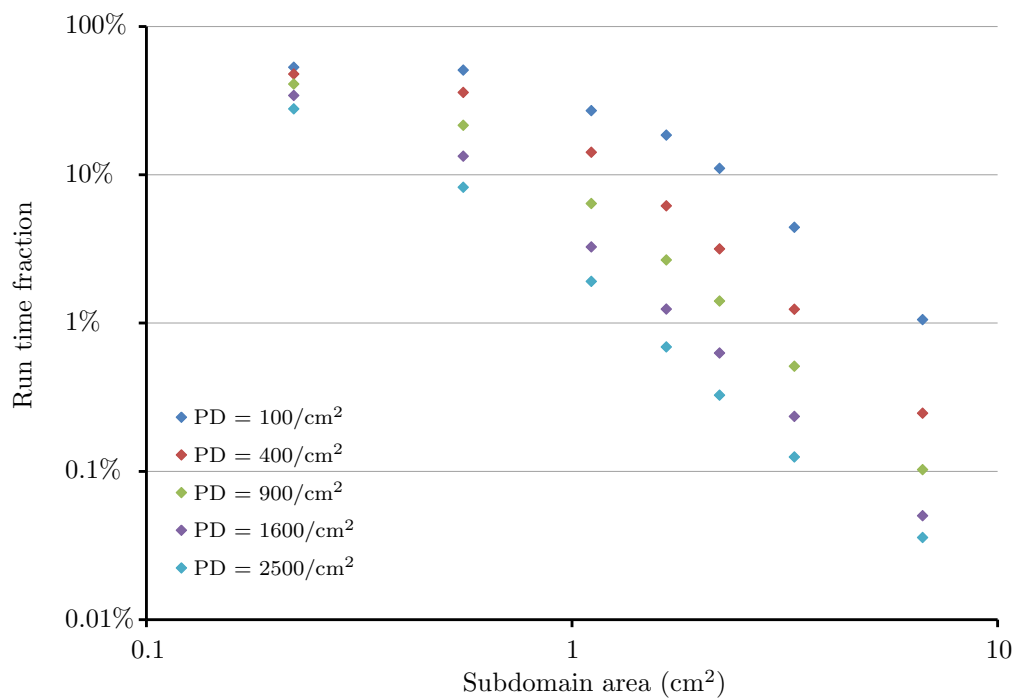


Figure 6.2: Change in the fraction of run time required by the solution of Algorithm 6.1 with subdomain area for a single, no flow reaction step in a 9cm by 9cm domain at a range of initial particle densities.

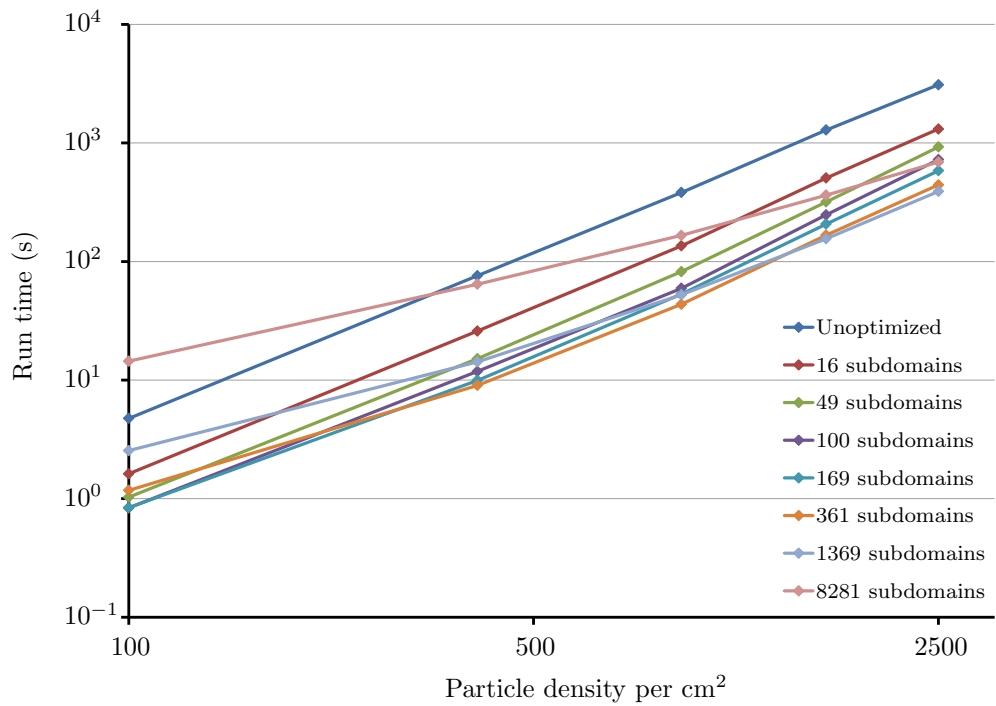


Figure 6.3: Change in run time with particle density for a single, no flow reaction step in a 9cm by 9cm domain for the unoptimized solution and optimized solution at a range of different number of subdomains.

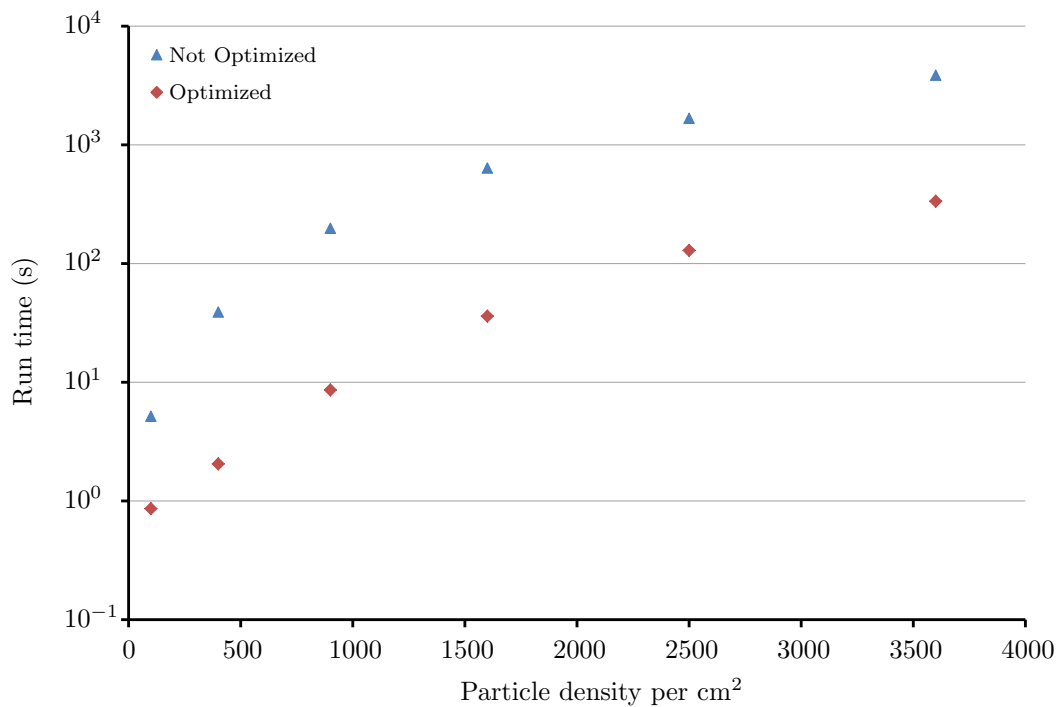


Figure 6.4: Comparison between optimized and unoptimized reaction solutions run times for a single, no flow reaction step in a 9cm by 9cm domain with a range of initial particle densities.

## 6.3 Code Acceleration Using Graphics Processing Units

Despite the optimization described above the run time for particle tracking simulations is still large. In the algorithm used to solve DTRW transport the solution of each particle's movement is independent of every other particle's movement. This makes the transport solution well suited to acceleration by some parallel computing method as it should scale well with the number of processors being used. As no communication is needed between the different parallel threads and a large number of similar operations are being performed, DTRW solutions should be well suited to acceleration using Graphics Processing Units (GPUs), processing units initially designed specifically for producing images though now capable of being utilized for scientific computing. A workstation or cluster utilizing GPUs contains one or more Central Processing Units (CPUs), referred to as the host, and one or more GPUs, referred to as the device(s). The code runs partially on each processor with the majority of the code on the CPU with computationally expensive sections being, in effect, outsourced to the GPU. A GPU is, as the name attests, a processor specifically for rendering computer graphics. Though GPUs can be included in the same silicon chip as a CPU or on a motherboard, all of the GPUs discussed here take the form of a separate card connected to the motherboard via a PCIe socket. This card contains the GPU chip and a separate bank of Random Access Memory (RAM).

Early use of GPUs for scientific computing involved utilizing an interface designed for graphics solutions for solving scientific problems. This difference between the original purpose of the programming interface and the scientific computing methods people wished to implement on GPUs made early GPU programming challenging. Later steps improved functionality for scientific applications but the languages used were still graphics based and so inaccessible to a large number of programmers [139]. Nvidia, one of the main manufacturers of GPUs, developed extensions for C, C++ and Fortran to utilize GPUs and began manufacturing GPUs intended for purposes other than computer graphics. The GPU extension of C and C++, referred to as Compute Unified Device Architecture (CUDA) C and CUDA C++ respectively, were developed first, followed by CUDA Fortran. These can be incorporated into existing code files and individual sections of the code outsourced to the GPU. The potential of GPUs for scientific computing is clear. A modern, top of the line CPU can have up to 16 processor cores running at 2.8 GHz within a single silicon chip [140] whereas modern, top of the line GPU can have up to 2688 processor cores running at 732 MHz within a single silicon chip [141]. Despite this some tasks are not well suited to running on GPUs as architecture of GPUs differs from that of CPUs and so the way in which parallel tasks can be performed is also different.

Flynn's taxonomy of computer architectures [142] sorts computers into one of four categories; Single Instruction Single Data (SISD), Single Instruction Multiple Data (SIMD), Multiple Instruction Single Data (MISD) and Multiple Instruction Multiple Data (MIMD). Of these we are only interested in SIMD and MIMD in a discussion of parallel computing. A CPU cluster or a modern, multi-core CPU is a MIMD computer. Each processor can perform different operations, or the same operations asynchronously on different pieces of data. The number of processor cores tends to be lower and so each core operates on a large section of the total data set [143]. By comparison GPUs are SIMD computers. Here each processor core performs the same operation at the same time as the other processor cores but on different pieces of data. The number of processor cores in GPUs tends to be higher and so the processors operate on smaller parts of the total data set. The GPU card used in this research is an Nvidia Tesla C2075, with 448 processor cores, each running at 1.15 GHz, and 6 GB of GDDR5 RAM (Figure 6.5). The 448 processor cores are divided into blocks of 32, referred to as Streaming Multiprocessors (SMs). Each SM acts as a SIMD, in that each of the cores within it must perform the same operations at the same time. Each different SM can act independently of the others within the chip.

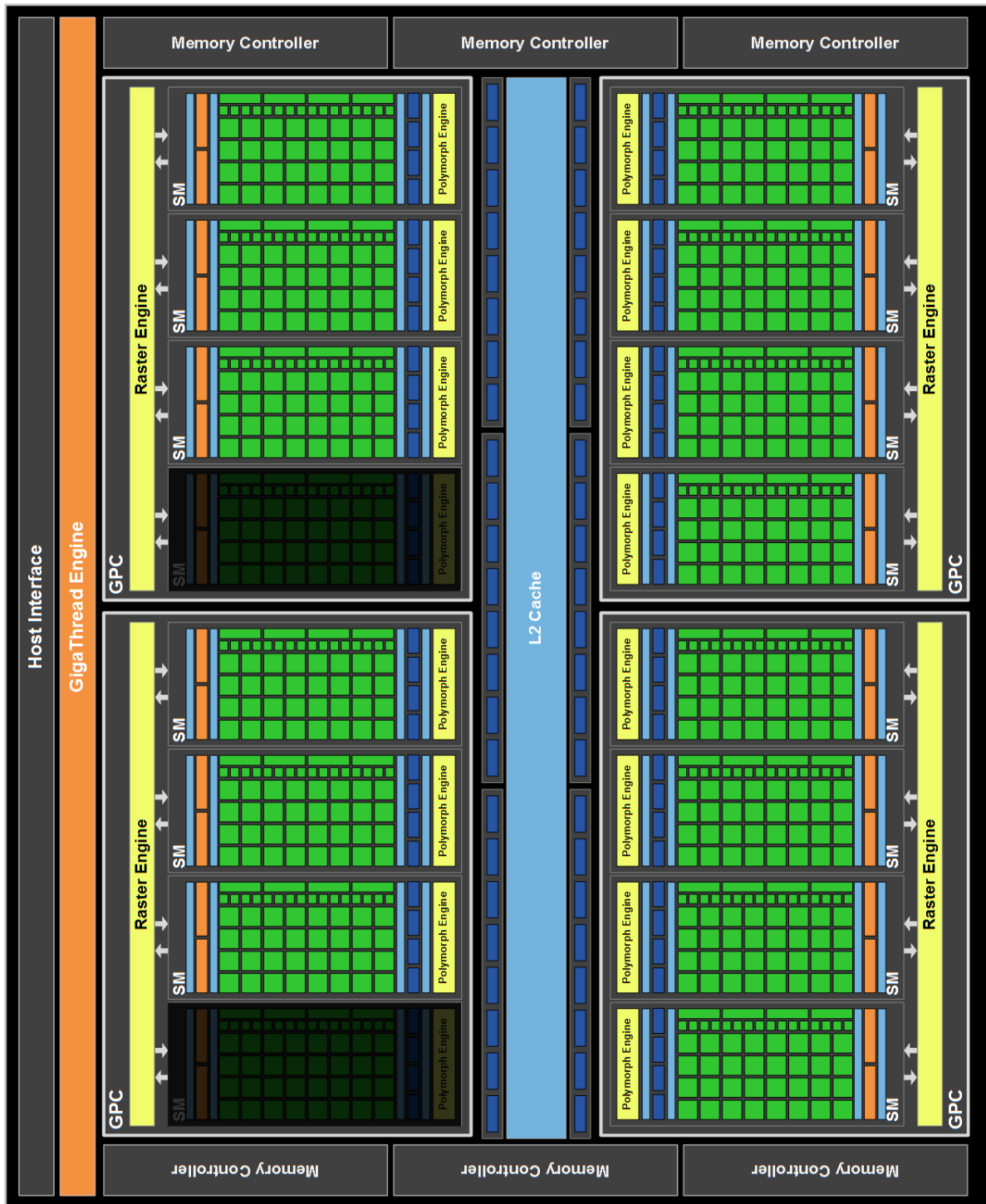


Figure 6.5: A schematic diagram showing the architecture of the chip used in an Nvidia Tesla C2075 GPU [144]. The blacked out SMs exist physically on the chip but are deactivated during the manufacturing process.

This type of parallelism is not well suited to all computing problems but it is well suited to the solution of particle tracking methods. The transport of each particle within a DTRW solution is entirely independent from all of the other particles and the solution of the particle transport problem requires the some thing to be done many times to different pieces of data.

Converting Fortran code to include GPU acceleration is relatively straightforward but, despite the significant difference in computation power, large, or indeed any, gains in run speed are not guaranteed. The GPU chip can only operate on data arrays stored on the device RAM. To perform a set of calculations the input data is passed from the host RAM to the device RAM and operated on by the GPU then the results are passed back to the host RAM. The transfer rate is limited by the speed of the host and device RAM and the PCIe bus. The PCIe bus is limited to 4 GB/s for PCIe x16 v1.x, which is the version of the bus in the computer used in this work. This is increased to 8 GB/s for PCIe x16 v2.x, and 15.75 GB/s for v3.0 [145]. The bandwidth of the Nvidia Tesla C2075 used here is 144 GB/s [146] and the bandwidth of the host RAM is 6.4 GB/s. The gains in run speed gained by performing operations on the GPU can end up being negated by the time required to transfer inputs and outputs to and from the device RAM if the problem is not well suited to solving on a GPU or if the code is poorly written. The computer used here has a dual core, 2.4 GHz processor and an Nvidia Tesla C2075 GPU card connected to the motherboard via a PCIe x16 v1.0 bus.

The method by which the DTRW transport solution is altered to run using a GPU is straightforward. The outer loop of Algorithm 4.1 is the parallelized loop, so each microprocessor within the GPU chip performs the entire transport solution for one particle. This can be counteracted by performing transfers and execution asynchronously to cover part of the transfer times with the execution times [143]. In addition to this the pre-allocation, inner ‘do’ loops of Algorithm 6.1 are also performed using the GPU.

The total run time using the GPU accelerated code is  $\sim 1.94$  hours, approximately 3.5 times faster than the CPU based code. Of this the transport simulation takes up  $\sim 130$  s ( $\sim 1.9\%$  of the total run time) and the reactions  $\sim 1.9$  hours ( $\sim 98.1\%$  of the total run time). This gives a speed up of  $\sim 100$  times for the transport simulation and  $\sim 1.7$  times for the reaction simulations. One of the main issues associated with the DTRW method is that the computational cost of the solution is far higher than that of FEM or Finite Difference Method (FDM) solutions of reactive mass transport. The use of a GPU for the acceleration of the code reduces the run time to more acceptable levels, especially for conservative transport simulations. Figure 6.6 shows the effect of increasing particle density on the run times required for the transport and reactions solutions with GPU acceleration in comparison with the run times for the unaccelerated transport and reactions simulations. The reduction in transport run time with the use of the GPU is clear, but it is also worth noting that the increase in run time with particle density is much less than the increase in reaction speed. This leads to a repeat of the initial situation where the reaction simulations dominate the run time requirements.

One of the aims of this research was to develop a model which generated a DTRW solution but could be run in a reasonable time on a desktop machine. Any large scale parallelism implemented could not have utilized a large number of CPUs to achieve an acceptable run speed for the solution and still used a desktop machine. Though having a CPU parallelized solution for comparison with the GPU accelerated solutions presented above would provide another interesting topic of discussion, the time required to alter the code for such a computer is not negligible, and so doing so for an example is not worthwhile. A precise comparison of how much CPU would be required to match the speed ups provided by the GPU is not possible but a brief discussion is still illuminating. Achieving the speedups produced for the reactive transport problem would not be difficult or require a large number of CPUs, but achieving the sort of speed up produced by the GPU for the conservative transport case would.

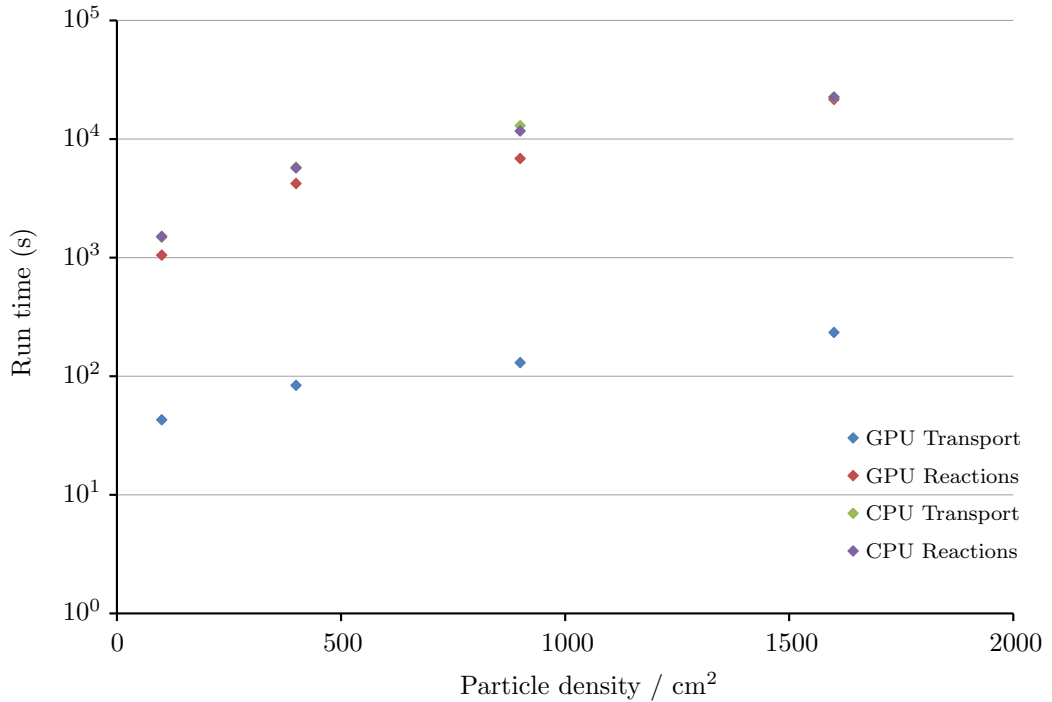


Figure 6.6: A comparison of the run times required for the transport and reaction solutions in the simulations of the reactive transport problem presented by [75] for the GPU accelerated and CPU based version of the solution. The simulations are to 619s run initial particle density is set to 900 particles per cm<sup>2</sup> and  $\Delta t=1s$ .

Parallel computing is well known to suffer from the law of diminishing returns, *i.e.* that doubling the number of processors does not always half the run time. The main cause of this is that it is generally not possible to parallelize all of a program and so reductions in run time asymptotically approach the run time of the non parallel components of the program. This is described by Amdahl’s Law [147] which states that for a program of which the fraction of the run time taken up by the non parallelizable components of the program is  $\alpha$ , the maximum speed up possible is

$$\lim_{P \rightarrow \infty} = \left( \frac{1 - \alpha}{P} + \alpha \right)^{-1} = \frac{1}{\alpha} \quad (6.3)$$

where  $P$  is the number of processors used in the parallel components of the program and  $\alpha$  is the fraction of the program which is not parallelizable. Amdahl’s Law [147] gives a general idea of the speed gains that can be achieved by parallelizing code but is on overly simplistic view. Linear, or even superlinear speed ups, where doubling the number of processors decreases the run time by more than half, are possible, even if not all the program can be parallelized. This can be due to the parallel algorithm for the solution of problem being a in a different form to the serial algorithm which is more efficient, in that the computational cost is lower, or it can be a caching effect. CPUs possess a cache of memory which is faster than the motherboard RAM though there is a smaller amount of it. If a program requires more memory than is available in the cache then it utilises the motherboard RAM. By increasing the number of processors, the amount of fast, cache memory available is increased and so the proportion of the storage required by the program held in the cache is increased. This decreases the total time required for memory access by the program, potentially producing a superlinear speed up [148].

The DTRW transport solution is of the type referred to as ‘embarassingly parallel’ as there is no

communication required between the different solutions of each particle's transport. As such a close to linear speed up, where doubling the number of processors halves the run time, could be possible but would require 100 CPU cores (this could be, for example, 25 quad core CPUs) to achieve the speed up produced by a single GPU. The power consumption required by a cluster 25 CPUs is roughly and order of magnitude greater than that required by a desktop with a single GPU.

The sorption simulations, as described in Chapters 4 and 5, are also accelerated using a GPU. The switching of the particle sorption states and the calculation of nodal concentration values from the particle field are both parallelized. The sorption subroutine was developed from the outset to make use of a GPU as its development took place after the transport and reaction solutions had been parallelized. Due to this there is no available comparison in speed up between CPU and GPU solutions as there is for the transport and reaction solutions.

Despite the useful increase in run speed produced by the use of a GPU the speed at which the GPU machine is able to perform the particle tracking simulations is limited by several factors. These include both software and hardware issues. The speed gains for reactive transport problems are limited. The speed gain produced by parallelizing the reaction simulations is much less than that which can be gained by parallelizing the transport simulations. The overall speed gain is therefore limited in a similar manner to the limitations on speed up described by Amdahl's Law [147]. As the reactions simulations make up  $\sim 50\%$  of the run time, achieving a total speed up greater than two times is impossible without increasing their run speed. A GPU is most effective when it can be given a large loop to operate over so that the gains from parallel processing can mask the losses caused by the necessary memory transfers. The largest loop in the reaction simulation is the outer loop over the number of particles in one of the reactant species. To parallelize this loop and maintain the mass balance of the system is complicated to implement. The transport simulation is effective as it is able to parallelize the outermost loop. Though the transport simulations are significantly faster than when performed with just a CPU there is still room for them to be made faster. The random numbers generated for use in the random walk part of the DTRW solution are performed on the host and then the array of random numbers is transferred to the device. This is done as the intrinsic Fortran PRNG does not yet operate within the CUDA Fortran environment. It is possible to call the CUDA C PRNG through Fortran but, as the transport simulations make up such a small fraction of the total run time at their current speed, this would not yield worthwhile increases in run speed for the effort required to implement it.

In addition to this the run speed is affected by some hardware limitations. It goes without saying that using a faster CPU would increase the run speed, especially as the limiting factor is the reaction simulations which are not parallelized. The speed ups which can be gained by the use of GPUs is limited by the rate of memory transfers to and from the device. The PCIe bus on the motherboard in the computer used here is a PCIe v1.0 bus which has a maximum memory transfer rate of 4 GB/s. Though the GPU is a high end model it is limited by this bottle neck in memory transfer between the host and the device. It is important for anyone thinking of utilizing a GPU for the acceleration of their code to ensure that it is not limited by quality of the host computer, and that the speed of the CPU is not the only factor which is important.

## 6.4 Conclusion

The primary issue with using particle tracking methods to simulate reactive transport is the run time required for the nearest neighbour searches in reaction simulation subroutine. In the most naïve approach they dominate the runtime required for the solution making optimization or acceleration of any other part of the solution worthless unless they are also addressed. Methods for reducing this computational

burden, such as the  $k$ -d trees used by Ding *et al.* [36] or the spatial hashing algorithm used here, are the most important step in reducing the run times required for the reaction solution. This optimization brings the reaction run times down to a level where acceleration of other parts of the solution via parallel processing techniques becomes worthwhile. The nature of the transport solution, in that the transport of each particle is independent of all the others, means that it is ideally suited to acceleration using a GPU. The speed up provided is shown to be of the order that would be expected from using a small cluster, but with much lower power consumption and with the convenience of being a desktop machine. The GPU is less successful at reducing the run times of the reaction simulations due to the limitations of the GPU chip architecture and so the balance in run times reverts to the initial situation of the reactions dominating the run times. Any further acceleration should prioritize the reaction simulations to produce the greatest gains in run speed. The overall effect of the optimization and acceleration techniques applied to the DTRW solution has significantly reduced the run times and so brought them down to more acceptable levels, especially when the reaction simulations are not required by the solution, such as in conservative transport simulations.

## Chapter 7

# Conclusions

This thesis has focused on the development and investigation of the behaviour of a Discrete Time Random Walk (DTRW) particle tracking model for the simulation of bimolecular reactions, sorption and transport of solutes in soils. The desired application was the simulation of the effects of Water Treatment Residual (WTR) addition on soils contaminated with Pb, which was achieved by using the developed DTRW model in tandem with the chemical speciation Windermere Humic Aqueous Model (WHAM) [24].

A two dimensional DTRW particle tracking model for the simulation of solute transport in porous media is used, based upon the method presented in Prickett *et al.* [61]. The method is implemented using the semianalytical path line method presented by Pollock [66] under the assumption that any porous media flow solution used to drive the advective transport is produced using the Finite Element Method (FEM) using four-noded bilinear isoparametric elements. The use of regular shaped finite elements or the Finite Difference Method (FDM) are therefore also possible as they would be treated as a simple case of isoparametric finite elements. This model is benchmarked against experimental data from Gramling *et al.* [75] and its robustness under varying non-physical controls assessed.

A bimolecular reaction model was then developed based on the Colocation Probability Function (CLPF) method presented by Benson & Meerschaert [35]. The probability density function used to describe the dispersive or diffusive transport of the simulation particles are used to determine the probability of two particles being colocated over a given timestep, based on their current positions and their rates of dispersive, or in no flow conditions diffusive, transport. The behaviour of this scheme under variation of the three controlling factors, particle density, maximum reaction probability and CLPF standard deviation are presented and analysed, for both the DTRW method, where particles can be located at any location within the simulation domain, and the Continuous Time Random Walk (CTRW) method, where particles are constrained to a lattice of locations. It was shown that by restricting particle locations to lattice sites the minimum reaction rate as a function of CLPF standard deviation is artificially inflated.

This method was then benchmarked against experimental data for an instantaneous, bimolecular reaction which had also been used for the benchmarking of several other simulation studies [75]. The experimental reaction rate is limited by the imperfect mixing of the two reactants. This effect is simulated in the DTRW method by limiting the maximum reaction probability,  $P_{max}$ . The results are compared with other simulation studies [36, 78, 92] and the pros and cons of each method discussed with respect to those of the DTRW method presented here. The DTRW method compares well with the methods presented by other simulation studies and is a more robust and flexible method, with regards to simulation of more complicated scenarios, whether this includes more complicated reaction systems or flow regimes. This flexibility is achieved by using variable parameters to control the reaction rate within a system.

Relying on the particle density to control reaction rate *e.g.* [36, 96] works well in constant flow regimes but cannot be expanded to systems with either spatially or temporally variable flow regimes.

A method for the simulation of sorption in the DTRW framework was also then developed. Sorption simulations using CTRW methods have generally been achieved by altering the time dependency of the transport simulation *e.g.* [80, 81]. This includes no description of the partitioning of the adsorbate between the pore fluid and the soil solids. The method developed here includes such a description by switching particles between a free and an immobilized state. The local ratio between the amount of particles between these two states, and the desired ratio are used to determine the probability of particle switching state, and so drive the simulation towards an equilibrium position. This method was tested against experimental data using a purely empirical fit, and a fit based on an equilibrium position derived from a non-linear Freundlich isotherm presented by Rubin *et al.*, [83], and shown to produce good fits in both cases.

The methods for the simulation of sorption of bimolecular transport presented in Chapter 4 are then, with the addition of a reverse reaction mechanism, applied to the simulation of the effects of adding WTR to contaminated soils on the partitioning of Pb between the soil solids, pore fluids and Dissolved Organic Matter (DOM). Simulating all of the various trace element species and their interactions within a soil using the DTRW is beyond the scope of this work, but simply ignoring certain species without knowing anything about their effects on the desired output is not acceptable. To address this the chemical speciation model WHAM [23, 24] was used to assess the net effect of WTR addition on the partitioning of Pb. The ratios between adsorbed Pb and Pb in true solution,  $K_d$ , and Pb bound to DOM and total Pb,  $K_c$  were determined using WHAM. Curves empirically relating  $K_d$  to total Soil Organic Matter (SOM) and  $K_c$  to total DOM were then produced and used to control the partitioning of Pb between its three potential states, in solution, adsorbed to soil solids and bound to DOM, in the DTRW model. A simple simulation assessing the change in mobility of Pb over a four year period for the original soil and three different levels of WTR addition was then performed for the soil which the reduced complexity rules best fitted to the WHAM outputs. Though very simple in nature, the fitted partitioning rules were able to reproduce the situations predicted by WHAM well for two of the soils sample data sets available, though the quality of the results for the third data set were of a lower quality.

Most studies of non-conservative transport in porous media using particle tracking methods have either focused on bimolecular reactions [35, 36, 77–79, 96] or sorption of single solute [80, 81, 83], though a small number of studies have simulated systems of greater complexity *e.g.* [98]. The results presented in Chapter 5 show that the DTRW method can be used to simulate systems of reasonable complexity, and that by utilizing chemical speciation models such as WHAM reasonable approximations of the behaviour of systems with a large number of interacting components can be simulated using a small number of particle species.

In addition to the expansion of the DTRW method to more complicated systems and the application of a reduced complexity scheme to reduce the number of chemical species required by simulations this thesis also presents the optimization and acceleration of the developed code. Despite the advantages of the method and the expansions to its capabilities presented in this thesis the computational expense of simulations using the DTRW method will still limit its popularity. The scheme described in Chapter 6 for the optimization of the reaction solution is shown to reduce the computation time required by the reaction solution by approximately an order of magnitude. This increase in speed was observed over a set of simulations with a total difference in the number of particles of one order of magnitude. By decreasing the fraction of the total run time required by the reaction simulation, the optimization or acceleration of other aspect of the solution became worthwhile. The acceleration of the transport solution using an Nvidia

Graphics Processing Unit (GPU) was able to reduce the run times require by approximately two orders of magnitude. Though the acceleration of the reaction simulations was not as effective, the net effect was a speed up of  $\sim 3.5$  times. The combination of these two approaches significantly reduced the run times required by the reactive transport simulations performed for this thesis and have brought particle tracking methods into a realm of more acceptable run times.

Though advancements to the functionality of the DTRW method have been made by this work a number of useful advancements were beyond the scope of this work and so were not included. The most important of these is the inclusion of variable flow fields in the simulations. The DTRW solution has been implemented with the assumption that the FEM would be used for any flow solution used to drive the advective transport. The combination of this with dispersivity data would allow for more in depth simulation of the effect of WTR on the partitioning of Pb. Other extensions to the model that could improve the quality of the simulations presented in this thesis are more complicated fitted rules including effects such as competition between solutes for adsorption sites, creation and destruction of DOM and SOM and variable pH. This could allow the reduced complexity to work effectively for a greater range of soils.

The simulation of a greater range of experiments to allow for the relationship between, flow rate, dispersivity and mixing limited reactions, and the reaction rate controls  $P_{max}$  and  $\sigma_s$  would also be an interesting and useful direction for further work related to the research presented in this thesis. The reaction method presented has been designed for flexibility though limited characterization of its links to physical processes have been possible.

The work presented in this thesis provides an expansion to the field of particle tracking methods, both expanding the capabilities of the method, and investigating, in depth, the behaviour of existing techniques used within it.

# References

- [1] “Previously-developed land that may be available for development: England 2007 - Results from the national land use database of previously-developed land,” tech. rep., U.K. Department for Communities and Local Government, 2007.
- [2] “Dealing with contaminated land in England and Wales: A review of progress from 2000-2007 with Part 2A of the Environmental Protection Act,” tech. rep., U.K. Environment Agency, 2009.
- [3] T. Cairney and D. Hobson, *Contaminated Land: Problems and Solutions*. E & FN Spon, 2nd ed., 1998.
- [4] D. K. Asante-Duah, *Managing contaminated sites: Problem diagnosis and development of site restoration*. Wiley, 1996.
- [5] T. Cairney, “Soil cover reclamations,” in *Reclaiming contaminated land*, Blackie, 1987.
- [6] C. Bamba, S. Robertson, A. Kasim, J. Smith, J. M. Cairns-Nagi, A. Copeland, N. Finlay, and K. Johnson, “Healthy land? an examination of the area-level association between brownfield land and morbidity and mortality in England,” *Environment and Planning A*, In Press.
- [7] J.-Q. Jiang and B. Lloyd, “Progress in the development and use of ferrate (vi) salt as an oxidant and coagulant for water and wastewater treatment,” *Water Research*, vol. 36, no. 6, pp. 1397–1408, 2002.
- [8] A. Babatunde, Y. Zhao, Y. Yang, and P. Kearney, “Reuse of dewatered aluminium-coagulated water treatment residual to immobilize phosphorus: Batch and column trials using a condensed phosphate,” *Chemical Engineering Journal*, vol. 136, no. 2, pp. 108–115, 2008.
- [9] M. G. McDonald and A. W. Harbaugh, *A modular three-dimensional finite-difference ground-water flow model*. Scientific Publications Company, 1984.
- [10] M. C. Hill, “A computer program(MODFLOWP) for estimating parameters of a transient, three-dimensional, ground-water flow model using nonlinear regression,” tech. rep., U.S. Geological Survey, 1992.
- [11] A. W. Harbaugh, E. R. Banta, M. C. Hill, and M. G. McDonald, *MODFLOW-2000, the U.S. Geological Survey modular ground-water model: User guide to modularization concepts and the ground-water flow process*. U.S. Geological Survey Reston, 2000.
- [12] A. W. Harbaugh, *MODFLOW-2005, the U.S. Geological Survey modular ground-water model: The ground-water flow process*. U.S. Geological Survey, 2005.

- [13] C. Zheng, “MT3D, a modular three-dimensional transport model for simulation of advection, dispersion and chemical reactions of contaminants in groundwater systems,” tech. rep., U.S. Environmental Protection Agency, 1990.
- [14] C. Zheng and P. Wang, “MT3DMS, a modular three-dimensional multi-species transport model for simulation of advection, dispersion and chemical reactions of contaminants in groundwater systems; documentation and users guide,” tech. rep., U.S. Army Engineer Research and Development Center, 1999.
- [15] C. Zheng, “MT3DMS v5.2 supplemental users guide,” tech. rep., U.S. Army Engineer Research and Development Center, Department of Geological Sciences, University of Alabama, 2006.
- [16] T. Clement, “RT3D: A modular computer code for simulation reactive multispecies transport in 3-dimensional groundwater systems,” tech. rep., Pacific Northwest National Laboratory, 1997.
- [17] T. Clement, Y. Sun, B. Hooker, and J. Petersen, “Modeling multispecies reactive transport in ground water,” *Ground Water Monitoring & Remediation*, vol. 18, no. 2, pp. 79–92, 1998.
- [18] J. Šimůnek, K. Huang, M. Šejna, and M. T. H. van Genuchten, “The HYDRUS-1D software package for simulating the one-dimensional movement of water, heat, and multiple solutes in variably saturated media. Version 1.0, IGWMC-TPS-70,” *International Ground Water Modeling Center, Colorado School of Mines, Golden, Colorado*, p. 186, 1998a.
- [19] J. Šimůnek, M. Šejna, and M. T. H. van Genuchten, “The HYDRUS-1D software package for simulating two-dimensional movement of water, heat, and multiple solutes in variably saturated media. Version 2.0, IGWMC-TPS-53,” *International Ground Water Modeling Center, Colorado School of Mines, Golden, Colorado*, p. 202, 1998b.
- [20] H. Lin, D. Richards, C. Talbot, G. Yeh, J. Cheng, H. Cheng, and N. Jones, “FEMWATER: A three-dimensional finite element computer model for simulating density-dependent flow and transport in variably saturated media.,” *US Army Corps of Engineers, Waterways Experiment Station. Technical Report no. CHL-9712*, 1997.
- [21] M. D. White and M. Oostrom, “STOMP, subsurface transport over multiple phases, theory guide,” tech. rep., Pacific Northwest National Lab, 1996.
- [22] W. E. Nichols, N. Aimo, M. Oostrom, and M. D. White, “STOMP: Subsurface transport over multiple phases. application guide,” tech. rep., Pacific Northwest National Laboratory, 1997.
- [23] E. Tipping, “Humic ion-binding model VI: an improved description of the interactions of protons and metal ions with humic substances,” *Aquatic geochemistry*, vol. 4, no. 1, pp. 3–47, 1998.
- [24] E. Tipping, “WHAMC-A chemical equilibrium model and computer code for waters, sediments, and soils incorporating a discrete site/electrostatic model of ion-binding by humic substances,” *Computers & Geosciences*, vol. 20, no. 6, pp. 973–1023, 1994.
- [25] N. Ottosen and H. Petersson, *Introduction to the Finite Element Method*. Prentice Hall, 1992.
- [26] H. Darcy, “Public fountains in the city of Dijon.,” *Dalmont, Paris*, vol. 647, 1856.
- [27] A. Einstein, “On the molecular kinetic theory of heat required by the movement of particles suspended in liquids at rest.,” *Annalen der Physik*, vol. 322, no. 8, pp. 549–560, 1905.

- [28] J. Bear and A. H. D. Cheng, *Modeling Groundwater Flow and Contaminant Transport.*, vol. 23 of *Theory and Application of Transport in Porous Media*. Springer, 2010.
- [29] L. Neumann, J. Šimůnek, and F. Cook, “Implementation of quadratic upstream interpolation schemes for solute transport into hydrus-1d,” *Environmental Modelling & Software*, vol. 26, no. 11, pp. 1298–1308, 2011.
- [30] K. Huang, J. Simunek, and M. T. H. Van Genuchten, “A third-order numerical scheme with upwind weighting for solving the solute transport equation,” *International Journal for Numerical Methods in Engineering*, vol. 40, no. 9, pp. 1623–1637, 1997.
- [31] M. T. H. Van Genuchten and W. G. Gray, “Analysis of some dispersion corrected numerical schemes for solution of the transport equation,” *International Journal for Numerical Methods in Engineering*, vol. 12, no. 3, pp. 387–404, 1978.
- [32] B. P. Leonard, “A stable and accurate convective modelling procedure based on quadratic upstream interpolation,” *Computer Methods in Applied Mechanics and Engineering*, vol. 19, no. 1, pp. 59–98, 1979.
- [33] X. Chu and M. A. Mariño, “Improved compartmental modeling and application to three-phase contaminant transport in unsaturated porous media,” *Journal of Environmental Engineering*, vol. 132, no. 2, pp. 211–219, 2006.
- [34] Y.-C. Lin and M. A. Medina Jr., “Incorporating transient storage in conjunctive stream–aquifer modeling,” *Advances in Water Resources*, vol. 26, no. 9, pp. 1001–1019, 2003.
- [35] D. Benson and M. Meerschaert, “Simulation of chemical reaction via particle tracking: Diffusion-limited versus thermodynamic rate-limited regimes,” *Water Resources Research*, vol. 44, p. W12201, 2008.
- [36] D. Ding, D. A. Benson, A. Paster, and D. Bolster, “Modeling bimolecular reactions and transport in porous media via particle tracking,” *Advances in Water Resources*, 2012.
- [37] D. Toussaint and F. Wilczek, “Particle–antiparticle annihilation in diffusive motion,” *The Journal of Chemical Physics*, vol. 78, p. 2642, 1983.
- [38] A. Garder, D. Peaceman, and A. Pozzi, “Numerical calculation of multidimensional miscible displacement by the method of characteristics,” *Society of Petroleum Engineers Journal*, vol. 4, no. 1, pp. 26–36, 1964.
- [39] G. Pinder and H. Cooper, “A numerical technique for calculating the transient position of the saltwater front,” *Water Resources Research*, vol. 6, no. 3, pp. 875–882, 1970.
- [40] S. Neuman, “A Eulerian-Lagrangian numerical scheme for the dispersion-convection equation using conjugate space-time grids,” *Journal of Computational Physics*, vol. 41, no. 2, pp. 270–294, 1981.
- [41] S. Neuman, “Adaptive Eulerian–Lagrangian finite element method for advection–dispersion,” *International Journal for Numerical Methods in Engineering*, vol. 20, no. 2, pp. 321–337, 1984.
- [42] K. Itō, “On stochastic differential equations,” *Memoirs of the American Mathematical Society*, vol. 4, pp. 289–302, 1951.

- [43] A. D. Fokker, “The mean energy of rotating electrical dipoles in radiation fields,” *Annalen der Physik*, vol. 348, no. 5, pp. 810–820, 1914.
- [44] M. Planck *Sitzungsberichte der Königlich Preussischen Akademie der Wissenschaften zu Berlin*, p. 324, 1917.
- [45] A. Kolmogoroff, “On analytical methods in the theory of probability,” *Mathematische Annalen*, vol. 104, pp. 415–458, 1931.
- [46] E. Montroll and G. Weiss, “Random walks on lattices. II.,” *Journal of Mathematical Physics*, vol. 6, p. 167, 1965.
- [47] E. W. Montroll, “Random walks on lattices. III. Calculation of first-passage times with application to exciton trapping on photosynthetic units.,” *Journal of Mathematical Physics*, vol. 10, p. 753, 1969.
- [48] E. W. Montroll and H. Scher, “Random walks on lattices. IV. Continuous-time walks and influence of absorbing boundaries.,” *Journal of Statistical Physics*, vol. 9, no. 2, pp. 101–135, 1973.
- [49] H. Scher and M. Lax, “Stochastic transport in a disordered solid. i. theory.,” *Physical Review B*, vol. 7, pp. 4491–4502, May 1973.
- [50] B. Berkowitz and H. Scher, “On characterization of anomalous dispersion in porous and fractured media.,” *Water Resources Research*, vol. 31, no. 6, pp. 1461–1466, 1995.
- [51] B. Berkowitz and H. Scher, “Anomalous transport in random fracture networks.,” *Physical Review Letters*, vol. 79, no. 20, pp. 4038–4041, 1997.
- [52] B. Berkowitz and H. Scher, “Theory of anomalous chemical transport in random fracture networks.,” *Physical Review E*, vol. 57, no. 5, p. 5858, 1998.
- [53] B. Berkowitz, H. Scher, and S. Silliman, “Anomalous transport in laboratory-scale, heterogeneous porous media.,” *Water Resources Research*, vol. 36, no. 1, pp. 149–158, 2000.
- [54] G. Margolin and B. Berkowitz, “Application of continuous time random walks to transport in porous media.,” *The Journal of Physical Chemistry B*, vol. 104, no. 16, pp. 3942–3947, 2000.
- [55] B. Berkowitz, G. Kosakowski, G. Margolin, and H. Scher, “Application of continuous time random walk theory to tracer test measurements in fractured and heterogeneous porous media.,” *Ground Water*, vol. 39, no. 4, pp. 593–604, 2001.
- [56] G. Kosakowski, B. Berkowitz, and H. Scher, “Analysis of field observations of tracer transport in a fractured till.,” *Journal of Contaminant Hydrology*, vol. 47, no. 1, pp. 29–51, 2001.
- [57] G. Margolin and B. Berkowitz, “Spatial behavior of anomalous transport.,” *Physical Review E*, vol. 65, no. 3, p. 031101, 2002.
- [58] M. Dentz, A. Cortis, H. Scher, and B. Berkowitz, “Time behavior of solute transport in heterogeneous media: Transition from anomalous to normal transport.,” *Advances in Water Resources*, vol. 27, no. 2, pp. 155–173, 2004.
- [59] M. Dentz, H. Scher, D. Holder, and B. Berkowitz, “Transport behavior of coupled continuous-time random walks.,” *Physical Review E*, vol. 78, no. 4, p. 041110, 2008.

- [60] S. Ahlstrom, H. Foote, R. Arnett, C. Cole, and R. Serne, “Multi-component mass transport model: theory and numerical implementation (discrete parcel random walk version).,” *Report BNWL-2127, Battelle Pacific Northwest Lab*, 1977.
- [61] T. Prickett, T. Naymik, and C. Lonnquist, “A ‘random walk’ solute transport model for selected groundwater quality evaluations.,” *Illinois State Water Survey Bulletin*, vol. 65, 1981.
- [62] A. Tompson and L. Gelhar, “Numerical simulation of solute transport in three-dimensional, randomly heterogeneous porous media.,” *Water Resour. Res.*, vol. 26, no. 10, pp. 2541–2562, 1990.
- [63] A. F. Tompson, R. D. Falgout, S. G. Smith, W. J. Bosl, and S. F. Ashby, “Analysis of subsurface contaminant migration and remediation using high performance computing,” *Advances in Water Resources*, vol. 22, no. 3, pp. 203–221, 1998.
- [64] P. Salamon, D. Fernández-García, and J. J. Gómez-Hernández, “A review and numerical assessment of the random walk particle tracking method.,” *Journal of Contaminant Hydrology*, vol. 87, no. 3, pp. 277–305, 2006.
- [65] G. Uffink, “A random walk method for the simulation of macrodispersion in a stratified aquifer.,” *Relation of Groundwater Quality and Quantity, Proceedings of the Hamburg symposium*, vol. 146, pp. 103–114, 1985.
- [66] D. Pollock, “Semianalytical computation of path lines for finite-difference models.,” *Ground Water*, vol. 26, no. 6, pp. 743–750, 1988.
- [67] B. Arnold, S. Kuzio, and B. Robinson, “Radionuclide transport simulation and uncertainty analyses with the saturated-zone site-scale model at yucca mountain, nevada,” *Journal of Contaminant Hydrology*, vol. 62, pp. 401–419, 2003.
- [68] M. Bechtold, J. Vanderborght, O. Ippisch, and H. Vereecken, “Efficient random walk particle tracking algorithm for advective-dispersive transport in media with discontinuous dispersion coefficients and water contents,” *Water Resources Research*, vol. 47, no. 10, p. W10526, 2011.
- [69] D. A. Benson, M. M. Meerschaert, and J. Revielle, “Fractional calculus in hydrologic modeling: A numerical perspective,” *Advances in Water Resources*, vol. 51, pp. 479–497, 2013.
- [70] E. M. LaBolle, G. E. Fogg, and A. F. Tompson, “Random-walk simulation of transport in heterogeneous porous media: Local mass-conservation problem and implementation methods,” *Water Resources Research*, vol. 32, no. 3, pp. 583–593, 1996.
- [71] P. Mostaghimi, B. Bijeljic, and M. Blunt, “Simulation of flow and dispersion on pore-space images,” *SPE Journal*, vol. 17, no. 4, pp. 1131–1141, 2012.
- [72] C. Cordes and W. Kinzelbach, “Continuous groundwater velocity fields and path lines in linear, bilinear, and trilinear finite elements.,” *Water Resources Research*, vol. 28, no. 11, pp. 2903–2911, 1992.
- [73] W. Kinzelbach and G. Uffink, “The random walk method and extensions in groundwater modelling.,” in *Transport Processes in Porous Media*, pp. 761–787, Springer, 1991.
- [74] R. Stratonovich, “A new representation for stochastic integrals and equations,” *SIAM Journal on Control*, vol. 4, no. 2, pp. 362–371, 1966.

- [75] C. Gramling, C. Harvey, and L. Meigs, “Reactive transport in porous media: A comparison of model prediction with laboratory visualization.,” *Environmental Science & Technology*, vol. 36, no. 11, pp. 2508–2514, 2002.
- [76] D. S. Rajee and V. Kapoor, “Experimental study of bimolecular reaction kinetics in porous media.,” *Environmental Science & Technology*, vol. 34, no. 7, pp. 1234–1239, 2000.
- [77] Y. Edery, H. Scher, and B. Berkowitz, “Modeling bimolecular reactions and transport in porous media.,” *Geophysical Research Letters*, vol. 36, no. 2, 2009.
- [78] Y. Edery, H. Scher, and B. Berkowitz, “Particle tracking model of bimolecular reactive transport in porous media.,” *Water Resources Research*, vol. 46, no. 7, p. W07524, 2010.
- [79] A. Paster, D. Bolster, and D. Benson, “Particle tracking and the diffusion-reaction equation.,” *Water Resources Research*, 2013.
- [80] J. Deng, X. Jiang, X. Zhang, W. Hu, and J. W. Crawford, “Continuous time random walk model better describes the tailing of atrazine transport in soil.,” *Chemosphere*, vol. 71, no. 11, pp. 2150–2157, 2008.
- [81] N. Li and L. Ren, “Application of continuous time random walk theory to nonequilibrium transport in soil.,” *Journal of Contaminant Hydrology*, vol. 108, no. 3, pp. 134–151, 2009.
- [82] G. Margolin, M. Dentz, and B. Berkowitz, “Continuous time random walk and multirate mass transfer modeling of sorption.,” *Chemical Physics*, vol. 295, no. 1, pp. 71–80, 2003.
- [83] S. Rubin, I. Dror, and B. Berkowitz, “Experimental and modeling analysis of coupled non-fickian transport and sorption in natural soils.,” *Journal of Contaminant Hydrology*, vol. 132, pp. 28–36, 2012.
- [84] A. D. McNaught and A. Wilkinson, *IUPAC. Compendium of Chemical Terminology, (the "Gold Book")*. Blackwell Scientific Publications, 2nd ed., 1997.
- [85] M. von Smoluchowski, “Attempt a mathematical theory of the coagulation kinetics of colloidal solutions.,” *Zeitschrift für Physikalische Chemie*, vol. 92, no. 129-168, p. 9, 1917.
- [86] T. Engel and P. Reid, *Physical Chemistry*. Pearson, 3rd ed., 2006.
- [87] M. von Smoluchowski, “Three lectures about diffusion, Brownian motion and coagulation of colloidal particles.,” *Zeitschrift für Physik*, vol. 17, pp. 557–585, 1916.
- [88] A. Tompson and D. Dougherty, “Particle-grid methods for reacting flows in porous media with application to fisher’s equation.,” *Applied Mathematical Modelling*, vol. 16, no. 7, pp. 374–383, 1992.
- [89] D. T. Gillespie, “A general method for numerically simulating the stochastic time evolution of coupled chemical reactions.,” *Journal of Computational Physics*, vol. 22, no. 4, pp. 403–434, 1976.
- [90] D. T. Gillespie, “Exact stochastic simulation of coupled chemical reactions.,” *The Journal of Physical Chemistry*, vol. 81, no. 25, pp. 2340–2361, 1977.
- [91] Y. Edery, A. Guadagnini, H. Scher, and B. Berkowitz, “Reactive transport in disordered media: Role of fluctuations in interpretation of laboratory experiments.,” *Advances in Water Resources*, 2011.

- [92] X. Sanchez-Vila, D. Fernàndez-Garcia, and A. Guadagnini, “Interpretation of column experiments of transport of solutes undergoing an irreversible bimolecular reaction using a continuum approximation.,” *Water Resources Research*, vol. 46, no. 12, 2010.
- [93] A. Rubio, A. Zalts, and C. El Hasi, “Numerical solution of the advection–reaction–diffusion equation at different scales.,” *Environmental Modelling & Software*, vol. 23, no. 1, pp. 90–95, 2008.
- [94] R. Haggerty, C. F. Harvey, C. Freiherr von Schwerin, and L. C. Meigs, “What controls the apparent timescale of solute mass transfer in aquifers and soils? a comparison of experimental results,” *Water Resources Research*, vol. 40, no. 1, 2004.
- [95] Y. Awakura, T. Doi, and H. Majima, “Determination of the diffusion coefficients of  $\text{CuSO}_4$ ,  $\text{ZnSO}_4$ , and  $\text{NiSO}_4$  in aqueous solution,” *Metallurgical Transactions B*, vol. 19, no. 1, pp. 5–12, 1988.
- [96] Y. Zhang, C. Papelis, P. Sun, and Z. Yu, “Evaluation and linking of effective parameters in particle-based models and continuum models for mixing-limited bimolecular reactions,” *Water Resources Research*, vol. 49, no. 8, pp. 4845–4865, 2013.
- [97] G. Sposito, *The Chemistry of Soils*. Oxford University Press, 1989.
- [98] Y. Edery, H. Scher, and B. Berkowitz, “Dissolution and precipitation dynamics during dedolomitization,” *Water Resources Research*, vol. 47, no. 8, p. W08535, 2011.
- [99] A. M. Tartakovsky, G. Redden, P. C. Lichtner, T. D. Scheibe, and P. Meakin, “Mixing-induced precipitation: Experimental study and multiscale numerical analysis,” *Water Resources Research*, vol. 44, no. 6, 2008.
- [100] B. Berkowitz, A. Cortis, M. Dentz, and H. Scher, “Modeling non-fickian transport in geological formations as a continuous time random walk.,” *Reviews of Geophysics*, vol. 44, no. 2, 2006.
- [101] M. Levy and B. Berkowitz, “Measurement and analysis of non-fickian dispersion in heterogeneous porous media.,” *Journal of Contaminant Hydrology*, vol. 64, no. 3-4, pp. 203–226, 2003.
- [102] D. Hillel, *Environmental Soil Physics*. Academic Press, 1998.
- [103] M. B. McBride, *Environmental Chemistry of Soils*. Oxford University Press, 1994.
- [104] P. V. Brady, R. T. Cygan, and K. L. Nagy, “Surface charge and metal sorption to kaolinite,” in *Adsorption of Metals by Geomedia*, Academic Press, 1998.
- [105] M. E. Essington, *Soil and water chemistry: An integrative approach*. CRC press, 2003.
- [106] C. A. Impellitteri, Y. Lu, J. K. Saxe, H. E. Allen, and W. J. Peijnenburg, “Correlation of the partitioning of dissolved organic matter fractions with the desorption of Cd, Cu, Ni, Pb and Zn from 18 Dutch soils,” *Environment International*, vol. 28, no. 5, pp. 401–410, 2002.
- [107] H. Irving and R. J. P. Williams, “The stability of transition-metal complexes,” *Journal of the Chemical Society*, pp. 3192–3210, 1953.
- [108] A. Okorie, J. Entwistle, and J. R. Dean, “The application of *in vitro* gastrointestinal extraction to assess oral bioaccessibility of potentially toxic elements from an urban recreational site,” *Applied Geochemistry*, vol. 26, no. 5, pp. 789–796, 2011.

- [109] M. F. Azizian and P. O. Nelson, “Lead sorption, chemically enhanced desorption, and equilibrium modeling in an iron-oxide-coated sand and synthetic groundwater system,” in *Adsorption of Metals by Geomaterials*, Academic Press, 1998.
- [110] S. Sauve, M. McBride, and W. Hendershot, “Soil solution speciation of Lead (II): Effects of organic matter and pH,” *Soil Science Society of America Journal*, vol. 62, no. 3, pp. 618–621, 1998.
- [111] E. A. Jenne, “Adsorption of metals by geomedia: Data analysis, modeling, controlling factors, and related issues,” in *Adsorption of Metals by Geomedia*, Academic Press, 1998.
- [112] H. B. Bradl, “Adsorption of heavy metal ions on soils and soils constituents,” *Journal of Colloid and Interface Science*, vol. 277, no. 1, pp. 1–18, 2004.
- [113] H. M. F. Freundlich, “On adsorption in solutions,” *Zeitschrift für Physikalische Chemie*, vol. 57, pp. 385–470, 1906.
- [114] I. Langmuir, “The constitution and fundamental properties of solids and liquids. Part I. Solids,” *Journal of the American Chemical Society*, vol. 38, no. 11, pp. 2221–2295, 1916.
- [115] S. Sauve, W. Hendershot, and H. E. Allen, “Solid-solution partitioning of metals in contaminated soils: dependence on pH, total metal burden, and organic matter,” *Environmental Science & Technology*, vol. 34, no. 7, pp. 1125–1131, 2000.
- [116] W. Stumm, C. Huang, and S. Jenkins, “Specific chemical interaction affecting the stability of dispersed systems,” *Croatica Chemica Acta*, vol. 42, pp. 223–244, 1970.
- [117] D. Dzombak and F. Morel, *Surface Complexation Modelling*. Wiley, 1990.
- [118] N. Barrow, “Reaction of anions and cations with variable-charge soils,” *Advances in Agronomy*, vol. 38, pp. 183–230, 1985.
- [119] J. Westall and H. Hohl, “A comparison of electrostatic models for the oxide/solution interface,” *Advances in Colloid and Interface Science*, vol. 12, no. 4, pp. 265–294, 1980.
- [120] D. L. Parkhurst and C. Appelo, “Description of input and examples for PHREEQC version 3. a computer program for speciation, batch-reaction, one-dimensional transport, and inverse geochemical calculations,” *US Geological Survey Techniques and Methods, Book 6, Modeling Techniques*, 2013.
- [121] C. E. Halim, S. A. Short, J. A. Scott, R. Amal, and G. Low, “Modelling the leaching of Pb, Cd, As, and Cr from cementitious waste using PHREEQC,” *Journal of hazardous materials*, vol. 125, no. 1, pp. 45–61, 2005.
- [122] S.-P. Han, W. Naito, Y. Hanai, and S. Masunaga, “Evaluation of trace metals bioavailability in Japanese river waters using DGT and a chemical equilibrium model,” *Water Research*, 2013.
- [123] X. Mao, X. Liu, and D. Barry, “Application of PHREEQC on solute transport in groundwater,” *Hydrogeology and Engineering Geology*, vol. 31, no. 2, pp. 20–24, 2004.
- [124] R. Marsac, M. Davranche, G. Gruau, M. Bouhnik-Le Coz, and A. Dia, “An improved description of the interactions between rare earth elements and humic acids by modeling: PHREEQC-Model VI coupling,” *Geochimica et Cosmochimica Acta*, vol. 75, no. 19, pp. 5625–5637, 2011.

- [125] Z. Shi, D. M. D. Toro, H. E. Allen, and D. L. Sparks, “A WHAM- based kinetics model for Zn adsorption and desorption to soils,” *Environmental Science & Technology*, vol. 42, no. 15, pp. 5630–5636, 2008.
- [126] Z. Shi, D. M. Di Toro, H. E. Allen, and D. L. Sparks, “A general model for kinetics of heavy metal adsorption and desorption on soils,” *Environmental Science & Technology*, vol. 47, no. 8, pp. 3761–3767, 2013.
- [127] E. Tipping, J. Rieuwerts, G. Pan, M. Ashmore, S. Lofts, M. Hill, M. Farago, and I. Thornton, “The solid–solution partitioning of heavy metals (Cu, Zn, Cd, Pb) in upland soils of England and Wales.,” *Environmental pollution*, vol. 125, no. 2, pp. 213–225, 2003.
- [128] L. Weng, E. J. Temminghoff, S. Lofts, E. Tipping, and W. H. Van Riemsdijk, “Complexation with dissolved organic matter and solubility control of heavy metals in a sandy soil,” *Environmental Science & Technology*, vol. 36, no. 22, pp. 4804–4810, 2002.
- [129] L. Watson, K. Johnson, and S. Roberston, “Development of a sustainable methodology using recycled minerals and organic waste to remediate contaminated land,” *Durham University MEng 4th Year Project, Unpublished*, 2011.
- [130] H. Sato, M. Yui, and H. Yoshikawa, “Ionic diffusion coefficients of  $\text{Cs}^+$ ,  $\text{Pb}^{2+}$ ,  $\text{Sm}^{3+}$ ,  $\text{Ni}^{2+}$ ,  $\text{SeO}_4^{2-}$  and  $\text{TcO}_4^-$  in free water determined from conductivity measurements,” *Journal of Nuclear Science and Technology*, vol. 33, no. 12, pp. 950–955, 1996.
- [131] R. Beckett, Z. Jue, and J. C. Giddings, “Determination of molecular weight distributions of fulvic and humic acids using flow field-flow fractionation,” *Environmental Science & Technology*, vol. 21, no. 3, pp. 289–295, 1987.
- [132] R. N. Jordan, D. R. Yonge, and W. E. Hathhorn, “Enhanced mobility of Pb in the presence of dissolved natural organic matter,” *Journal of Contaminant Hydrology*, vol. 29, no. 1, pp. 59–80, 1997.
- [133] F. Qin, X.-q. Shan, and B. Wei, “Effects of low-molecular-weight organic acids and residence time on desorption of Cu, Cd, and Pb from soils,” *Chemosphere*, vol. 57, no. 4, pp. 253–263, 2004.
- [134] C. P. Lowe and D. Frenkel, “Do hydrodynamic dispersion coefficients exist?,” *Physical Review Letters*, vol. 77, pp. 4552–4555, Nov 1996.
- [135] D. L. Rowell, *Soil Science: Methods and Applications*. Longman, 1994.
- [136] J. L. Bentley, “Multidimensional binary search trees used for associative searching,” *Communications of the Association for Computing Machinery*, vol. 18, no. 9, pp. 509–517, 1975.
- [137] J. H. Friedman, J. L. Bentley, and R. A. Finkel, “An algorithm for finding best matches in logarithmic expected time,” *Association for Computing Machinery Transactions on Mathematical Software*, vol. 3, no. 3, pp. 209–226, 1977.
- [138] M. Datar, N. Immorlica, P. Indyk, and V. S. Mirrokni, “Locality-sensitive hashing scheme based on p-stable distributions,” in *Proceedings of the twentieth annual symposium on Computational geometry*, pp. 253–262, ACM, 2004.
- [139] J. D. Owens, M. Houston, D. Luebke, S. Green, J. E. Stone, and J. C. Phillips, “Gpu computing,” *Proceedings of the IEEE*, vol. 96, no. 5, pp. 879–899, 2008.

- [140] Advanced Micro Devices Inc., “<http://products.amd.com/en-us/opteroncpuresult.aspx?f1=>,” 2013.
- [141] NVIDIA Corporation, “<http://www.nvidia.co.uk/object/tesla-server-gpus-uk.html>,” 2013.
- [142] M. J. Flynn, “Some computer organizations and their effectiveness,” *Computers, IEEE Transactions on*, vol. 100, no. 9, pp. 948–960, 1972.
- [143] G. Ruestsch and M. Fatica, *CUDA Fortran for Scientists and Engineers*. NVIDIA Corporation, 2011.
- [144] “[http://www.tomshardware.com/gallery/block\\_diagram\\_two\\_off,0101-242385-0-2-3-1-png-.html](http://www.tomshardware.com/gallery/block_diagram_two_off,0101-242385-0-2-3-1-png-.html),”
- [145] PCI-SIG, “<http://www.pcisig.com/specifications/pciexpress/>,” 2013.
- [146] NVIDIA Corporation, “<http://www.nvidia.com/object/personal-supercomputing.html>,” 2013.
- [147] G. M. Amdahl, “Validity of the single processor approach to achieving large scale computing capabilities,” in *Proceedings of the April 18-20, 1967, Spring Joint Computer Conference, AFIPS '67 (Spring)*, (New York, NY, USA), pp. 483–485, ACM, 1967.
- [148] A. Grama, A. Gupta, G. Karypis, and V. Kumar, *Introduction to Parallel Computing*. Pearson, 2003.